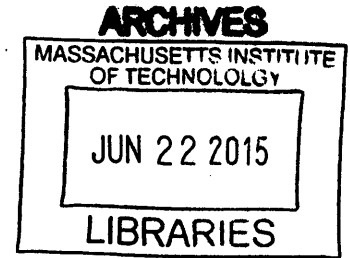Engineering Nanostructured Selective Layers
for Reverse Osmosis Membranes

by

Jason Richard Kovacs

B.S. Chemical and Biomolecular Engineering
Georgia Institute of Technology, Atlanta, GA – 2008

SUBMITTED TO THE DEPARTMENT OF CHEMICAL ENGINEERING IN PARTIAL FULFILLMENT
OF THE REQUIREMENTS FOR THE DEGREE OF

DOCTORATE OF PHILOSOPHY IN CHEMICAL ENGINEERING
AT THE
MASSACHUSETTS INSTITUTE OF TECHNOLOGY

June 2015

©2015, Jason Richard Kovacs. All rights reserved.

The author hereby grants to MIT permission to reproduce and to distribute publicly paper and
electronic copies of this thesis document in whole or in part in any medium now known or
hereafter created.

Signature redacted

Signature of Author: _____
Department of Chemical Engineering
May 4th, 2015

Signature redacted

Certified by: _____
Dr. Paula T. Hammond
David H. Koch (1962) Professor in Engineering
Thesis Supervisor

Signature redacted

Accepted by: _____
Dr. Richard D. Braatz
Professor of Chemical Engineering
Chairman, Committee for Graduate Studies

Engineering Nanostructured Selective Layers
for Reverse Osmosis Membranes

by

Jason Richard Kovacs

Submitted to the Department of Chemical Engineering on May 4th, 2015 in Partial Fulfillment of the Requirements for the Degree of Doctorate of Philosophy in Chemical Engineering

TECHNICAL SUMMARY

A major challenge to communities across the world in the next century will be ensuring millions have access to adequate freshwater resources. Studies from the UN World Health Organization indicate that over 1.1 billion people currently lack access to reliable and secure freshwater supplies, with an estimated 2.5 million deaths per year from diseases associated with poor access and sanitation in 2007. Reverse osmosis (RO), a process through which water is desalted via pressurized flow past a salt-selective membrane, is an energy-efficient method to generate freshwater from oceanic, brackish, and waste water sources. However, there are a number of challenges to scaling up RO processes to large scale production, including the need to improve membrane selectivity and throughput.

One method to assemble selective layers for RO membranes is layer-by-layer (LbL) assembly, which is a flexible, scalable assembly technique that enables the incorporation of a myriad of polyelectrolytes and inorganic nanoparticles into thin films. There is a gap in the scientific literature concerning the use of LbL to generate RO selective layers where previous approaches have not taken full advantage of the LbL process to incorporate nanomaterials that can generate ordered nanostructures for salt rejection. In particular, high-aspect ratio clay platelets are ideal for such a purpose; it was hypothesized that effective salt rejection could be achieved by hindering the diffusion of solvated ions through nano-channels formed by the platelets embedded within a polymer matrix. This body of work examines the application of spray layer-by-layer (spray-LbL) assembly with clay composite thin film architectures to generate nanostructured selective layers for use in RO membrane technology.

First, appropriate substrates were identified as support layers for the deposition of spray-LbL assembled clay composite thin films. Both electrospun bisphenol-A polysulfone (PSU) mats of varying fiber diameter and polyethersulfone (PES) ultrafiltration (UF) membranes with varying pore diameters were examined. Second, a range of materials were investigated for the spray-LbL deposition of clay composite films. Laponite clay platelets were incorporated into several different film architectures including strong polyelectrolytes as well as cross-linkable weak polyelectrolytes

to form both bilayer and tetralayer film architectures. The clay content was controlled via manipulating assembly conditions such as the pH and spray times of the film components.

Assembled membrane architectures were tested at industrial RO operating conditions in dead-end permeation cells and evaluated for salt rejection, water permeability, and mechanical strength. Ultimately, it was determined the most uniform and robust films were those deposited on PES membranes with 30 nm pores, closely matching the characteristic length of the LAP clay platelets to reduce the impact of bridging. Although all the film architectures tested exhibited significantly greater water permeability than commercially available RO selective layers, the salt selectivity was found to be highly dependent on the film architecture and assembly conditions. The best performing film architecture consisted of a cross-linked clay composite tetralayer film, exhibiting salt rejection of 89% for aqueous 10,000 ppm NaCl solution with an order of magnitude increase in water permeability over a commercially-available thin film composite membrane. The key conclusion drawn from the studies indicate the presence of an optimal zone where the incorporation of clay platelets introduces additional salt selectivity via size exclusion, balanced with the cross-linked polymer component of the film to improve the mechanical strength and reduce the risk of critical defect formation during operation.

Taken together, these investigations represent a new approach using structured nanomaterials to develop next generation clay composite RO selective layers. The increased water permeability of the clay composite selective layers offers an attractive advantage in desalting applications where high flux is desirable, such as with brackish water resources as well as in membrane unit operations near their thermodynamic limit.

Thesis Supervisor: Dr. Paula T. Hammond
Title: David H. Koch (1962) Professor in Engineering

MEMBERS OF THESIS COMMITTEE

Thesis Supervisor
Dr. Paula T. Hammond
Professor of Chemical Engineering
Massachusetts Institute of Technology

Thesis Committee Chair
Dr. Martin Z. Bazant
Professor of Chemical Engineering
Massachusetts Institute of Technology

Thesis Committee Member
Dr. Gregory C. Rutledge
Professor of Chemical Engineering
Massachusetts Institute of Technology

"I thought that if we could ever competitively, at a cheap rate, get fresh water from salt water, that it would be in the long-range interests of humanity which would really dwarf any other scientific accomplishment. I am hopeful that we will intensify our efforts in that area."

– John F. Kennedy, 35th President of the United States

April 12th, 1962

Table of Contents

Acknowledgments

Completing a thesis at MIT is a Herculean endeavor and at times appears all but impossible, but thankfully I have had the opportunity to engage with a community of people to aid in the process. I would like to take a moment and reflect on these contributions to this final report.

First and foremost, I would like to thank my fellow labmates who have trained me on equipment, given expertise and insight on research and presenting data, aided in running experiments, proofread my drafts, and provided valued conversation on subjects scientific and otherwise: Ben Almquist, Steven Castleberry, Fevzi Cebeci, Nicole Davis, Amanda Engler, Bryan Hsu, Nasim Hyder, Kevin Krogman, Becky Ladewski, David Liu, Sun Hwa Lee, Younjin Min, Abby Oelker, Michael Petr, Ray Samuel, Anita Shukla, Kittipong Saetia, and Liz Welch. I would like to thank my UROP, Chaoyang Liu, for bringing her energy and an extra set of hands to the project. In particular, my office mates at the ISN have provided a welcome diversion and sanity break from the long days.

I would also like to thank my adviser, Prof. Paula Hammond, who gave me the opportunity to work in her lab and provided mentorship over the last six years, from the first steps until completion and every pitfall. My committee members, Profs. Gregory Rutledge and Martin Bazant, have also challenged me to put forth the best product I could, and this document is stronger for it.

Additionally, the staff at the Department of Chemical Engineering Office have been amazing to work with and understanding of the difficulties encountered along the way: Joel Danshaw and Suzanne MacGuire. The administrative assistants for our lab, Christine Preston and Liz Galoyan, have also been excellent and have hammered together schedules from a million conflicts.

The staff at the ISN, both the technical experts as well as the administrative side, has been quick to answer questions and wonderful to work with: Bill DiNatale, Donna Johnson, Steve Kooi, Marlisha McDaniels, and Amy Tatem-Bannister. I would also like to thank Tim McClure of the CMSE at MIT and Deborah Pheasant from the Biophysical Instrumentation Facility for their aid.

Since arriving at MIT, I have met several people outside of the department who have provided a friendly ear when they seemed far and few between. I'd like to thank my good friends at Ashdown, the board gaming group, the television crew, and my fellow history buffs for the late nights, the conversation, the entertainment, and the weekend trips: Frederike Ahr, Nicole Casasnovas, Orpheus Chatzivasileiou, Gabriel Collins, Andrea Dubin, Amneet Gulati, Arghavan Safani-Naini, Alex Leder, Will Leight, Brandon Luders, Jordan Romvary, Drew Rzeznik, Theja Tulabandhula, Tiffany Chen, Andy Wright, Yvonne Yamanaka, and last but not least Amanda Zangari. I would like to thank the housemasters at Ashdown for building such a fun and inviting community: Terry & Ann Orlando, Yuriy & Katie Roman, and Adam Berinsky & Deidre Logan.

Finally, I would like to dedicate this work to my parents, Richard and Denise Kovacs, as well as my brother Andrew. They have been steadfast and beloved friends, and have been with me every step of the way. Their support has been invaluable to me not just over the last six years but a lifetime. Without it, I cannot imagine completing this venture and tackling the next. Thank you.

List of Abbreviations and Terminology

α	aspect ratio [of clay platelets]
AFM	atomic force microscopy
ATR-FTIR	attenuated total reflectance – FTIR
BPEI	branched poly(ethylenimine)
BPEIC	catechol-modified branched poly(ethylenimine)
CP	concentration polarization
Dip-LbL	dipping layer-by-layer [assembly]
DHHCA	3,4-dihydroxyhydrocinnamic acid
DLS	dynamic light scattering
Dopamine	3,4-dihydroxyphenethylamine
ED	electrodialysis
EDC	1-ethyl-3-(3-dimethylaminopropyl)carbodiimide hydrochloride
FO	forward osmosis
FTIR	Fourier transform infrared spectroscopy
Espun	electrospun [mats]
GO	graphene oxide
Hexa-LAP	hexalayer-laponite films (PAH/PAA/PAH/PAA/PAH/LAP)
LAP	laponite clay
LbL	layer-by-layer [assembly]
LPEI	linear poly(ethylenimine)
MD	membrane distillation
MED	multiple-effect distillation
MES	2-(N-morpholino)ethanesulfonic acid (buffer)
MF	microfiltration
MSF	multi-stage flash
MMT	montmorillonite
MWCO	molecular weight cut-off
NaAc	sodium acetate (buffer)
NF	nanofiltration
NHS	N-hydroxysuccinimide
P_s	permeability of salt
P_w	permeability of water

p_x	pressure (of feed, f or permeate, p)
PAA	poly(acrylic acid)
PAAC	catechol-modified poly(acrylic acid)
PAH	poly(allylamine)
PAHC	catechol-modifed poly(allylamine)
PBS	phosphate buffered saline (buffer solution)
PDAC	poly(dimethyldiallylammonium chloride)
PES	polyethersulfone
PES[-N]	polyethersulfone UF membrane with [-manufacturer pore size in nm]
ϕ	volume fraction of clay platelets
PSU	bisphenol-A derived polysulfone
PVS	poly(vinyl sulfate)
QCM	quartz crystal microbalance
SEM	scanning electron microscopy/microscope
Spray-LbL	spray layer-by-layer [assembly]
SPPO	sulfonated poly(phenylene oxide)
SPS	sulfonated poly(styrene)
Sulfo-NHS	N-hydroxysulfosuccinimide
SWRO	seawater reverse osmosis
RO	reverse osmosis
τ	tortuosity
TDS	total dissolved solids
TEM	tunneling electron microscopy/microscope
Tetra-LAP	Tetralayer-laponite films (PAH/PAA/PAH/LAP)
Tetra-MMT	Tetralayer-montmorillonite films (PAH/PAA/PAH/MMT)
TFC	thin film composite [membrane]
TGA	thermogravimetric analyzer/analysis
UF	ultrafiltration

List of Figures

List of Tables

I. Introduction

1.1 – Global Water Resources and the Need for Desalination

One of the great engineering challenges of the 21st century will be providing basic living needs for a burgeoning human population, including access to freshwater. Already, studies from the UN World Health Organization indicate that over 1.1 billion people currently lack access to reliable and secure freshwater supplies[1, 2], with an estimated 2.5 million deaths per year from diseases associated with poor access and sanitation in 2007[3]. Several factors including but not limited to global climate change and altered weather patterns, population growth, political instability and conflict, and inequitable economic power structures leading to poverty, contribute to a growing crisis in freshwater availability[4-10]. Natural disasters can also damage or destroy local water infrastructure, necessitating the use of easily-mobilized technologies for emergency relief[11, 12]. Another particular problem are droughts, which are a significant burden due not only to a reduction in freshwater volume but also the impact on water quality: hydrological studies have shown the impact of drought conditions on freshwater resources are increased salinity, higher algae and toxic cyanobacteria content, and significant damage to local ecosystems[13]. Contemporary events such as droughts in the states of California and Georgia and water access issues in Michigan further illustrate how close to home the greater issues around water purification and usage is. Effective and efficient desalination is already and will continue to be vital to sustaining the quality of life for populations living with marginal access to freshwater.

Major public health organizations such as the UN World Health Organization have defined the standard for freshwater as containing less than 1000 mg/L of salts and other dissolved solids, collectively referred to as total dissolved solids (TDS)[14]. However, for potable water used for human consumption, the same health organizations including the U.S. Environmental Protection Agency recommend less than 250 mg/L TDS[15-17]. Additionally, specific restrictions such as those imposed by the Safe Drinking Water Act are established on particularly toxic and undesirable contaminants such as arsenic, lead, selenium, and boron to insure water quality[18].

Geological surveys indicate approximately 0.8% of Earth's surface water resources meet this minimum standard for freshwater, and are unevenly distributed which aggravates access issues[19]. The overwhelming majority of Earth's surface water is in seas and oceans (96.5%) with an additional fraction of surface freshwater frozen in glaciers (1.7%)[19]. Most of the available surface water is unfit for human consumption due to the presence of significant impurities: saline concentrations in oceans average 3.1 to 3.8 wt. % with a pH between 7.5 and 8.4, and in brackish water resources the saline concentration ranges between 0 and 1.0 wt. %[20, 21]. The primary salt ions present in seawater are sodium and chloride (combined 85.6 wt.%), although sulfate, magnesium, calcium, and potassium ions are also present[21]. Other common contaminants include microbial life, organic solutes, silt, minerals, and miscellaneous toxicants. Additionally, agriculture and poor irrigation practices[22-24], mining operations[25-27], industrial production[28-30], electrical power generation[31], and other human activity[32] can produce

significant amounts of wastewater that must be treated before it can be reused or discharged to the environment without a significant ecological impact.

1.2 – Methods for Large-Scale Water Desalination

Large scale water desalination plants can be broadly categorized into two groups based on the technology used to achieve the separation: a thermal approach[33] or a membrane approach [17, 34]. Thermal approaches achieve separation through vaporizing the water and collecting the purified condensate, while membrane approaches utilize a selective membrane to reject contaminants and ions, resulting in a purified permeate stream and a concentrated retentate stream. Common thermal processes include multiple-effect distillation (MED), which is derived from common distillation processes where the feed for each stage (termed effect) is preheated by the condensing steam product, and multi-stage flash (MSF), where the preheated brine is pressurized and successively throttled to draw off steam via multiple flash vessels[33]. Although various schemes have been proposed to reduce the energy consumption of the thermal processes, these modifications incur either increased capital investment or chemical consumption[35].

Common membrane processes include microfiltration (MF), ultrafiltration (UF), and nanofiltration (NF) which eliminate large solutes via a size exclusion transport mechanism. While this is effective for removing solutes with disparately larger sizes than water such as micron-sized and larger particulates, small lifeforms such as algae and bacteria, etc., small solutes such as salts that fully dissolve under aqueous conditions are significantly more difficult to remove via this method as it would require the regular and large-scale assembly of pores on the order of single nanometers in diameter. Reverse osmosis (RO), where the feed brine is passed by a dense, semi-selective polymer membrane, is capable of desalting. Alternative membrane approaches exist but are not as economically scalable as the above processes; electrodialysis (ED), for example, accomplishes the separation by utilizing an applied electrical potential difference across an ion-permeable membrane to drive ions out of the feed stream[36]. Membrane distillation (MD), which employs membranes that are impermeable to the liquid phase but permeable to the vapor phase, is a process that accomplishes a separation by utilizing a partial vapor pressure gradient across a membrane and less thermal energy than via the thermal processes listed above[37, 38]. However, the focus of this report is on salt-selective membrane processes, particularly RO.

1.3 – Brief History of Desalting Processes

The history of desalination begins with the rise of human civilization; evidence of salt production and consumption dates back at least eight millennia to peoples living around the Black Sea and in China; salt was extracted from mineral deposits or manufactured via early desalting processes[39]. For centuries, it was a valuable commodity and traded heavily overseas in locations as distant as England and the North Sea[40, 41], the civilizations of the classical and medieval Mediterranean[42, 43], central Africa[44], the Americas[45, 46], China[47], India[48], and everywhere in between. Cost-effective salt production is still an active business interest[49], and as

of 2013, salt production was a $1.6 billion industry in the United States alone[50]. The predominant use of salt was for nutrition and as a food preservative[51-53], although it was also used to manufacture goods such as clay pottery[54-57], served as a currency in some regions of Africa[58, 59] and New Guinea[60], and in the form of natron as a mummification agent for Egyptian burial practices[61]. By the 19th and 20th centuries, population growth and demand for freshwater led to a greater interest in what was formerly considered a byproduct of salt production[62]. Blue water navies, particularly the US Navy[63], were also motivated to invest in efficient and practical distillation technologies to ease resupply for fleets at sea.

Following the Second World War, there was a major push by the US government to develop more efficient desalting processes, starting with the Saline Water Conversion Act of 1952 that founded the Department of the Interior's Office of Saline Water (later retitled the Office for Water Research and Technology in 1974). This organization allocated investment to basic and applied research in large thermal systems for seawater desalination and the first forays into membrane processes for brackish water desalination. Thermal processes were initially favored in large-scale desalting because of the relatively lower cost of energy and technological maturity of the unit operations. However, as early as the 1960s, early desalting membranes comprised of cellulose acetate and derivative materials were investigated[64]. Thin-film composite (TFC) membranes with polyamide selective layers, with significantly increased water permeability and thus lower pressure requirements, were first pioneered in the mid-1970s[65].

Ultimately, the office was closed in the 1980s and current research is predominantly funded by non-profit organizations and the private sector[62]. The research has also expanded to include new applications such as wastewater treatment of particular contaminants[66-70], especially pesticides and agricultural runoff[71, 72], small-scale RO installations for impoverished communities in developing countries[73, 74], forward and pressure-retarded osmosis applications[75], and photovoltaic-driven or other renewable energy-powered RO modules[76, 77]. Additionally, interesting work is being done to generate antifouling coatings for RO membranes that will lower maintenance costs[78-81] (elaborated upon in 1.5.3). Finally, research is being conducted in areas unrelated to the RO membrane itself; in the SWRO industry, for example, major issues include pipe corrosion[82, 83], the management and discharge of the retentate brine[84, 85], the management of specific contaminants such as boron[82, 83], and environmental impacts of large-scale desalting operations[86-88].

Thermal processes such as MED and MSF are becoming increasingly costly in light of increasing energy prices and the minimum capital cost required for the installation. For these reasons, there is a trend in favor of installing RO plants for small- to medium-sized desalting capacities (with production rates on the order of 10,000 m^3/day or less). Additionally, since the 1970s, there has been a significant increase in the number of large-scale plants with production rates on the order of 100,000 m^3/day or greater[17]. The early installations predominantly utilized thermal processes because the water production rate for RO processes scales fairly linearly and the

cost curve was more favorable for MSF and MED. However, RO is rapidly achieving parity in this field as well due to reduced manufacturing costs[17].

Numerically, the growth in the installed water production capacity is rapid, progressing from approximately 5 million cubic meters of water per day in 1980 to 42 million in 2005[62]. Freshwater production is projected to surpass 100 million cubic meters of water per day by 2016, approximately twice the figure reported for 2007-2008[89]. As of 2009, roughly 50% of the global desalting capacity utilized reverse osmosis (RO) or nanofiltration (NF) membrane processes and over 80% of new plant installations employ at least one of these membrane unit operations[17]. In the United States, this figure is significantly greater: approximately 96% of U.S. desalting capacity is dominated by membrane processes, including nearly all municipal water treatment[90].

1.4 – Comparative Energy Consumption of Desalting Processes

The energy consumed in a thermal desalination process is maximally determined by the heat required to vaporize the feed water (the sum of the heat added to raise the water to boiling and the subsequent heat of vaporization) and system losses. These can be reduced mainly via preheating the feed with the condensate and insulation. This can be accomplished through the heat transfer between the vapor and liquid phases in the stages of MED and the countercurrent heat exchange system used in MSF[33]. For membrane processes, the minimum energy requirement is determined by the energy required to compress the water to a pressure greater than the osmotic pressure of the feed solution, which to a first order approximation is directly proportional to the feed concentration of salt and dissolved solids (see 1.5.3).

Quantitatively, a single stage evaporation process of seawater with an average TDS concentration and without energy-saving engineering measures requires approximately 650 kWh_t/m^3 of water produced[91]. However, with appropriate engineering to preheat the feed streams with the condensate, the energy consumption for thermal processes such as MED (15-58 kWh_e/m^3) and MSF (21-58 kWh_e/m^3) can be reduced by an order of magnitude[91]. By comparison, the energy cost for common RO processes is largely driven by the electrical pumping cost of the feed water, a largely incompressible fluid. For most installations, this figure is approximately 3-6 kWh_e/m^3 of water produced—note this energy requirement is approximately an order of magnitude less than the efficient MED and MSF thermal processes and two orders of magnitude less than a direct single stage evaporation method. Optimized, state-of-the-art RO installations can operate at 1.58 to 3.0 kWh_e/m^3 of water produced, which is close to the thermodynamic energy limit for RO processes of 0.7 to 1.06 kWh_e/m^3[89, 92]. Note this thermodynamic minimum does not contain the energy consumption for associated processes such as feed pretreatment, permeate post-treatment, and brine discharge, which can potentially exceed 1 kWh_e/m^3 of water produced[93].

The thermodynamic efficiency of RO processes, and thus the overall energy consumption, can be significantly impacted by biofouling, where either organic material or microorganisms such

as bacteria and algae, deposit on the surface of the RO membrane[78]. Feed pretreatment and proper cleaning methods[94-96] can be used to control biofouling as well as operating at or below particular critical fluxes to retard the process[97], although research into novel membrane materials to prevent the formation of biofouling films is ongoing. Increased membrane water permeability is a second factor that could further reduce the energy consumption of RO unit operations, with recent literature indicating a tripling of permeability could reduce the energy consumption of seawater RO processes by 15% and brackish water RO processes by 46%[98].

1.5 – Reverse Osmosis

Reverse osmosis (RO) is a process through which water is desalted via pressurized flow past a salt-selective membrane, producing two product streams: a desalted permeate stream and a retentate stream of concentrated brine. The natural driving force in this system is the chemical potential gradient for the solvent (water) from the permeate stream to the retentate stream, which is a function of the concentration gradient in the membrane and the pressure in the flow streams. To accomplish a permeate flow, the applied pressure must be greater than the osmotic pressure, which reverses the osmotic flow of water from the permeate stream to the retentate stream. Although initial forays into RO did not focus on designing membrane structures to select particular ionic species for rejection, recent theoretical work has been conducted in this area[99-101].

1.5.1 – Structure of TFC RO Membranes

Reverse osmosis is already the preferred method for water desalination on a small- to medium- scale, and is a prime area of research for large-scale desalination operations. Porous cellulose acetate was the preferred material until the development of thin film composite (TFC) membranes in the 1970s, which had comparable water permeability properties and under most experimental conditions rejected on the order of 90% or greater of monovalent salts[102]. State-of-the-art commercial TFC membranes are comprised of two or more layers: 1) a dense polyamide selective layer deposited through interfacial polymerization that accomplishes the separation, 2) a polysulfone or polyethersulfone support layer to provide a mechanically robust, porous support for the selective layer, and optionally 3) polyester or other backing materials for mounting the RO membrane into an appropriate module (see 1.5.3)[103, 104]. The selection of materials for each layer is driven not only by efficiency and selectivity, but additional considerations such as expected solutes, foulants, cleaning protocols, scaling, public and regulatory acceptance, and manufacturing cost[105].

The selective layer for commercial TFC RO membranes is deposited via interfacial polymerization[65, 103]. Although the reaction conditions for particular commercial products are proprietary, some general notes on the process can be presented from the literature. The selective layer is formed from the reaction of aqueous diamine and diacid chloride in an organic solvent to produce polyamide and hydrogen chloride at the interface[106], yielding a polyamide layer on the order of 30 to 200 nm thick with a ridge-and-valley structure[107, 108]. The particular selection of organic solvent and reaction conditions such as temperature can significantly affect the thickness,

roughness, density, and other characteristics of the polyamide layer[109]. One advantage of the interfacial polymerization technique is that it is self-healing, meaning that defects at the film interface serve as the nucleation sites for subsequent polymerization[110]. There is a significant degree of current research on the polymer composition of TFC membranes, or the addition of nanomaterials such as silver salts to the polymerization process, to improve overall fouling resistance and optimize control over selective layer deposition[111, 112].

The underlying support layers common in RO membranes are also utilized in MF, UF, and NF applications. Tiraferri et al. have demonstrated mixed structures, with a dense skin layer consisting of an array of small pores on the surface and a highly porous macrovoid structure underneath[113], are optimal support layers that maximize water flux[114]. There are a number of phase inversion techniques that can generate these asymmetric membrane morphologies, including solvent evaporation, precipitation through evaporation or thermal means, and immersion[115]. The key factors in determining the morphology, physical characteristics, and performance of the phase inversion support layers are the selection of the solvent-nonsolvent pair, the monomer and its concentration, the presence of any additives to the system, processing time, and the formation temperature[116-118].

1.5.2 – RO Membrane Modules

RO Membranes are typically mounted in one of two assemblies: hollow fiber modules or spiral wound modules[105] (Figure 1-1).
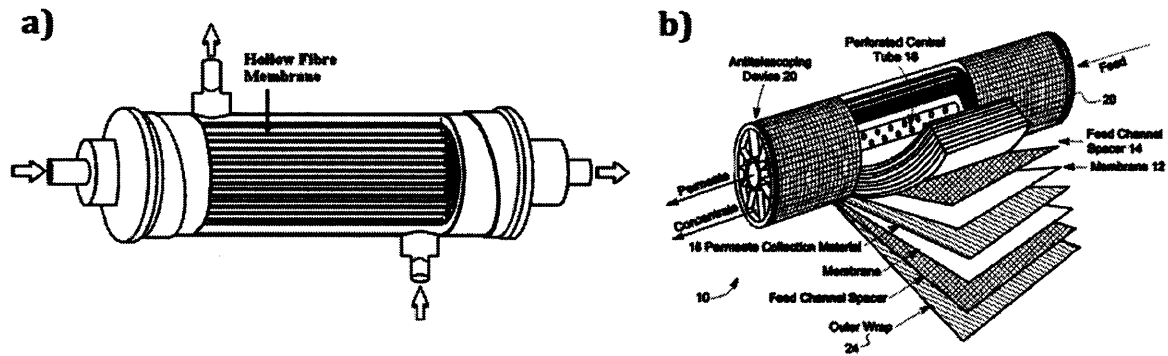
Figure 1-1: Schematics from patent documents of RO modules commonly used in industrial applications: a) a hollow-fiber RO module[119], and b) a spiral-wound RO module[120].

Hollow fiber modules are comprised of an external shell that contains bundles of cylindrical RO membranes, with the permeate stream collected in the shell and drawn off (Figure 1-1a)[119, 121]. These are less expensive to maintain than spiral-wound modules because it is possible to replace individual fibers, however the maximum operating pressure of such assemblies generally ranges between 100 and 200 psi because the fibers are loose in the module without a stiff backing material. These modules can operate at pressures sufficient for brackish water feeds but not for seawater feeds as the osmotic pressure for seawater RO generally exceeds 300-350 psi. Spiral

wound modules contain a single sheet RO membrane wound around a core assembly with narrow gaps to allow for permeate collection (Figure 1-1b)[120, 122]. These assemblies can be operated at pressures up to 1,500 psi and thus are idea for high salinity feeds such as seawater and some industrial wastewater streams, but the modules are more difficult to clean and must be completely replaced if a defect develops on the membrane surface, leading to higher maintenance and capital costs.

Membrane modules are typically installed in series fashion, with the number of modules installed largely dependent on the intended recovery rate and the quality of the feed water. The recovery rate is often expressed as a percentage of the feed flow and corresponds to the quantity of permeate water drawn. Detailed work has been done to estimate the performance of RO installations given an intended recovery rate, quality of feed water, and specifications on the modules installed[123].

1.5.3 – Osmotic Pressure and Minimum Energy Requirement

In a RO process, a pressurized feed solution is passed by a semi-selective membrane that rejects salt ions but not water molecules, producing two product streams: a desalted permeate stream and a retentate stream of concentrated brine. To accomplish a water flux, the applied pressure must be greater than the osmotic pressure between the feed and permeate streams[124], which is calculated from equating the chemical potential of water on the feed and permeate sides of the membrane[92]. To a first order approximation for an ideal solution, this is proportional to the concentration of TDS in solution via the Morse equation:

$$\Pi = iMRT$$

...where i is the van't Hoff factor reflecting the number of ions produced when the salt is dissolved in water, M is the concentration (molarity) of TDS present, R is the universal gas constant, and T is the absolute temperature. Generally, this relationship holds for most saline water sources except for highly concentrated solutions[125].

Notably, this osmotic pressure is the absolute minimum figure required to generate a positive water flux, and in practice applied pressures will be significantly greater. As the permeate is drawn off from the feed stream, the retentate will necessarily increase in salt concentration and thus increase in osmotic pressure. Additionally, solvated ions diffuse through the membrane at different rates (see 1.6 for a more detailed discussion), resulting in the development of a charged boundary layer on the upstream membrane surface, called concentration polarization (CP) which increases the effective osmotic pressure as well. Research on continuous-flow high-permeability RO module configurations has shown the greater of these two factors in reducing water flux is this increase in the osmotic pressure resulting from the increased concentration of rejected solvated ions. The thermodynamic restriction is a greater factor than increased CP along the membrane surface[126].

This tradeoff is indicative of an inverse relationship between salt rejection and water flux: manipulating operating conditions to maximize one desired attribute will reduce the other, with novel material systems required to surpass this practical limitation. Most RO operations are run at applied pressures significantly greater than the osmotic pressure to increase the water production rate at the expense of salt leakage. The overall production rate of water is largely determined by the permeability of the membrane, the total membrane surface area including the number of RO modules in sequence, and the applied overpressure[92].

For a stock solution of NaCl at brackish water concentrations (1.0 wt.%), the osmotic pressure is roughly 8.42 atm while for a solution at seawater concentration (3.5 wt.%), the osmotic pressure is approximately 29.8 atm. From these figures, a theoretical minimum energy can be calculated from modeling RO as an ideal, reversible thermodynamic process with a given recovery rate, which yield the figures given for the energy consumption above[127]; for example, a 50% recovery rate at seawater concentration yields a minimum energy requirement of 1.06 kWh/m³ of water produced[92].

1.5.4 – Forward Osmosis

Forward osmosis (FO) is a closely related process to RO, and due to these similar characteristics a brief discussion on the subject is merited. In a FO process, a concentrated draw solution is used to generate an osmotic flow of water across a salt-selective semipermeable membrane. FO modules can be utilized in liquid-liquid extraction modules for multistep water treatment[128-131], particularly the removal of small molecule drugs[132] and other trace organic compounds[133] from waste streams, the operation of bioreactors[134, 135], and potentially for power generation[75, 131]. The salt-selective membranes used in these applications tend to be similar to the TFC membranes used for RO applications, except higher water permeability is desirable[136-138]. High flux membranes used for FO applications run into similar design challenges that high flux RO systems experience, including significant fouling, reduced efficiency due to CP, and solute diffusion across the membrane[139]. Furthermore, optimizing the draw solution is an additional area of research for FO that does not have a direct analog in RO unit operations[139-141].

From the perspective of energy consumption and thermodynamic efficiency, the modeling literature has demonstrated that it is nearly impossible to find reasonable operating conditions under which FO processes would improve upon the thermodynamic efficiency of RO processes[142].

1.6 – Transport Mechanisms in Selective Layers

1.6.1 – Transport in Ultrafiltration and Nanofiltration Membranes

Transport through porous MF, UF, and NF membranes can be modelled as a series of cylindrical pores with a fixed diameter with a continuous pressure drop across the membrane as a

driving force for the flow of water and solutes[143]. The predominant mechanism to reject solutes in these membranes is size exclusion, where molecules larger than the pore size are hindered and unable to pass through the membrane. Some of the important assumptions for this model are that the fluid are in equilibrium with the membrane at both interfaces, leading to a chemical potential gradient across the membrane that is a function of the applied pressure and no activity gradient[144]. This model is not often used for solute transport in RO membranes because it does not account for the effects of tortuosity and the fixed pore model does not accurately reflect the physics of transport through dense polymer layers such as those used for RO membranes.

Commercial manufacturers of these types of membranes often report a molecular weight cut-off (MWCO) that corresponds to the point where 90% of an organic solute with the specified molecular weight is rejected; this is used as an indicator of pore size[145, 146]. The MWCO analysis assumes, however, a near-perfect correlation between molecular size and molecular weight[71] which does not hold for some common organic toxicants such as pesticides[147, 148]. The key driving force for water and solutes small enough to flow through the pores is the applied pressure across the membrane.

1.6.2 – Diffusion of Ions in Nonporous Media

As discussed in 1.5.1, the selective layer of commercial TFC RO membranes is a dense polymer layer comprised of cross-linked polyamide. With the primary exception being defects in the selective layer, there is not a regular porous structure of appreciable pore size that allows for hydraulic flow, although some papers have reported effective pore sizes on the order of 0.2 to 2 nm in modeling exercises and via high-resolution microscopy on commercial NF and RO membranes[108, 149-153]. For this reason, some modelers use diffusion in porous media models[154, 155] but agreement with experimental data is lacking[144]. Instead, a number of better models for the transport of ions across these membranes assume the lack of convective mass transport and that molecular diffusion dominates the transport through the selective layer. One of these models, the solution-diffusion model, assumes that solutes such as water and solvated ions partition into the selective layer, diffuse through the polymer matrix, and then desorb into the pores in the support layer[144].

Diffusion through the dense polymer layer is a function of several factors, including the hydrodynamic radius of the molecule, the charge or lack thereof on the molecule, and environmental factors such as temperature that affect the activity and chemical potential of the molecules[156, 157]. Most correlations apply an inverse proportionality between the hydrodynamic Stokes radius of the molecule and the diffusion coefficient, and either linear or greater proportionality with respect to temperature (i.e. $\propto T^{3/2}$).

Charge effects between multiple solutes play an important role as well; although the independent diffusion coefficients for different solvated ions, such as sodium and chloride ions, will be different, an imbalance in the overall flux of one ionic species yields an electrical potential over the membrane, termed a Donnan potential[158]. The Donnan potential serves a second driving

force for the diffusion of the less mobile ionic species and increases the osmotic effects for the more mobile species by generating a boundary layer. The emergence of these concentration gradients of different ionic species leads to the buildup of concentration polarization (CP) along the upstream membrane surface (section 1.5.3), and ultimately ensures that charge remains balanced across the membrane.

Putting aside the electrochemical aspects for a moment, the hydrodynamic radius of a diffusing ion is not simply the radius of the ion or the polyatomic species, but also includes the shell of closely hydrogen-bonded water molecules around the ion, termed a solvated ion. The size of the solvation shell is a function of the attractive electrostatic forces between the ion and the oppositely-charged dipole of the water molecules and the repulsive forces between the nuclei[159, 160]. These solvation shells increase the effective size of the solute to the order of a single nanometer for common monatomic ions like sodium and chloride to several nanometers for larger polyatomic ions such as sulfates, with lighter monatomic ions being relatively larger than heavier monatomic ions due to the increased charge density[161-163]. Divalent as opposed to monovalent ions or polyatomic species have larger solvation shells, which increase the effective radius of the solute.

Thus, the most difficult ions to desalt from feeds are those that have the smallest charge density and smallest hydrodynamic radius such as sodium and chloride ions. Divalent cations such as magnesium and calcium are significantly less mobile than monovalent cations, and large polyatomic ions such as sulfates, nitrates, etc. are significantly hindered from a diffusion perspective[164].

1.6.3 – Size Exclusion and Tortuosity with Impermeable Particles

For heterogeneous selective layers, in particular those that incorporate impermeable platelets into the polymer matrix, there is an additional consideration in the form of the increased effective path length for diffusion through the membrane[165-167]. Impermeable platelets that are intercalated throughout the film introduce nano-channels can exclude solutes based on size[168]. Intuitively, for effective separation of solutes via size exclusion, the spacing of the nano-channels formed by the platelets should be on the order of the effective hydrodynamic radii of the solvated ions and larger than the hydrodynamic radius of water.

The incorporation of any impermeable particle such as a clay platelet within the selective layer increases the effective diffusive path length for any solute traversing the membrane, termed tortuosity. There are several correlations for tortuosity that depend largely on the volume fraction of clay, ϕ, and the aspect ratio, α, of the clay platelets in the film. The first of these correlations, the Nielsen correlation[169], is most appropriate under the dilute conditions where $\phi \ll 1$ and $\alpha\phi < 1$:

$$\tau_{Nielsen} = 1 + \alpha\phi$$

...and the Cussler correlation[170] for films with greater concentrations of clay platelets under the semi-dilute conditions $\phi < 1$ and $\alpha\phi > 1$:

$$\tau_{Cussler} = 1 + \mu \left(\frac{\alpha^2 \phi^2}{1 - \phi} \right)$$

...where μ is the geometric ratio for the particles in question, and is approximately 0.5 for clay platelets[171]. For the densely-packed high clay content films that can be assembled via layer-by-layer, the second correlation is most appropriate; it predicts significantly greater diffusive path lengths due to solutes reflecting inside nano-channels formed by multiple platelets instead of passing each solute through the layers without interaction. It is observed that the tortuosity is proportional to the square of the aspect ratio and the volume fraction of clay in the film in the semi-dilute limit[172]. There is generally good agreement with these two correlations and the literature on polymer and clay nanocomposites[173-176].

1.6.4 – Discussion of Mathematical Models for RO Processes

Generally, MF, UF, and NF processes are modeled via a pore-flow model with fitted transport parameters that correspond to the resistance to flow through the pores and a driving force that is directly proportional to the applied pressure across the membrane. A common example of this is Darcy's Law:

$$J_w = \frac{A}{\delta}(P_f - P_p)$$

...where J_w is the flux of water, A is the water phase transport parameter, δ is the pore length, P_f is the pressure on the feed side, and P_p is the pressure on the permeate side. The key assumptions behind this model are 1) the membrane is in thermodynamic equilibrium with the feed and permeate streams, 2) there are no solute or solvent activity gradients across the membrane thus allowing the chemical potential gradient to be a function of the applied pressure only, and 3) flux is only in the axial direction through the pores[144]. Although this particular model does not assume a particular pore geometry, modifications can be made to the transport parameter and pore length to fit the equation to new geometries. The solute flux takes a similar form but is proportional to the square of the operating pressure:

$$J_s = \frac{B}{\delta}(P_f^2 - P_p^2)$$

...where J_s is the flux of the particular solute and B is the corresponding solute phase transport parameter. This equation will yield significant errors unless terms are added to account for osmotic pressure of the solutes and CP along the upstream surface[177]. Work has been done to account for both membrane structure parameters such as the pore geometry as well as the interactions between the membrane and the solutes including electrostatics[178], CP[179], and other membrane parameters[180], but these models are still insufficient for modeling RO processes[144]. Unlike MF, UF, and NF processes, the selective layer of a TFC RO membrane is a dense polymer film without a clearly defined porous structure for the hydraulic flow of water[181], although some papers have applied variations on the pore-flow model with solute-membrane affinity parameters and friction effects to describe the water and salt transport[182-184].

Alternative models accounting for the diffusion and electrokinetics more appropriately describe the flux of solutes through the selective layer. The class of solute-diffusion models assume the selective layer is nonporous and the separation is accomplished through differences in the solubility and diffusivity of the solutes in the membrane[185]. The basic mechanism involves solutes adsorbing at the interface between the bulk feed fluid and the membrane interface, diffusing through the membrane along the concentration gradient as the rate limiting step, and then desorbing into the pores of the support layer[144]. Additional assumptions include 1) the membrane is homogeneous, 2) that transport for each solute is independent of other solutes, and 3) the chemical potential gradient is a function of the concentration and pressure gradients across the membrane[185, 186]. This is expressed in the form:

$$\Delta\mu_i = R_g T ln \Delta\alpha_i + V_i \Delta P$$

...where the chemical potential $\Delta\mu_i$ is a function of the thermodynamic temperature, the natural logarithm of the activity gradient $\Delta\alpha_i$, the molar volume of the solute V_i, and the trans-membrane pressure gradient ΔP. It is generally accepted that solvated ions diffuse at a slower rate than water molecules through the polymer matrix due to a combination of charge effects and larger solute size (represented by V_i, see Section 1.6.2). Ultimately, the flux of water is described by the equation:

$$J_w = \frac{S_w D_w}{\Delta z} \frac{V_w}{R_g T} (\Delta P - \Delta \pi)$$

...where the permeability is broken down into the Henry's Law partition coefficient for water in the membrane, S_w, and the diffusion coefficient in the polymeric matrix D_w. The other parameters include the membrane thickness Δz and the pressure term that is the applied pressure gradient minus the osmotic pressure gradient. For the flux of solutes, it is generally assumed the pressure gradient has a negligible effect on the chemical potential and the solute flux follows Fick's Law:

$$J_s = \frac{S_s D_w}{\Delta z} (C_m - C_p)$$

...where the concentration gradient is defined in terms of the solute concentration in the membrane on the permeate side, C_m, and the bulk concentration in the permeate C_p.

As a number of transport mechanisms can partially describe the flux of solvated ions and water through the selective layer, which of the expanded solution-diffusion and pore-flow models are applied can vary based on how well it matches experimental data[144]. Corrections to it have been successfully applied to NF and RO experimental data[187-189]. However, a significant drawback of using the solution-diffusion model is the assumption the membrane structure is homogeneous. The additional inclusion of clay platelets into the thin film significantly impacts the diffusive path length as discussed in 1.6.3 and invalidates this assumption. Thus, it is appealing to use irreversible thermodynamics models such as the Spiegler-Kedem model to obtain a generalized water permeability coefficient that is independent of the transport mechanism through the

membrane (see Appendix 1 for the regression method to calculate the permeability coefficient utilizing with this model, and 1.6.5 for the overview and key assumptions made).

1.6.5 – Spiegler-Kedem Model for RO Processes

Given the widespread utilization of this model in both literature and for the data analyzed in this report, a separate section detailing the Spiegler-Kedem model is warranted. This model returns a water permeability that treats the membrane architecture as a black box and therefore does not assume an internal structure, and thus can be used to describe the solute flux for a number of membrane applications. The key assumptions for this model are: 1) the membrane is in thermodynamic equilibrium with the feed and permeate streams, 2) the driving force for the flux is defined in terms of the trans-membrane pressure gradient, and 3) the concentration of solutes in the membrane do not significantly affect the permeability properties of that solute in the membrane[190, 191]. For water permeability, both the Kedem-Katchalsky and the Spiegler-Kedem model take the form of:

$$J_w = P_w(\Delta p - \sigma \Delta \pi)$$

...where J_w is the observed water flux, P_w is the generalized water permeability coefficient for the membrane, Δp is the applied pressure gradient across the membrane, $\Delta \pi$ is the osmotic pressure gradient, and σ is the reflection coefficient, a fitted parameter that ensures the flux is zero when the applied pressure is equal to the osmotic pressure of the feed solution. The key difference between the Kedem-Katchalsky model and the Spiegler-Kedem model is that the solute permeability and reflection coefficient are independent of concentration[192, 193], which is a disadvantage of the Kedem-Katchalsky model that can yield nonphysical results[186]. A reflection coefficient of one indicates the solute (in this case water) is perfectly impermeable, while any value less than one indicates the solute is semi-permeable[194].

For salt permeation, the Spiegler-Kedem model takes the form of:

$$J_s = P_s \Delta z \frac{dC_{sl}}{dz} + (1 - \sigma)J_w C_{av}$$

...where J_s is the observed salt flux, P_s is the salt permeability, z is the axial coordinate (i.e. thickness of the selective layer), C_{sl} is the concentration of salts within the selective layer, and C_{av} is the average salt concentration at the membrane surface.

1.7 – Applications of Polymer-Clay Composites in Thin Films

1.7.1 – Nanomaterial Composites in Various Applications

Significant research has been conducted on polymer-nanomaterial composites with micro- and nano-scale assembly methods[195-200]. In particular, polymer-clay composites have unique properties, particularly cytotoxic properties that have been observed in some nanoscale clay platelet systems[201, 202], which have been utilized in a number of applications including gas barriers[171, 203-206], medical devices, bandages, and biocompatible materials[207-210], FO

membranes[137], and the release of chemical agents[211]. Additionally, there are improved mechanical properties associated with polymer-clay composites, such as an increase in the hardness and toughness of the materials, which is observed to be a function of the platelet aspect ratio, α[212-214].

1.7.2 - Nanomaterials for RO Membrane Applications

The application of inorganic nanoparticles to selective layers in membranes is an active area of research[215, 216] to generate high-permeability membranes that address the trade-off between flux and selectivity. Researchers have investigated the use of nanostructured materials that enable less-hindered water transport while still providing mechanisms for salt rejection in the membrane[217, 218]. The literature on nanostructured materials for RO membranes contains experimental and theoretical work on selective layers utilizing single and multi-walled carbon nanotubes[218-223] and nanotube-silver composites[224], graphene[225, 226], metal oxide nanoparticles[227-230], silica nanoparticles[231], and zeolites[232-236] with varying degrees of success. Carbon nanotube-containing films were found to be exceptionally permeable and exhibit at maximum 50-60% salt rejection[219, 223], while an array of zeolite-containing membranes were found to reject salts on the order of 70-95% but with reduced water permeability relative to TFC RO membranes[232, 237]. Reviews of modeling literature paint a rosy picture of the future application of carbon nanotubes for desalting membranes[238-240], but notably the structures produced by expensive carbon nanotubes can be replicated with relatively inexpensive cellulose nanofibers with a tunable diameter, which may make this particular path of research obsolete[241].

Underlying these investigations is the hypothesis that the incorporation of impermeable nanomaterials into a selective layer introduces effective nano-channels inhibiting the flux of large solutes. Particularly, the focus is on developing channels or pores with a length scale on the order of 1 nm, which enables solute rejection via size exclusion[215], as this figure is between the hydrodynamic radius of a water molecule and small solvated ions such as Na^+ and Cl^-[144]. For this reason, smectite clays are interesting nanomaterials to investigate for RO selective layers; these high-aspect ratio clay platelets may be layered into films to form nano-channels that create a highly tortuous diffusive pathway for solvated ions. Clay-containing ceramic membranes have been used with some success in water microfiltration applications[242], adsorption purification materials[243], and oil-water separations[244], but recent research into the use of similar composite thin films as selective layers in RO membranes has primarily focused on the incorporation of carbon nanotubes and zeolites[217].

Outside of the field of water purification, clay composite membranes have been shown to inhibit the in-plane mobility of Li^+ ions by up to two orders of magnitude compared to the cross-plane mobility[245], and in gas separation membranes laponite and montmorillonite clay composite films have been shown serve as an effective small molecule barrier layer[171, 203-205]. It has been shown that the degree of tortuosity in the clay composite membranes is a function of the number of clay layers and the aspect ratio of the clay platelets[199]. Additionally, in recent studies

on RO membranes containing inorganic nanomaterials, modelers suggest the possibility of preferential water flow channels through the selective layer generated by the presence of nanomaterials[144].

1.7.3 – Techniques to Incorporate Nanomaterials into Selective Layers

Many of the assembly techniques commonly used to incorporate these nanomaterials into membranes, such as the intercalative polymerization step of the selective layer, exfoliation adsorption, or melt intercalation, generate composites with a disordered internal structure that do not form uniform barrier layers[196, 200]. Additionally, the incorporation of nanomaterials into these selective layers is relatively low, with weight fractions generally on the order of 10% or less[196, 198]. A potential improvement to this approach would be to design a more uniform and nanomaterial-dense selective layer through a sequential assembly process with a focus on the lateral order of nanomaterials, enabling finer control over the internal structure of the selective layer.

1.8 – Layer-by-Layer Assembly Method for Assembling Thin Films

1.8.1 – Dipping Layer-by-Layer Assembly

Layer-by-layer (LbL) assembly is a process through which thin films are assembled via the sequential deposition of film components with complementary functionality, such as electrostatic interactions[246] or hydrogen-bonding[247]. The dipping process (dip-LbL) involves dipping a functionalized substrate into a bath containing a film component with a complementary functionality. After a period of time to allow for the adsorption of material to reach thermodynamic equilibrium, the substrate is removed and sequentially rinsed to remove any unabsorbed material[248, 249]. It is important to note that while electrostatic interactions or hydrogen-bonding may be the key driving force for the buildup of LbL films, the process through which this adsorption and film rearrangement occurs is through a minimization of the free energy of the film[250]. This process is repeated for the complementary film component to assemble a bilayer, the elementary unit of LbL-assembled films. This process can then be repeated to deposit a film of a desired thickness, or combined with other bilayers to form more complicated film architectures.

The composition of LbL-assembled thin films can be controlled via manipulation of the process conditions such as deposition and drain times, concentration of the solutions, and ionic strength of the film components[251, 252]. Polymer films assembled via LbL do not retain rigid delineations between deposited layers but instead form a polymer blend, with interpenetration of polyelectrolytes from one layer up to five layers distant[246]. Generally, films grow linearly with respect to the number of layers deposited, but low molecular weight and weakly-charged polyelectrolytes[253-255] can simultaneously adsorb at the film interface and diffuse into the multilayer to form complexes with oppositely-functionalized polyelectrolytes during long deposition steps in a process termed interdiffusion[256]. This phenomenon causes films containing these polyelectrolyte systems to build at an exponential growth rate with respect to the number of layers deposited[257].

This assembly technique has been used to incorporate diverse materials such as polyelectrolytes[246], carbon nanotubes[258, 259], nanoparticles and nanowires[260-263], nano-platelets[214, 260, 264-267], graphite and graphene oxide[259, 265, 268-270], small molecules such as dyes[271], and biological compounds such as drugs[272-274], RNA[275-278], growth factors[279, 280], and other biomaterials[281-283] into thin films on a diverse array of substrates including not just flat surfaces but various microstructures and nanoparticles[284-287]. Surfaces can be patterned both with selective functionalization of the substrate[288] and choice of polyelectrolyte deposition[289] to generate more complex nano- and micro-patterned structures, or via acidic post-treatment dense polyelectrolyte films can be converted into nanoporous meshes[290]. Given the wide array of polyelectrolytes and nanomaterials that can be incorporated into LbL-assembled thin films, the technique is ideal for crafting functional and structured nano-assemblies for a diverse array of non-membrane[288, 291-295] and membrane applications[296], including medical devices[297-299], fuel cell proton exchange membranes and electronic devices[300-303], optical devices[304, 305], ion exchange membranes[306], chemical agent sensors[300, 307], anti-reflection and anti-fogging coatings[262], gas barrier and separation membranes[199, 308, 309], and most importantly for this application water purification membranes[310-316].

1.8.2 – Spray Layer-by-Layer Assembly

Another method for assembling LbL films involves aerosolizing the film components with a forcing gas and spraying the components onto the substrate, in what is termed spray layer-by-layer (spray-LbL). Spray-LbL assembly can decrease the processing time for depositing large, asymmetric films by one to two orders of magnitude[317]. Similar to the dip-LbL assembly process, film components are instead sprayed for a time period on the order of seconds, then a time period is allotted for drainage and adsorption to the film interface on the order of seconds, and then a rinse and drain is applied with water to remove any unabsorbed material; this process is repeated to layer each component in the film architecture. The timescales for the deposition and rinse times most commonly used in spray-LbL assembly is significantly less than what would be required to reach full thermodynamic equilibrium with each deposition, resulting in thinner films being deposited when compared to dip-LbL processing[318]. Some investigation on alternative spray-LbL processing schemes involve the continuous spraying of polyelectrolytes and the elimination of the rinsing step; both of these modifications have been shown to cause an increase in film thickness with a corresponding increase in the surface roughness[319]. Additionally, spray-LbL is a flexible process that allows the deposition of thin, conformal coatings around fibers or within pores of porous substrates by drawing a vacuum across the substrate during the deposition process[320]. Comparisons of films assembled via spray-LbL and dip-LbL have found spray-LbL assembled films are on average less thick and rougher than the same film architecture deposited via dipping, but otherwise are qualitatively similar to spray-LbL assembled films[321-323].

Through tuning of the assembly conditions, thin films can be assembled with a relatively high degree of incorporation of nanomaterials into the polymer matrix, on the order of 50% of the weight fraction of the film[324, 325], compared to weight fractions under 10% observed in traditional polymer composites[198]. This is a unique property of LbL deposition that enables the exploration of densely-packed clay-polymer composite nanostructures that could serve as effective selective systems. Interdiffusion was thought to be impossible with LbL systems containing strong barrier layers such as clay platelets, but has been observed for particular film architectures where the clay does not form a uniform barrier in each deposited layer[326].

1.8.3 – Prior Application of LbL to RO Selective Layers

Previous research has been conducted on dip-assembled and spin-assembled LbL films to serve as selective layers in osmotic membranes; examining the use of LbL films containing polyelectrolytes[312-316, 327-330] and metal-ion complexed polymers[311]. Diffusion studies, high resolution microscopy, and other techniques confirm that LbL-assembled thin films have similar characteristics to the selective layers of TFC membranes down to the nanoporous surface structure[331]. Generally, this body of research examines the water and salt permeation characteristics of LbL-assembled thin films as selective layers with an array of salts including sodium, chloride, magnesium, and calcium ions along with polyatomic ions commonly found in saline water supplies such as sulfate. However, the film architectures examined do not take advantage of the unique properties of LbL assembly to incorporate nanomaterials and instead improve upon mediocre salt rejection through the deposition of extraordinarily thick layers compared to what could be deposited more cheaply and uniformly via interfacial polymerization. Thus, many of these films are instead simply more expensive-to-manufacture and less-effective selective layers.

The key performance metrics reported in these works are generally experimental variables such as water flux and salt rejection, and while useable for comparison between different films and experimental conditions within the context of a single paper, these figures are not intrinsic to the material. Thus it is challenging to draw conclusions on between film architectures generated by different lab groups using vastly different deposition and experimental conditions. To some degree, it appears reporting water and salt permeability values directly has been avoided due to difficulty in modeling and the structural assumptions required about the selective layer. Most of the research groups use 1,000 or 2,000 ppm salt concentrations, common values for low-grade brackish water trials but significantly below the maximum of 10,000 ppm for brackish water and the average for seawater at 35,000 ppm.

More specifically, the observed salt rejection for this body of literature ranges from the order of 10% to a maximum of 60%. Ritchareon et al. worked with film architectures comprised of chitosan paired with either sodium alginate or sulfonated polymers such as sulfonated polystyrene are weak barriers with 6% to 15% salt rejection that is largely a function of the thickness of the membrane[312]. A similar film architecture of chitosan and sodium alginate with 35 bilayer films was used by Lajimi et al. that reported approximately 60% salt rejection for NaCl feed

solution[330]. More efficacious systems such as cross-linked poly(allylamine) and poly(acrylic acid) such as the system used by Fadhillah et al. were able to achieve on the order of 65% salt rejection, but only with 120 bilayer films at very low feed concentrations[315]. Some interesting work from the Tieke group has utilized copper-complexed azacrown-6 as a film component in LbL assembly of membrane selective layers, paired with poly(vinyl sulfate) (PVS). With 60 bilayer films deposited, the (aza6/PVS) bilayer system was observed to reject Cl^- at 45.7% and SO_4^- at 91.9% with an operating pressure of 25 bar, on the order of brackish water desalination[311].

Several papers observe an increase in the rejection of Mg^{2+} and SO_4^{2-} ions over Na^+ and Cl^- [330]. Other research has examined the rejection of larger solutes such as sucrose with similar material systems as those utilized above such as (PAH/PAA) and (PAH/SPS), and were able to attain rejection on the order of 99% or greater with 7 bilayer films and match the data to pore flow models to estimate a pore size on the order of 0.4-0.5 nm[331]. Five bilayer films of the same architecture deposited on porous alumina instead of polysulfone have been shown to exhibit excellent SO_4^{2-} and $Fe(CN)_6^{3-}$ selectivity with regards to Cl^- ion permeation[332], however overall monovalent ion permeation remained high. This is expected due to the larger ionic radius and increased charge density for these polyatomic species as discussed in above in the factors affecting diffusion of ions in a dense polymer layer (section 1.6.2).

As of the writing of this report, the only major salt-selective LbL-assembled film was a recently published film architecture comprised of poly(allylamine) with sulfonated poly(styrene) or sulfonated polysulfone chemically cross-linked with glutaraldehyde, which was able to reject on the order of 90-95% of monovalent ions with demonstrable chlorine resistance[333]. It is important to note this work was carried out with 2,000 ppm NaCl solution, significantly lower than the 10,000 ppm used in this report for brackish water RO, which yields significant advantages in terms of lower osmotic pressure.

These authors focus on charge effects as the key selective mechanism, with an increase in the number of functional groups corresponding to the increase in the number of charged groups in the polymer matrix. It is thought these charged groups inhibit the flow of solvated ions because of ionic interactions within the membrane matrix. Across the literature, salt rejection on the order of 60% for 10,000 ppm NaCl feed solutions and the equivalent appears to be the best figure obtainable for LbL assembled films with various polyelectrolytes. To exceed these limitations, I propose an approach of engineering nano-channels into the selective layer with impermeable platelets, which would introduce size-selection transport mechanisms for solvated ions.

1.9 – Scope of Thesis

This thesis aims to explore the intersection between spray-LbL assembly and inorganic nanomaterials to generate nanostructured selective layers for RO membranes. There is a gap in the literature where LbL has been used to generate selective layers, but not taken full advantage of the unique aspects of the LbL assembly process to incorporate materials that can generate ordered

nanostructures for salt rejection. Nanomaterials such as zeolites and carbon nanotubes have been incorporated into nanostructured membranes for water purification, but not high-aspect ratio clay platelets which appear ideal for the purpose. Taken together, these individual aims represent a structured nanomaterials approach to developing a next generation clay composite selective layer.

Aim #1: Polymeric Substrates as RO Membrane Support Layers (Chapter II)

First, in chapter II, substrates were investigated as support layers for the deposition of spray-LbL assembled clay composite thin films that are more rigorously characterized in chapters III-V. Electrospun (espun) nylon-6 and bisphenol-A polysulfone (PSU) mats of varying fiber diameter and polyethersulfone (PES) ultrafiltration (UF) membranes with varying pore diameters were examined with a basic (PDAC/LAP) clay composite bilayer film architecture. These membranes were subjected to RO conditions in dead-end and cross-flow cells, and then examined for the formation of critical defects. Additionally, a filled-electrospun fiber membrane structure was constructed and considered as a possible single-layer alternative to replace the selective and support layer structure of TFC RO membranes.

Aim #2: Laponite Clay Composite Films as Selective Layers (Chapters III-IV)

Second, in chapters III and IV, materials were investigated and identified for the spray-LbL deposition of simple polymer and composite bilayer films to serve as selective layers in RO membranes. It was hypothesized that effective salt rejection could be achieved through hindering the diffusion of solvated ions through the film by charge interactions with functional groups on strong polyelectrolytes such as quaternary amines and charged nanomaterials. The most thoroughly evaluated material system consisted of the strong polycation poly(diallyl dimethyl ammonium chloride) (PDAC), and laponite clay platelets (LAP).

The second major group of spray-LbL assembled clay composite films was manufactured from weak polyelectrolytes and LAP clay. The cross-linked tetralayer architecture was comprised of alternating (PAH/PAA) bilayers between clay-containing (PAH/LAP) bilayers. As both PAH and PAA are weak polyelectrolytes their degree of ionization depend on assembly pH, enabling the control of film thickness and composition via manipulating this variable and holding the spray times for each component constant. These polyelectrolytes were selected for being inexpensive, off-the-shelf polyelectrolytes and the ability to form amide cross-links that mimic the functionality of commercial RO membranes. The overall goal was to explore the impact of cross-linking on the physical properties of clay composite thin films such as swelling, hardness, and the spacing between clay platelet layers, and how these properties ultimately impact the water and salt permeability properties of the thin films.

Aim #3: Alternative Materials for Selective Layer Assembly (Chapters V-VI)

Third, alternative nanomaterials to laponite clay were examined, including spray-LbL assembled thin films containing high-aspect ratio montmorillonite (MMT) clay platelets and with graphene oxide (GO) platelets (chapter V), and an alternate chemical cross-linking scheme involving catechol-modified polyelectrolytes (chapter VI) that would shortcut the long thermal

cross-linking process. The focus was on the practical spray assembly of membranes containing these materials and identifying the problems that have prevented the easy incorporation of these materials via spray-LbL in prior research.

II. Polymeric Substrates as RO Membrane Support Layers

2.1 – Introduction

2.1.1 – Summary

A qualitative study was conducted to determine the optimal substrate for the deposition of spray-LbL assembled clay composite thin films that are more rigorously characterized in chapters III-V (Figure 2-1). Electrospun (espun) mats of varying fiber diameter and polyethersulfone (PES) ultrafiltration (UF) membranes with varying pore diameters were examined with a surface deposition of a (PDAC/LAP) clay composite bilayer (Figure 2-1a) and subjected to 200 psi flow in a cross-flow cell, applying a shear stress across the surface of the membranes. Additionally, an LbL-filled espun membrane was investigated as an alternative membrane architecture to replace both the selective and support layer structure of TFC RO membranes (Figure 2-1b).
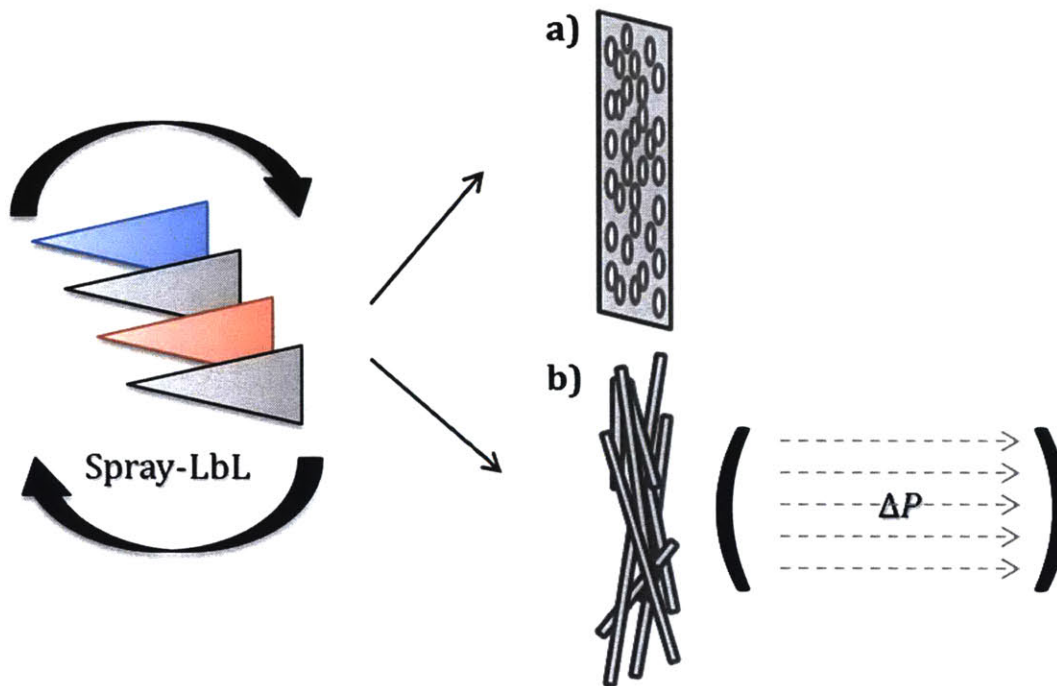
Figure 2-1: Schematic of spray-LbL deposition on a) PES UF membranes; b) espun mats with optional vacuum draw for fiber coating.

Ultimately, the PES UF membranes with the smallest pore size were selected to minimize the formation of critical defects in the membrane under RO conditions. The filled espun membrane structure was determined to be a poor design choice for building a novel RO membrane as the effective flux was too low to be of practical value.

2.1.2 – Investigated Substrates

Several possible supporting layers were considered for spray-LbL deposition of the active layer. One key requirement was that the substrate be either natively charged or could be plasma-cleaned to deposit surface oxide charges without significantly altering the substrate's mechanical robustness. Polymeric substrates were preferred because these were the clearest analog to commercially-available TFC RO membranes[103, 104], are easy to manufacture, and serve effectively as mechanically strong porous supports. Thus, these substrates were interesting from a device fabrication perspective. Of the polysulfone family of polymers, either polysulfone (T_g = 185°C) or a bisphenol-A derived polysulfone (referred to as polyethersulfone) (Tg = 190°C), were of interest because these are common membranes for water purification and support layers for RO membranes (Figure 2-2).
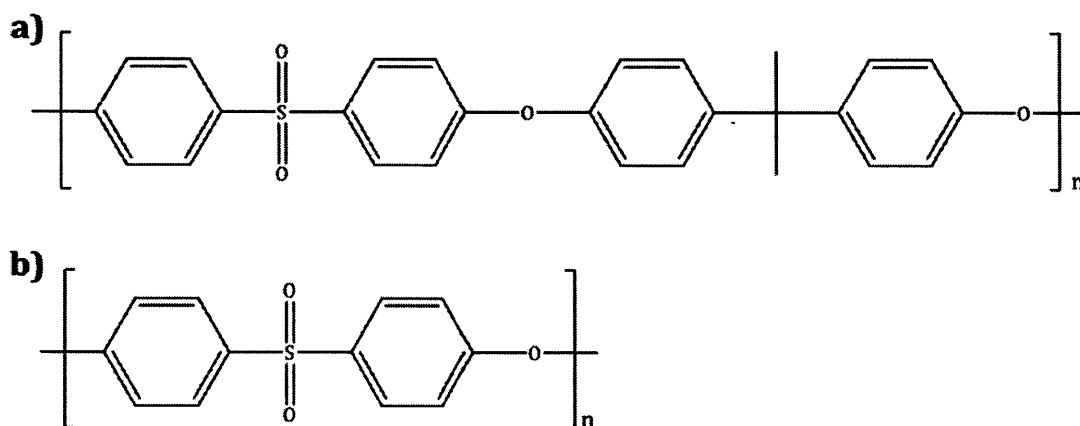
Figure 2-2: Repeat monomer structure of common porous support materials for TFC RO membranes and various UF/NF applications: a) polysulfone; and b) polyethersulfone.

UF membranes, which are commonly used for the filtration of small particulate matter but are generally not salt-selective, were selected as a substrate because the structures bear a strong resemblance to the polysulfone support layers in RO membranes[103]. In membrane compaction studies, polysulfone membranes exhibited less elastic behavior than cellulose acetate membranes[334], an important attribute for an RO support layer as elastic deformation will apply mechanical stress on the selective layer. Volume porosity in UF membranes ranges from 80% for smaller pore diameters (100 nm) down to 60% for larger pore diameters, and under an applied 0.2 MPa (2 bar) pressure the volume porosity decreases approximately 8%[334].

In collaboration with the Rutledge lab, electrospun mats of approximately 33.1 ± 6.9 μm thickness were assembled from nylon-6 and polysulfone to investigate as high-flux replacements for the phase-inversion support layers commonly used in TFC RO membranes. It was hypothesized that replacing the support layer with a highly porous espun mat could increase overall water flux for the assembled membrane. The fibers in an espun mat are not uniformly oriented nor have a standard pore size or structure[335]. Instead, the espun processing generates a mesh with an

average effective pore size that is a function of the fiber diameter, with a common rule-of-thumb being the pore size is approximately 3.5 to 5 times the fiber diameter based on the particular measurement technique used[336, 337]. However, there is a design challenge for the selective layer if the support layer is replaced by an espun mat as more porous materials are generally more compressible. Espun mats, even those with fiber welding through annealing, exhibit low solidity and thus are compressible under the pressures found in RO applications; for pressures as low as 20 kPa (0.2 bar), significant deformation was reported that follows a power-law relationship[335].

The full list of support layers for spray-LbL deposition is compiled in Table 2-1.

Table 2-1: Support layers investigated for spray-LbL deposition, with pore sizes and material noted.

Substrate	Polymer	Pore Sizes Investigated
UF/MF Membranes	Polyethersulfone	30, 100, 220 nm; 1 µm
Electrospun Mats	Nylon-6	D = 0.7 µm; ≈2.5-3.5 µm
Electrospun Mats	Polysulfone	D = 0.4 µm; ≈1.4-2 µm

2.2 – Results and Discussion

2.2.1 – Plasma Cleaning Conditions for Polyethersulfone Ultrafiltration Membranes

The UF membranes were purchased from Millipore and Sterlitech in a range of pore sizes: 30 nm, 100 nm, 220 nm, and 1 µm (Table 2-1). The thickness of the PES UF membranes was fairly uniform at 136 µm ± 1.0 µm for the 100 nm and greater pore sizes, but the measured thickness for the PES-30 UF membranes was greater: 154 µm ± 3.3 µm. Before LbL assembly, it is necessary to functionalize the membrane surface so the film components adsorb and adhere to the surface. Plasma-cleaning, which removes surface contaminants and oxidizes the exposed surface, greatly increases the hydrophilicity of the membranes[338-340] and is an excellent method to prepare substrates for LbL deposition[341]. For substrates such as glass or silicon wafers, the standard lab protocol recommends 5 minutes of O_2 plasma at 18 W. However, plasma-cleaning PES membranes at these conditions turned the substrates so brittle that regular handling would cause the membranes to fracture and splinter. After examining plasma-cleaning times of 1, 2, 3, and 4 minutes as well as 30 seconds, 30 seconds of air plasma (atmospheric O_2) was selected because the films were fully wetted by water and there was no visual discoloration or induced brittleness as the result of the plasma-cleaning.

Water uptake was examined for PES UF membranes under DI and saline water conditions to determine how the plasma treatment altered the behavior of the support layer (Figure 2-3). For this experiment, PES UF membranes with 30 nm pores were plasma-cleaned according to the 30 second protocol and then exposed to DI water and NaCl solutions with concentrations up to 3.5 wt.%, corresponding to the average concentration of seawater. In untreated PES UF membranes, the mass of the wet support layer was approximately 193% greater than the mass of the dry support layer, corresponding to an uptake of water held in the pores of the PES membrane (Figure

2-3a). This figure was decreased to 162% as the saline concentration was increased to 3.5 wt.%, indicating the interactions between the mostly hydrophobic PES and the hydrophilic solvated ions result in a crowding-out effect that reduces the total water uptake in the pores. This effect is not observed for the plasma-cleaned samples, where the percentage increase was roughly constant at 233% (Figure 2-3a); because the membrane surface becomes hydrophilic during the plasma cleaning process, significantly more water is taken up in the membranes and there are not any hydrophobic interactions with solvated ions that prevent this uptake as the saline concentration is increased. Using a micrometer, the change in thickness was also measured for the UF membranes under the same conditions (Figure 2-3b). The initial measured thickness of 154 μm ± 3.3 μm for the PES-30 UF membranes held roughly constant under the experimental conditions, with at most a 2% increase in thickness observed for the plasma-cleaned membranes and no statistically significant increase observed for the untreated membranes. This indicates the PES UF membranes are a good candidate for the deposition of LbL-assembled composite films, as the plasma-cleaning required for LbL deposition does not significantly alter the support layer thickness under saline conditions.
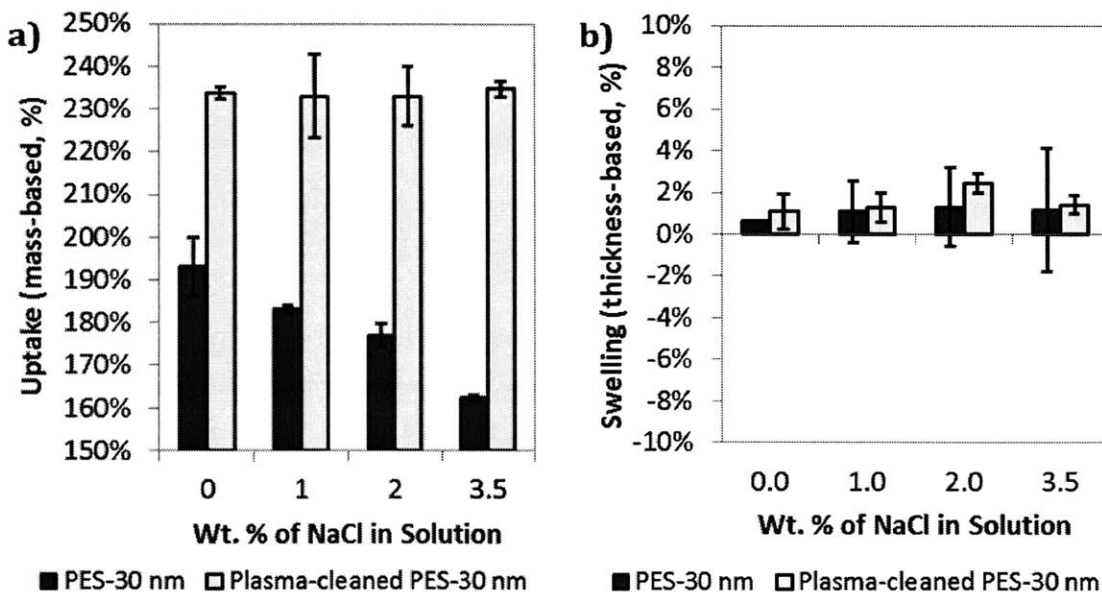
Figure 2-3: Swelling in PES UF membrane support layers, 30 nm pores: a) mass-based water uptake when exposed to DI water and saline solution for untreated (black) and plasma-cleaned (white) membranes; b) increase in support layer thickness for untreated (black) and plasma-cleaned (white) membranes.

Goniometer experiments to determine the contact angle of a water droplet on the surface of the porous substrates (Table 2-2). These experiments could not be conducted reliably on electrospun mats as water filled large pores and did not bead on the surface, however it was possible to take measurements on the mostly hydrophobic skin layer of PES UF membranes and the commercially available Koch TFC-HR membranes.

Table 2-2: Contact angle measurements on substrates for spray-LbL deposition.

Substrate	Untreated	Plasma-Treated
All Espun	≤5.0°	≤5.0°
Koch TFC-HR	78.4° ± 2.2°	60.4°± 0.7°
UF Mem., PES-30 nm	87.8° ± 1.1°	(wetted) ≤5.0°
UF Mem., PES-100 nm	86.6° ± 1.9°	(wetted) ≤5.0°

For plasma-cleaned substrates, water fully wetted the surface and yielded no appreciable contact angle, indicating the surface was fully hydrophobic for LbL deposition. For untreated substrates, the Koch TFC-HR membrane, used as a control membrane, exhibited a somewhat hydrophobic contact angle of 78.4° and after plasma cleaning of 30 seconds at 18 W approximately 60.4°. This indicates the surface was made slightly more hydrophilic but not fully so; it is likely the number of oxide groups deposited on the dense and cross-linked polyamide surface layer was lower than was observed for the PES UF membranes. For these samples, the measured contact angles were on average 87.8° and 86.6°, independent of the underlying pore size. Following plasma treatment, water fully wet the surfaces of the PES UF membranes, indicating the surface was significantly more hydrophilic than the polyamide selective layer of the TFC-HR membrane.

2.2.2 – Layer-by-Layer Deposition on Polyethersulfone Ultrafiltration Membranes

Composite (PDAC/LAP) films were then deposited on PES membranes and then examined under the SEM to determine whether the sprayed film components bridged the pores to form uniform coatings. Micrographs of the uncoated and coated membranes are shown in Figure 2-4.
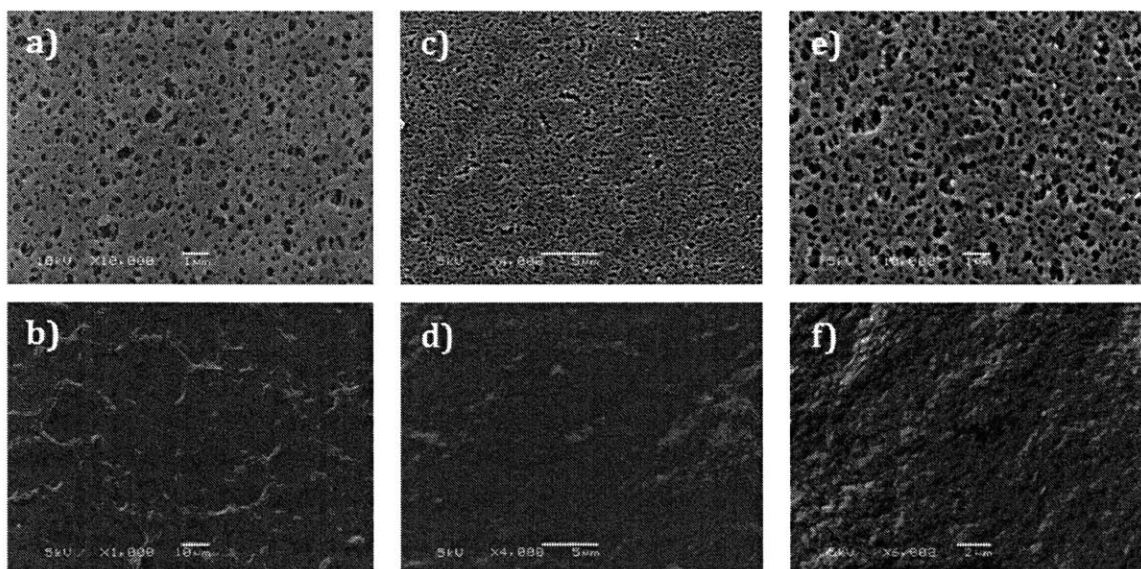
Figure 2-4: SEM micrographs of clay composite bilayer films deposited on PES UF membranes: a) uncoated PES-220 UF membrane; b) PES-220 membrane coated with (PDAC/LAP)₆₀ 3s:3s film, pH 10.0 assembly; c) uncoated PES-100 UF membrane; d) PES-100 membrane coated with (PDAC/LAP)₂₀ 3s:3s film, pH 10.0

assembly; e) uncoated PES-30 UF membrane; f) PES-30 membrane coated with (PDAC/LAP)$_{60}$ 3s:3s film, pH 10.0 assembly.

The uncoated membranes have a skin layer that is relatively uniform for the pore sizes examined (Figure 2-4a, 2-4c, 2-4e). The underlying pores were fully bridged with the deposition of 20 bilayers or more of the (PDAC/LAP) composite film architecture, and such would be observed for later evolutions of the clay composite film architecture. This corresponds to the linear growth regime of the film architecture as discussed in Chapter III. Additionally, larger surface macrostructures were observed for the films deposited on the 220 nm pore substrates (Figure 2-4b) than for the 100 nm or 30 nm substrates (Figure 2-4d, 2-4f), which are suspected to result from the film bridging the pores with the first layer depositions to form a scaffold for further layers to be deposited. With pores on the order of 100 nm or smaller, these bridges could be formed with relatively few bilayers, leading to smoother surfaces of the deposited films. The approximate diameter of the LAP clay platelets is between 50 nm and 100 nm, and it was observed this characteristic length scale matches the underlying pores for the 30 nm and 100 nm substrates closely. Macrostructures such as those observed in Figure 2-4b were always observed for the clay composite films deposited on substrates with pore sizes significantly greater than the underlying substrate.

The small granular structures observed in Figure 2-4f correspond to individual platelets on the surface of the film. Whether or not these are observable in the micrographs is a function of the thickness of the Au/Pd coating deposited on the surface of the films prior to SEM imaging. For optimal visibility while still coating the sample adequately to prevent surface damage caused by the beam and surface charging, 20 seconds of Au/Pd sputter coating is recommended. This corresponds to an approximate thickness of 4 nm. Thicker Au and Au/Pd coatings as are commonly proscribed in training (on the order of 10-15 nm) will obscure surface features of the LbL films.

Additionally, it is recommended that SEM imaging of these types of clay composite films be down with less than or equal to 5 kV beam strength. The majority of SEM micrographs presented in this report are imaged with 2-3 kV beam strength and a spot size below 30, which increases resolution and prevents surface charging effects that damage the film; popcorn-like exploded structures and crack formation were observed real-time for samples taken at 10 kV.

Cross-sectional SEM samples were prepared through cryo-fracturing, where the films are submerged in liquid N$_2$ and then manually separated with forceps, to observe if the film solely bridged the surface or had penetrated into the pores of the UF membrane (Figure 2-5).
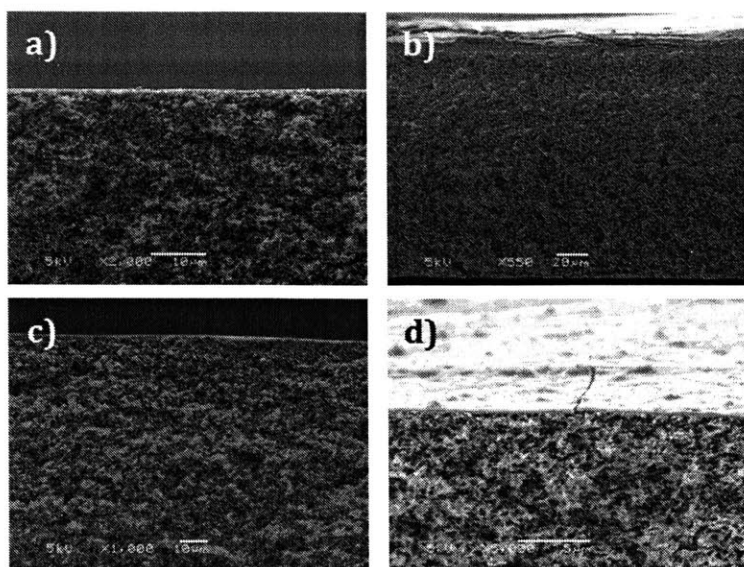
Figure 2-5: Cross-sectional SEM micrographs of clay composite films deposited on UF membranes: a) uncoated PES-100 membrane; b) PES-100 membrane coated with $(PDAC/LAP)_{50}$ 3s:3s film, pH 10.0; c) uncoated PES-30 membrane; d) PES-30 membrane coated with $(PDAC/LAP)_{60}$ 3s:3s film, pH 10.0.

By visual inspection, the clay composite films appear to deposit across the surface of the films and do not penetrate the surface of the PES UF membrane into the porous polymer mesh (Figure 2-5b, 2-5d). This indicates that despite the pores wetting as the result of the plasma treatment, the sprayed solutions and clay dispersion are kinetically trapped at the surface during film deposition. The film components adsorb at the film interface, bridging the pores, and then are rinsed away during the drainage and rinsing steps of the spray-LbL assembly process. This is a function of the surface tension of water at the interface between the skin layer and the sprayed solutions/dispersion for the first layers deposited.

Based on these observations, the PES UF membrane with the smallest pore size, 30 nm, was selected to proceed with the optimization of the clay composite layers, as described in later chapters of this work. These particular polymeric membranes required the fewest bilayer depositions to build up uniform surface films and film bridging across pores was minimized.

2.2.3 – BET Surface Analysis to Determine Pore Size

Although all the PES-30 UF membranes were marked as containing as 0.03 μm (30 nm) pores, the surface SEM micrographs of the uncoated membrane in Figure 2-4e, the cross-sectional SEM micrographs in Figure 2-5, and others taken throughout this report consistently show pores that appear to be greater than 30 nm. BET surface analysis was conducted on a sample PES-30 UF membrane with a total mass of 0.0803 g (Figure 2-6) to calculate a pore size distribution via adsorption at the nitrogen isotherm[342, 343]. The calculated specific surface area via the nitrogen adsorption was 20.7 m^2/g of PES-30 UF membrane.
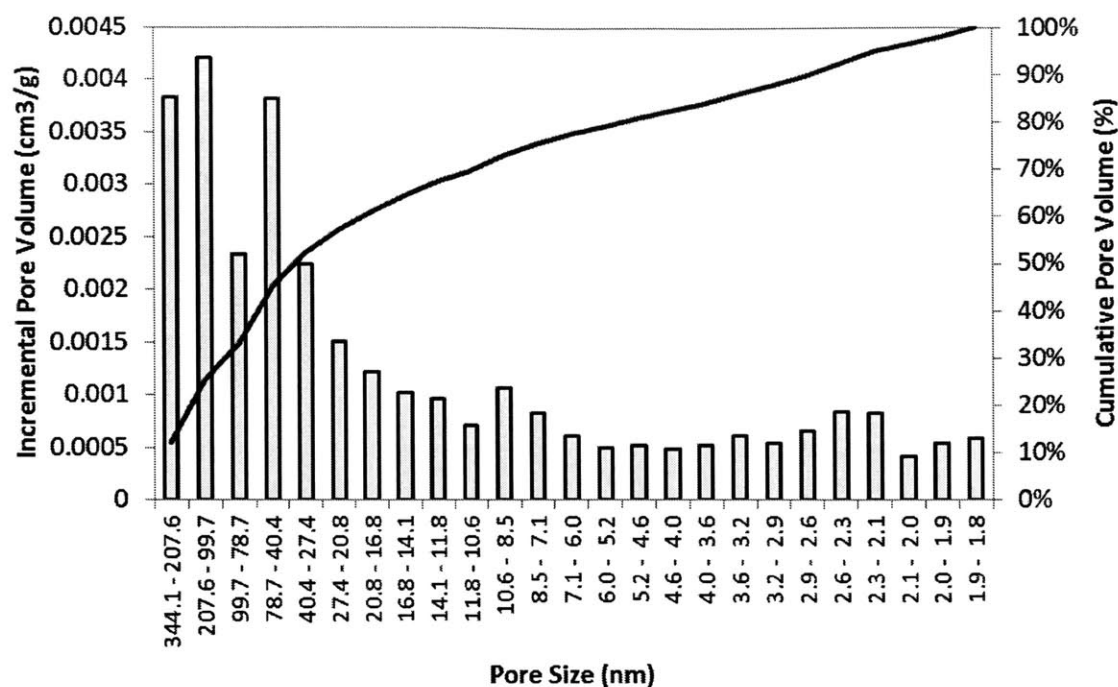
Figure 2-6: Histogram of pore size distribution for Sterlitech PES-30 nm UF membranes measured through BET N_2 surface analysis with DFT pore size distribution model.

The distribution of pore sizes (Figure 2-6) appeared to be bimodal, with a significant fraction of pores greater than the advertised 30 nm size in the 100-350 nm range, and a second smaller concentration of pores with sizes between 80 nm to 27 nm. A significant number of pores, corresponding approximately 39% of the cumulative pore volume, were estimated to have average pore diameters less than 20 nm. This distribution is representative of an asymmetric membrane with a larger macroporous void structure that was discussed in section 1.5.1.

2.2.4 – Layer-by-Layer Deposition on Electrospun Mats

Nylon-6 and polysulfone espun mats were coated according to the above protocols and examined under SEM to observe whether the same bridging behavior was possible with the larger micron-sized pores (Table 2-1); micrographs are shown in Figure 2-7.

The micrographs of uncoated nylon-6 and bisphenol-A derived polysulfone (PSU) (corresponding to structure 2-2b) are shown in Figure 2-7a and 2-7d respectively. Compared to the PES UF membranes above, the uncoated espun mats do not have a skin layer with a regular and porous structure, but rather are a mesh of fibers with irregular pores that range from roughly 3.5 to 5 times the fiber diameter. The annealed PSU mats, such as those depicted in Figure 2-7d, have a surface topology that more resembles the UF membranes. However, the minimum pore size estimate for these support layers is on the order of 1.4 μm or greater (ranges noted in Table 2-1).

These mats were used to study how spray-LbL assembled clay composites bridge larger pores and what conditions would be required to build a uniform selective layer.
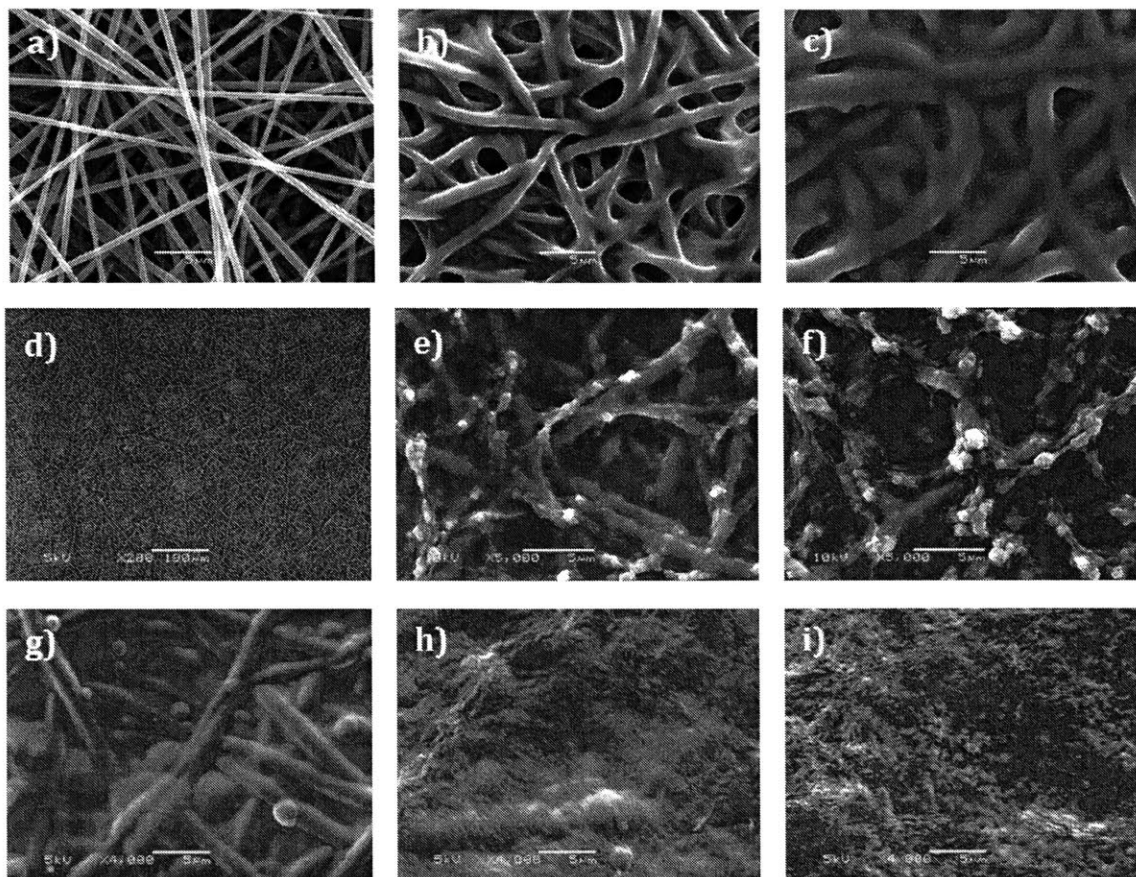
Figure 2-7: SEM micrographs of bilayer films deposited on espun mats: a) uncoated espun nylon-6 mat, 0.56 μm fiber diameter; b) nylon-6 coated with $(PAH/PAA)_{50}$, pH 6 film; c) nylon-6 coated with $(PDAC/SPPO)_{200}$ film; d) espun PSU mat, 0.40 μm fiber diameter; e) PSU coated with $(PDAC/LAP)_{80}$ 9s:9s film, pH 10.0; f) PSU coated with $(PDAC/LAP)_{100}$ 9s:9s film, pH 10.0; g) PSU coated with $(PDAC/LAP)_{75}$ 3s:3s film, pH 10.0; PSU coated with $(PDAC/LAP)_{100}$ 3s:3s film, pH 10.0; PSU coated with $(PDAC/LAP)_{150}$ 3s:3s film, pH 10.0.

Polymeric bilayer systems such as (PAH/PAA) and (PDAC/SPPO) films bridged the pores in the nylon-6 espun mats only with the deposition of more than 100 bilayers. Films with less than 100 bilayers (such as the 50 bilayer film in Figure 2-7b), would bridge narrow gaps in the espun mat and form what appear to be polymer welds to join nearby fibers. However, a significantly greater number of bilayers were required to fully bridge the pores, such as the $(PDAC/SPPO)_{200}$ film (Figure 2-7c). From a design perspective, this is incredibly wasteful of material, as each layer deposition in spray-LbL results in less than 10% of the sprayed material adsorbing to the membrane. While some kinetic capturing may occur within the irregular surface of the espun mat, it was necessary to select a substrate that could be bridged easily and quickly with the spray-LbL assembly process.

The annealed PSU mats were more easily bridged with spray-LbL deposited thin films, with as few as 75 bilayers of the (PDAC/LAP) 3s:3s film fully bridging the pores (Figure 2-7g). The macrostructures observed correspond to the LbL-assembled film coating the espun fibers, and was apparent even with 100 bilayers deposited (Figure 2-7h), but with 150 bilayers deposited (Figure 2-7i) were finally masked and only the smaller structures associated with the clay platelet capping layer were easily visible.

Interesting surface structures were observed when the same (PDAC/LAP) film was deposited with 9 second spray times instead of 3 seconds (Figure 2-7e, 2-7f). The espun fibers appeared to serve as nucleation points for aggregations of clay platelets, which formed either knobs or ridge-like structures aligned with the espun fibers. As these structures were only observed with the clay composite films with the highest clay content (86%; see section 3.2.5), it is likely these structures are aggregates of LAP clay platelets. The nucleation points appear to be at fiber junctions, which may indicate the clay platelets were trapped between fibers and not rinsed away during the drainage and rinsing steps of LbL deposition.

Cross-sectional SEM imaging of films deposited on espun membranes were also conducted (Figure 2-8).
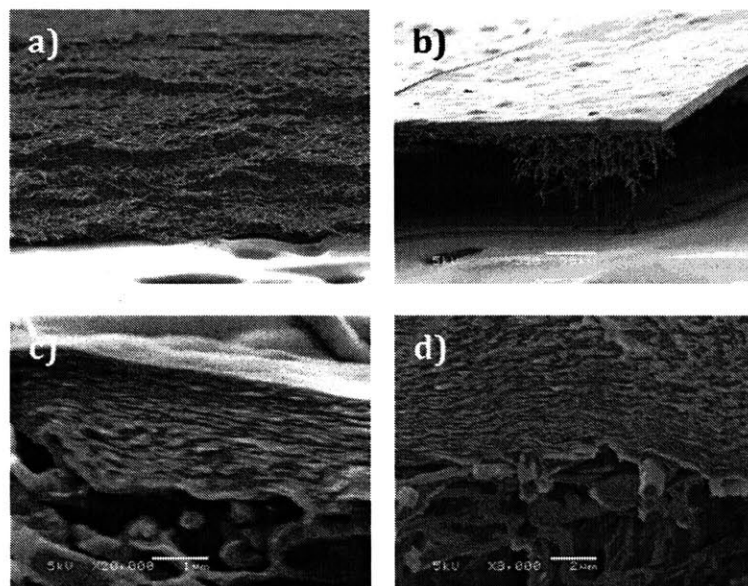
Figure 2-7: Cross-sectional images of LbL films on espun mats: a) uncoated PSU espun mat; b) same coated with (PDAC/LAP)$_{100}$ 3s:3s film, pH 10.0; c) same coated with (PDAC/LAP)$_{75}$ 3s:3s film, pH 10.0; d) same coated with (PDAC/LAP)$_{100}$ 3s:3s film, pH 10.0.

The cross-section for uncoated, untreated PSU espun mats with 0.4 μm fiber diameter is shown in Figure 2-8a; the greater pore volume is evident when compared to the PES UF membranes (Figure 2-5a). The first spray-deposited layers penetrated into the espun fiber matrix, and bridging was only evident for the later bilayers in the assembly process (Figure 2-8c, 2-8d). Interestingly, the

LbL-assembled film cryo-fractured along relatively straight and clean lines while the espun mat separated along a more jagged and irregular surface, resulting in free-standing LbL structures like the one depicted in Figure 2-8b. The random orientation of the fibers in the electrospun mat, the relative orientation of the clay platelets in the LbL-assembled film, as well as the relatively lower density of the espun mat contribute to this phenomenon.

There were several factors that led to the rejection of espun mats as a support layer for the clay composite RO membrane: 1) the high degree of variability in the surface topology, leading to difficulty in bridging the pores without the deposition of massive selective layers; 2) the large spans the films must bridge; and 3) the increase in compressibility of the espun mat substrates. These factors combined make it difficult to deposit an effective LbL-assembled selective layer, and even more difficult to prevent that film from forming critical defects under RO conditions where pressures in excess of 50 bar can be applied to the membrane.

2.2.5 – Filled Electrospun Mats as Novel RO Membranes

One alternative membrane design that was investigated involved the conformal coating idea first explored by Kevin Krogman and David Liu[320, 344, 345]. Instead of depositing a thin surface film on the electrospun mat, a vacuum was used to draw the film components through the espun mat, creating a filled composite membrane that could serve as its own support and backing layer. This was hypothesized as a method to reduce void volume and the compressibility of the espun mat under RO conditions by filling the mat with an LbL film, as well as a method to couple the selective and support layers together to prevent the formation of critical defects during RO operation.

Both the (PAH/PAA) bilayer system and a composite bilayer (PDAC/LAP) systems were applied to PSU espun mats under vacuum. To determine when the mat was filled, an anemometer was used to measure the velocity of the wind at the film interface after the deposition of 5 or 10 bilayers. This figure for the raw vacuum, with the substrate holder but without the substrate itself loaded, was 1.95 m/s (3.8 knots); with the substrate holder and substrate loaded before the first bilayer was deposited was 1.75-1.80 m/s (3.4-3.5 knots). The plot of this for both material systems is shown in Figure 2-9.

From this filling experiment, it was evident from the rapid drop in velocity that the PSU mat was nearing filled by the deposition of the 60th bilayer of the (PDAC/LAP) system, but by the 240th bilayer of (PAH/PAA) there was still an appreciable velocity measured of 0.57 m/s (1.1 knots). The mat was filled significantly more quickly with the clay composite material system, likely because the clay platelets are relatively large and have fixed geometry, which form large aggregates within the mat instead of being pulled through by the vacuum. Thus, it is hypothesized the film deposited is not truly an LbL-assembled architecture but rather reflects a bulk capture of clay material in geometrically confined pores in the espun mat. The polyelectrolytes, which have several more degrees of freedom, can conformally coat the fibers in a space-efficient manner that allows excess, unabsorbed material to pass through the mat. Ultimately, this requires the additional deposition of nearly 200 bilayers to fill the espun mat with the film components.
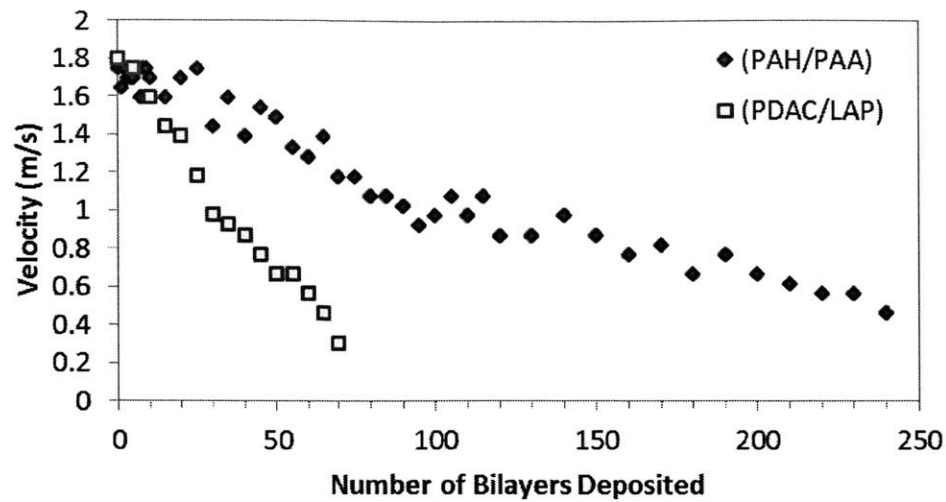
Figure 2-9: Plot of vacuum velocity through the espun mat against the number of bilayers deposited for filled PSU espun mats.

Both surface and cross-sectional SEM imaging was conducted on the filled (PAH/PAA) espun mats (Figure 2-10). It is clear from the deposition of 50 bilayers the polyelectrolytes are conformally coating the individual PSU fibers and bridging between fibers to form welds (Figure 2-10a). After the deposition of 190 bilayers, the surface of the espun mat was partially filled with polymer, but there were still small gaps present (Figure 2-10c). The back of the mat also has polymer coating the fibers, indicating the polyelectrolytes were pulled through and deposited throughout the entire espun mat (Figure 2-10b).
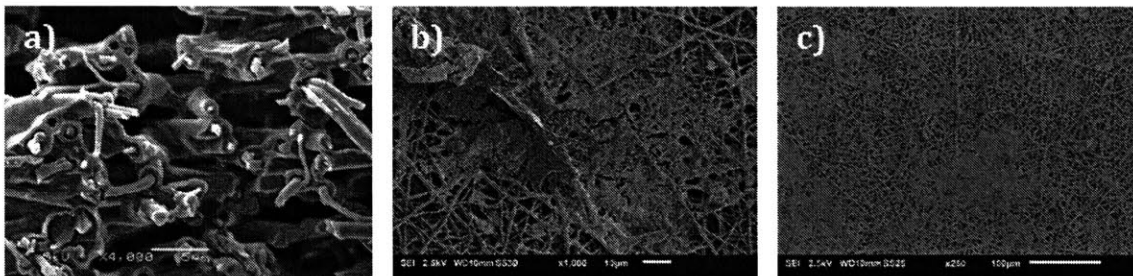
Figure 2-10: SEM micrographs of filled PSU mats with (PAH/PAA): a) cross-section after 50 bl.; b) back surface of the composite membrane after 190 bl. deposition; c) front surface of composite membrane after 190 bl. deposition.

No permeation data could be collected on the filled membranes (240+ bl.) from the dead end permeation cell for any operating pressures possible on the bench scale. This is because the effective selective layer for the filled membranes is on the order of 50 μm instead of the 100-200 nm thick that is common for commercial TFC RO membrane selective layers and the 100-400 nm range that is common for the spray-assembled films covered in this report, a factor approximately 250 times greater. It is suspected that whatever small channels or pores still existed from the film

deposition were compacted under the RO pressure to form essentially an espun-fiber reinforced polymer composite. This membrane has a structure reminiscent to reinforced concrete, with the espun fibers taking an analogous role to the rebar and the LbL film taking an analogous role to the concrete mix. The additional thickness reduced the effective flux to nil, even with the application of significant operating pressures. From an engineering perspective, optimizing the filling of the espun mat was not a worthwhile area of research because support layers with lower void space were already available off-the-shelf, and were far more economical from both a time and cost perspective. Thus, upon consideration, this approach was determined to be ineffective for developing an RO membrane.

2.3 – Conclusion

The primary conclusion drawn from this study was that all the examined substrates could be used as support layers for spray-LbL deposition; it was possible to deposit uniform films over all the substrates examined, with a minimum number of bilayers around 20 for small pore size substrates such as the PES-30 UF membranes, and up to 75 to 100 required for a uniform film on the espun mats with micron-sized or larger pores.

One hypothesis taken away from this study was that matching platelet size as closely as possible to the pore size of the underlying substrate would minimize film bridging over the substrate. This could potentially reduce the rate of failure under RO conditions, which led the future investigations to be conducted on PES UF membranes with 30 nm pores. Although the espun mats are an attractive substrate in terms of water permeability, the substantial void volume and large pore size are inconvenient to assemble LbL-assembled selective layers on, especially clay composite selective layers. These two factors also lead to significant compressibility under RO conditions, which applies additional compressive and shear stresses to the selective layer that cracked the films during operation.

Additionally, the filled espun mat concept was determined to be an inefficient route to assembling a new combined selective-support layer that could potentially be useful for hollow fiber RO applications. This process generates a massive filled composite membrane that may have similar permeability properties to the selective layers investigated in chapters III and IV, but was so thick as to yield effectively no flux. This is an expected result from increasing the effective thickness of the selective layer from 30-200 nm, which is common for TFC composites, to over 40 μm, an increase of two to three orders of magnitude. There is a significant tradeoff between selectivity and raw water flux, which was one of the key insights that led to the development of TFC membranes and is further confirmed in this experiment.

2.4 – Materials and Methods

2.4.1 – Materials

LAP clay was provided by Southern Clay Products; clay dispersions were prepared at a concentration of 1.0 wt.% clay and the balance reagent-grade water. PDAC (MW: 200-350 kDa) was

obtained from Sigma-Aldrich. Both PAH (MW: 60 kDa) and PAA (MW: 20 kDa) were obtained from Polysciences, Inc. The polyelectrolyte solution was prepared at 10 mM concentration and was adjusted to the assembly pH of 10 by using a Φ340 pH/Temp Meter and concentrated NaOH solution.

Ultrafiltration polyethersulfone membranes were purchased from Millipore, 220 nm pores (GPWP04700), and Sterlitech: 30 nm pores (PES00347100), 100 nm pores (PES0147100), 1 μm pores (PES1247100). Heat-compressed nylon-6 and polysulfone espun mats were obtained from the Rutledge lab. All PES membranes and espun mats were plasma-cleaned in a Harrick Plasma Cleaner/Sterilizer PDC-32G at 18 W for 30 seconds and soaked in PDAC or PAH solutions before spray-LbL film assembly, corresponding to the first layer deposited in the film.

2.4.2 – Spray Layer-by-Layer Deposition

Films were constructed using a custom-built spraying apparatus. Solutions and clay dispersions were aerosolized with N_2 gas at 20 psi and are sprayed onto the substrate rotated at 10 rpm. The basic program for each layer involved spraying the film component for 3 seconds, pausing for a 5 second drain period, rinsing for 10 seconds with pH-adjusted water, and then and then a final 5 second drain period. The sequence is repeated for each film component listed to assemble a bilayer.

For the filling experiments, a smaller 2 cm-wide custom-built PVC assembly was employed as a substrate holder, which could be connected to a vacuum flask and the in-house vacuum. The samples were mounted on a fine mesh to distribute the vacuum pressure equally across the film interface. The rinse steps were eliminated and the drain times were extended to 20 seconds to allow the vacuum to clear the solution from the substrate holder before spraying a subsequent layer.

2.4.3 – Characterization

A Mitutoyo Series 293 MDC-MX micrometer was used to measure the thickness of the PES membranes. Both a JEOL JSM-6060 and a JSM-6010LA Scanning Electron Microscope (SEM) were used to image both film surfaces and cross-sections. Cross-sectional SEM samples were prepared via the cryo-fracture method by submerging the sample in liquid N_2 and then physically tearing the sample with forceps and mounted on Ted Pella, Inc. #16104 Low Profile SEM Mount Pins. A Rame-Hart Contact Angle Goniometer with 1 μm water droplet size was used to measure the contact angle on TFC-HR and PES UF membranes. An ExTech Instruments Mini Thermo-Anemometer Model #45118 was used to measure the velocity drawn by the vacuum at the film interface during the filling experiments.

III. Laponite Clay-Composite Bilayer Film Architectures

3.1 – Introduction

3.1.1 – Summary

In this chapter of the report, materials were investigated and identified for the spray-LbL deposition of simple polymer and composite bilayer films to serve as selective layers in RO membranes. It was initially hypothesized that effective salt rejection could be achieved through hindering the diffusion of solvated ions through the film by charge interactions with functional groups on strong polyelectrolytes such as quaternary amines, sulfonates, carboxylic acids, and charged nanomaterials. The most thoroughly evaluated material system consisted of the strong polycation poly(diallyl dimethyl ammonium chloride) (PDAC), and laponite clay platelets (LAP) (Figure 3-1).
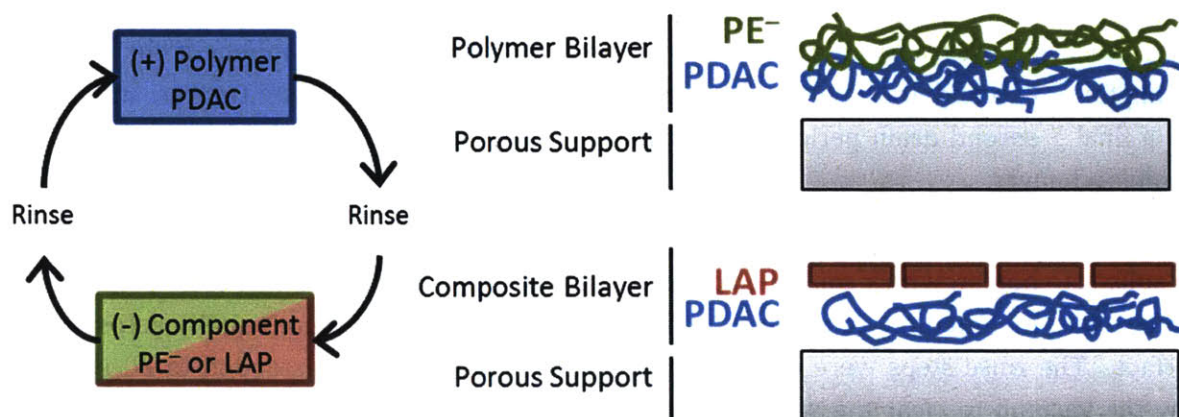
Figure 3-1: Schematic of spray-LbL deposition for a polymer and clay composite bilayer.

The study on strong polyelectrolyte film systems and the composite clay bilayer system show demonstrated simultaneously that clay composite thin films can serve as selective layers in RO membranes, but a more complicated film architecture that incorporates a cross-linkable polyelectrolyte system is required to improve mechanical strength of the films and ultimately salt rejection. Additionally, attention shifted to developing nano-channels that maximized salt rejection through the size exclusion transport mechanism, which became the overriding focus of Chapter IV.

3.1.2 – The Generation of Clay Composite Film Architectures

Polymer and clay composite bilayer films were initially deposited on various porous substrates via spray-LbL as depicted in Chapter II to identify the appropriate support layer for the RO membrane. Concurrently, proper techniques for preparing clay dispersions for spray-LbL assembly were developed, and the kinetics of spray-LbL deposition were used to develop several different films of varying physical properties that were evaluated for water and salt permeability.

Films containing PDAC and sulfonated polyanions such as sulfonated polystyrene (SPS) and sulfonated poly(phenyleneoxide) (SPPO) were briefly explored to investigate films that rejected

salts via hindered diffusion caused by increased charge interactions (see summary in 1.8.3, cursory observations presented in 3.2.10). However, these material systems were deemed too similar to existing work in the literature[313-316, 327-329] (see section 1.8.3) and did not take advantage of the unique properties of LbL to incorporate charged nanomaterials into the thin film architecture. As discussed in 1.5 and 1.6, incorporating charged high-aspect ratio nanomaterials and polyelectrolytes into brick-and-mortar type structures creates thin nano-channels between impermeable plates that inhibit the flow of large solutes. By fine-tuning the spray-LbL assembly conditions, it is hypothesized the spacing between platelet layers and thus the width of these nano-channels can be controlled and reduced to the order of 1-3 nm, which would introduce a size exclusion transport mechanism that could increase salt selectivity while providing a mechanism for water to traverse the membrane.

The first clay composite film architectures examined were formed between strong polycation PDAC and negatively-charged LAP clay. Some literature has been published on this film architecture in prior years, including structural analysis through X-ray reflectometry and photoelectron spectroscopy studies[346], QCM-D studies on the buildup of (PDAC/LAP) films compared to other strong polyelectrolyte films[266, 347], and the application of the films as barrier layers to tune the delivery of therapeutics in LbL films[348]. By manipulating the spray times from the set of [1, 3, 6, 9] seconds for each of the film, drastically different films with different clay compositions were generated. It was hypothesized these films would combine the hindered diffusion through charge effects from the first film architectures and introduce a size exclusion transport mechanism.

The synthetic laponite clay platelets used to generate all the films in this report were LAP-XLG batch platelets acquired from Southern Clay Products. Laponite clay is a 2:1 smectite clay, meaning it is a silicate with a regular lattice structure of consisting of tetrahedral, octahedral, and tetrahedral layers[349] that can be dispersed in aqueous solution[350]. These synthetic clay platelets have an aspect ratio of approximately 30:1[351, 352] (verified in section 3.2.1), and are cation-exchanged, giving the clay platelets a negative surface charge when dispersed in water so they may be incorporated into LbL films. Aqueous LAP clay dispersions will form aggregate complexes and gel structures, with a rate proportional to the ionic strength of the solution[353, 354] although there is some evidence this effect caps in high ionic strength solutions[355]. Dispersions of LAP clay amongst other smectite clays can be stabilized through the addition of a surfactant such as poly(isobutylene), however the solvent used for this research was poly(decene)[356], an organic solvent incompatible with spray-LbL assembly. Similar to other smectite clays of this type, LAP is an excellent material for building clay-polymer nanocomposites because of its cation exchange capacity, relative platelet uniformity, and high surface area for functionalization[357].

3.2 – Results and Discussion

3.2.1 – Preparation of Laponite Clay Platelet Dispersions

First, proper dispersion protocols had to be developed to suspend the clay platelets in water for spray-LbL deposition. Prior literature on dip-LbL assembled films with LAP and similar clays have used a range of 0.5 to 2.0 wt.% dispersions[171, 203-205, 245, 260, 302, 324, 326, 358, 359]. The 1.0 wt.% dispersion was selected because it fell in an optimal zone of being concentrated enough to deposit easily via spray-LbL assembly but also disperse enough that clay aggregates would not form in the dispersion; the spray nozzles were clogged by 2.0 wt.% dispersions. This is due to the formation of clay gels, which is dependent on the overall ionic strength of the aqueous LAP dispersion and is accelerated at greater concentrations than 3 g/L, which is approximately 0.12% by volume[360].

Initially, dispersions were prepared by mixing the bulk laponite clay into the required volume of water in a glass bottle. The mixture was stirred for a half-hour to break up large bulk and then transferred to a sonicator for a minimum of 8 hours or more generally overnight. However, a second method was developed that consisted of slowly adding the laponite clay into rapidly-stirred water over the course of five minutes followed by an hour of steady mixing proved. Visual turbidity inspection is one method to determine the degree to which the clay platelets have dispersed, with cloudiness indicating aggregates were still present and clarity indicating the clay platelets are either fully exfoliated or in small oligomers[352]. No detergents were required to exfoliate the platelets as they were sufficiently hydrophilic, but the addition of significant amounts of salt or pH adjustment directly increases the ionic strength and causes the platelet aggregation[350, 352]. Thus, the dispersion was used near its native pH (10.0), with the other polyelectrolyte solutions and rinses being adjusted to the assembly pH.

Clay dispersions prepared via these methods were analyzed using dynamic light scattering (DLS) to determine a hydrodynamic radius for the clay platelets (Table 3-1).

Table 3-1: DLS measurements on LAP clay dispersions for different sonication and mixing methods.

Dispersion Method	Sample Prep.	Hydrodynamic Radius (nm)	Zeta Potential (mV)
Bulk addition, mixing, 20 hr. sonication	40x dilution, dust cutoff 20	53.7 ± 11.9 nm	-73.8 mV
Bulk addition, mixing, 8 hr. sonication	100x dilution, dust cutoff 15	58.9 ± 17.9 nm	-72.5 mV
Slow addition, 1 hr. mixing	100x dilution, dust cutoff 15	61.9 ± 11.5 nm	-73.0 mV

Allowing for the standard error in the measurement, it was not possible to statistically distinguish the bulk addition and sonication methods from the slow addition and mixing method. The measured hydrodynamic radius for the bulk addition method was approximately 53.7 and 58.9

nm for the 8 hr. and 20 hr. sonication protocols, respectively. The slow addition and hour mixing process that was ultimately adopted resulted in a measured hydrodynamic radius of 61.9 nm, so it was confirmable the abbreviated mixing processes was sufficient to near-fully exfoliate the platelets. Zeta potential measurements were conducted on the different clay platelet dispersions and the measurements were fairly uniform at -73.1 mV ± 0.76 mV given a density estimate for the clay platelets of 2.53 g/cm^3, the standard refractive index for water (the solvent), and the hydrodynamic radius calculated above, however the values were not sensitive to approximately 50% shifts in the hydrodynamic radius of the platelets.

Individual platelets were imaged via TEM to use a confirming second measurement for the DLS measurements (Figure 3-2). Measurement via the software package indicated the clay platelets had a characteristic length scale on the order of 100 nm, however these platelets were taken from 10x diluted dispersions placed on TEM grids so platelet aggregations were still observed (Figure 3-2a). Individual platelets were also distinguishable and appeared to have a characteristic length scale on the order of 80 nm or less, but were not aligned with the plane of the TEM grid to allow for accurate measurement of the platelets (Figure 3-2b). These correspond to the observed particle size from light scattering studies in literature[352]. Attempts to image individual platelets via AFM were unsuccessful as only aggregates could be found on the glass slides used for sample preparation, yielding similar or larger figures than the TEM.
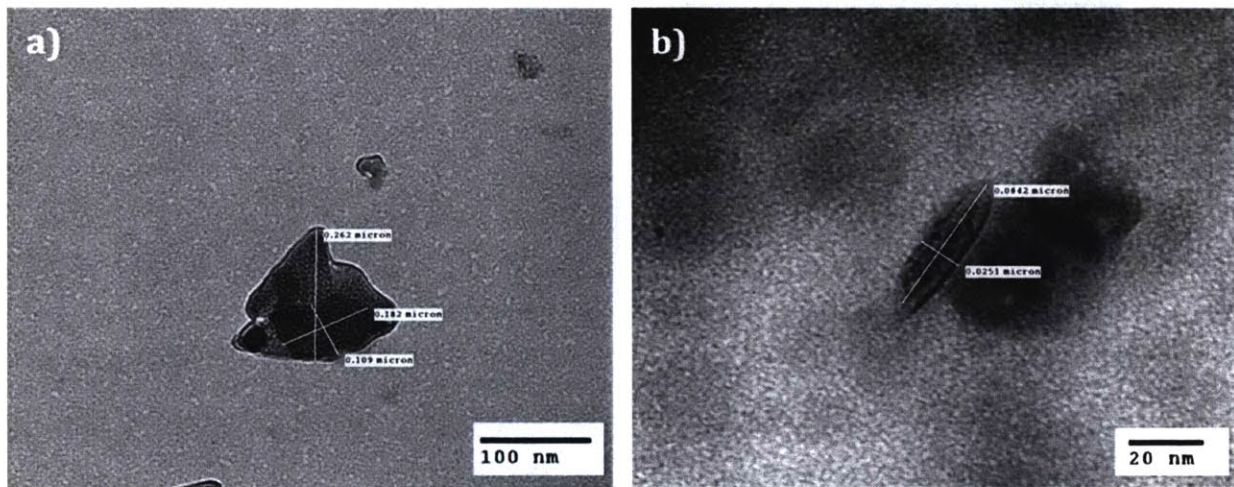
Figure 3-2: TEM micrographs of exfoliated LAP clay platelets: a) platelet aggregation observed at 21,000x magnification; b) individual clay platelet at 85,000x magnification.

3.2.2 – Notes on Optimizing Spray-LbL for Clay Deposition

Spray settings and programs for the spray-LbL equipment were originally provided by Kevin Krogman[361] and adjusted for the deposition of clay composite films. Calibration was done entirely on a mass basis, with the target flow rate through each nozzle being 4.0 ± 0.1 mg per 20 seconds (0.2 mg/s) with 20 psi N$_2$ forcing gas, yielding droplet sizes on the order of 30 μm. The substrate was mounted vertically approximately 8 inches (20.3 cm) away from the nozzles, which

yields a spray cone that generates fairly uniform films approximately 3.5 to 4.0 cm in diameter with the ISN sprayer equipment. The higher spray pressures form tighter spray cones and build films more towards the 3.5 cm diameter part of that range, while lower spray pressures such as 20 psi generate films more towards the 4.0 cm diameter part of the range. This met the minimum membrane size specifications for the Sterlitech HP4750 dead-end permeation cell (Appendix 2) used to generate the salt rejection and water permeability data in this report.

Films deposited on substrates mounted vertically in the original spray booth were not uniform in thickness. A maximum thickness was observed in the center of the film with the thickness tapering off as function of the radius and the gravity vector. At the top edge, the film thickness was thinner than at the bottom edge, which was found to be the result of increased exposure of the bottom edge of the film to the sprayed solution during the drainage and rinsing steps[362]. To counteract this, a motorized substrate holder was designed in conjunction with the MIT Central Machine Shop to rotate the samples at a rate of 10 rpm, which improved film uniformity by averaging out the gravity gradient over the deposition of the film (illustrated in Figure 3-3).
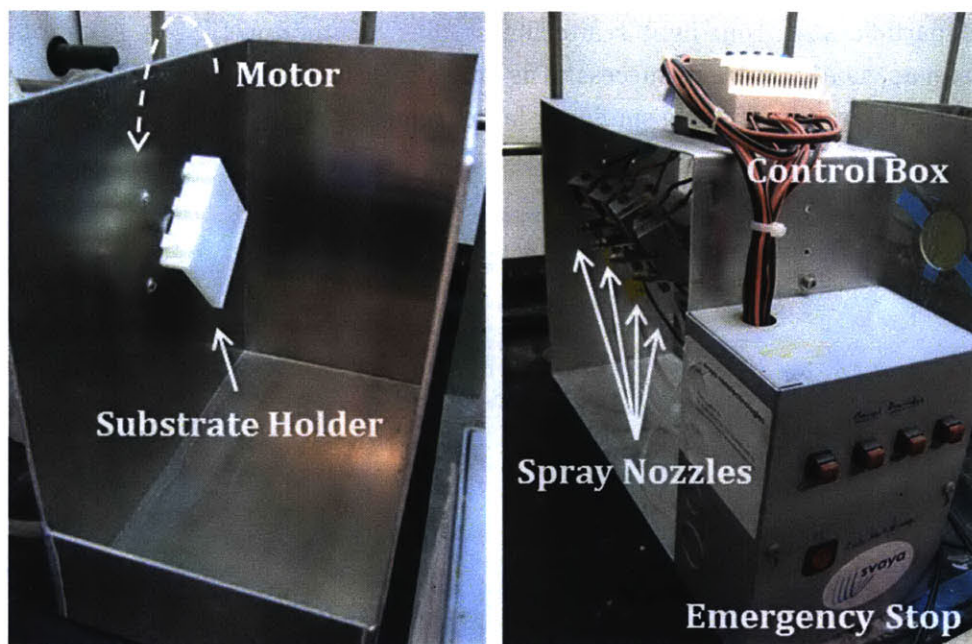
Figure 3-3: Labeled illustration of customized spray booth with motorized substrate holder developed for this project (left) and Krogman's sprayer control system (right)[361] for spray-LbL deposition of uniform clay composite thin films.

Early experiments were conducted with a sprayer calibration at 9.0 ± 0.2 mg per 30 seconds (0.3 mg/s) with 25 psi N_2 forcing gas. However, increasing the pressure of the forcing gas tightens the spray cone, and the substrate holder already reduces the distance between the nozzle tip and the substrate by approximately 1 inch (2.5 cm). Overall, this reduces the effective uniform film diameter of the sprayed films to less than 3.5 cm, which were too small to be characterized with the dead-end permeation cell.

3.2.3 – Preparation Protocols for Substrates for Spray-LbL Deposition

Plasma cleaning protocols for developed for PES UF membranes and PSU/nylon-6 espun mats in Chapter II. However, for some analytical techniques it was necessary to deposit films on different substrates. For profilometry, AFM, and ATR-FTIR, film samples were deposited on glass slides and silicon wafers plasma-cleaned for 5 minutes at 18 W (high).

After early experimentation, films were discovered to be building unevenly with substrates that were plasma cleaned and stored dry until LbL deposition. This was attributable to two factors: 1) airborne dust adhering to the substrates after being removed from the plasma cleaner, and 2) a pattern of extended island growth during early layer depositions instead of a transition to uniform layer depositions. To address this, substrates were stored in a 10 mM polycation solution (i.e. PDAC) after plasma cleaning for at least 20 minutes before LbL deposition, in a similar fashion to what has been reported for the hydrophilic modification of PES UF membranes in literature[363]. This allows the deposition of a uniform base layer of polyelectrolyte across the surface and prevents the adsorption of dust or other contaminants leading to non-uniform film buildup.

3.2.4 – Growth Curves of Clay Composite Bilayer Films

PDAC (Figure 3-4) has a quaternary amine functional group that retains a positive charge irrelevant of solution pH. This enables the deposition of PDAC-containing clay composite films at relatively high assembly pHs and the film will not dissociate or rearrange when the pH is shifted to the 7.5-8.4 range, common for seawater and RO processes.
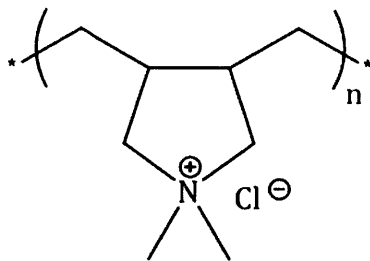
Figure 3-4: Repeat monomer structure of PDAC polymer.

Manipulating the spray times for each film component in the (PDAC/LAP) bilayer system yielded films of significantly different thicknesses and composition. Films with spray times that differed from the default 3 second spray times were given the descriptor $ns:ms$, where n refers to the spray time of PDAC and m refers to the spray time of LAP in seconds. The dry thicknesses of (PDAC/LAP) films with selected spray times were measured via profilometry (Figure 3-5). The films all appeared to grow linearly with respect to the number of bilayers despite varying the spray times, with $R^2 \geq 0.98$ for all calculated regression lines (Table 3-2). This is not surprising given a number of factors: 1) the (PDAC/LAP) bilayer contains a strong polyelectrolyte and highly charged platelet and thus less prone to interdiffusion[364], 2) the time scale for interdiffusion is greater than the time scale for the assembly steps in spray-LbL[361, 365], and 3) even partial coverage of LAP clay platelets serve as an effective barrier to the diffusion of large polyelectrolytes in the film.

Table 3-2: (PDAC/LAP) film thickness per bilayer and regression data for a selection of spray times.

Spray Times	Thickness	Lin. R^2	# of Base Layers
3s:3s	3.06 nm/bl	0.9948	5.57
6s:6s	3.66 nm/bl	0.9913	6.76
9s:9s	4.75 nm/bl	0.9859	7.33
3s:9s	6.47 nm/bl	0.9844	8.44
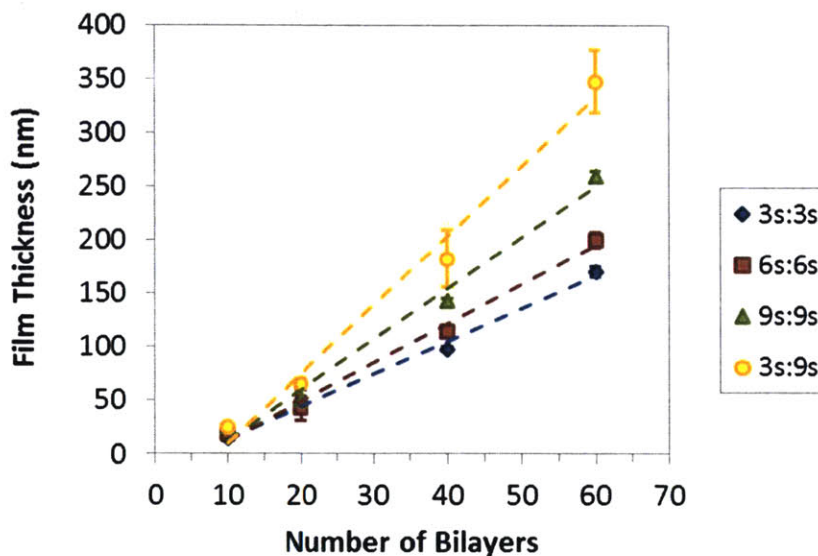
Figure 3-5: Growth curves for (PDAC/LAP)$_n$ films at assorted spray times: 3s:3s (blue), 6s:6s (red), 9s:9s (green), and 3s:9s (yellow).

Generally, an increase in the spray times for each component yielded an increase in the overall film thickness per bilayer, which ranged from 3.06 nm/bl for the 3s:3s film to 6.47 nm/bl for the 3s:9s film, approximately 109% thicker (Table 3-2). The thickness increased approximately 55% for the series of films consisting of 3s:3s to 6s:6s to 9s:9s, demonstrating the spray-LbL deposition is taking place in the kinetically-limited regime. One of the important takeaways from being in the kinetically-limited regime is that films will exhibit an island growth pattern where the first layers will not uniformly deposit across the substrate but will grow from nucleation points across the substrate. These islands increase coverage gradually until the substrate is fully coated and uniform layers begin depositing with a calculable average thickness per bilayer. Based on the intercepts calculated in the linear regression, it is estimated that between 5 and 9 bilayer depositions were required to reach the point of full coverage of the substrate. The high clay content films (9s:9s, 3s:9s) were towards the 9 bilayer edge of this range while the lower clay content films were towards the 5 bilayer end of the range (3s:3s, 6s:6s). This is likely a function of the clay platelets having fewer degrees of freedom than flexible polymer chains, which are better able to conform to the substrate and spread out to form a low surface roughness and uniform layer.

It is notable the 3s:9s film is consistently thicker than the 9s:9s film (4.75 nm/bl). The surfaces of the 3s:9s films were significantly rougher than the 9s:9s films; this implies the deposition of less polycation increased the average adsorption of clay for each deposited layer. It was hypothesized that some kinetic trapping of clay platelets occurred at the film interface that would increase the overall clay content of the film, the film thickness, and the surface roughness. The additional quantity of PDAC sprayed in the 9s:9s films smoothed the surface and eliminated locations where clay platelets could be physically trapped.

For some applications, salts can be added to the polyelectrolyte solution to increase the overall ionic strength and thicken the layers deposited[366-368]; the mechanism through which this occurs is that salt ions shield the charged functional groups along the polyelectrolyte backbone, causing the polyelectrolytes to deposit in more tightly coiled or loopy structures over a smaller surface area at the film interface. This approach was considered and rejected for this application because loopier, less-dense polymer layers would form a less effective diffusive barrier, and salts cause LAP clay platelets to accelerate the formation aggregate complexes in dispersion[353, 354] which inhibits LbL deposition, and saturating the film with salt would complicate sample preparation for salt rejection studies and seemed counter-intuitive. Instead, film composition and structure was controlled via the spray times of the film components and assembly pH during the kinetically-limited phase of spray-LbL deposition.

3.2.5 – Composition Analysis of Clay Composite Bilayer Films

The clay content of the films was measured through thermo-gravimetric analysis (TGA). The PDAC undergoes thermal decomposition at temperatures significantly greater than the glass transition temperature, specifically around 320°C and 450°C corresponding to the two-step decomposition of the polyelectrolyte[369], likely corresponding to breaking of the quaternary amine ring and the oxidation of the hydrocarbon backbone. Since silicate clays do not undergo decomposition at temperatures less than 900°C, the TGA can be used to burn off the polymer fraction of the film and a mass balance used to determine the weight fraction of clay in clay composite films.

Samples for TGA were prepared on polystyrene chips prepared with 10 seconds of plasma cleaning at the low setting because limited functionalization was required for LbL film deposition, but the relative hydrophobicity of the substrate compared to the Chapter II protocols made the films easier to lift off for analysis. Films were assembled with 150-200 bilayers to maximize the quantity of film deposited—a minimum of 0.3 mg of film needed to be harvested to obtain reliable TGA measurements for use in the composition analysis. When the films could not be detached easily from the substrate, they were dissolved with ethanol and deposited on the TGA pan. The program used consisted of the following steps: isothermal hold at 85°C for 10 minutes to evaporate excess ethanol, heat at 10°C/min to 800°C, and hold isotherm for 5 minutes. The ratio of masses taken at the end of the process and after the ethanol evaporation step was used to determine the weight fraction of clay present in the films for varying spray times, tabulated in Table 3-3.

Table 3-3: Clay content of (PDAC/LAP) films as a function of the spray time of individual film components.

Spray Times	LAP 1s	LAP 3s	LAP 6s	LAP 9s
PDAC 1s	56.7 ± 14.8	62.0 ± 1.7	68.2 ± 5.1	73.3 ± 4.7
PDAC 3s	38.0 ± 22.6	52.5 ± 6.9	56.3 ± 6.6	82.6 ± 2.2
PDAC 6s	51.3 ± 20.7	70.2 ± 7.9	77.7 ± 4.5	86.2 ± 4.8
PDAC 9s		75.7 ± 6.1	70.7 ± 10.7	72.4 ± 1.0

The films assembled with 1 second LAP spray time were extremely irregular and could not be reliably characterized. This can be traced to the geometry of the clay platelets; since the clay lacks flexibility and the degrees of freedom to rearrange and adsorb at the film interface that a polyelectrolyte has, a longer spray and drain time is required to allow the clay platelets to adsorb. A general trend was observed that for increasing the spray time of LAP from 3 seconds to 9 seconds, a greater weight fraction of clay was incorporated into the film. When pushed to the more extreme figure of 3s:30s, the films were not substantially different in clay composition from the 9 second LAP spray. Thus, the range of compositions that can be reliably assembled via spray-LbL for the (PDAC/LAP) composite bilayer system is between 53% and 86%.

Interestingly, the same trend was generally observed for an increase in the PDAC spray time, particularly for the LAP 3 second and 6 second columns for spray times of greater than 3 seconds. This observation implies that both the quantity of material sprayed as well as the driving force for adsorption that affects the incorporation of that material into the film. Thus, an increased quantity of PDAC deposited on the surface will increase LAP adsorption in the subsequent layer deposition. Ultimately, these observations suggest kinetic control of LbL film content, which contrasts to the equilibrium-controlled mass content usually observed with dip-LbL systems.

Experimentally, a secondary technique was investigated to confirm these observations by spraying the films into a customized quartz crystal microbalance (QCM-D) setup in conjunction with Kittipong Saetia[370]. The QCM monitors the rate of deposition of material on a quartz crystal via the Sauerbrey equation which correlates the change in oscillatory frequency to the change in mass. However, there was difficulty in assembling a combined spray-LbL/QCM-D device. The secondary containment required by the CMSE lab for the spray-LbL equipment contained a small atmospheric volume that became saturated with polyelectrolyte-clay complexes as the spray deposition progressed, leading to uneven film growth and nozzle clogging. Attempts to remove the excess material via attaching a vacuum to the assembly resulted in significant air cross-currents that inhibited the deposition of the LbL films. Thus, no data could be collected via spray-LbL/QCM-D that accurately reflected the spray conditions of spray-LbL alone.

3.2.6 – Adjusting Spray Drain Times for Clay Composite Film Assembly

The default spray program was originally optimized for the spraying of polyelectrolytes and TiO$_2$ nanoparticles[361], and experiments were designed to test whether or not the drainage times between film component and rinse sprays were sufficient to build smooth films. Composite bilayer

(PDAC/LAP) 3s:3s films with drainage times from the set of 5, 8, and 20 seconds were assembled and characterized via AFM to determine surface roughness (R_q) (Figure 3-6). Additionally, films were assembled without a rinsing step and a 5 second drainage step.
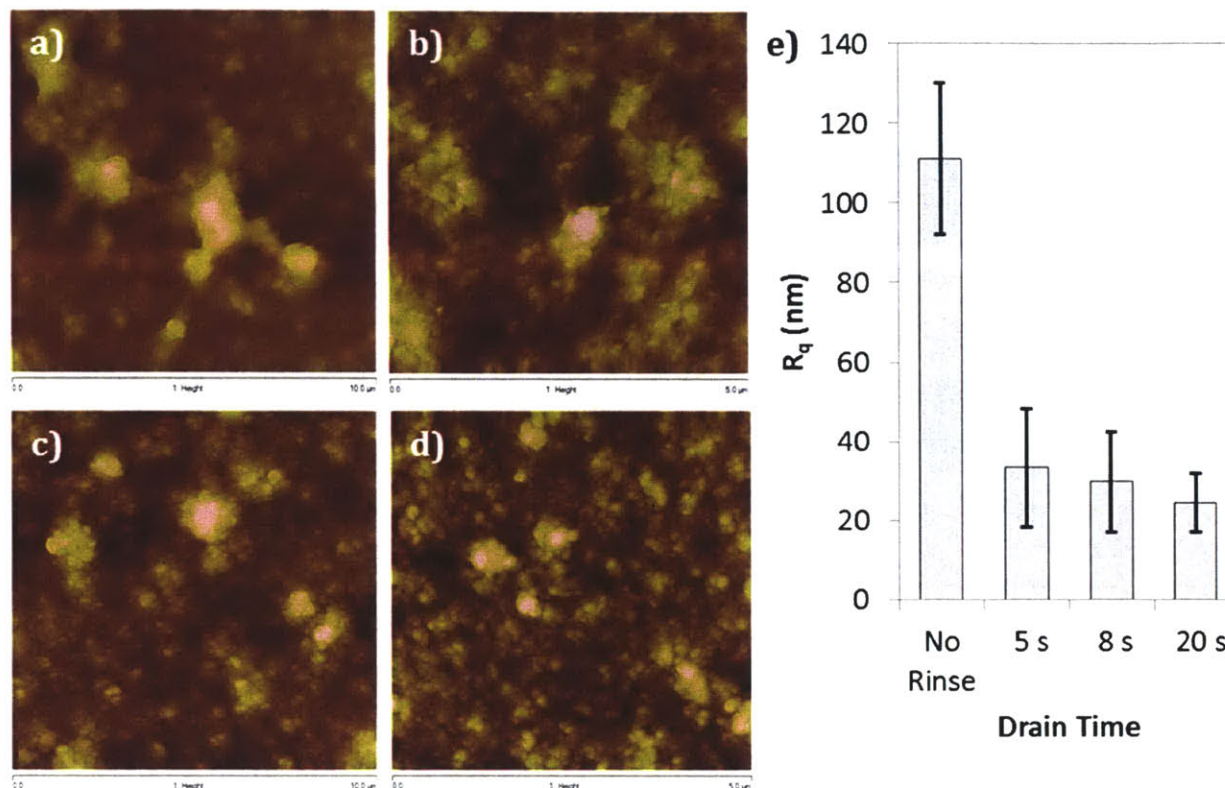
Figure 3-6: AFM micrographs of (PDAC/LAP)$_{20}$ 3s:3s films assembled with a) no rinsing step and 5s drainage time, b) 5s drainage time, c) 8s drainage time, and d) 20s drainage time; e) graph of average R_q for (PDAC/LAP)$_{20}$ films vs. drainage time.

Films assembled without a rinsing step (Figure 3-6a) were significantly rougher than all films assembled with the rinsing step (Figure 3-6b, 3-6c, 3-6d). This is because the rinsing step removes unabsorbed material from the film interface between layer depositions, and without it large aggregates formed on the surface of the film which trapped material sprayed by subsequent deposition steps. Numerically, this behavior was quantified with the Nanoscope Analysis software package to find the average surface roughness, R_q, for 10x10 μm^2 samples with similar numbers of bilayers deposited. For (PDAC/LAP)$_{20}$ 3s:3s films, eliminating the rinse step increased the surface roughness to an average value of 111 nm, as opposed to the 33.3 nm observed when the rinse step was included (Figure 3-6e). No significant reduction in surface roughness was observed for increasing the drainage time; as the drainage time was increased from 5 seconds to 8 seconds to 20 seconds, the average surface roughness decreased from 33.3 nm to 29.8 nm to 24.4 nm respectively. However, this observed decrease was not statistically significant (standard deviations were on the order of 10 nm for each series), so 5 second drainage times were retained in the standard film assembly protocol.

3.2.7 – Pre-Permeation Film Imaging

Fully assembled membranes with clay composite selective layers on PES UF membranes with 30 nm pores were imaged via SEM (Figure 3-7).
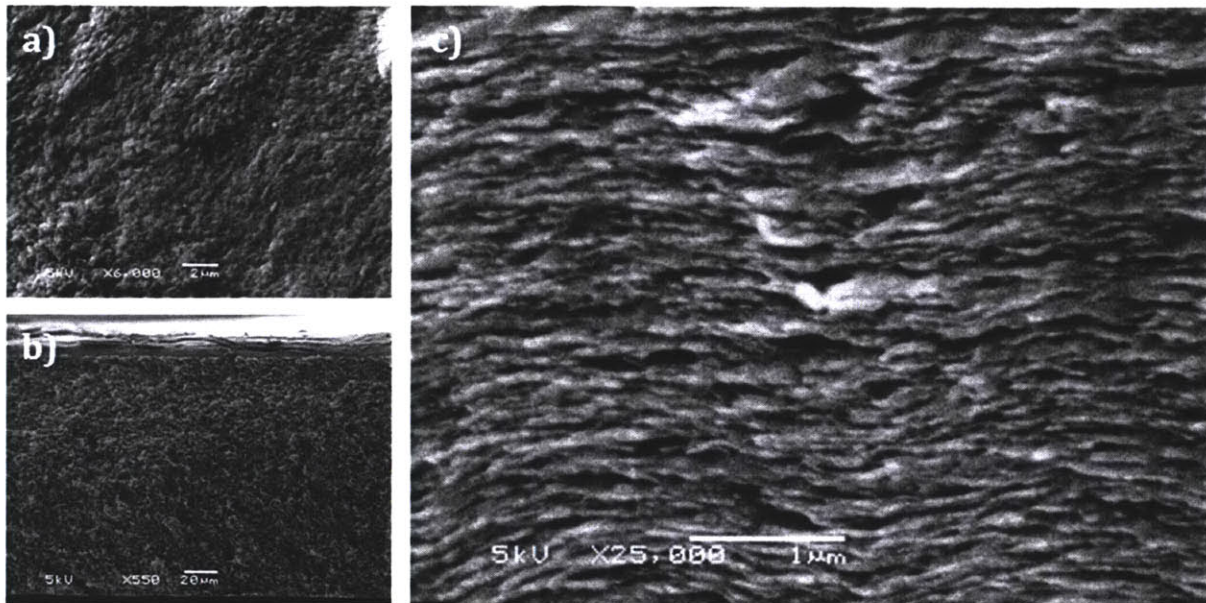
Figure 3-7: SEM micrographs of LbL films: a) surface of (PDAC/LAP)$_{60}$ 3s:3s film on PES UF membrane; b) surface of (PDAC/LAP)$_{50}$ 3s:3s film on PES UF membrane; and c) cross-section of (PDAC/LAP)$_{100}$ 9s:9s film on espun nylon-6.

By visual inspection, films containing greater than 50 bilayers formed uniform selective layers over the porous substrate as discussed in Chapter II (Figure 3-7a). The film appears to deposit solely on the surface with a thickness that corresponds closely to the expected values measured by profilometry (Figure 3-7b). The fracture patterns observed in high-magnification cross-sectional SEM micrographs is indicative of the clay layering with respect to the membrane surface (Figure 3-7c). Combined with the growth curves indicating a maximum film growth rate of approximately 5 nm/bl, it is believed the clay platelets are not orienting in random directions and only aggregating on the surface with spray times in excess of 9s for LAP. Higher resolution TEM imaging of clay composite layers, which confirms the clay layering pattern in spray-LbL assembled thin films discussed here, is presented in Chapter IV for the tetralayer film architecture.

The degree of surface roughness for films of varying spray times was characterized via the AFM as in the previous section. It was hypothesized that an increased clay spray time, which generally correlates with an increased degree of clay incorporation into the film, would also correlate with an increase in surface roughness. This was tested on the thick films assembled for the composition analysis presented above (Figure 3-8).
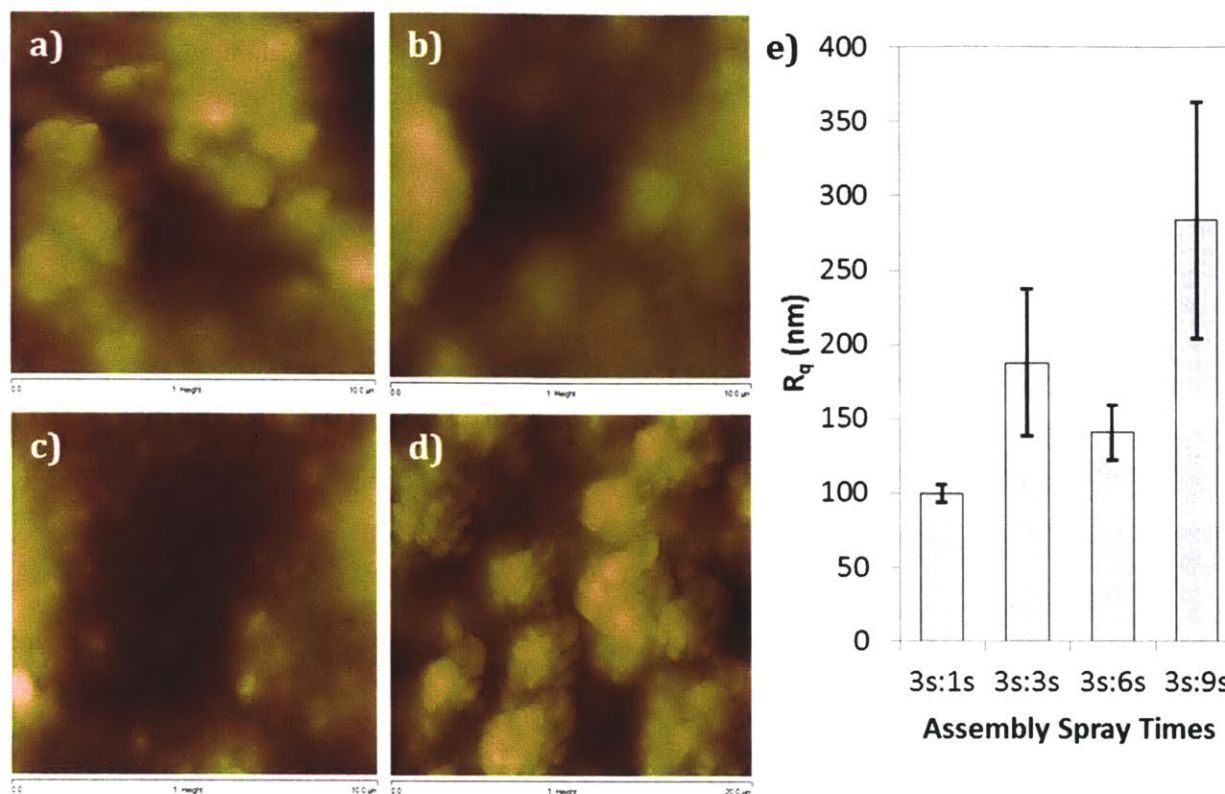
Figure 3-8: AFM micrographs of (PDAC/LAP)$_{150}$ films assembled with a) 3s:1s spray times, b) 3s:3s spray times, c) 3s:6s spray times, and d) 3s:9s spray times; e) graph of average R_q for (PDAC/LAP)$_{150}$ films vs. assembly spray times.

The 3s:9s films exhibited the greatest degree of surface roughness, with an average R_q of 284 nm. The 3s:1s films exhibited the lowest average surface roughness of 99.8 nm, likely due to the low quantity of clay incorporated into the film. However, there was not a readily apparent trend for films assembled from 3s:1s to 3s:9s, as the 3s:3s films appeared to be rougher than both the 3s:1s films and 3s:6s films. There is a loose correlation between the clay content of the film (Table 3-3) and the overall surface roughness (Figure 3-8), with $R^2 = 0.8954$, however this figure is unreliable due to high variability in the composition of the 3s:1s film.

3.2.8 – Permeation Studies on Clay Composite Films

Ultimately, three candidate films were selected for in-depth water permeation and salt rejection studies on the basis of covering the range in film composition observed in the prior sections. The 3s:3s film, with a clay composition of 53%, 3s:6s film with 56%, and 3s:9s film with 86%. The Koch TFC-HR RO membrane with a polyamide selective layer was used as a control and a point of comparison for the performance of the clay composite films. Uncoated PES-30 and PES-100 nm UF membranes were used as negative controls as well.

Water flux and salt rejection data on the thin films were collected from dead-end permeation cell measurements over a pressure range of 50 psig to 250 psig with deionized water

and 1.0 wt. % (10,000 ppm) NaCl solution (Figure 3-9) (Appendix 2). A localized water permeability coefficient was calculated through a regression of the Spiegler-Kedem model to yield a single value to compare films where several different transport mechanisms are at work (regression method in Appendix 1).
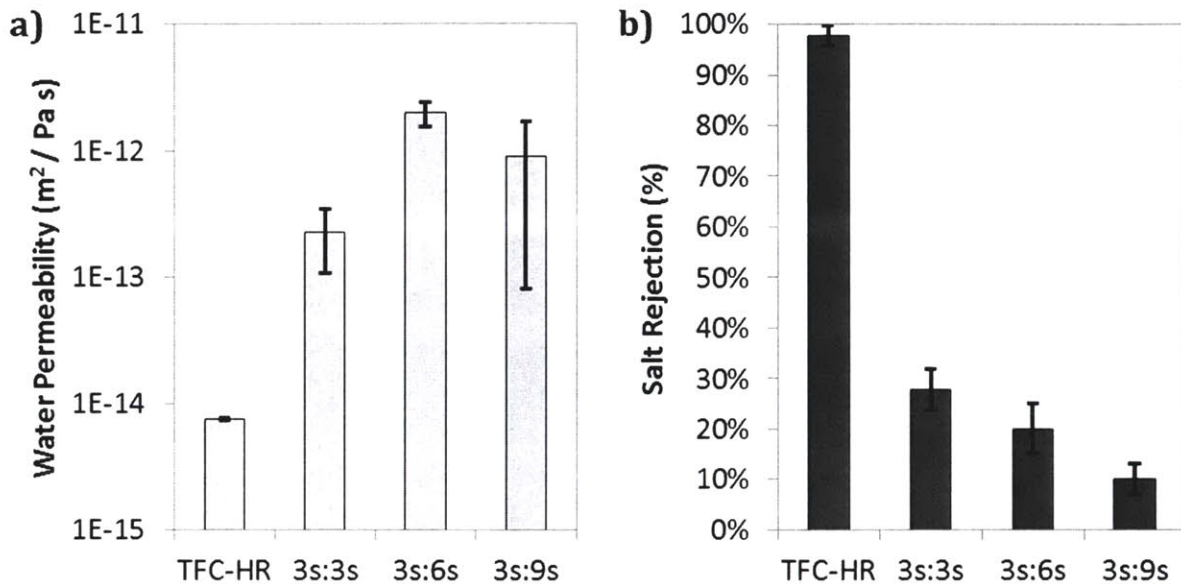
Figure 3-9: Dead-end permeation cell data for clay composite bilayer films: a) calculated water permeability via the Spiegler-Kedem model; and b) observed salt rejection.

The water permeability of the commercial TFC-HR polyamide active layer under these operating conditions is $7.6 \cdot 10^{-15}$ m^2 / Pa s with 98% salt rejection. All the examined LbL films exhibited significantly greater water permeability, on the order of one to two orders of magnitude. The PES-30 and PES-100 nm UF membranes had water permeability values of $2 \cdot 10^{-9}$ m^2 / Pa s and $1 \cdot 10^{-9}$ m^2 / Pa s respectively, several orders of magnitude greater than any of the selective layers examined. This was expected as hydrostatic pressure was sufficient to drive flow through the pores of the membrane. The observed flow rate was directly proportional to the applied pressure, consistent with pore-flow models such as Darcy's Law:

$$J_w = \frac{A}{\delta}\left(P_f - P_p\right)$$

...where J_w is the flux of water, A is the water phase transport parameter, δ is the pore length, P_f is the pressure on the feed side, and P_p is the pressure on the permeate side. The pressure drop quantity reflects the gauge pressure due to the particular apparatus used (Appendix 2). The ratio of A and δ was treated as a fitted parameter. In terms of salt rejection, the PES UF membranes were not salt selective; the measured salt concentration in the permeate and feed were within the margin of error of the conductivity meter, indicating the salt rejection was effectively 0%.

For the clay composite films, the observed salt rejection was low: 28% for the 3s:3s film and 10% for the 3s:9s film. The water permeability for the 3s:3s film was $2.27 \cdot 10^{-13}$ m^2 / Pa s and for

the 3s:9s film 8.96·10⁻¹³ m² / Pa s, roughly four times greater. It was hypothesized that the lower salt rejection and increased water flux correspond to the formation of critical defects in the clay composite selective layer that form under RO conditions in the desalination cell (see following section). It is also notable that the overall clay content of the film correlated inversely to its performance in the salt rejection trials. Extremely high clay content films (i.e. 3s:9s) assembled via the (PDAC/LAP) method performed similarly to films with moderate clay content (i.e. 3s:3s) with regards to water permeation, but exhibited a poor capacity for salt rejection: the 83% clay 3s:9s film rejected on average 10% of the 10k ppm NaCl feed solution, while the 53% clay 3s:3s film rejected on average 28% of the same solution. This indicates the number of defects formed seems proportional, at least, to the clay content in the composite film.

Films containing both 40 bilayers and 60 bilayers were examined for all three systems presented in Figure 3-9, but the measured permeability was indistinguishable. This was expected, as permeability coefficients normalize for the thickness of the membrane, and the calculated permeability coefficient likely reflects not only diffusion through the selective layer but also hydraulic flow through any cracks formed in the film. Thus, it is concluded that for films of at least 40 bilayers of thickness, corresponding to approximately 100 nm thick or greater, the rate of defect formation is not a strong function of the film thickness for the range of thicknesses tested.

The salt rejection for films containing 40 bilayers compared against films with 60 bilayers also fell within the same margins of error. This is interesting because salt rejection is not an intrinsic property of the film but a measured variable like flux that should be a function of the experimental variables such as film thickness. It was hypothesized that no statistical significance could be observed between these samples because of the leaking of concentrated salt solution through the cracks in the films.

3.2.9 – Post-Permeation Film Imaging

Permeate flux was observed at 50 psi and 100 psi, a figure below the expected osmotic pressure of the feed solution of 124 psi for a 10,000 ppm NaCl solution. This greater-than-expected flux, combined with the low salt selectivity, led to the hypothesis these membranes formed cirtical defects during the RO trials that led to the results presented in section 3.2.8. To examine this, sample membranes were examined before and after water and salt permeation trials with the SEM (Figure 3-10).

Observed was clear evidence of surface fractures on the films; membranes examined after permeation trials, under both water (Figure 3-10b) and saline (Figure 3-10d) conditions, were found to contain significant fractures on the order of millimeters long and on the order of 0.1 to 1 μm wide. These fractures are not observed as the result of sample preparation for the SEM, as they were not observed in pre-permeation membranes (Figure 3-10a, 3-10c). Qualitatively, no significant difference was observed between the surfaces of 3s:3s and 3s:9s films post-permeation, but the factor of approximately 3 difference in the salt rejection would imply a greater degree of

fractures in the higher clay content 3s:9s film. It is possible these films were more brittle than the 3s:3s films, accounting for the quantity of fractures and thus the difference in performance between these two films.
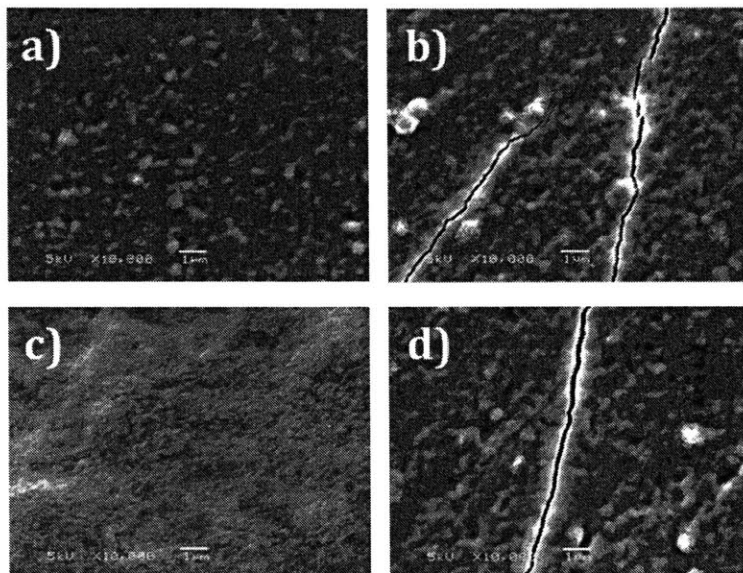
Figure 3-10: SEM micrographs of (PDAC/LAP) films before and after permeation trials: a) surface of (PDAC/LAP)$_{40}$ 3s:3s film, before permeation; b) surface of (PDAC/LAP)$_{40}$ 3s:3s film, after water permeation; c) surface of (PDAC/LAP)$_{60}$ 3s:9s film, before permeation; and d) surface of (PDAC/LAP)$_{60}$ 3s:9s film, after water and salt permeation.

Additionally, following the salt permeation trials, small, bright structures were observed on the surface of the membranes (Figure 3-11).
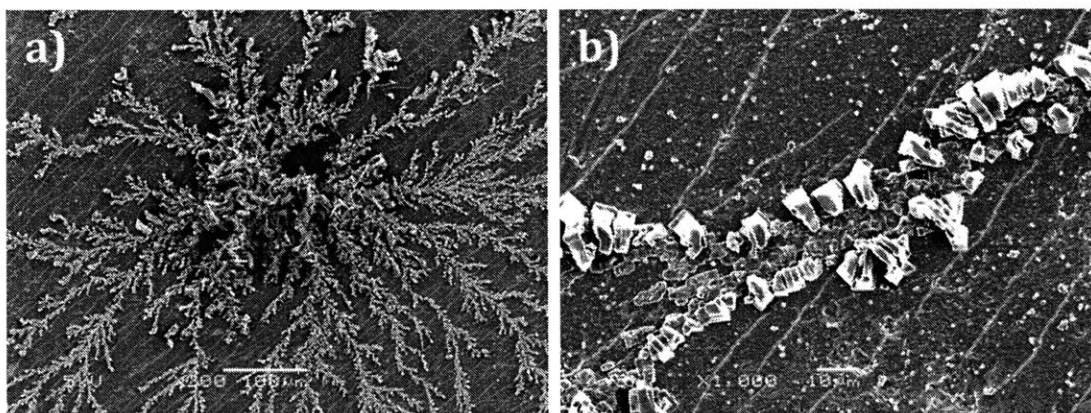
Figure 3-11: NaCl crystals observed on surface of membranes following salt permeation trials: a) nucleus of several NaCl crystals; and b) branch of the network of salt crystals.

These millimeter-sized structure structures are dried NaCl salt crystals that deposited on the surface of un-rinsed membranes after salt permeation trials. These crystals appeared independently of the cracks observed in (PDAC/LAP) films (compare Figure 3-10 and 3-11), and

were eliminated by a three-step rinsing procedure following the permeation trials and before SEM sample preparation.

3.2.10 – LbL-Augmented TFC RO Membranes

The deposition of spray LbL-assembled thin films on existing commercial RO membranes as an additional selective layer was briefly considered. Both Koch TFC-HR RO membranes and GE Osmonics RO membranes were used as substrates for (PDAC/SPS) and (PDAC/SPPO) films. Beyond confirming that deposition was possible due to the hydrophilicity of the polyamide surface layer of TFC RO membranes, no design purpose was served via these structures because the flux properties could not be improved upon (the deposition would add an additional barrier in a series resistance model) and LbL-assembled films were still subject to the same fouling that affects commercial polyamide surface layers. With no practical benefit realizable, this approach was abandoned in favor of the clay composite selective layers on UF membranes presented in this chapter and the next.

The growth curve for the investigated (PDAC/SPS) film appeared to fit a mostly linear growth pattern (Figure 3-11). The overall films were significantly smoother than the clay composite (PDAC/LAP) films presented above, with R_q ranging from 2.7 nm for 10 bilayer films up to 4.2 nm for 40 bilayer films. The low degree of surface roughness is expected from polyelectrolyte films as compared to clay composite films as neither film component has the fixed aspect ratio and fixed geometry of the LAP clay platelets. The measured R_q is on par with what would be observed for dipped LbL films.
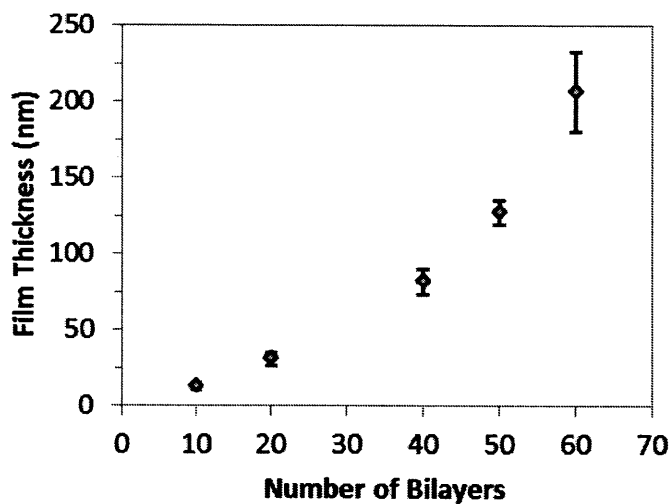
Figure 3-12: Growth curve for (PDAC/SPS)$_n$, 0.5 M NaCl film.

3.3 – Conclusion

There are two major conclusions that can be drawn from the composite (PDAC/LAP) bilayer study, one regarding the nature of the films assembled and the second regarding the practical application of the films.

First, the flexibility of the spray-LbL technique enables the deposition of films with significantly greater clay content (and more generally, inorganic nanomaterial content) than is possible via other assembly methods. Although literature reports clay compositions for LbL-assembled thin films upwards of 50%, the right combination of spray times enabled the deposition of films that were 86% by weight clay. Instead of considering these films as organic, polymeric selective layers with incorporated nanomaterials, it may be more accurate to describe the high-clay content films as largely ceramic, inorganic selective layers with a polyelectrolyte binding agent.

Second, the high-clay content films were the worst-performing selective layers, prone to the formation of massive critical defects despite the work done in chapter II to select an appropriate support layer for the clay composite films. Qualitatively, this indicates the clay-containing films are brittle and not mechanically strong enough to serve as selective layers under RO conditions, even for brackish water sources where 200-250 psi would be a feasible operating pressure. The lesson here is the ionic bonding between the LAP platelets and PDAC is insufficient to hold the film together under RO conditions, and an additional focus must be placed on the polyelectrolyte component of the film to prevent the defect formation. It demonstrates the importance of introducing a cross-linked polymeric matrix that can reduce the brittleness of the film and prevent the formation of cracking and critical faults under RO conditions.

However, in the greater context of this thesis work, it has been demonstrated that ordered clay composites can be assembled via rapid spray-LbL deposition on porous substrates, which can serve as selective membranes. Further exploration and optimization on this building block is presented in the following chapters.

3.4 – Materials and Methods

3.4.1 – Materials

LAP clay was provided by Southern Clay Products, Inc.; clay dispersions were prepared at a concentration of 1.0 wt.% clay and the balance reagent-grade water. PDAC (MW: 200-350 kDa; 100-200 kDa) and SPS (MW: 70 kDa) were obtained from Sigma-Aldrich. The polyelectrolyte solution was prepared at 10 mM concentration and was adjusted to the assembly pH of 10 by using a Φ340 pH/Temp Meter and concentrated NaOH solution.

PES UF membranes with 30 nm pores were purchased from Sterlitech (PES00347100) and used as a substrate for deposition. The membranes were plasma-cleaned in a Harrick Plasma Cleaner/Sterilizer PDC-32G at 18 W for 30 seconds and soaked in PDAC solutions before spray-LbL film assembly.

NaCl was obtained from Mallinckrodt (CAS #7647-14-5) for the preparation of 1.0 wt.% (10,000 ppm) NaCl solutions to use as the feed solution for the dead-end desalination cell.

3.4.2 – Spray Layer-by-Layer Deposition

Films were constructed using a custom-built spraying apparatus. Solutions and clay dispersions were aerosolized with N_2 gas at 20 or 25 psi and are sprayed onto the substrate rotated at 10 rpm. The basic program for each layer involved spraying the film component for a time period from the set of [1, 3, 6, 9 seconds], pausing for a 5 second drain period, rinsing for 10 seconds with pH-adjusted water, and then and then a final 5 second drain period. The sequence is repeated for each film component listed to assemble a bilayer. Films assembled at different component spray times are identified by the expression ns:ms, where n refers to the spray time of PDAC, and m refers to the spray time of LAP.

3.4.3 – Characterization

A Brookhaven ZetaPALS Zeta Potential Analyzer was used to determine the LAP dispersion particle size and charge density. A KLA-Tencor P-16 and a Dektak 150 profilometer was used to determine the film thickness. Profilometry samples were deposited on glass slides plasma-cleaned using the above equipment for 5 minutes; otherwise, the standard protocol above was used. Both a JEOL JSM-6060 and a JSM-6010LA Scanning Electron Microscopes (SEM) were used to image both film surfaces and cross-sections. Cross-sectional SEM samples were prepared via the cryo-fracture method by submerging the sample in liquid N_2 and then physically tearing the sample with forceps and mounted on Ted Pella, Inc. #16104 Low Profile SEM Mount Pins. AFM imaging was conducted with a Vecco Dimension 3100 AFM with Nanoscope Controller and 1929G scanner head, with the typical scan size at 10x10 μm^2, scan rate of 0.4 Hz and 512 samples/line yielding a maximum tip velocity of 8 $\mu m/s$. The AFM tips used were Vecco Si tips on nitride levers with f_o = 50-90 kHz and k=0.4 N/m. A TA Instruments Discovery Series Thermogravimetric Analyzer was used to determine the film composition of LbL films with the following program: temperature equilibration at 85 °C for 5 minutes, followed by a ramp up to 800 °C at the rate of 10 °C/min, followed by a final temperature equilibration at 800 °C for 5 minutes. A Sterlitech HP4750 dead-end permeation cell was used to determine both water and salt permeability. The cell was operated between 50 and 250 psi for films assembled on UF membranes. A Spiegler-Kedem model was then applied to determine the local water permeability constants. The chloride ion concentration of the collected permeate was measured with an Oakton Ion 700 conductivity meter and Thermo-Scientific Orion 9617BNWP IonPlus Probe.

IV. Laponite Clay-Composite Tetralayer Film Architectures

4.1 – Introduction

4.1.1 – Summary

The second major group of spray-LbL assembled clay composite films were manufactured from cross-linkable PAH and PAA polyelectrolytes and LAP clay. Both PAH and PAA are weak polyelectrolytes and the degree of ionization depends on the assembly pH, enabling the control of film thickness and composition via manipulating this variable and holding the spray times for each component constant. These polyelectrolytes were selected for being inexpensive, off-the-shelf materials and the ability to form amide cross-links that mimic the functionality of commercial RO membranes, which was believed to be able to eliminate the defect formation observed for the clay composite films presented in Chapter III. The two key constituent bilayers were polymeric (PAH/PAA) bilayers and clay-containing (PAH/LAP) bilayers. From these building blocks, more complex film architectures were assembled, including tetralayer-laponite films (Tetra-LAP) with one polymeric and one clay bilayer (PAH/PAA/PAH/LAP), and hexalayer-laponite films (Hexa-LAP) containing two polymeric and one clay bilayer (PAH/PAA/PAH/PAA/PAH/LAP).
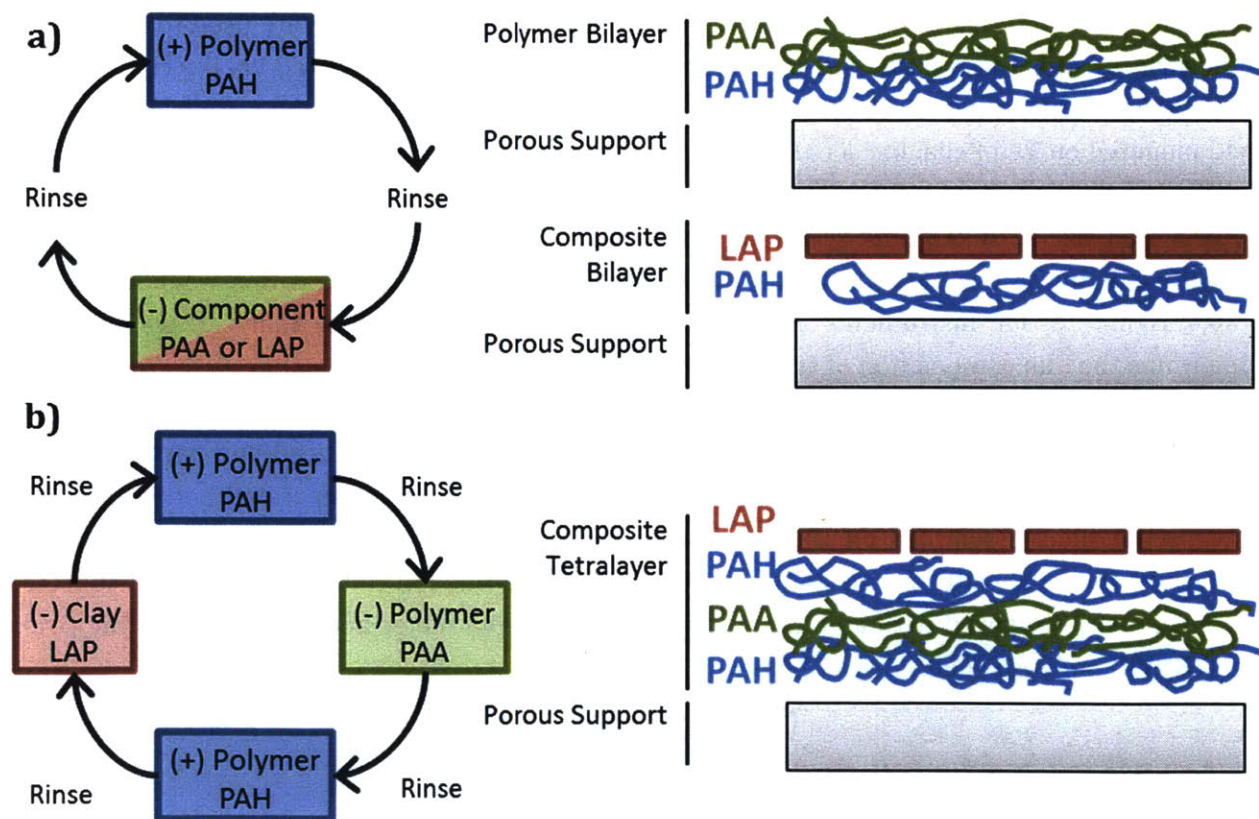
Figure 4-1: Schematic of spray-LbL deposition for a) the constituent polymer and composite bilayers of tetralayer and hexalayer clay composite films, and b) a schematic of the tetralayer clay composite film.

The key conclusion drawn from this work was that a strong, cross-linked polymer matrix with embedded clay platelets served as effective salt-selective layers. The permeation characteristics of these films were closely related to the clay content of the films and the degree of cross-linking.

4.1.2 – Why Cross-linkable Composites Were Investigated

A cross-linked tetralayer architecture was explored because it was believed to be able to eliminate the crack formation observed in the polymer bilayer films discussed in chapter III. The material selection for this process was driven by 1) cost concerns, as a large quantity of the film components in spray-LbL deposition are washed away from the film interface so relatively inexpensive off-the-shelf polyelectrolytes were preferred; and 2) ease of forming a covalently bound polymeric matrix. The polyelectrolytes PAH and PAA were selected for this task because they are available cheaply off-the-shelf, have a high degree of functional group uniformity, and the ease of forming amide bonds via thermal cross-linking. Briefly, linear and branched poly(ethylenimine) (LPEI, BPEI) were investigated as a complement to PAA, but were ultimately rejected due to the greater concentration of primary amines in PAH[371].

The (PAH/PAA) bilayer system, particularly assembled through dip-LbL, is well-characterized in prior literature[251, 254, 372-378], including work on swelling and nanoporous transitions accomplished by shifting the pH of the films post-assembly[379, 380]. PAH and PAA are weak polyelectrolytes, with the degree of ionization on the amine and carboxylic acid functional groups a function of the assembly and post-treatment pH. From this, a range of pH values (5.0 to 6.0) were selected that reflect both thick and thin film depositions to generate films of different properties. Films assembled at pH 7.0 and higher, closer to the native pH of the LAP dispersion, were considered but ultimately rejected as these conditions did not yield significant polyelectrolyte depositions per layer and thus did not build uniformly. These films will swell under aqueous and RO conditions (pH 7.0-8.4)[17], as is expected for most LbL polyelectrolyte film systems[253-255], so thermal cross-linking was introduced to form covalent bonds in the polymer matrix to restrict this behavior as highly swollen, hydrated sponge-like structures are not effective barrier layers[257]. The optimal cross-linking conditions for this material system have been explored in literature[374-377, 379], but some experimentation is required to tweak the process given the optimal temperature for this reaction, between 225°C and 250°C, is greater than the T_g of the PES support layer at 190°C. With the particular equipment restrictions in the ISN, cross-linking temperatures between 125°C and 175°C were investigated.

The cross-linking step is important to the integrity of the LbL films under RO conditions. Although naively one would expect additional covalent bonds to increase the brittleness of the films, the bonds formed between polyelectrolytes serve to form a mechanically harder mesh with the clay platelets embedded within. This serves to link together the film and maintain the spacing between the clay platelets under the shear forces the films are exposed to in cross-flow cells and the swelling that occurs as the result of salts and water hydrating the film. Control of this film

property was not possible with the material system investigated in chapter III, whereas with the chapter IV film architectures the hypothesis as to whether simultaneously toughening the polymer matrix and maintaining channel spacing will maintain an effective barrier layer can be tested. After demonstrating the thermal cross-linking reaction had occurred, it is important to demonstrate that the physical properties of the films had been impacted, which was accomplished by directly measuring the swelling of the film under aqueous conditions via change in film thickness, and the film hardness via nanoindentation.

As discussed in section 1.6.3, the incorporation of any impermeable particle such as a clay platelet in the selective layer increases the effective diffusive path length, or tortuosity, for any solute traversing the membrane. The incorporation of these clay platelets into films as explored previously was successful if the only measure of success was the formation of a clay composite film, but in this chapter the cross-linking architecture was used to fully embed these platelets within a polymeric matrix capable of withstanding the pressures applied under RO operation.

The cross-linked polymer bilayer (PAH/PAA) film was assembled at pH 5.0 to be used as a secondary control for the efficacy of incorporating clay into the selective layer. The same film architecture was utilized by fellow collaborators on the CCWCE funding[315] and assembled through spin-assisted LbL assembly. It serves as a moderately effective diffusive barrier layer as discussed in chapter I, but is not on par with the polyamide selective layers of TFC RO membranes. Additionally, the films were incredibly thick; the 120 bilayer depositions were at maximum on the order of a micron in thickness, which is far greater than is commonly observed for TFC RO selective layers, and the selectivity of the films were not good enough to warrant the material cost and lower overall flux due to the thickness. The work presented in this chapter and the next build upon the use of the (PAH/PAA) film for selective layers in RO membranes by incorporating ordered nanostructures into the film, with the intention of generating films of a similar thickness to TFC RO selective layers with better salt selectivity and water flux than has been observed for other LbL film architectures in literature. The LAP clay platelets, similar to the secondary hypothesis in chapter III with the clay composite (PDAC/LAP) bilayer, were hypothesized to introduce size exclusion transport mechanisms that would increase salt rejection over what is observed for the polyelectrolyte (PAH/PAA) bilayer system.

4.2 – Results and Discussion

4.2.1 – Tetralayer Growth Curves and Composition Analysis
The dry thicknesses of the tetra-LAP clay composite films with assembly pH values of 5.0, 5.5, and 6.0 as well as (PAH/PAA) pH 5.0 bilayer films were measured through profilometry (Figure 4-2). The thickness per repeat unit and clay content measured via TGA were also tabulated (Table 4-1) for comparison against the (PDAC/LAP) architecture that was developed in the prior chapter. These films were assembled using the optimized spray protocol from Chapter III, with 5 second drainage times and 3 second sprays for all film components.

Table 4-1: Clay content and film thickness per repeat unit for tetra-LAP film architectures compared to (PAH/PAA) bilayer and selected (PDAC/LAP) clay composite bilayer films.

Film Architecture	Clay Content (wt. %)	Thickness per Repeat Unit
(PAH/PAA), pH 5.0	0%	1.7 nm/bl
(Tetra-LAP), pH 5.0	37.8% ± 4.9%	5.1 nm/tl
(Tetra-LAP), pH 5.5	--	4.8 nm/tl
(Tetra-LAP), pH 6.0	56.3% ± 6.6%	2.6 nm/tl
(PDAC/LAP), 3s:3s	52.5% ± 6.9%	2.6 nm/bl
(PDAC/LAP), 3s:9s	82.6% ± 2.2%	5.2 nm/bl
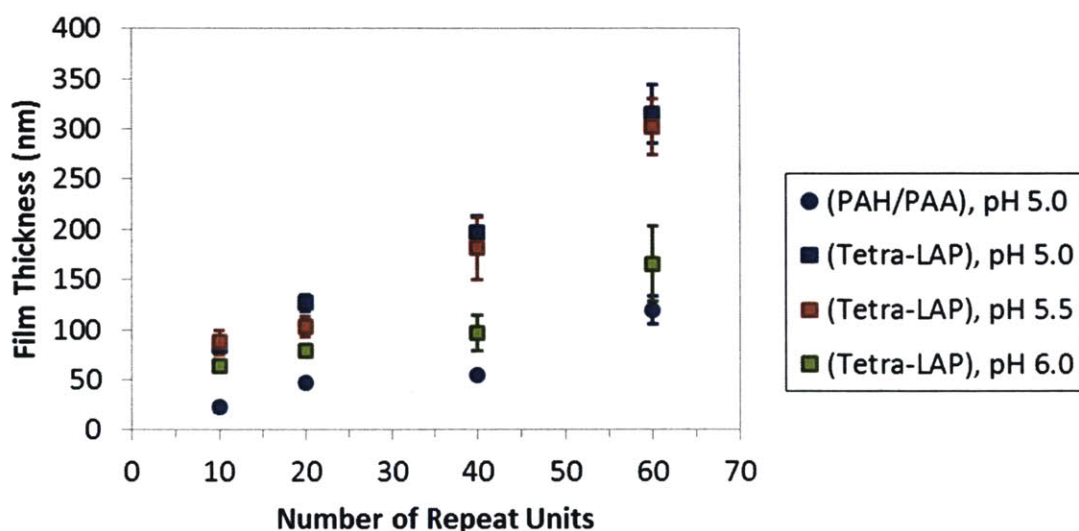
Figure 4-2: Growth curves for (PAH/PAA) bilayer and tetra-LAP clay composite films at varying assembly conditions: pH 5.0 (blue), pH 5.5 (red), and pH 6.0 (green).

At pH 6.0, the PAH and PAA are both highly ionized when deposited at the film interface based on their respective pKa values (PAA pK_a = 6.0-6.5; PAH pK_a = 8.0-9.0[373]), which results in very thin, dense polymer layers being deposited. At pH 5.0 assembly conditions, the PAA chains are less ionized, resulting in the deposition of thicker polyelectrolyte layers between the clay layers and decreasing the overall clay content of the film. In terms of thickness, the dry thickness for (Tetra-LAP) pH 6.0 films was 2.6 nm per tetralayer (Figure 4-2). The (Tetra-LAP) pH 5.0 and pH 5.5 films assembled were significantly thicker than the pH 6.0 films of the same architecture, with a thickness of approximately 5.1 nm and 4.8 nm per tetralayer deposited, respectively (Figure 4-2). This is a similar trend to what is observed in the literature for dipped (PAH/PAA) bilayer films over

the same pH range[251]. Rubner et al. note their dipped (PAH/PAA) bilayers are thickest when assembled at pH 5.0 because both polyelectrolytes are partially ionized, whereas the chains are more fully ionized as the pH approaches 6.0. Within the margin of error, the thickness of the tetralayer pH 5.0 film appears to be a linear sum of the LAP-containing bilayer and the (PAH/PAA) pH 5.0 bilayer, implying the intercalating clay layers do not have a significant impact on the dynamics on the polyelectrolyte deposition. This difference in film thickness is largely accounted for in the clay composition, as the overall clay content of the tetra-LAP films at pH 5.0 assembly conditions was approximately 38%, as contrasted with the pH 6.0 films, where the overall clay content was 56% (Table 4-1).

Comparing the (Tetra-LAP) and the (PDAC/LAP) film architectures, the observed dry thickness for the (Tetra-LAP) pH 6.0 films was similar to what was observed for the (PDAC/LAP) 3s:3s assembly conditions (Table 4-1). The clay content of these two films were also statistically indistinguishable (Table 4-1), indicating the polymeric matrices of the (PDAC/LAP) 3s:3s and (Tetra-LAP) pH 6.0 films were of similar dry thickness. Overall, the lowest clay content in the clay composite film architectures was the pH 5.0 architecture, which had a similar film thickness to the (PDAC/LAP) 3s:9s films but only 38% clay content as opposed to 83%.

4.2.2 – Thermal Cross-linking

The reaction to form amides from the amine functional groups in PAH and the carboxylic functional groups in PAA is driven by heat, usually in excess of 200°C (Figure 4-3).
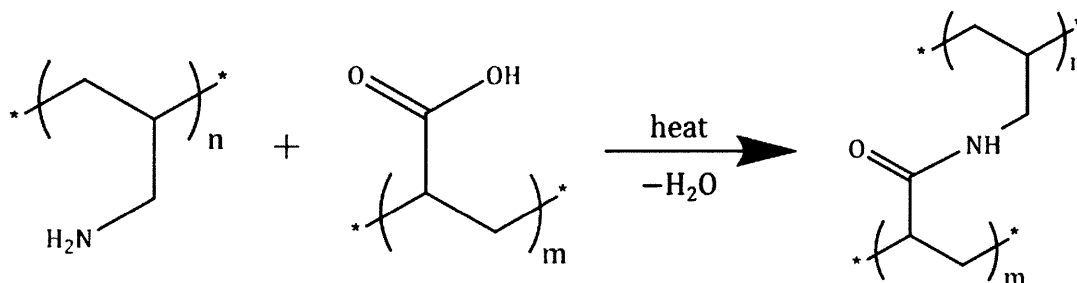
Figure 4-3: Thermal cross-linking reaction with PAH and PAA to form secondary amide.

Cross-linking was directly verified through ATR-FTIR spectral analysis on the untreated and thermally cross-linked films. The ATR microscope attachment was selected because it can be used on a sample deposited on a flat surface that is similar to the final membrane product, and the measured data corresponds to the average absorbance as a function of IR wavelength over the penetration depth. This penetration depth is a function of the crystal material and geometry; for a hemispherical Germanium crystal head and an angle of incidence of 55°, the penetration depth is approximately 400 nm. Thus, films were deposited that were greater than 400 nm thick to maximize the signal corresponding to the thin film. Although the ATR head is exposed to the atmosphere and thus H_2O and CO_2 peaks will be observed in the spectra, these can be minimized by drying the samples fully ahead of time, appropriate cleaning of the ATR head, and purging the FTIR system with N_2 overnight before running the samples.

For data analysis, the region from 2000 cm^{-1} to 1300 cm^{-1} was used because a significant silicate peak was observed between 1250 cm^{-1} and 1000 cm^{-1} which precluded reliable deconvolution and analysis of peaks in this area. The key peaks in the ATR-FTIR spectra used to determine the degree of covalent bond formation were the amide I and II peaks. The shift in the amide II peak around 1650-1515 cm^{-1}, corresponding to the N-H bending in the amine, is significantly reduced after cross-linking. This is the result of the reaction of primary amines to form secondary amides: PAH is a primary amine, contains two N-H bonds per functional group, and upon cross-linking with PAA becomes a secondary amide, with only one N-H bond (Figure 4-3). The amide I peak around 1700-1670 cm^{-1}, primarily corresponding to the C=O stretching, was considered for quantification but due to the convoluted nature of that part of the spectra it was difficult to reliably isolate the integrated peak area. Thus, the amide II peak was used for quantification. Utilizing the ORIGIN software package for linear baseline adjustment, peak deconvolution, and peak integration, the relative area of each peak could be assessed and used to calculate an approximate degree of cross-linking. The degree of cross-linking was estimated with the formula:

$$\chi = 2 \left(\frac{A_{ut} - A_{cl}}{A_{ut}} \right)$$

...where χ is the degree of cross-linking i.e. corresponds to the fraction of N-H bonds in the amine groups that were cross-linked, with 0% corresponding to an untreated film and 100% corresponding to a fully cross-linked film, A_{ut} corresponds to the peak area for the amide II peak measured for the uncross-linked film, and A_{cl} corresponds to the peak area for the same peak in the cross-linked film.

Initial trials were conducted on cross-linking the tetra-LAP composite films via uncatalyzed exposure at 125°C in an oven at atmospheric pressure for a half-hour to 2 hours (Figure 4-4). The peak apparently centered around 1550-1500 cm^{-1} is the amide II peak, used for quantification. After baseline adjustment and peak deconvolution through the ORIGIN software, no discernable degree of cross-linking could be calculated from the films cross-linked at 125°C. The sharp peak observed at 1690 cm^{-1} corresponds to the carbonyl group from the carboxylic acid and the cross-linked polyamide. The relatively large and sharp peak centered at 1590 cm^{-1} possibly corresponds to nitrate groups, possibly formed from the amines undergoing oxidation as a side reaction. The 2 hour spectra (Figure 4-4c) does not show strong peak signals for any functional group besides at 1650 cm^{-1}; this spectra is likely a failed experimental run due to the films being too thin. Acid anhydride identification peaks, in particular the 1800 cm^{-1} peak, were not observed for these films. The final conclusion drawn from this study was the temperature was too far below the optimal temperature to reliably cross-link the tetralayer films.
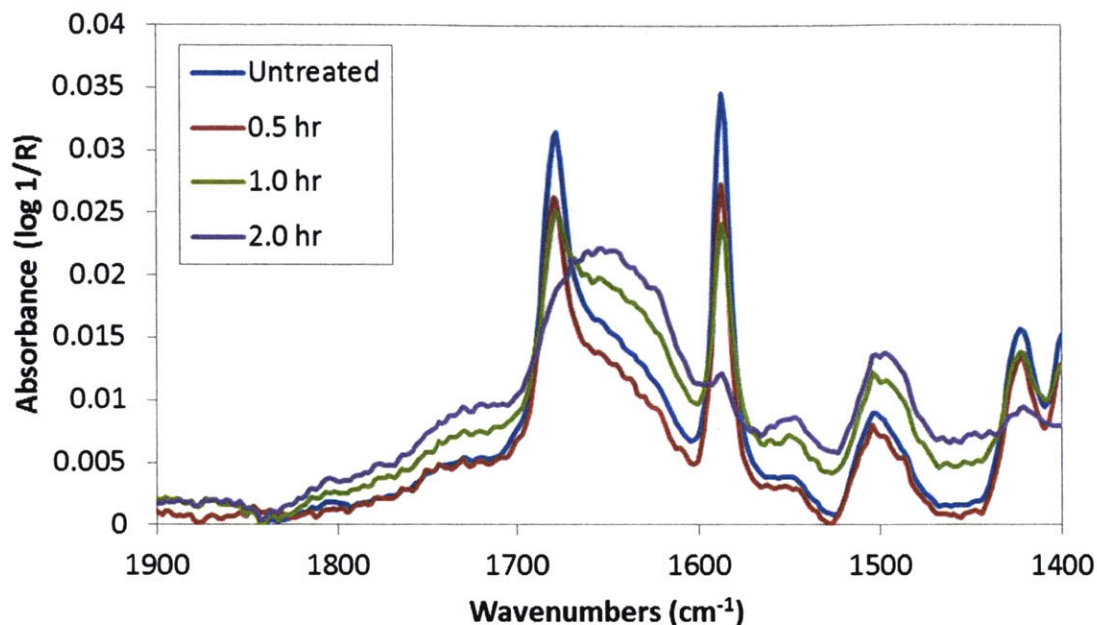
Figure 4-4: ATR-FTIR spectra for thermal cross-linking reaction of PAH and PAA in tetra-LAP clay composite films assembled at pH 6.0 films at 125°C for: a) 0.5 hour (red), b) 1 hour (green), c) 2 hours (purple), and d) untreated films (blue).

The tetra-LAP with assembly pH values of 5.0 and 6.0 were then cross-linked via an uncatalyzed exposure at 175°C in a vacuum oven for 5 hours (Figure 4-5). This temperature was selected because it was less than the T_g of the support layer (PES) at 190°C, and the ovens in the ISN have approximately a 10-15 °C margin of error. The vacuum was applied to remove free oxygen from the system as well as to drive the reaction forward by removing water from the environment.
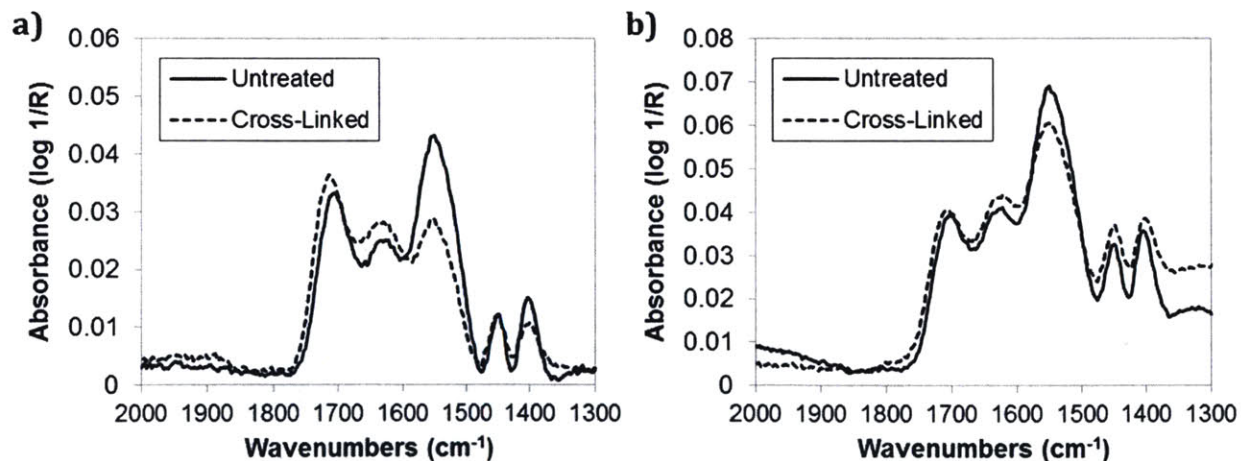
Figure 4-5: ATR-FTIR spectra for untreated (solid line) and thermal cross-linked (dashed line) films of PAH and PAA at 175°C, 5 hr. for a) tetra-LAP pH 5.0 films, and b) tetra-LAP pH 6.0 films.

Through the application of ORIGIN software for linear baseline adjustment, peak deconvolution, and peak integration as described above, χ was estimated at 20.6% for the pH 5.0 films (Figure 4-5a), compared to 12.8% for pH 6.0 films (Figure 4-5b). This is attributable to the increased number of free acid functional groups not bound in ionic bonds present in the pH 5.0 films that are available at the lower pH of assembly.

The formation of acid anhydride bonds between multiple carboxylic acid groups was possible but not strongly observed in these spectra. The key peak for the identification of these bonds is in the 1830-1800 cm^{-1} range, and while a small blip was observed for the pH 5.0 films, nothing significant was observed for the pH 6.0 films cross-linked at 175°C. The key identification peaks for acid anhydrides, such as the 1800 cm^{-1} peak, were not observed for these films either. These bonds form more strongly when the sample is isolated at a lower pH, but at the pH values the tetra-LAP films were isolated at the acid anhydride linkages were not formed.

4.2.3 – Swelling in Untreated and Cross-Linked Films

After demonstrating the thermal cross-linking reaction had occurred, it was important to determine whether the cross-linking had an impact on the physical properties of the films. Of particular interest was the degree to which the films swelled under aqueous conditions because swelling can be used as a proxy for understanding how the spacing between the clay platelet layers increases as a result of hydration. This holds so long as the swelling occurs entirely within the polymer matrix between clay platelets, which is reasonable because the silicate clays have a well-ordered crystalline structure with covalent bonds that are not susceptible to being broken under these experimental conditions. The swelling of the different film architectures under aqueous conditions with DI water was measured via spectroscopic ellipsometry (Table 4-2) utilizing previously published techniques for measuring LbL-assembled thin films[381].

Table 4-2: Measured swelling in both untreated and cross-linked bilayer and clay composite films.

Film Architecturec	Untreated	Cross-linked
(PAH/LAP), pH 5.0	62% ± 5%	--
(PAH/PAA), pH 5.0	110% ± 38%	11% ± 13%
(PAH/PAA), pH 6.0	19% ± 2%	10% ± 10%
(Tetra-LAP), pH 5.0	147% ± 3%	15% ± 3%
(Tetra-LAP), pH 6.0	37% ± 2%	11% ± 1%

The lesser degree of swelling observed for the pH 6.0 films when compared to the pH 5.0 films was expected because of the greater shift in pH. The uncross-linked (PAH/PAA) pH 5.0 films were observed to significantly swell as the films undergo a significant pH shift from the assembly

conditions as well as have significantly more free amine and carboxylic acid groups present to form hydrogen bonds with water molecules. The composite bilayer of (PAH/LAP) swelled approximately 62% upon exposure to DI water, significantly less than the polyelectrolyte (PAH/PAA) pH 5.0 films but greater than the (PAH/PAA) pH 6.0 films. For these films, the swelling was relatively more constrained, likely because the polyelectrolytes were more ionized when assembled and thus formed more ionic bonds between the PAH and PAA polyelectrolyte chains.

Cross-linking reduced the observed film swelling to roughly 10-15% regardless of assembly pH. This suggests that the covalent bonds formed during the cross-linking process both reduce the number of free amine and carboxylic acid groups that can interact with water and physically constrain the swelling of the film. The difference in swelling behavior of the two film architectures can be largely attributed to the thickness of the polymer matrix between the individual platelet layers based on three factors. First, note the clay content of the films from Table 4-1, with 38% at pH 5.0 to 56% at pH 6.0. Second, note from the profilometry that films assembled at the pH 5.0 are approximately twice as thick as the films assembled at pH 6.0. Third, with the knowledge that the individual platelets do not swell, but rather water closely adsorbs around the surface of the tetrahedral layers, the swelling can be attributed to that polymeric matrix. Finally, because the swelling in the cross-linked films is statistically indistinguishable at 10% and the spray times for the clay film component are the same for these two, it is possible to use the ratio of film thicknesses as a proxy for the spacing between the clay platelets under RO conditions.

Additionally, the tetra-LAP films exhibited swelling behavior between the (PAH/PAA) bilayer and (PAH/LAP) clay bilayer. Since it is a combination of these two constituent pieces, it is not unexpected that the properties of the tetralayer architecture is an arithmetic average of the two constituent bilayer architectures.

Briefly, a profilometer was employed to attempt to measure the film swelling under aqueous conditions. A large petri dish partially filled with water was used as a bath for the samples, but even with a 5" petri dish the profilometer head had limited mobility, meaning very short scan lengths had to be employed. Evaporation throughout the process and partial coverage of the substrate due to the slight tilt of the sample stage compounded the issues with using the profilometer. Additionally, even with the minimum tip force (1 mg) the swollen films were visibly deformed by the profilometer tip. Thus, the measurements taken via profilometry were deemed unreliable and ellipsometry was preferred.

4.2.4 – Nanoindentation Measurements

Nanoindentation was used to measure the impact of the cross-linking on the hardness of the clay composite films in both the dry and wet state. A Berkovich diamond tip was employed with shallow indents of 10-20 nm, as the film thicknesses did not exceed 400 nm. Thus, the penetration depth was less than 10% of the film thickness, which prevents the underlying substrate from skewing the results. The reduced modulus (E) was calculated through Oliver-Pharr analysis. The dry-state data was collected for tetra-LAP and (PAH/PAA) films at pH 5.0 and 6.0 (Figure 4-6).
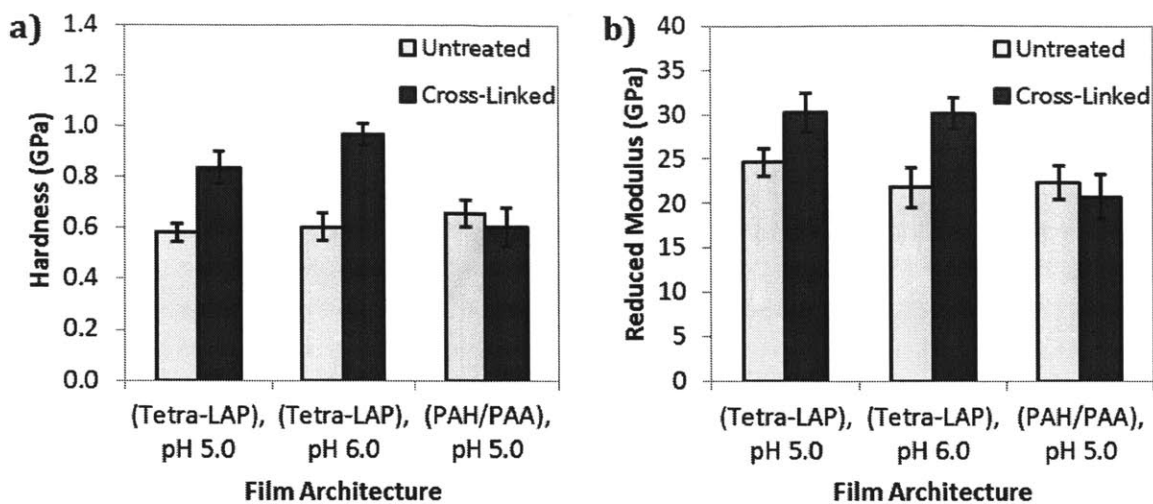
Figure 4-6: Mechanical properties measured through nanoindentation conducted on dry films both in the untreated (white) and cross-linked (black) state: a) hardness in GPa; b) calculated reduced modulus (E).

No difference of statistical significance was observed for the hardness or calculated reduced modulus (E) for the (PAH/PAA) bilayer films before and after cross-linking. This could be the result of very thin films being used and incomplete information being gathered on the film. However, both of the tetra-LAP films showed a statistically significant increase in hardness as the result of the cross-linking, indicating the covalent bonding increased the toughness of the films. For films assembled at pH 5.0, the cross-linking increased hardness by approximately 44% and for films assembled at pH 6.0, the hardness was increased by 60%. Notably, the clay content of the pH 6.0 films was greater than at pH 5.0 (Table 4-1), and the degree of cross-linking was lower (Figure 4-5). Although the degree of cross-linking was lower, the increased clay content was sufficient to harden the pH 6.0 films more than the pH 5.0 films.

Wet AFM nanoindentation measurements were conducted on the same film architectures to determine whether these observations held for the films in the hydrated state (Figure 4-7). The measured elastic modulus was lower for all the films examined, which is expected because the 1) the swelled film is less dense than the dry film, and 2) water solvates the polymer chains and enables the film to rearrange when pressure is applied. The data collected on the cross-linked films were not statistically distinct from the untreated films, which may indicate the difference in hardness observed is a function of the film thickness and clay content more than the degree of cross-linking in the water-swelled films. However, the error bars were too large on these measurements to make this assertion with confidence.
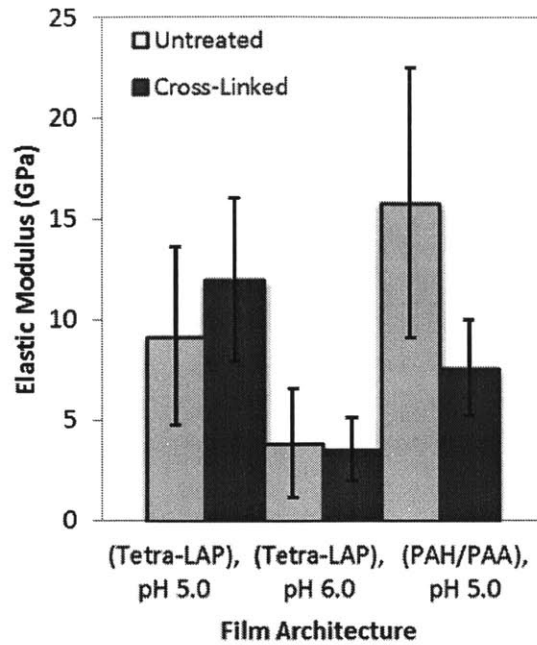
Figure 4-7: Mechanical properties measured through nanoindentation conducted on wet films both in the untreated (white) and cross-linked (black) state: a) hardness in GPa; b) calculated reduced modulus (E).

4.2.5 – Micrography on Tetralayer Films

Tetra-LAP films deposited on PES UF membranes were imaged with both SEM and TEM. First, surface and cross-sectional images of coated membranes were taken with SEM (Figure 4-8).

Figure 4-8: SEM micrographs of LAP clay composite tetralayer films deposited on PES UF membranes: a) uncoated PES-100 UF membrane; b) PES-30 UF membrane coated with (Tetra-LAP)$_{40}$ pH 6.0 film; c) cross-section of (Tetra-LAP)$_{40}$ pH 6.0 film on PES-30 UF membrane, with the membrane surface visible; d) uncoated

PES-30 UF membrane; e) PES-30 UF membrane coated with (Tetra-LAP)$_{40}$ pH 5.0 film; f) cross-section of (Tetra-LAP)$_{40}$ pH 5.0 film on PES-30 UF membrane, no membrane surface visible.

The uncoated substrate, a PES-30 UF membrane, has a regular distribution of surface pores of approximately 30 nm diameter (Figure 4-8d). Films were also deposited on PES-100 UF membranes, although these were not used for permeation studies (Figure 4-8a). The surfaces of the (Tetra-LAP) films, both assembled at pH 6.0 (Figure 4-8b) and pH 5.0 (Figure 4-8e) were much smoother than the composite bilayer film architectures explored in chapter III. The films fully bridged the underlying pores, similar to what was observed with the (PDAC/LAP) composite bilayer film architectures as shown in chapter III. From the cross-sectional images of both the pH 6.0 films (Figure 4-8c) and pH 5.0 films (Figure 4-8f), the film components do not appear to penetrate into the underlying pores of the PES-30 nm membranes. The film thicknesses were measured with the JEOL SEM software and compared to the expected thicknesses from the profilometry data (Figure 4-2), and good agreement was observed for both the pH 5.0 and pH 6.0 films.

Cross-sectional micrographs were also taken with the TEM to obtain high-resolution images of the films and observe the layered structure of the clay platelets (Figure 4-9).
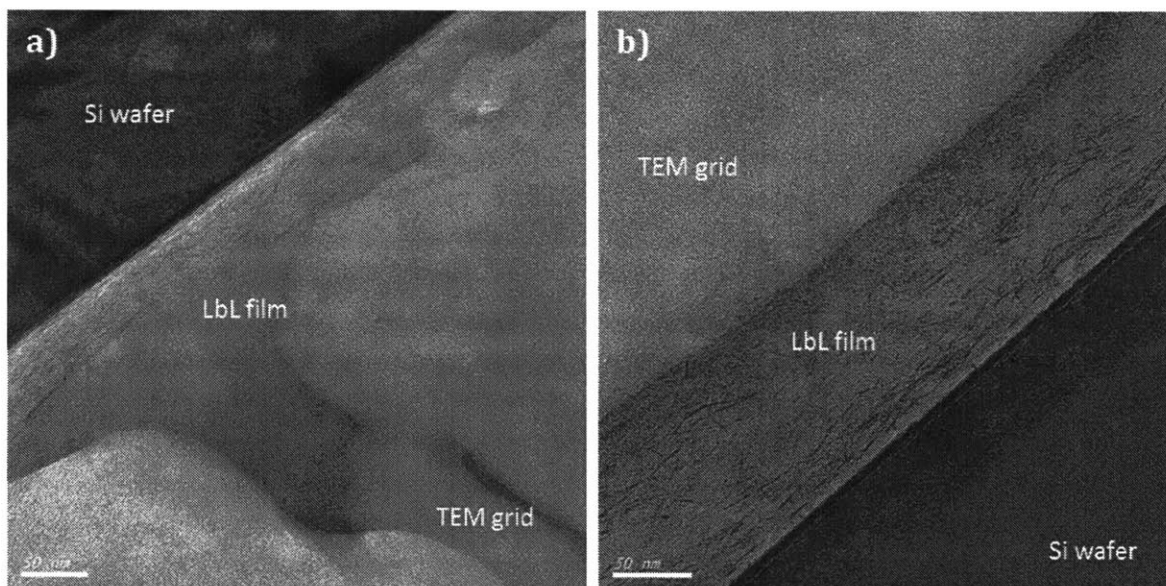
Figure 4-9: Cross-sectional TEM micrographs of (Tetra-LAP)$_{40}$ pH 5.0 films deposited on plasma-cleaned Si wafers with Au/Pd capping layers: a) untreated (not cross-linked) state; b) cross-linked at 175°C for 5 hours.

Clay platelets with intercalating polymer regions were observed by TEM imaging of the cross-sections of these membranes, shown in Figure 4-9. Through ImageJ software analysis, the approximate size of the clay platelets observed in the cross-sectional SEM was on the order of 50 nm, indicating the clay platelets are not aggregated within the film and are intercalated within the polymer matrix. The average measured platelet spacing was 2.41±0.23 nm for the uncross-linked

pH 5.0 films and 2.57±0.39 nm for the cross-linked pH 5.0 films, with no statistically significant difference apparent. A histogram of the platelet distribution shows a fairly regular distribution of nano-channel sizes for the uncross-linked films (Figure 4-10a) and the cross-linked samples seemed to exhibit a greater range of values around the mean (Figure 4-10b). The minimum platelet spacing appeared to be approximately 1 nm, no platelets were found that were aggregated or with a smaller gap between them.
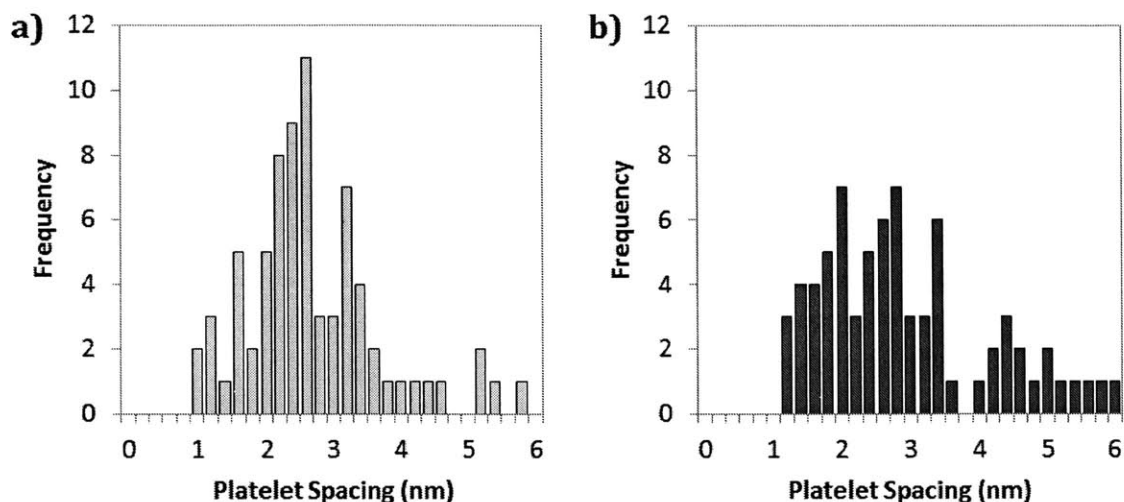
Figure 4-10: Histogram of platelet spacing measurements on two films presented in Figure 7-9: a) uncross-linked (Tetra-LAP) pH 5.0 films (white), and b) cross-linked (Tetra-LAP) pH 5.0 films (black).

Micrographs were also taken of the membranes as assembled and after water permeation experiments were conducted (Figure 4-11).
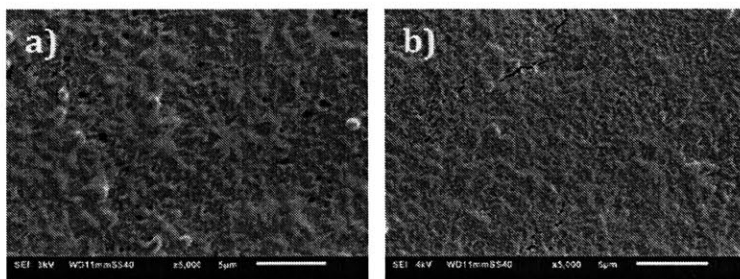
Figure 4-11: Post-water permeation SEM micrographs of clay composite tetralayer films: a) (Tetra-LAP)$_{40}$ pH 6.0 on PES-30 membrane; b) (Tetra-LAP)$_{40}$ pH 5.0 on PES-30 membrane.

The critical defects that correlated to low salt selectivity for (PDAC/LAP) clay composite films do not appear in the SEMs taken of post-permeation (Tetra-LAP) films. The pH 6.0 films (Figure 4-11a) generally exhibited more pinhole defects than the pH 5.0 films (Figure 4-11b), although no major defects such as cracks on the order of micron-sized or greater were observed for the tetra-LAP films. This is additional evidence the cross-linked (Tetra-LAP)$_{40}$ and (Tetra-LAP)$_{60}$

films are tougher and thus able to withstand the range of pressures applied under at least brackish RO conditions.

4.2.6 – Permeation Studies on Clay Composite Tetralayer Films

As with the composite bilayer films presented last chapter, the above tetralayer films were measured in the dead-end permeation cell to determine the water permeability and salt rejection properties (Appendix 2). Water flux and salt rejection data on the films were collected from dead-end permeation cell measurements over a pressure range of 50 psig to 300 psig with deionized water and 1.0 wt. % (10,000 ppm) NaCl solution (Figure 4-12).
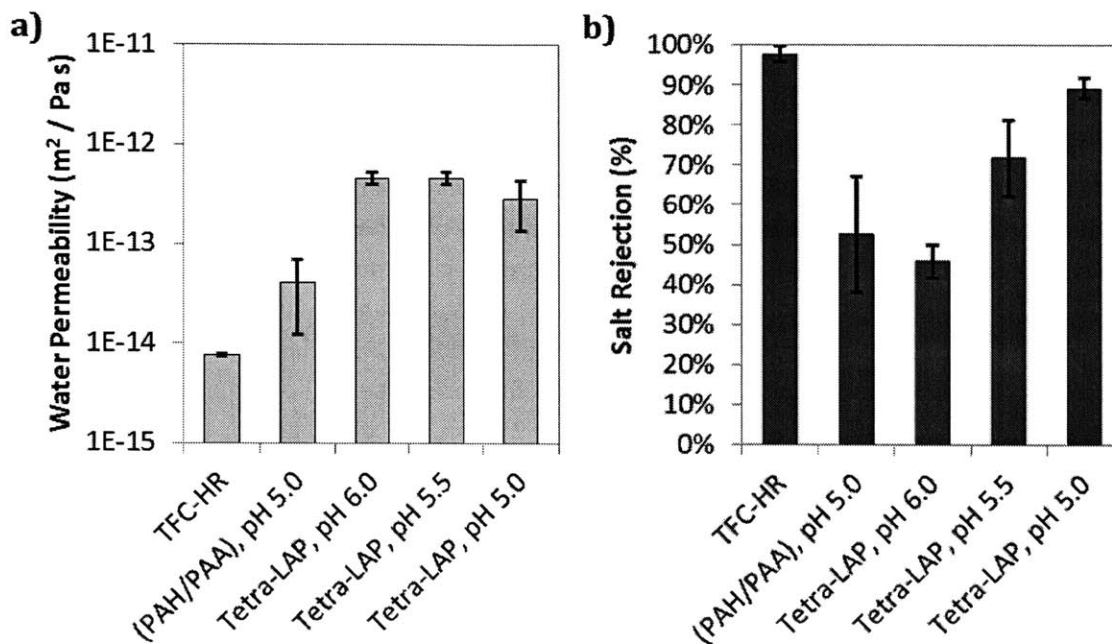
Figure 4-12: Dead-end permeation cell data for polymer bilayer and clay composite tetralayer films: a) measured water permeability (grey); and b) measured salt rejection (black).

As noted previously, the PES-30 and PES-100 nm UF membranes had water permeability values of $2 \cdot 10^{-9}$ m^2 / Pa s and $1 \cdot 10^{-9}$ m^2 / Pa s respectively, significantly greater than any of the selective layers examined. It is notable that for the composite tetralayer series from pH 6.0 to 5.0, the water permeability dropped by approximately a factor of two from $4.60 \cdot 10^{-13}$ m^2 / Pa s to $2.82 \cdot 10^{-13}$ m^2 / Pa s. However, the salt rejection increased from an average of 46% to 89%. It is hypothesized this occurs for two reasons: 1) the increased degree of cross-linking in pH 5.0 films holds the effective nano-channel width between clay layers closer together after swelling under in situ RO conditions, and 2) additional free carboxylic acid groups present in the pH 5.0 film slow the diffusion of solvated ions due to charge effects as discussed in section 1.5. Here, it is observed that an increase in the tortuosity of the films via an increased volume fraction of clay in a cross-linked

polymeric matrix (i.e. using the Cussler equation, section 1.6.3) yielded an increase in salt selectivity.

This demonstrates the absolute importance of the cross-linked polymeric matrix that reduces the brittleness of the film; these cross-links fortify the polymeric matrix encompassing the clay platelets, and prevent the formation of cracking and critical faults under in situ desalination conditions. The film architecture without clay, the cross-linked (PAH/PAA) bilayer architecture, only exhibited 53% salt rejection with a permeability of $4.01 \cdot 10^{-14}$ m^2 / Pa s. This is indicative that even a cross-linked and less-swollen polymeric matrix does not serve as an effective barrier to solvated ion diffusion due to the lack of size exclusion-driven rejection through the nano-channels present in the clay composite films, which is largely in-line with what has been observed in literature for LbL-assembled polyelectrolyte films as discussed in section 1.8.3.

4.2.7 – Increasing the Spacing between Platelet Layers via Hexalayer Films

Although the greatest selectivity was observed for tetralayer clay composite films with an interplatelet spacing of approximately 2.5 nm, an additional tweak investigated to the system was to increase the number of polymer bilayers between each clay composite bilayer. The adopted term hexalayer was used as a shorthand description for films assembled with two polymer bilayers between each clay composite bilayer: (PAH/PAA/PAH/PAA/PAH/LAP) (Hexa-LAP). The additional polymer bilayer will have two effects on the overall film properties: 1) a lower per-weight clay content and increased polymer weight, which leads to 2) more functional groups that can be cross-linked to form a tightly bound polymeric matrix. The growth curves for this hexa-LAP film assembled at pH 5.0 is shown in Figure 4-13.
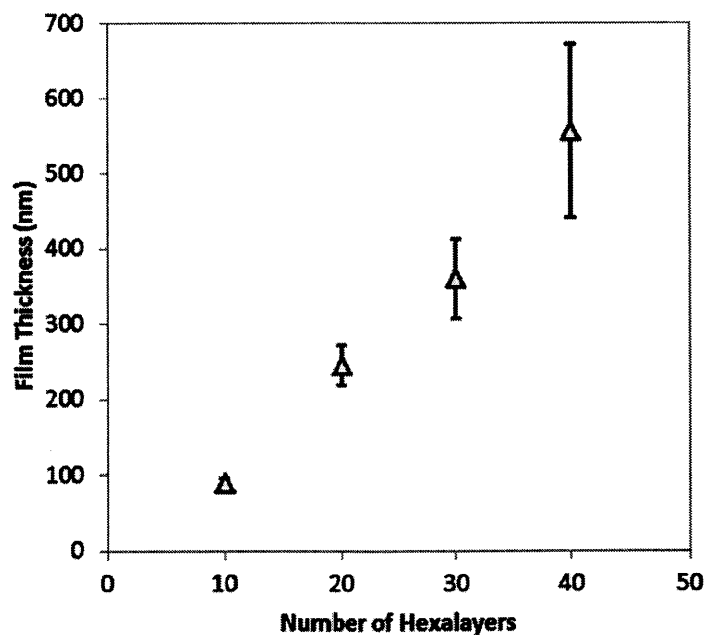
Figure 4-13: Growth curve for spray-LbL assembled clay composite hexa-LAP film, pH 5.0 assembly.

These films grew on the order of 11.8 nm per hexalayer, significantly thicker than the maximum 6.5 nm/bl for the (PDAC/LAP) clay composites from chapter III and the 5.1 nm/tl for the (Tetra-LAP) film architecture presented here in chapter IV. The per-bilayer thickness of the polymer depositions is greater than what was observed for the tetralayer architectures, possibly indicating a greater degree of interdiffusion present in the hexalayer films that was not possible in higher clay content films. The expected clay content for these films was also below 38% by weight, the value observed for the (Tetra-LAP) film assembled at the same pH. The films were imaged via SEM (Figure 4-14).
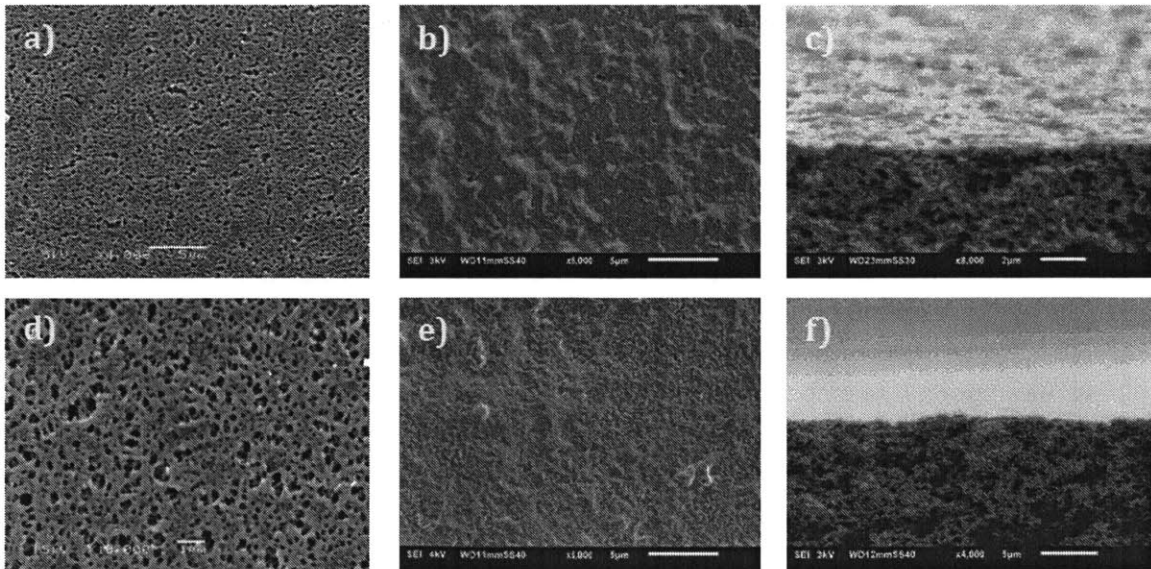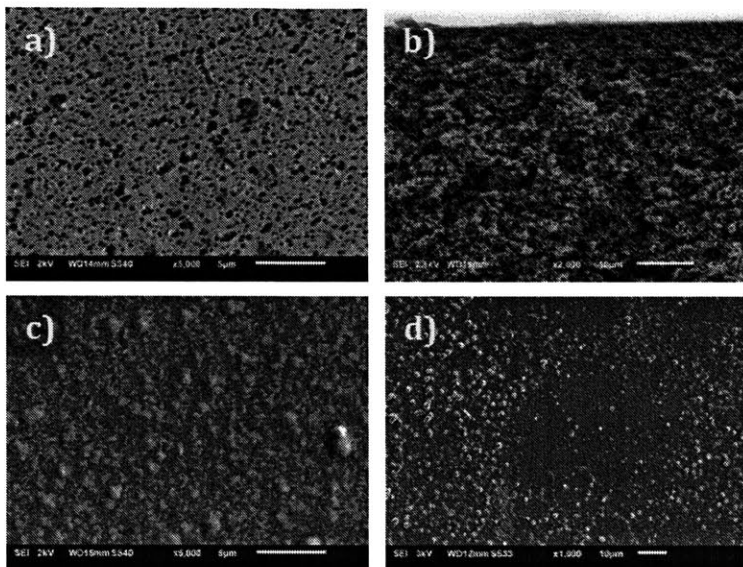

Figure 4-14: SEM micrographs of LAP clay composite hexalayer films deposited on PES-30 UF membranes: a) uncoated PES-30 UF membrane; b) cross-section of PES-30 UF membrane coated with (Hexa-LAP)$_{30}$ pH 5.0 film; c) surface of pre-permeation (Hexa-LAP)$_{30}$ pH 5.0 film on PES-30 UF membrane; d) surface of post-water and post-salt permeation (Hexa-LAP)$_{30}$ pH 5.0 film on PES-30 UF membrane.

Similar to the tetra-LAP films, the hexa-LAP films coated the surface of the PES-30 UF membrane (Figure 4-14a) and did not penetrate into the pores (Figure 4-14b). This was expected as the same materials were being deposited as in section 4.2.5. Although some knob-like structures were observed on the surface of the films (Figure 4-14c), there were not a significant number of pinhole defects or other large cracks in the deposited films. Salt crystals were observed on the membrane post-salt permeation (such as those in Figure 4-14d), but no major cracks were observed after the permeation trials up to 250 psig.

The hexa-LAP film architecture was also tested in the dead-end permeation cell with DI water and 10,000 ppm NaCl (Appendix 2), with operating pressures between 50 psig and 250 psig; the results were compared against the tetra-LAP films from section 4.2.6 (Figure 4-15).

The water permeability for the hexalayer films was greater than $1 \cdot 10^{-12}$ m^2 / Pa s, still two to three orders of magnitude lower than the raw water permeability measured for the PES-30 UF

membranes but significantly greater than the tetralayer film architectures. From a salt rejection perspective, these hexa-LAP pH 5.0 films performed approximately as well as the polymer bilayer and tetra-LAP pH 6.0 films at 42% salt rejection. Referring back to 4-12, the permeability properties for these hexa-LAP films appear to be between the tetra-LAP pH 5.0 and (PAH/PAA) bilayer films at pH 5.0, which makes sense as the films were assembled at the same pH and form a series of increasing clay content.
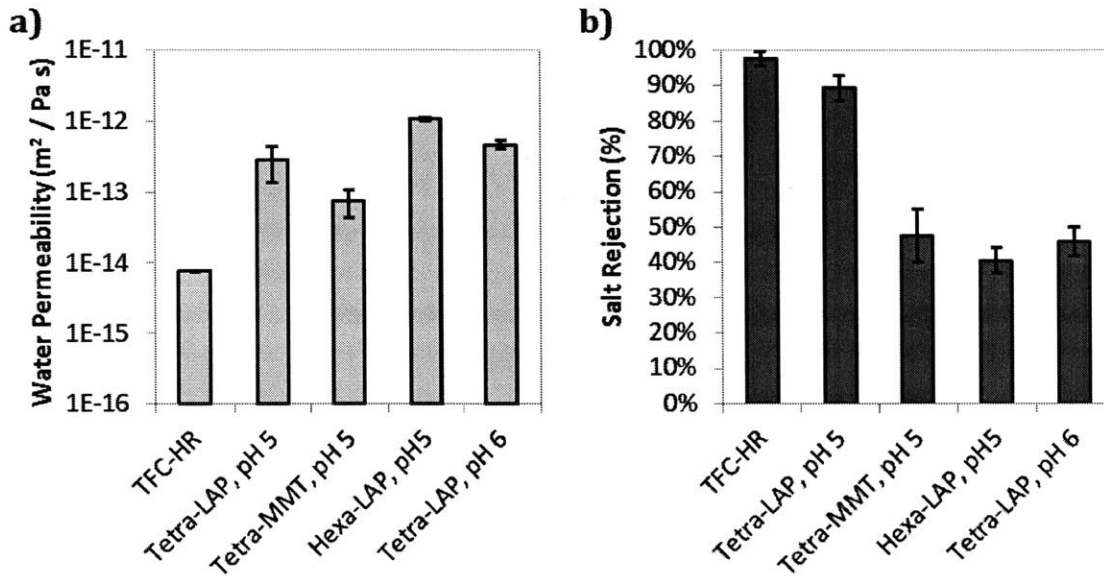
Figure 4-15: Dead-end permeation cell data for clay composite hexalayer films compared to clay composite tetralayer data: a) measured water permeability (grey); and b) measured salt rejection (white).

Ultimately, the incorporation of an extra polymer bilayer per clay layer will negatively impact τ on these films, yielding a diffusive pathway that is between the polymer bilayer and clay composite tetralayer in tortuosity. What was observed was a decrease in salt rejection and an increase in water permeability, which makes sense when compared in the series to the (Tetra-LAP) pH 5.0 film as these two films are of approximately the same thickness but the tetra-LAP film had 40 clay layers deposited as opposed to the 30 clay layers in the hexa-LAP film. Additionally, the spacing between the clay platelet layers was greater for the hexa-LAP films. The performance is roughly on par with the (PAH/PAA) bilayer film, which is an interesting result, indicating there might be a minimum fraction of clay that needs to be incorporated before significant improvements in salt rejection can be realized via the size exclusion mechanism.

4.3 – Conclusions

In this chapter, the basic composite clay (PDAC/LAP) bilayer architecture was refitted with a cross-linkable polyelectrolyte system of PAH and PAA to form films with a lower overall clay composition than was explored in chapter III. Variations on this architecture, including assembly at different pH values and manipulating the number of polymer spacing layers between the clay

layers, were explored to tease out the impact of cross-linking and clay content on the assembled composite films.

The work performed in this chapter demonstrates the utility of LAP clay platelets in spray-LbL assembled selective layers for RO membranes. The water permeability for all tetralayer clay composite thin films was between one and tw orders of magnitude greater than what was observed for a commercially-available RO membranes and equivalent to the high water permeability observed for the clay composite bilayers in chapter III, but also yielded significantly increased salt selectivity. The pH 6.0 films, comprised of roughly 56% clay by weight, yielded salt rejection at 46%, a significant improvement over the 10-28% observed for similar and greater clay content films in chapter III. For the pH 5.0 films containing 38% clay by weight, the maximum observed salt rejection was 89%, far and away ahead of the clay composite bilayer films from chapter III and close to the minimum salt rejection figure of 93% for a single-pass seawater-to-freshwater RO process. For FO and brackish water RO, the tetralayer pH 5.0 architecture is more than sufficient to produce freshwater without further optimization.

The (PDAC/LAP) composite bilayer film architectures were too brittle under in situ conditions and formed critical defects during operation. These defects were effectively eliminated by the introduction of a cross-linkable polymer matrix of PAH and PAA that reduced brittleness and film swelling under aqueous conditions, which made the composite films more mechanically robust. It is hypothesized the selective salt rejection and high water permeability is the result of a combination of two transport mechanisms: a size-exclusion transport mechanism that hinders the flow of solvated ions between clay layers to a greater degree than individual water molecules, and charge interactions between the unreacted polyelectrolytes and the solvated ions in the selective layer. The greater efficacy of the pH 5.0 tetralayer films over the pH 6.0 films is attributable to the increased degree of cross-linking via free carboxylic acid groups which strengthens the polymeric matrix, as well as the enhanced presence of free carboxylic acid groups that may act as hydrated regions to further enhance water permeability while retarding ion transport.

Increasing the spacing in the clay platelet layers beyond the tetralayer film architecture, as attempted with the hexa-LAP film architecture, was found to reduce overall salt rejection for no discernable benefit. The sweet spot for clay content and salt rejection is likely close to the 38% by weight clay content calculated for the tetra-LAP pH 5.0 film based on a regression of the available TGA and salt permeability data.

4.4 – Materials and Methods

4.4.1 – Materials

LAP clay was provided by Southern Clay Products, Inc.; clay dispersions were prepared at a concentration of 1.0 wt.% clay and the balance reagent-grade water. Both PAH (MW: 60 kDa) and PAA (MW: 20 kDa) were obtained from Polysciences, Inc. Polyelectrolyte solutions were prepared

at 10 mM concentration and were adjusted to the assembly pH by using a Φ340 pH/Temp Meter and concentrated HCl or NaOH solution as appropriate.

Millipore PES ultrafiltration membranes with 30 nm pores were purchased and used as a substrate for deposition. PES UF membranes were plasma-cleaned in a Harrick Plasma Cleaner/Sterilizer PDC-32G at 18 W for 30 seconds and soaked in PAH solution before spray-LbL film assembly.

NaCl was obtained from Mallinckrodt (CAS #7647-14-5) for the preparation of 1.0 wt.% (10,000 ppm) NaCl solutions to use as the feed solution for the dead-end desalination cell.

4.4.2 – Spray Layer-by-Layer Deposition

Films were constructed using a custom-built spraying apparatus. Solutions and clay dispersions were aerosolized with N_2 gas at 20 psi and are sprayed onto the substrate rotated at 10 rpm. The basic program for each layer involved spraying the film component for 3 seconds, pausing for a 5 second drain period, rinsing for 10 seconds with pH-adjusted water, and then and then a final 5 second drain period. The sequence is repeated for each film component listed to assemble a bilayer or tetralayer.

4.4.3 – Characterization

A Dektak 150 profilometer was used to determine the film thickness. Profilometry samples were deposited on glass slides plasma-cleaned using the above equipment for 5 minutes; otherwise, the standard protocol above was used. Both a JEOL JSM-6060 and a JSM-6010LA Scanning Electron Microscopes (SEM) were used to image both film surfaces and cross-sections. Cross-sectional SEM samples were prepared via the cryo-fracture method by submerging the sample in liquid N_2 and then physically tearing the sample with forceps and mounted on Ted Pella, Inc. #16104 Low Profile SEM Mount Pins. A TA Instruments Discovery Series Thermogravimetric Analyzer was used to determine the film composition of LbL films with the following program: temperature equilibration at 85 °C for 5 minutes, followed by a ramp up to 800 °C at the rate of 10 °C/min, followed by a final temperature equilibration at 800 °C for 5 minutes. The nanoindentation measurements were taken with a DMSE NanoMechanical Tech Lab Hysitron Triboindenter with a Berkovich diamond tip, with a pattern of 8x8 indentations with 3 μm gaps between each indentation, yielding a total area of 21x21 μm². A Sterlitech HP4750 dead-end permeation cell was used to determine both water and salt permeability. The cell was operated between 50 and 300 psi for films assembled on UF membranes. A Spiegler-Kedem model was then applied to determine the local water permeability constants. The chloride ion concentration of the collected permeate was measured with an Oakton Ion 700 conductivity meter and Thermo-Scientific Orion 9617BNWP IonPlus Probe.

V. Montmorillonite Clay Film Architectures

5.1 – Introduction

5.1.1 – Summary

Montmorillonite (MMT) clay was substituted for LAP clay in the prior architectures with the goal of teasing out the impact of platelet size and aspect ratio on the salt selectivity. MMT clay was selected as a replacement for LAP in the film architectures presented in chapters III and IV because MMT clay platelets are approximately the same thickness (2-3 nm), but have significantly greater aspect ratios, on the order of 100:1 to 200:1.
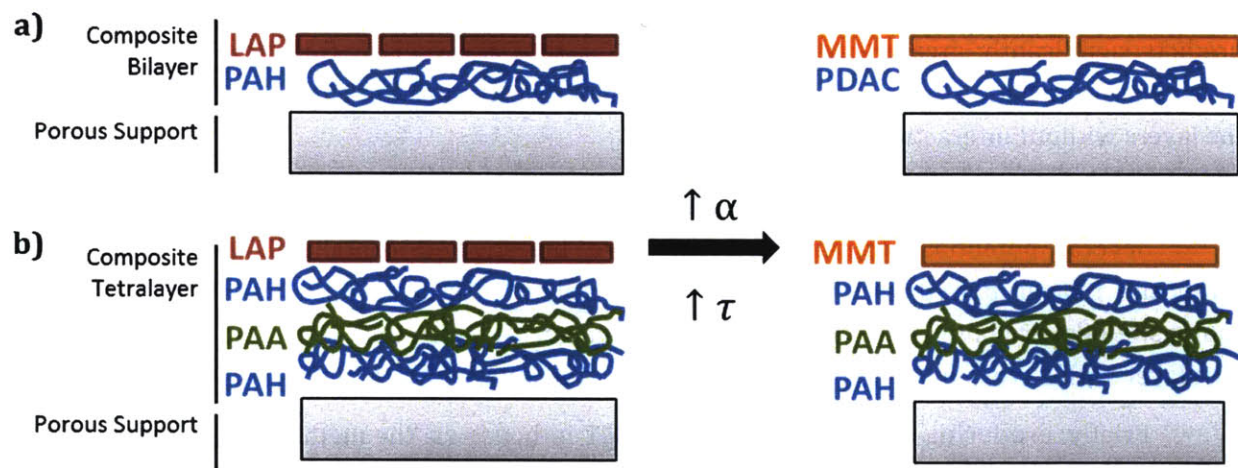
Figure 5-1: Schematic illustrating the replacement of LAP with MMT clay platelets in films to increase tortuosity: a) composite bilayer architecture, and b) composite tetralayer architecture.

The key conclusion drawn from this work was that MMT clay platelets are more difficult to incorporate into spray-LbL assembled thin films, which is hypothesized to be the result of the increased particle size and lower charge density. However, there is an opportunity to develop new spray-LbL equipment or switch to dip-LbL assembly to incorporate these platelets into selective layers.

5.1.2 – Aspect Ratio and Selectivity

As the diffusive path length is proportional to the aspect ratio of the clay platelets in the film, an obvious route to build upon the films presented in chapters III and IV is to replace the smaller LAP clay platelets with ones of a larger aspect ratio, such as MMT clay platelets. These have been efficacious in gas separation membranes[171, 174, 175], fire retardant coatings[204], electrochemical applications[302, 359], antimicrobial coatings[358], and barrier layers[172, 203, 382], moreso than LAP clay platelets, and also have not been previously applied to RO selective layers.

Montmorillonite is a commonly used material in clay-polymer nanocomposites because of its high surface area, cation exchange capacity, and hydrophilicity[357]. As discussed in section 1.6.3, the incorporation of any impermeable particle such as a clay platelet in the selective layer increases the effective diffusive path length, or tortuosity, for any solute traversing the membrane. From work done by Grunlan et al., the most appropriate correlation to use with MMT clay and its greater aspect ratio than LAP clay platelets is the Cussler correlation[170] for the semi-dilute conditions $\phi < 1$ and $\alpha\phi > 1$:

$$\tau_{Cussler} = 1 + \mu\left(\frac{\alpha^2\phi^2}{1-\phi}\right)$$

...where ϕ is the volume fraction of the clay platelets, α is the aspect ratio of the clay platelets, and μ is the geometric ratio, which is approximately 0.5 for clay platelets[171]. The Cussler correlation predicts significantly greater diffusive path lengths than the Nielsen correlation due to solutes reflecting inside nano-channels formed by multiple platelets instead of passing each solute through the layers without interaction.

5.1.3 – Clay Composite Films with MMT Clay

Several potential film architectures were investigated containing MMT clay: a clay composite bilayer paired with a strong polyelectrolyte (PDAC/MMT), a variation on the clay composite bilayer containing sulfonated polymer groups (PDAC/SPS-MMT), and a clay composite tetralayer with a cross-linkable polyelectrolyte pair (PAH/PAA/PAH/MMT) (Tetra-MMT).

Briefly, producing cation-exchanged H+-MMT in-house via the method presented by Alonso et al. was considered[382]. This method consists of passing the MMT clay through beads containing a sulfonic acid resin. However, Na+-exchanged MMT clay is available commercially and this was selected for the following reasons: 1) availability in large batches to prevent batch-to-batch variation from being a significant source of error, and 2) the charge density of H+-exchanged and Na+-exchanged MMT clay is similar, yielding no significant benefit from the process.

5.2 – Results and Discussion

5.2.1 – Montmorillonite Bilayer Films

The first composite films assembled contained PDAC and MMT in a simple bilayer film architecture: (PDAC/MMT) (Figure 5-1a). This film architecture is the MMT equivalent to the LAP clay architecture used in chapters II and III. Assembly pH values of 4.0 to 10.0 in 1.0 pH increments were examined with the (PDAC/MMT) architecture and 3 second spray times. Although films in literature have been assembled at this pH range via dip-LbL, no films could be assembled with spray-LbL. The deposited material came off with the touch of a gloved hand, and no uniform layers could be found via profilometry. The measured surface roughness was on the order of several times the expected film thickness from similar (PDAC/LAP) films and on the same order of magnitude as the estimated film thickness, indicating that only large aggregations were deposited on the glass slides, not well-integrated and layered LbL film structures.

5.2.2 – Montmorillonite Mixed-Bilayer Films

Another early approach attempted to incorporate MMT clay into a deposited LbL film was to deposit a strong polyanion simultaneously with the MMT clay to form a mixed bilayer film: (PDAC/SPS-MMT) (Figure 5-2). This approach is similar to published work with nanoblended layers by Caruso[383] but with clay platelets replacing one of the polyanions in the formulation.
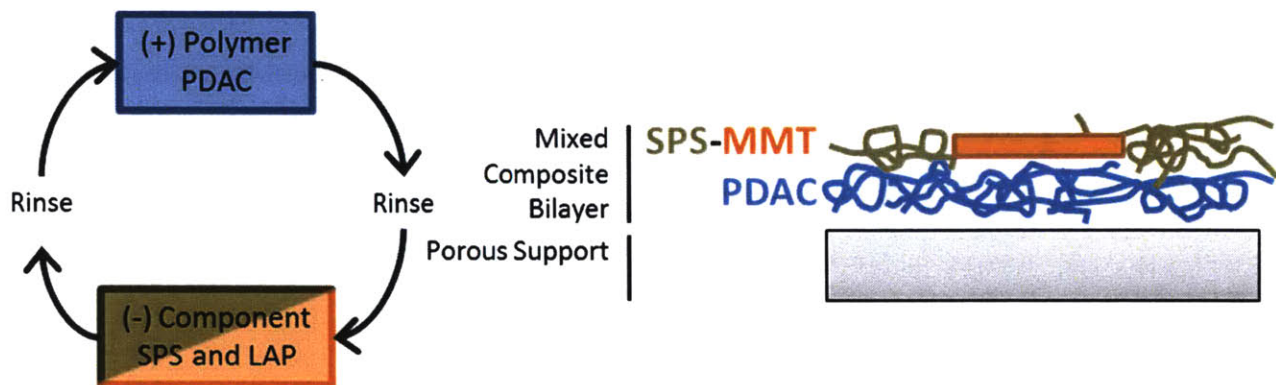
Figure 5-2: Schematic of mixed bilayer films with a joint deposition of SPS and MMT platelets.

Films were assembled with this spray formulation, but the films generated of this architecture greatly resembled the (PDAC/SPS) polyelectrolyte films discussed in 3.2.10. TGA analysis on the assembled films showed no appreciable clay incorporation into the selective layer, and this unreliable assembly was abandoned in favor of the tetralayer-MMT architecture.

5.2.3 – Montmorillonite Tetralayer Films

Finally, the MMT clay was incorporated into a tetralayer film architecture similar to that presented in chapter IV: (PAH/PAA/PAH/MMT) (Tetra-MMT). This films are a close analog to the cross-linkable clay composite film architecture developed and characterized in chapter IV (Figure 5-1b). Unlike the prior film architectures, it was possible to build durable films with this formulation. Growth curves were assembled for the films both before and after cross-linking (Figure 5-3).

The films assembled were significantly thicker than the Tetra-LAP film architecture for 10 to 40 tetralayers deposited, but began leveling off at approximately 250-270 nm thick for 60 tetralayers deposited. The calculated confidence intervals in film thickness were greater for the Tetra-MMT films, on the order of 10 nm, than for LAP films, on the order of 1 nm. This was observed along with an associated increase in surface roughness. Likely, the surface roughness is a function of the platelet size and aspect ratio: larger MMT platelets will not be able to fit in small gaps and will protrude from uneven ridges and valleys at the film interface, which will generate an uneven film surface. LAP clay platelets, being significantly smaller than MMT platelets, are more able to fill these gaps smoothly and evenly, generating a more uniform film.
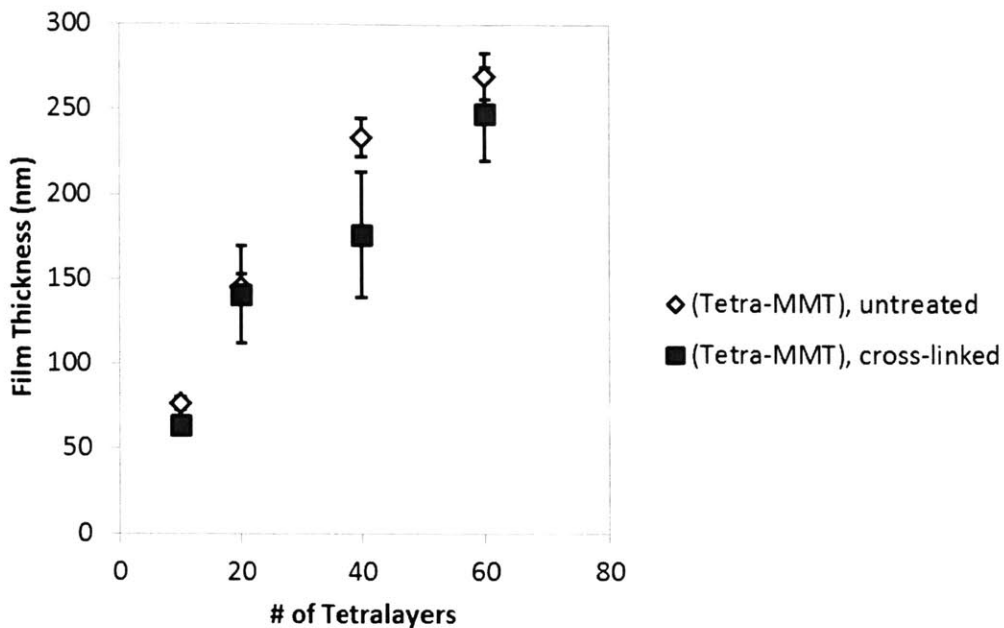
Figure 5-3: Growth curves for (Tetra-MMT) films, a) untreated (white), and b) cross-linked (black).

5.2.4 – Imaging on MMT-Containing Films

Tetralayer-MMT films were imaged via SEM to examine for defects both before and after permeation measurements were taken (Figure 5-4).
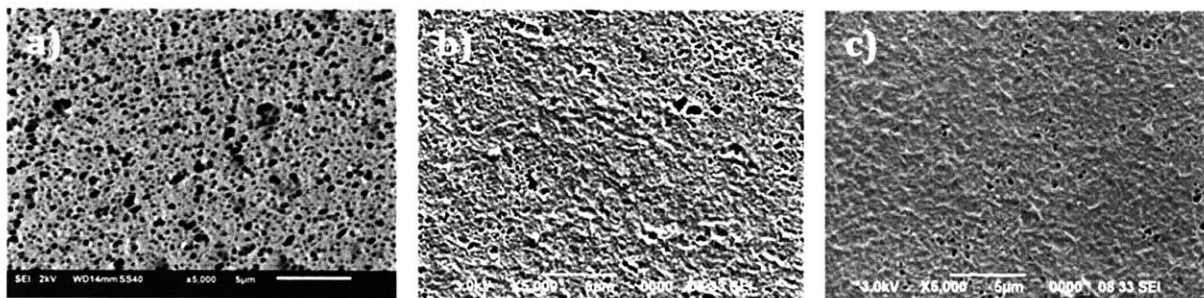
Figure 5-4: SEM micrographs of clay composite MMT films deposited on PES-30 UF membranes: a) uncoated PES-30 UF membrane; b) surface of pre-permeation (Tetra-MMT)$_{40}$ pH 5.0 film; d) surface of post-water and post-salt permeation (Tetra-MMT)$_{40}$ pH 5.0 film.

Although the tetra-MMT formed a partial film across the substrate, the resulting films were rougher than what was observed for the tetra-LAP films (section 4.2.5), and suffered from a greater number of pinhole defects (Figure 5-4b). This is an unusual observation; if the MMT clay platelets were not incorporating into the film, there are still two complementary film components being sprayed with rinsing steps between each deposition, including the polycation PAH and polyanion PAA. One would naively expect this spray program, if MMT was not layering into the film, to produce a (PAH/PAA) 6s:3s film. However, the number of pinhole defects seems to support the conclusion that the MMT platelets were not only rinsing off the surface, but stripping the surface of

the polyelectrolytes at the film interface. Following compaction under brackish RO conditions (250 psig), the films appeared smoother (Figure 5-4c).

5.2.5 – Permeation Measurements

The limited permeation measurements taken on the MMT films were conducted via both dead-end and cross-flow permeation cells (Appendix 2) with DI water and 10,000 ppm NaCl feed solution (Figure 5-5).
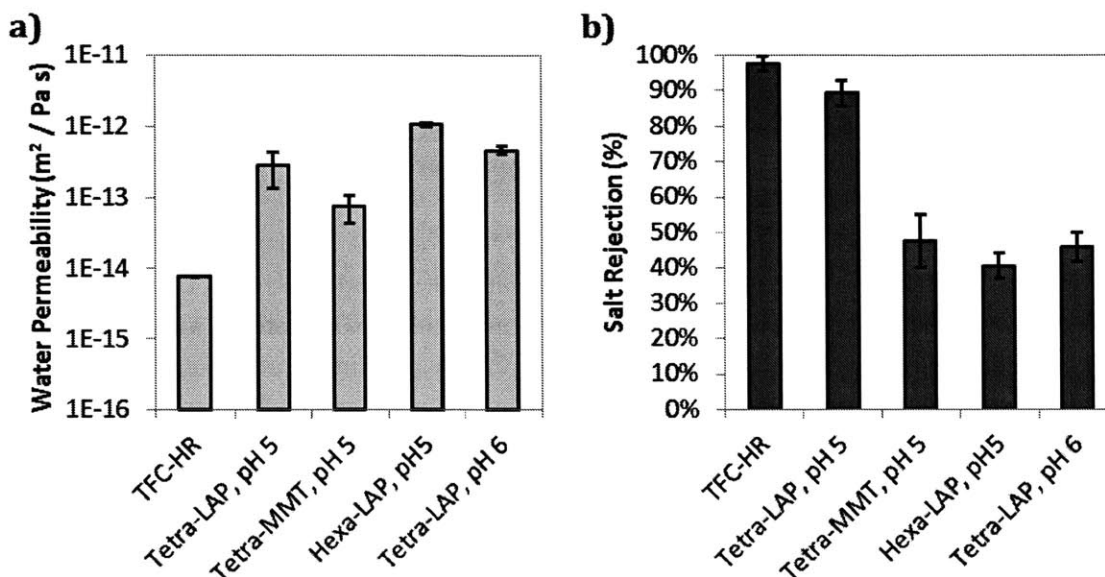
Figure 5-5: Dead-end permeation cell data for tetra-MMT films compared to prior data: a) measured water permeability (grey); and b) measured salt rejection (black).

The permeability properties for the tetra-MMT films most closely resembled the (PAH/PAA) polymer bilayer films, with observed salt rejection at approximately 50% and water permeability that was comparable to the tetra-LAP film, which was surprising given the number of defects observed on the membrane surface. However, note that only pinhole defects were observed, not large cracks as were observed for the (PDAC/LAP) bilayer films in chapter III. The relatively low salt rejection can be attributed to a low and irregular incorporation of clay into the selective layer, as well as the pinhole defects in the thin film.

5.2.6– Graphene Oxide Films

Briefly, graphene oxide (GO) platelets were considered as a substitution to MMT clay platelets because 1) these nanoparticles have a similar physical size and aspect ratio to MMT, 2) there is literature indicating these GO platelets can be incorporated into LbL film architectures via dipping[226], and 3) theoretical modeling has been done on graphene sheets to be used as membranes.

It is curious to note the salt selectivity effects of graphene oxide platelets is expected to follow a different size exclusion mechanism than the clay composite selective layers examined in chapters III-V. Instead of increasing the tortuosity of the diffusive path length through the film, defects of a specific size in otherwise uniform graphene oxide plates are thought to serve as pores through which water can pass but solvated ions are excluded[225]. Experimentally, this sort of structure cannot be generated via spray-LbL or by any industrial-scale process currently in use, for that matter.

The GO solutions, provided by Sun Hwa Lee in the Hammond Lab, had approximate particle dimensions of 1 μm in two dimensions and approximately 1-2 nm in the third, with an effective α of approximately 500:1. Film architectures with GO, including (PDAC/GO) and (PAH/GO) at pH ranges from 4.0 to 10.0 were investigated. Assembly was done on plasma-treated glass slides and silicon wafers under the same protocols developed for the clay composite films presented in chapters III-V. At pH values between 4.0 and 6.0, GO layers could not be deposited into LbL films. The films were visually inconsistent, and could be scratched off with the touch of a glove. This indicates the polyelectrolytes were not forming ionic bonds with the GO platelets and building into a regular, ordered film structure. It was hypothesized that increasing the processing time such as the drainage steps would improve the deposition of films, and although the films appeared visually more consistent they were still removable by touch and thus were not run in the permeation cell. Another modification attempted to the spray procedure was to eliminate the rinsing steps, but films still did not deposit in a uniform manner. Visually, the (PAH/GO) membranes (Figure 5-6) appeared similar to the tetra-MMT films above (Figure 5-4).
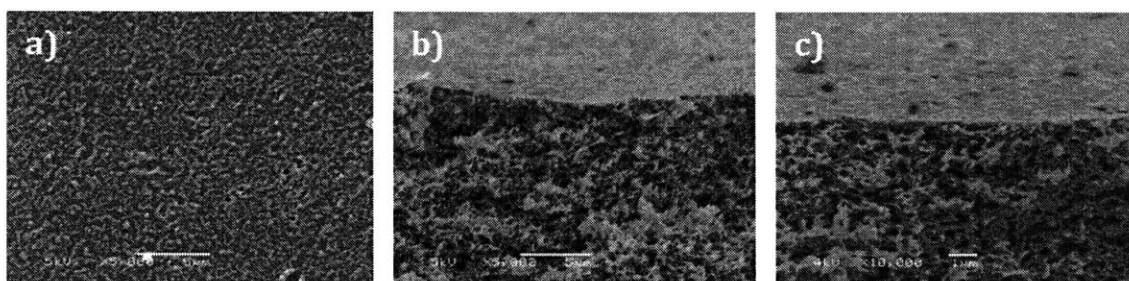
Figure 5-6: SEM micrographs of (PAH/GO)$_{40}$ pH 4.0 films deposited on PES-30 UF membranes: a) surface; b) and c) cross-sectional micrographs prepared via cryofracturing technique.

The hypothesis as to why incorporating the GO layers was so difficult has to do with the low surface charge of the GO sheets, and it being largely concentrated along the edges of the plates. This leaves large hydrophobic regions without surface charge that attract polyelectrolytes for deposition. While the longer assembly times of dip-LbL may be sufficient to enable films to build up, nothing was observed on the time scale for deposition by spray-LbL.

5.3 – Conclusions

The conclusions drawn from this portion of research are limited due to the lack of solid permeation data to base an argument on. The difficulty in assembling films via spray-LbL that

contain MMT clay and GO platelets may derive from the effective particle size of these two film components: both have aspect ratios significantly greater than LAP, on the order of 100:1 or greater, and both have micron-sized dimensions. It is possible the spray-LbL equipment was unable to aerosolize a significant fraction of the MMT platelets or GO solution, or the droplet size of 30 μm was too small for the size of these particles. Similar difficulties have not been reported for dip-assembled LbL films containing these film components, so the conflict likely lies with the assembly process and not necessarily with the selection of materials.

Hence, it is recommended that future investigations with MMT clay or other high aspect ratio, micron-sized particles utilize a larger spray apparatus that spray droplets with a diameter in excess of 30 μm. Alternatively, switching to dip-LbL processing to generate these MMT clay architectures, as has been employed in other published work as discussed in section 1.8, may yield more uniform and useable films.

However, from a design perspective, the MMT clay-containing films may run into the same limitation the filled espun mat structures do: despite the potential for increasing τ, the necessity to draw off a critical flux for characterization and regular operation may preclude the use of such high-aspect platelets for membranes of this architecture. Or, thinner, more uniform MMT-containing selective layers are required.

5.4 – Materials and Methods

5.4.1 – Materials
MMT clay was provided by Southern Clay Products, Inc.; clay dispersions were prepared at a concentration of 1.0 wt.% clay and the balance reagent-grade water. PDAC (MW: 200-350 kDa) was obtained from Sigma-Aldrich, and both PAH (MW: 60 kDa) and SPS (MW: 70 kDa) were obtained from Polysciences, Inc. Polyelectrolyte solutions were prepared at 10 mM concentration and were adjusted to the assembly pH by using a Φ340 pH/Temp Meter and concentrated HCl or NaOH solution as appropriate. GO solutions were prepared and provided by Sun Hwa Lee of the Hammond Lab, with approximately 1 μm diameter and 1 nm thickness at pH 10.0.

Millipore PES ultrafiltration membranes with 30 nm pores were purchased and used as a substrate for deposition. PES membranes were plasma-cleaned in a Harrick Plasma Cleaner/Sterilizer PDC-32G at 18 W for 30 seconds and soaked in PDAC or PAH solutions before spray-LbL film assembly.

5.4.2 – Spray Layer-by-Layer Deposition
Films were constructed using a custom-built spraying apparatus. Solutions and clay dispersions were aerosolized with N_2 gas at 20 psi and are sprayed onto the substrate rotated at 10 rpm. The basic program for each layer involved spraying the film component for 3 seconds, pausing for a 5 second drain period, rinsing for 10 seconds with pH-adjusted water, and then and

then a final 5 second drain period. The sequence is repeated for each film component listed to assemble a bilayer or tetralayer.

5.4.3 – Characterization

A Dektak 150 profilometer was used to determine the film thickness. Profilometry samples were deposited on glass slides plasma-cleaned using the above equipment for 5 minutes; otherwise, the standard protocol above was used. Both a JEOL JSM-6060 and a JSM-6010LA Scanning Electron Microscopes (SEM) were used to image both film surfaces and cross-sections. Cross-sectional SEM samples were prepared via the cryo-fracture method by submerging the sample in liquid N_2 and then physically tearing the sample with forceps and mounted on Ted Pella, Inc. #16104 Low Profile SEM Mount Pins. A TA Instruments Discovery Series Thermogravimetric Analyzer was used to determine the film composition of LbL films with the following program: temperature equilibration at 85 °C for 5 minutes, followed by a ramp up to 800 °C at the rate of 10 °C/min, followed by a final temperature equilibration at 800 °C for 5 minutes. The nanoindentation measurements were taken with a DMSE NanoMechanical Tech Lab Hysitron Triboindenter. A Sterlitech HP4750 dead-end permeation cell was used to determine both water and salt permeability. The cell was operated between 50 and 300 psi for films assembled on UF membranes. A Spiegler-Kedem model was then applied to determine the local water permeability constants. The chloride ion concentration of the collected permeate was measured with an Oakton Ion 700 conductivity meter and Thermo-Scientific Orion 9617BNWP IonPlus Probe.

VI. Catechol Modification

6.1 – Introduction

6.1.1 – Summary

The thermal cross-linking scheme introduced in chapter IV requires hours of processing time and the degree of cross-linking was at maximum approximately 20%. One shortfall in scaling up the manufacturing of films such as these to the industrial production is that length of time required to form polyamide. Alternative ways to effect a cross-linking of the LbL film with greater efficacy and less processing time, therefore, are interesting routes to take this work. One possibility is utilizing a film architecture with catechol-modified polyelectrolytes (Figure 6-1). These catechol groups are excellent adhesives that form strongly cross-linked networks with exposure to neutral and alkaline pH conditions such as seawater.
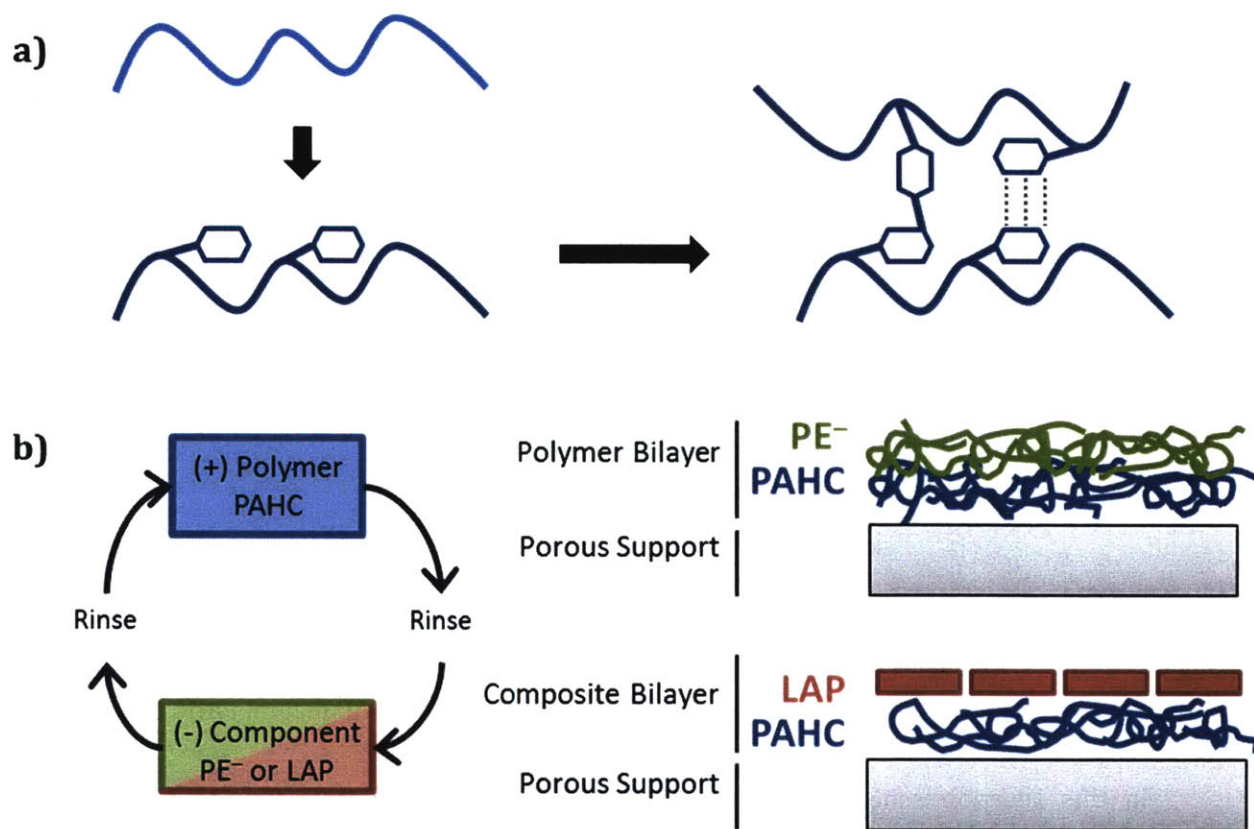
Figure 6-1: Schematic of catechol-modified clay composite film architectures: a) modification of a polyelectrolyte with catechol groups and the different bonds that can be formed between catechol groups, and b) different film architectures containing catechol-modified polyelectrolytes.

The protocols for developing these catechol-modified polyelectrolytes were examined, better buffer selections were identified, and some preliminary work was conducted with dip-LbL to build clay-composite thin films with catechol-modified polyelectrolytes.

6.1.2 – Application of Catechol-Modified Polyelectrolytes to LbL Thin Films

Catechol groups are derived from mussel proteins and are excellent adhesives at neutral pH values[384, 385]. Prior research on catechol-modified polyelectrolytes have shown these materials form several intermolecular bonds in the form of hydrogen bonds, covalent bonding in the form of ester groups, and $\pi - \pi$ stacking interactions at neutral and alkaline pH conditions[386, 387]. Dip-LbL assembled films with catechol-modified polyelectrolytes such as BPEI and PAA, abbreviated as BPEIC and PAAC, have been assembled and successfully used to tune drug release and for biomedical applications[388-390], in chemical sensors[391], functionalized surfaces and coatings[392, 393], and to functionalize a variety of substrates for the deposition of LbL films with catechol-modified polyelectrolytes[385, 394-397]. Only one other paper has been published on dip-LbL assembled films with catechol-modified polyethylene glycol and clay platelets to form a hardened nacre-like free-standing film, but there was not a focus on permeability properties[398].

The particular focus of this section of research is on modifying PAH and PAA with catechol groups in the scheme shown in Figure 6-2.
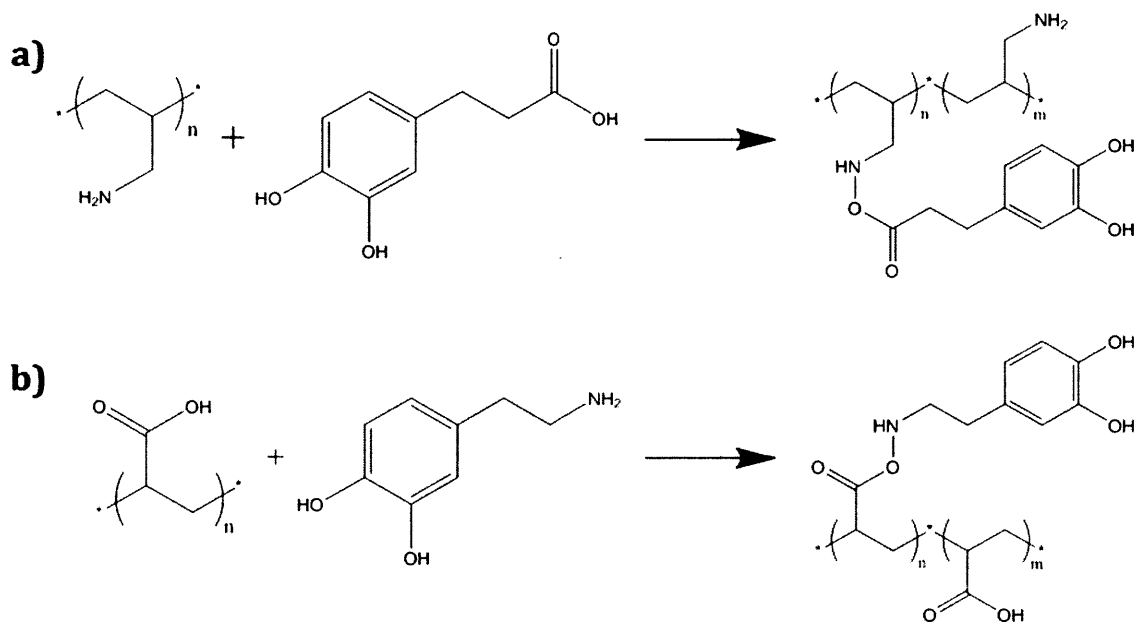
Figure 6-2: EDC chemistry to attach catechol groups to polyelectrolytes: a) PAH to form PAHC, and b) PAA to form PAAC.

In this reaction scheme, 1-ethyl-3-(3-dimethylaminopropyl)carbodiimide hydrochloride (EDC) serves as a catalyst for the amidation reaction between a carboxylic acid functional group and an amine functional group. For this application, EDC was used to catalyze the reaction between a functionalized catechol group, either 3,4-dihydroxyhydrocinnamic acid (DHHCA) or 3,4-dihydroxyphenethylamine (dopamine), and a polyelectrolyte backbone, PAH and PAA respectively. An additional catalyst, N-hydroxysulfosuccinimide (sulfo-NHS), can be added as a substitute leaving group for EDC that will accelerate the amidation with the polyelectrolyte backbone.

The full reaction scheme is illustrated in Figure 6-3.
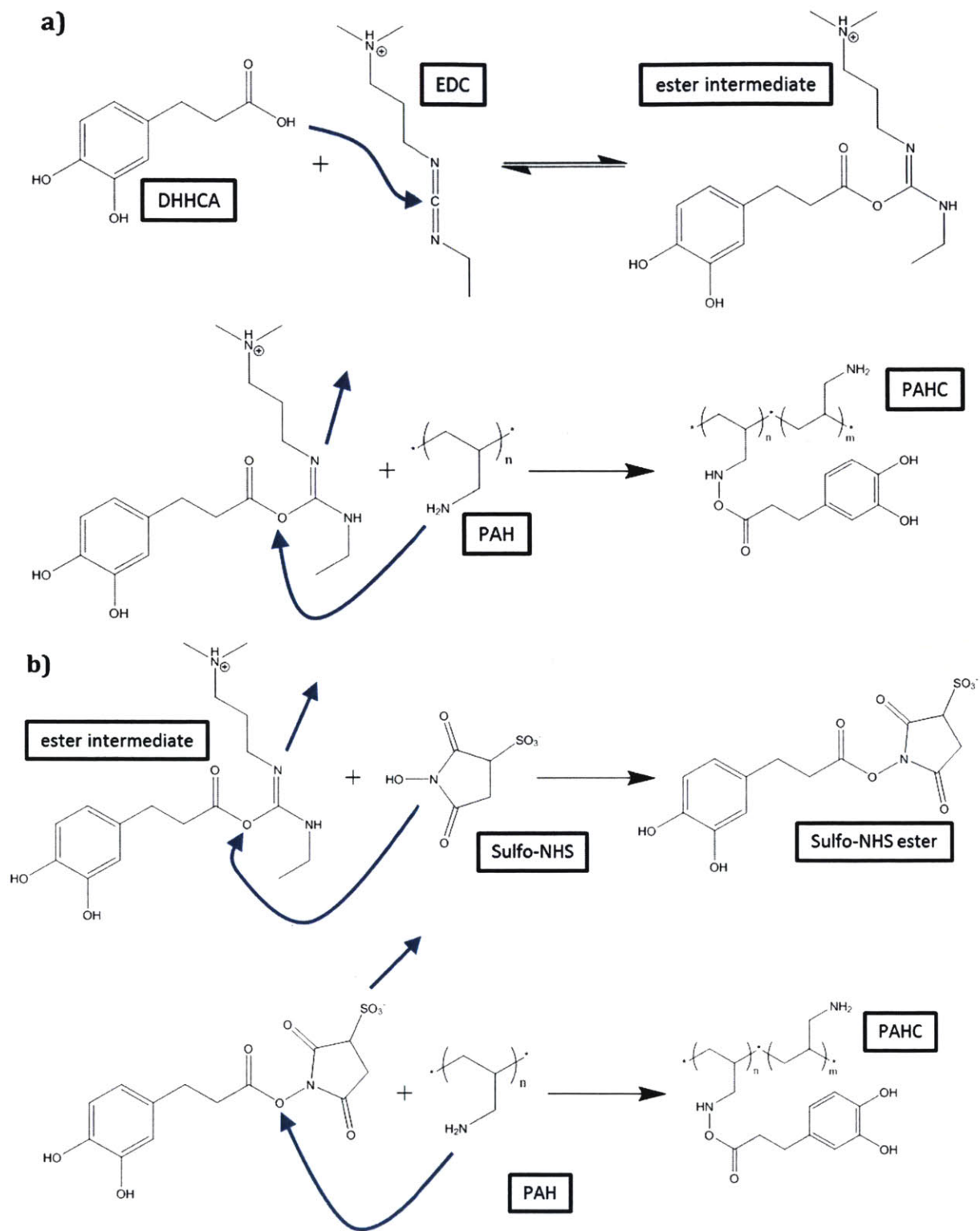
Figure 6-3: Full reaction scheme for attaching catechol groups to a) PAH to form PAHC, and b) PAH to form PAHC with sulfo-NHS to form a secondary intermediate product.

6.2 – Results and Discussion

6.2.1 – Solvent Selection for Catechol Modification

Previously, work was also carried out to modify BPEI, which has a 1:2:1 ratio of primary, secondary, and tertiary amine groups[388]; the EDC can only undergo the nucleophilic attack reaction with a primary amine as the other amines are too sterically hindered. As the goal was to generate as many cross-links as possible, PAH was selected for modification as each repeat unit has a primary amine group.

The prior work in the Hammond lab utilized phosphate-buffered saline (PBS) for the reaction solvent, which naturally buffers around pH 7.0 depending on the composition and quantity of added salts. As this reaction proceeds optimally at pH 4.5-5.0, continuous addition of acid was required to maintain the reaction pH below 5.0 otherwise the dopamine groups would cross-link as the pH rises to 7.0. This was a deleterious side reaction that would turn the batch into a rubbery substance with the consistency of taffy or thicker. Thus, different solvents were investigated with the hopes of finding one that prevented side reactions from occurring and naturally buffered closer to the optimal reaction pH.

Several common acidic buffers have carboxylic acid functional groups, such as acetic acid (Table 6-1).

Table 6-1: Investigated buffer solutions for PAHC modification, with approximate pH ranges and the presence of carboxylic acid functional groups noted.

Buffer	pK$_a$	Useful pH Range	R-COOH
PBS	varies, ≈ 7	$\approx 6 - 9$	No
Na$_2$HPO$_4$ – NaH$_2$PO$_4$	[2.15,] 7.20, [12.32]	5.8 – 8.0	No
Acetic Acid – Na Acetate	4.76	3.7 – 5.6	Yes
Citric Acid – Na Citrate	3.14, 4.75, 6.39	3.0 – 6.2	Yes
MES	6.16	5.5 – 6.7	No
MES + NaCl	6.16 (MES)	3.7 – 5.7	No
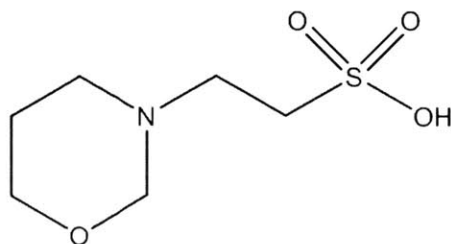
Figure 6-4: Chemical structure of 2-(N-morpholino)ethanesulfonic acid (MES).

These buffer solutions will react with EDC in a reaction scheme similar to Figure 6-3a. This complicates the solvent selection as the necessary buffer cannot contain an amine or carboxylic acid functional group. After some experimentation with different buffers, 2-(N-morpholino) ethanesulfonic acid (MES) with 0.5 M NaCl (Figure 6-4), which buffers at pH 4.7, was identified as a reasonable choice for a buffer solution. The buffer is close enough to the optimal reaction pH to forgo the necessity of additional acid or base as the reaction proceeds.

Table 6-2 documents the attempted reactions with the three different buffer solutions and quantities of reagents. The general procedure started with the dispersal of all reactants in the volumes of buffer solution listed in Table 6-2. First, the EDC was added to the carboxylic acid to form the first intermediate, and then sulfo-NHS if that was included in that particular batch, and finally the amine-containing reactant to form the product. Stirring was continuous for a minimum of three hours, followed by a sequential dialysis of a minimum of 3 days to remove unreacted chemicals and byproducts.

Table 6-2: Reaction batches attempted for catechol modification of PAH, with buffer selection, quantities of reactants, and notes on the product.

Batch	Buffer	PAH (g/mL)	EDC (g/mL)	S-NHS (g/mL)	DHHCA (g/mL)	Result
1	PBS	0.364/25	1.1/10	0	1.34/10	Negative, brown residue
2	PBS	0.468/15	1.200/5	0.743/3	0.592/5	Negative, brown residue
3	PBS	0.471/15	1.189/5	0.362/3	0.598/5	Negative, brown residue
4	MES	0.492/30	1.211/20	0.088/10	0.602/20	Negative, white residue
5	MES	0.469/20	7.189/35	0.738/5	0.178/20	Negative, pH off at end
6	MES	0.475/20	7.192/50	0.339/20	2.063/30	pH held const., still cloudy
7*	MES	0.260+0.175/33		0	1.660/15	Orange prod., pH 4.12-4.3
8*	MES	0.998/40	0.113/10	0	1.182/20	Dark cola prod., pH 4.5
9	NaAc	0.488/30	0.120/15	0	1.197/40	pH 5, muddy brown
10	NaAc	1.010/11	0.124/6	0.067/5	1.334/21	pH 5, dark residue

The trials run with the PBS buffer all produced a brown, rubbery residue and the final pH was significantly greater than the optimal reaction pH. Sodium acetate buffer (NaAc) resulted in a similarly unrecoverable mess of a product. All trials run with MES buffer remained closer to optimal reaction pH, with the final pH for the 7th batch around 4.3 and for the 8th batch at 4.5 (the prior runs with PBS buffer, to the extent that pH could be reliably measured with a large precipitated product, had solution pHs of 6.0 or greater). Trials run without sulfo-NHS generated a recoverable product (marked with an asterisk in Table 6-2, batches 7 and 8). This product was dialyzed for one week with a minimum of 8 rinses, stepping the buffer concentration down from full

strength to 1:100 strength, before the product was frozen and isolated via the lyophilizer. ^{1}H NMR was then used to characterize the reaction products after dialysis, an example spectra for the 8th batch shown in Figure 6-5.

The key peaks for quantifying the extent of reaction were associated with the aromatic group, which appear downfield between 6.0 and 7.0 ppm, and the amine group on the polyelectrolyte backbone, which appear around 2.5 to 3.0 ppm. Given the ratio of these two integrated peak areas and accounting for the fact that each catechol group has a benzene group with 6 carbons, the estimated degree of modification for the 8th batch of PAHC was approximately 4%.
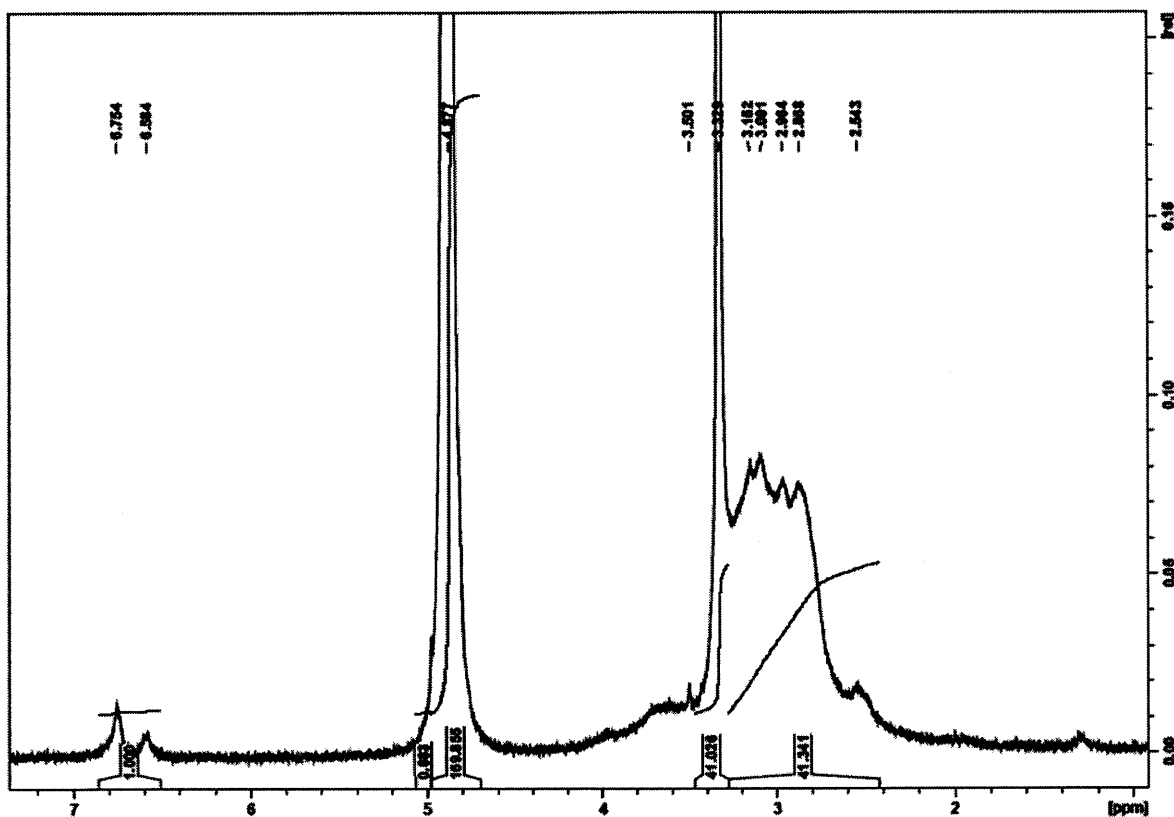
Figure 6-5: NMR spectra for PAHC with Me-d solvent.

The zeta potential measurement for the PAH solution was 50.83±5.72 mV, while for the PAHC solution was 31.58±2.80 mV at the same concentration, indicating some of the amine functional groups had been replaced.

6.2.2 – Clay Composite Films with Catechol-Modified Polyelectrolytes

Some clay composite films could be assembled using the catechol-modified polyelectrolytes left by Younjin Min in the Hammond Lab. The catechol-modified polyelectrolyte film components were at pH 5.0 with rinsing steps at neutral pH (7.0) to start the cross-linking process in two film architectures: (BPEIC/LAP) and (BPEIC/PAAC/LAP). The LAP clay dispersion was at pH 10.0 as

with the prior assembly protocols. Given the limited amount of material, dip-LbL was employed to conserve material.

The first bilayer architecture corresponds most closely to the clay composite bilayer films developed in chapter III, but with the ability to crosslink between catechol groups, is also a bilayer analog to the thermally cross-linked composite tetralayer films. The second trilayer architecture, consisting of both a catechol-modified polycation and polyanion, was an experimental architecture to see if it was possible to build up a film through alternating ionic interactions between the polyelectrolyte chains and $\pi - \pi$ stacking interactions with the LAP clay platelets. The growth curves for these films are shown in Figure 6-6.
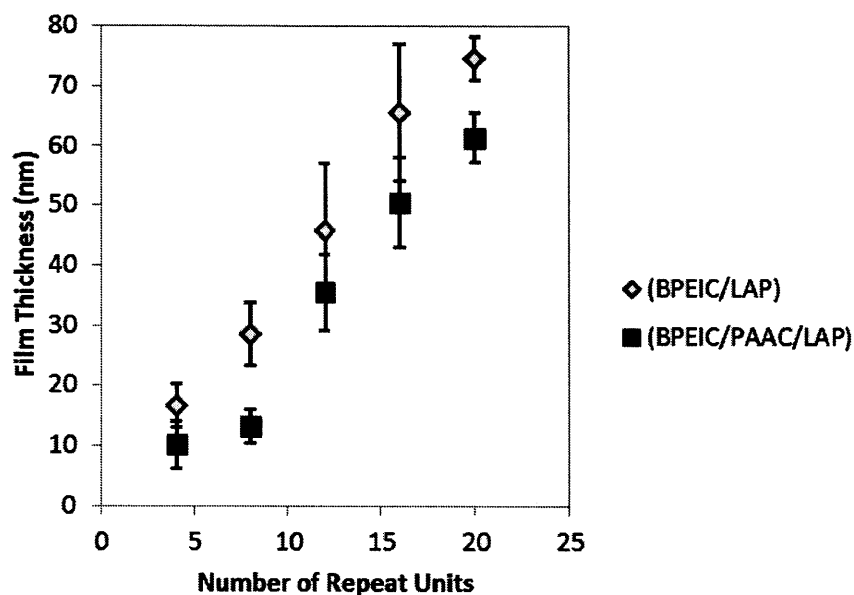
Figure 6-6: Growth curves for dipped catechol-clay composite films: a) (BPEIC/LAP) (white), and b) (BPEIC/PAAC/LAP) films (black).

Both films could be assembled with minimal difficulty. The (BPEIC/LAP) films were thicker than the trilayer (BPEIC/PAAC/LAP) films. Although this appears unusual at first glance, given the total number of layer depositions for the bilayer film at 20 repetitions is 40 layers and 60 for the trilayer film, the negative surface charge was likely not a strong driving force for the adsorption of negatively charged clays. Thus, the films likely contained a greater quantity of the two polymeric film components as opposed to the clay bilayer film, which contained a thickly adsorbed layer of clay platelets in each deposition. The average surface roughness measured via profilometry was on the order of 2 nm for the (BPEIC/LAP) films, significantly smoother than anything deposited via spray-LbL in this report. For the trilayer films, more surface roughness was observed, up to 7.2 nm for the 20 trilayer depositions and 2.5 nm for the 4 trilayer deposition. Although comparable to the

films deposited via spray-LbL, this increased surface roughness is indicative of the clay platelets not depositing in a uniform and smooth layer.

Films were also sprayed with two architectures: the (BPEIC/LAP) architecture and a (PAHC/LAP) with the PAHC produced by the process described in section 6.2.1 (Figure 6-7).
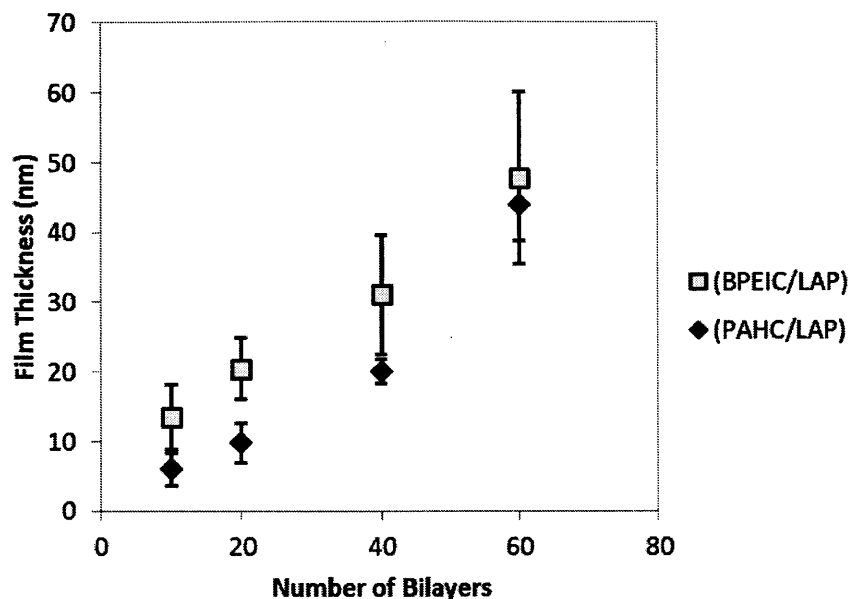
Figure 6-7: Growth curves for sprayed catechol-clay composite films: a) (BPEIC/LAP) (white), and b) (PAHC/LAP) films (black).

The films assembled via spray-LbL exhibited surface roughness on the order expected for the LAP clay-containing bilayer films, and were fairly unremarkable in this respect. The growth rate for these two films was approximately linear, with the (BPEIC/LAP) films growing at 0.81 nm/bl and (PAHC/LAP) films growing at 0.65 nm/bl. There are steric factors that cause BPEIC to form thicker monolayers per deposition than PAHC: 1) polymer chain branching, and 2) the degree of substitution on the polyelectrolyte backbone. First, the branched polymer chains on the BPEIC polyelectrolyte have fewer degrees of freedom than the long chain of the PAHC polyelectrolyte, which inhibits the ability of the BPEIC to layer across the surface smoothly. Second, the greater degree of substitution on the BPEIC modified polyelectrolyte (approximately 20%[388]) is significantly greater than the degree of substitution on the PAHC modified polyelectrolyte (approximately 4%), which increases the molecular weight of the polyelectrolyte and introduces additional steric restrictions.

6.3 – Conclusions

No significant quantity of films were able to be constructed with the catechol-modified PAHC, so ultimately no conclusion can be drawn about the efficacy of this approach for the

purposes of assembling clay composite selective layers, at least from the perspective of salt selectivity and water permeability.

However, a few conclusions can be drawn on how these polyelectrolytes are prepared and possible pitfalls that need to be addressed to spray these materials into films. First and foremost, the appropriate selection of buffer solution can significantly reduce the processing difficulty in producing the intended reaction product and limit the rate of deleterious side reactions. Given the array of buffer solutions attempted, the only useable product was recovered when MES buffer and no sulfo-NHS was used.

The films that were assembled via both dip-LbL and spray-LbL demonstrate that catechol-modified polyelectrolytes can be assembled into LbL films with LAP clay platelets, and in the case of dip-LbL films are uniquely smooth for polymer-clay composites. Although this is not a requirement for this particular application, it is a fairly interesting phenomenon that may have applications elsewhere. Additionally, the ability to spray catechol-modified polyelectrolytes that can be hardened with a subsequent exposure to water at neutral-to-basic pH is a key result from this body of work.

6.4 – Materials and Methods

6.4.1 – Materials

PAH (MW: 60 kDa) and PAA (MW: 20 kDa) were obtained from Polysciences, Inc. EDC (MW: 191.7 Da) was obtained from Thermo-Scientific, Inc., CAS #25952-53-8. DHHCA (MW: 182.17 Da) was obtained from Sigma-Aldrich, CAS #1078-61-1. Dopamine (MW: 153.18 Da) was obtained from Sigma-Aldrich, CAS #62-31-7. Sulfo-NHS (MW: 217.13 Da) was obtained from Thermo-Scientific, Inc., CAS #106627-54-7.

Solutions were prepared at specified concentrations in Table 6-2 and were adjusted to the reaction pH by using a Φ340 pH/Temp Meter and concentrated HCl or NaOH solution as appropriate.

6.4.2 – Reaction Protocol

Solutions were prepared at least one day in advance to fully disperse and solubilize the reactants. First, the EDC was added to the carboxylic acid to form the first intermediate product, and then optionally sulfo-NHS if that was included in that particular batch, and finally the amine-containing reactant to form the product. Stirring was continuous throughout the reaction and for a minimum of three hours afterwards, followed by a sequential dialysis in a 2 L beaker for a minimum of 3 days to remove unreacted chemicals and byproducts. The buffer solution was initially used at full strength, with a 10:1 after three dialysis batches on the first day, and 100:1 for the final dialysis step. The product was then rescued, frozen overnight in a Falcon tube, and finally lyophilized for two days to remove the excess water.

6.4.3 – Layer-by-Layer Assembly

Films were constructed using a custom-built spraying apparatus. Solutions and clay dispersions were aerosolized with N_2 gas at 20 psi and are sprayed onto the substrate rotated at 10 rpm. The basic program for each layer involved spraying the film component for 3 seconds, pausing for a 5 second drain period, rinsing for 10 seconds with pH-adjusted water, and then and then a final 5 second drain period. The sequence is repeated for each film component listed to assemble a bilayer or tetralayer.

Dipped films were assembled with a modified slide stainer in the ISN. Substrates were dipped for 5 minutes in each polyelectrolyte bath, with two intervening 1 minute rinse steps and shaking steps between each polyelectrolyte dip. 1.0 mg/mL polyelectrolyte bath concentrations, with an approximate volume of 20 mL, were used for the assembly of all films in this chapter of the report.

6.4.4 – Characterization

A Bruker Avance-400 ^{1}H NMR Spectrometer with a Magnex superconducting magnet was used to take the NMR spectra. A Dektak 150 profilometer was used to determine the film thickness. Profilometry samples were deposited on glass slides plasma-cleaned using the above equipment for 5 minutes; otherwise, the standard protocol above was used. AFM imaging was conducted with a Vecco Dimension 3100 AFM with Nanoscope Controller and 1929G scanner head, with the typical scan size at 10x10 μm^2, scan rate of 0.4 Hz and 512 samples/line yielding a maximum tip velocity of 8 $\mu m/s$. The AFM tips used were Vecco Si tips on nitride levers with f_o = 50-90 kHz and k=0.4 N/m.

VII. Conclusions

7.1 – Summary of Thesis

In chapter I, the state of global water resources and methods to desalt saline water sources, including oceanic water, brackish water, and wastewater, were discussed. This is a major motivating factor to design and construct high-efficiency and high-throughput RO membranes to address this challenge in the 21st century. Although there are incredibly effective TFC membranes on the market today, there are improvements in throughput and antifouling properties that could be made to further reduce maintenance costs, as well as the opportunity to develop similar membranes in a cheaper fashion to reduce the capital costs. One method that can be used to assemble selective layers similar to those formed via interfacial polymerization in TFC membranes is LbL assembly, and in particular spray-LbL assembly which is capable of rapidly depositing large, asymmetric membranes. A wide array of research being conducted on dip-LbL assembled composite thin films to serve as selective layers in RO membranes, but this body of prior research does not take advantage of the unique properties of LbL assembly and particularly spray-LbL assembly that enables the generation of structured nanocomposites that could potentially improve selectivity and throughput. These nanostructured membranes have been very successful in an array of other applications, including gas separation membranes and barrier layers, but have not been fully explored for RO selective layers. This thesis work aims to bridge this gap by taking a nanostructured materials approach to the design of a next generation selective layer for RO membranes. The design focus was on maximizing water permeability and salt rejection through introducing nanostructured materials, particularly clay platelets, into LbL-assembled film architectures. It was hypothesized the incorporation of these clay platelets would introduce highly tortuous diffusive pathways through the selective layer and nano-channels that could reject solvated ions via size exclusion; the impact of these two modifications was hypothesized to be a net increase in salt selectivity. Finally, three specific aims were enumerated which outline the work performed and reported on in the subsequent chapters.

In chapter II, spray-LbL assembled films were assembled on several candidate substrates to determine the optimal support layer for the clay composite selective layers. Clay composite films (further explored in chapters III and IV) were deposited on nylon-6 and PSU electrospun mats and PES UF membranes, which were then examined for defect formation. Qualitatively, the most uniform films with the lowest surface roughness were those deposited on PES membranes with 30 nm pores, which closely matched the characteristic length of the LAP clay platelets. Additionally, clay composite films assembled on PES-30 UF membranes were observed to crack less under RO conditions, leading to PES-30 UF membranes being the preferred substrate for the clay composite selective layers further explored in this report. Brief experiments were conducted on a filled clay-composite espun membrane that could potentially serve as a fortified free-standing selective layer. Although the generated films were interesting from a spray-LbL perspective, this process did not

yield an effective membrane because the membrane thickness was too great to allow for an appreciable flux.

In chapter III, clay composite bilayers comprised of the strong polycation PDAC and LAP clay platelets were investigated. First, conditions for dispersing the LAP clay platelets in aqueous suspension for spray-LbL deposition were explored. Then, these selective layers deposited on PES-30 UF membranes were examined and characterized. The sprayed clay composite thin films, for a variety of spraying conditions, were found to grow linearly with respect to the number of bilayers deposited, largely fitting in to what is known about the dynamics of spray-LbL deposition. Via manipulating the spray time of the PDAC and LAP film components, TGA composition analysis revealed the clay content of the films could be controlled between 53% and 86% by weight, with the balance polyelectrolyte. This is a significantly greater degree of clay incorporation into the selective layer than has been observed with other methods used to assemble clay composite films. Cross-sectional imaging of the films via SEM revealed fracture patterns that were indicative of the clay platelets layering across the surface of the film, building up a nano-scale brick-and-mortar-like structure. From the perspective of permeation properties, there was an inverse correlation between salt rejection and clay content: the most efficacious salt-selective films had the lowest clay content and vice-versa. This is hypothesized to be the result of films with higher inorganic clay content being more brittle and exhibited a greater degree of defect formation during RO operation.

In chapter IV, the methods and ideas to address the brittle mechanical properties of the clay composite film architecture were detailed. First, a cross-linkable polyelectrolyte film architecture containing PAH and PAA was introduced to form a clay composite tetralayer film: tetra-LAP. The films were observed to grow largely linearly with respect to the number of tetralayers deposited, which was a similar behavior that was observed for the clay composite bilayer films presented in the prior chapter. The degree of cross-linking was estimated on the basis of the amide II peak, corresponding to the bending of the N-H bond, and then impact of this cross-linking on the mechanical properties and swelling of the films was explored. The hardness of the cross-linked tetra-LAP composite films was 30-40% greater than the untreated tetra-LAP composite films. Swelling in the cross-linked tetra-LAP composite films was constrained to 10-15% for both the pH 5.0 and pH 6.0 films, but in the untreated films swelling on the order of 62% for clay composite bilayers and in excess of 100% for the pH 5.0 films was observed. These two observations are strong confirming evidence the cross-linking is occurring at 175°C, which is somewhat below the optimal cross-linking temperature between 200°C and 250°C. The tetra-LAP composite films had 38% to 56% clay content based on the assembly pH, a lower range than what was examined in chapter III and thus interesting for two reasons: 1) the fraction of clay is still greater than what has been reported on for other clay composite assembly techniques, and 2) the variable space of clay content against permeation properties is more fully explored. Interestingly, the calculated water permeability of these films was similar (on the same order of magnitude) as the clay composite bilayer films examined in chapter III, but exhibited significantly greater salt selectivity. The salt rejection figures ranged from a minimum at 46% for the pH 6.0 film architecture to a maximum at

89% for the pH 5.0 film architecture. From the data collected on salt rejection and the clay content of the films assembled in chapters III and IV, it was observed that lower clay content was correlated with higher salt rejection while the water permeability did not correlate at all. These relationships are further examined in section 7.2.

In chapter V, work is detailed that utilizes an alternative silicate clay platelet with a significantly greater aspect ratio than LAP clay, MMT. It was hypothesized that increasing the aspect ratio of the clay platelet, with a similar degree of clay incorporation, would increase the tortuosity of the diffusive pathways through the film and thus increase salt selectivity. MMT clay was investigated in three different film architectures: clay composite bilayers, mixed bilayers containing a joint deposition of SPS and MMT, and tetralayers. In all three cases, it was not possible to assemble similar MMT clay composite thin films via spray-LbL, but some pointers were identified to guide future researchers as to where effective work could be done to improve the deposition process with higher aspect ratio nanomaterials. Additionally, a collaboration to incorporate GO platelets, which have different chemistry and surface charge characteristics but similar platelet size to MMT clay, via spray-LbL deposition was attempted with only marginally more success. Different film assembly conditions including lower assembly pH values were required to incorporate graphene layers into films. However, due to the low mechanical toughness of the GO films as well as the irregular coverage of the substrates, no effective selective layers could be generated with this material.

In chapter VI, the focus is shifted to alternative cross-linking schemes with the potential to be more efficient than the thermal cross-linking process utilized in chapters III, IV, and V. The primary route examined was the catechol modification of polyelectrolytes. These catechol functional groups can interact via covalent linkages, hydrogen bonds, and π-π stacking interactions on the basis of pH shifts, which would enable the deposition of a tightly cross-linked polymeric matrix with significantly faster processing time than is possible via thermal cross-linking. However, the functionalization was difficult to replicate with the procedures found in literature; different buffer solutions were experimented with to find an experimental method that produced catechol-modified polyelectrolytes. It was determined that MES buffer, which contains a sulfonic acid functional group, was a better buffer selection than buffers containing carboxylic acid such as citric and acetic acid or PBS buffer for two reasons: 1) it buffers naturally near the optimal reaction pH, and 2) it does not undergo side reactions with the buffer solution. Primarily, two catechol-modified polycations, PAHC and BPEIC, were used to assemble films via both dipping and spraying, and the physical properties of these films were evaluated.

From this thesis work, one first-author paper was published on a selection of content from chapters I, III, and IV: Jason R. Kovacs, Chaoyang Liu, Paula T. Hammond. "Spray Layer-by-Layer Assembled Clay Composite Thin Films as Selective Layers in Reverse Osmosis Membranes" *ACS Applied Materials & Interfaces* (2015), submitted and just accepted as this document goes to print.

7.2 – Comparative Analysis on Clay Composite Films

In chapters III and IV, several clay composite selective layers of differing LAP clay contents were assembled. The incorporation of clay was found to have a direct impact on the permeability properties of the films, as well as the mechanical toughness of the films. These correlations are enumerated upon below.

7.2.1 – Salt Rejection as a Function of Clay Content in Composite Films

In chapter III, it was observed that (PDAC/LAP) selective layers exhibited salt rejection between 10% and 28% and this correlated inversely with the clay content of the films. The range of clay contents examined ranged from 53% to 86%. In chapter IV, films with clay contents ranging from 38% to 56% were examined, increasing the examined range from 38% to 86% by weight clay. It is notable that the overall clay content of the film does not directly correlate to its performance in the salt rejection trials. The best performing film, the (Tetra-LAP) pH 5.0 film architecture, had an average clay content of 38% and a salt rejection of 89%. Extremely high clay content films assembled via the (PDAC/LAP) method perform similarly with regards to water permeation, but were more brittle due to the high clay content, and thus more susceptible to critical defect formation during RO, with a 83% clay membrane only rejecting 10% of salt ions. A plot of the observed salt rejection against the clay content of the films is shown in Figure 7-1.
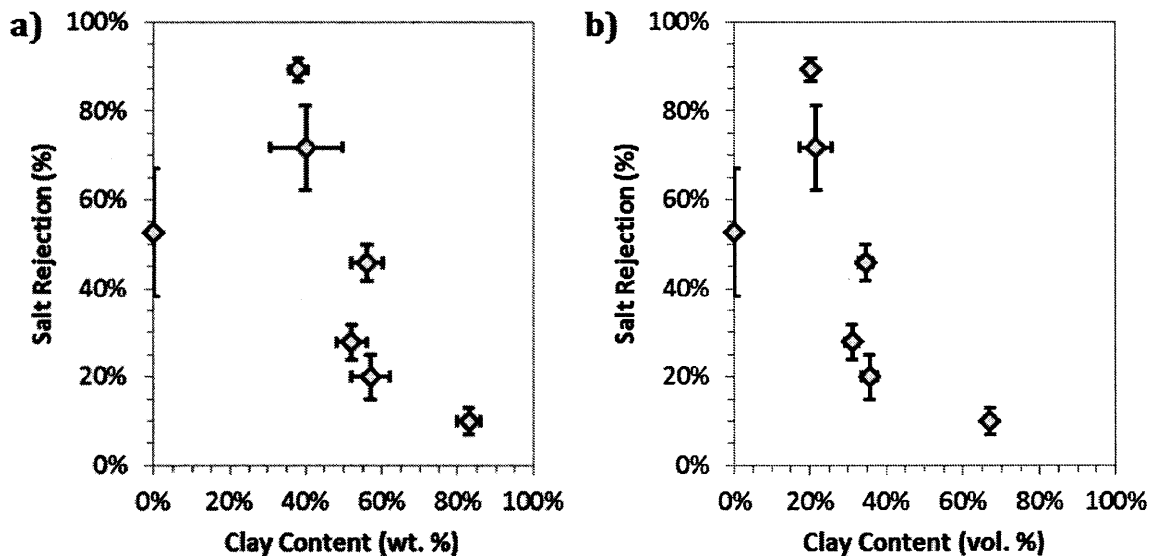
Figure 7-1: Plot of clay content of various clay composite film architectures vs. observed salt rejection: a) clay content by weight percent, and b) clay content by volume percent.

There appears to be a roughly linear trend between clay content and observed salt rejection with the exclusion of the 0% data point, with $R^2 = 0.7229$ (Figure 7-1a) or $R^2 = 0.6219$ (Figure 7-1b). It is noteworthy both that decreasing clay content resulted in increased salt rejection, and also that reported polyelectrolyte selective layers as well as those generated for this report exhibited

maximum salt rejection around 50-60%. It was hypothesized that increasing clay content would increase salt selectivity, but it appears this is counter-balanced by brittle films forming critical defects in operation that reduce the overall salt rejection. Additionally, we have a starting point for LbL films without incorporated nanomaterials that is significantly below the observed maximum of 89% in the clay composite studies presented in chapters III and IV. Thus, there must be a global maximum somewhere along this line, and it is likely to be near the 38% clay data point, given the 89% salt rejection observed there, corresponding to the (Tetra-LAP) pH 5.0 data point. The regression equation reaches a value of unity at 20.1% by weight clay content, although this extrapolation is suspect as the trend reverses towards 53% salt rejection with the (PAH/PAA) polymer bilayer films.

7.2.2 – Water Permeability as a Function of Clay Content in Composite Films

Similarly, the water permeability for several LAP-clay containing bilayer and tetralayer film architectures was plotted against the clay content (Figure 7-2).

a) Water Permeability (m² / Pa s) vs. Clay Content (wt. %)

b) Water Permeability (m² / Pa s) vs. Clay Content (vol. %)
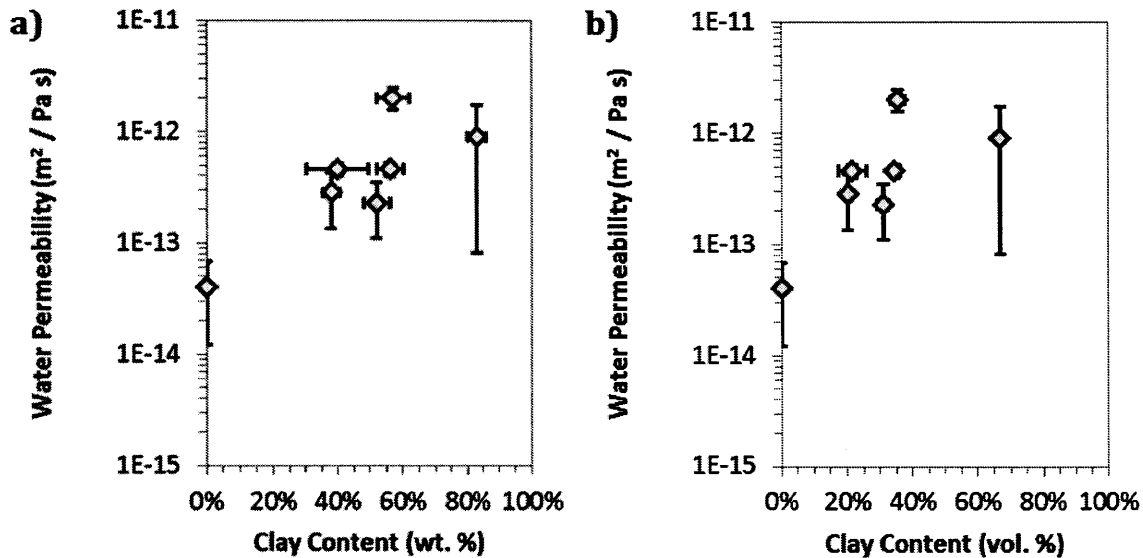
Figure 7-2: Plot of clay content of various clay composite film architectures vs. calculated water permeability: a) clay content by weight percent, and b) clay content by volume percent.

There was not a strong correlation observed in the water permeability as a function of the clay content for the clay containing thin films; the R^2 value for the linear regressions being 0.2655 (by weight, Figure 7-2a) and 0.2295 (by volume, Figure 7-2b). Although to the naked eye there appears to be a linear trend line, this is a function of the outlier 0% clay and 86% clay data points, one of which has a significant error margin attached. Upon eliminating those two data points, the correlation holds below 0.3 at 0.2771 and 0.2931 for the by weight and by volume correlations, respectively.

7.2.3 – Tortuosity Calculation and Correlation in Composite Film Architectures

As noted in section 1.6.3, there are multiple correlations that can be used to evaluate the tortuosity of the diffusive path length in a film that is comprised of a permeable matrix filled with impermeable platelets, which is largely a function of the volume fraction of clay, ϕ, and the aspect ratio, α, of the clay platelets in the film. The Cussler correlation[170] is most appropriate for the density of clay in the composite thin films in this report (under semi-dilute conditions $\phi < 1$ and $\alpha\phi > 1$). As noted in the section, the Cussler correlation takes the form:

$$\tau_{Cussler} = 1 + \mu\left(\frac{\alpha^2\phi^2}{1-\phi}\right)$$

...where μ is the geometric ratio for the particles in question, and is approximately 0.5 for clay platelets[171]. The density of the LAP clay platelets was taken as 2.53 g/cm^3, and the average polymer matrix density was estimated to be 1.05 g/cm^3 although perturbations of 5% on that value do not significantly affect the conclusions. Using this information, the salt rejection and water permeability can be plotted against tortuosity (Figure 7-3).
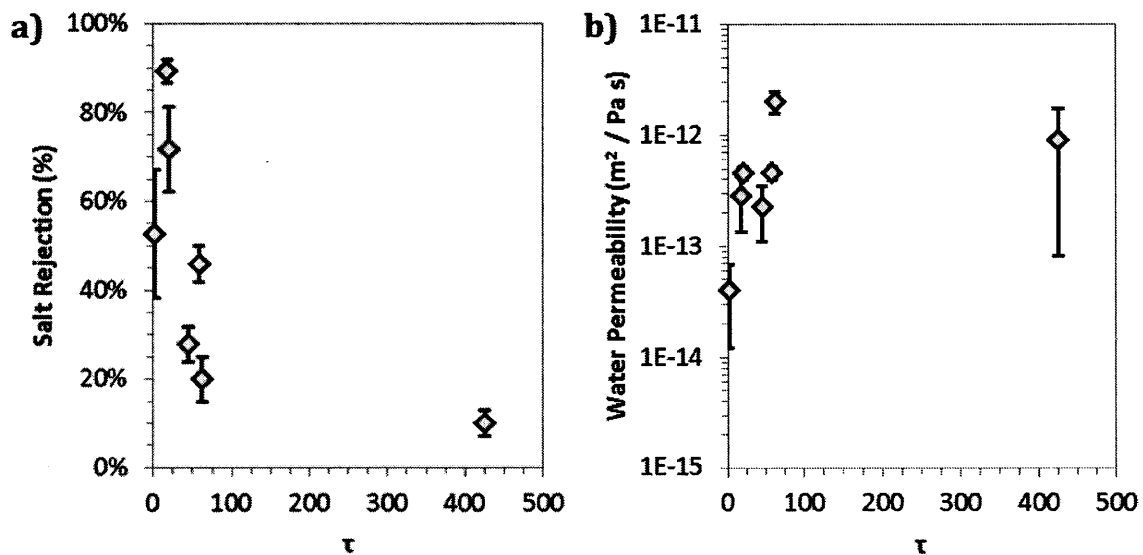
Figure 7-3: Plot of tortuosity calculated via the Cussler correlation of various clay composite film architectures vs. permeation properties: a) vs. observed salt rejection, and b) vs. calculated water permeability.

The shift from volume fraction of clay to tortuosity stretches the abscissa since the upper limit as ϕ approaches unity the tortuosity approaches ∞. Given the cluster of samples with tortuosity values ranging from 15 to 70 and the large impact of the 86% by weight clay sample, corresponding to $\tau \approx 424$ (Table 7-1), drawing too many conclusions from the correlation is not desirable. However, an exponential regression on τ v. R (Figure 7-3a) yields $R^2 = 0.6502$ and a power regression on τ v. p_w yields $R^2 = 0.6851$, much stronger correlations than what was observed

for the raw clay content plotted against the water permeability and comparable to the strength of the regression equations for salt rejection.

Table 7-1: Tortuosity calculated with the Cussler method from the clay content data.

Film	Clay (wt. %)	Clay (vol. %)	τ (Cussler)
(PDAC/LAP) 3s:3s	0.52 ± 0.04	0.31 ± 0.02	44.58
(PDAC/LAP) 3s:6s	0.57 ± 0.05	0.35 ± 0.02	62.01
(PDAC/LAP) 3s:9s	0.83 ± 0.03	0.67 ± 0.01	424.97
(PAH/PAA), pH 5.0	0	0	1
(Tetra-LAP), pH 6.0	0.56 ± 0.04	0.35 ± 0.02	58.05
(Tetra-LAP), pH 5.5	0.4 ± 0.10	0.22 ± 0.04	19.74
(Tetra-LAP), pH 5.0	0.38 ± 0.03	0.20 ± 0.01	17.12

7.2.4 – Hardness as a Function of Clay Content and Crosslinking in Composite Films

Finally, the hardness was plotted against the clay content (by weight) of the films to see if there was any conclusion that could be drawn (Figure 7-4).
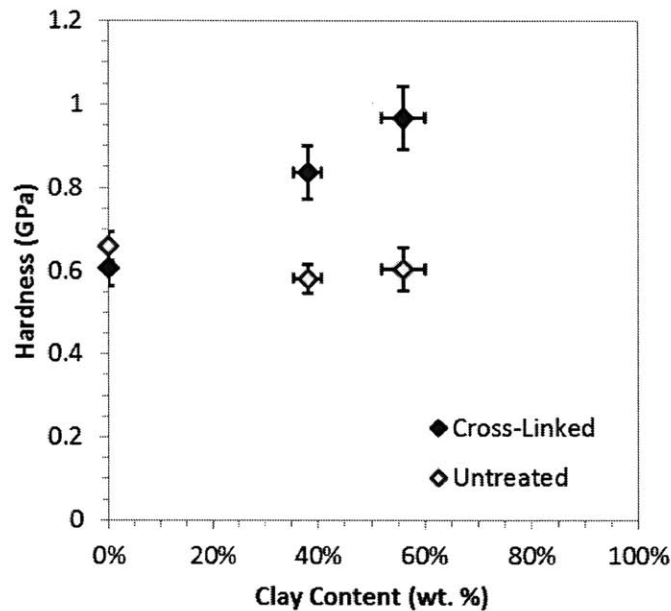
Figure 7-4: Plot of clay content of various clay composite film architectures, untreated (light) and cross-linked (dark) vs. dry film hardness measured via nanoindentation.

Although to the naked eye there appears to be a linear correlation for the hardness of both the untreated and cross-linked films, caution is advisable due to the small number of data points. The R^2 for the linear regression through the untreated films is 0.6777, and for the cross-linked films

is 0.9977. The hardness of the untreated films appears largely constant at 0.6 GPa regardless of clay content, which is somewhat unexpected as the incorporation of clay platelets was thought to increase this property. However, the trend of increasing hardness with respect to clay content was observed for the cross-linked films.

7.3 – Conclusions

Spray-assembled clay composite films are a promising area of investigation for the development of RO membrane selective layers. With the appropriate assembly conditions and material selection, it was possible to achieve approximately 89% salt rejection with significantly greater water flux than is possible with TFC RO membranes currently used on the market. The high flux nature of the clay composite membrane makes it a perfect fit for FO and RO-type applications, as well as a candidate to investigate further for brackish water RO. The target of 93% salt rejection for a single pass purification scheme, necessary for SWRO applications, was not achieved. However, it is likely that future optimization on the selective layer could achieve this figure?

It is also important to note the clay content of these films assembled via spray-LbL was over a range of 38% to 86%, a truly massive range that yielded significantly different material properties and is difficult to assemble via any technique besides spray-LbL. While there are significant drawbacks associated with LbL assembly including the amount of waste generated (with research ongoing into recycling systems for spray-LbL), the processing time (although spray-LbL significantly reduces this), particularly the thermal cross-linking time (a chemical method could be more efficacious here), these films have very unique properties such as a fully exfoliated and intercalated clay platelet structure within a polymer matrix. At the moment, if these types of films are to be investigated and applied not just for RO selective layers but for several applications, LbL assembly is an incredibly useful tool to build them. With sufficient work on recycling the large amount of waste generated by spray-LbL, it can be much more economically viable than it already may be due to the elimination of organic solvents.

The major conclusion drawn from the work in chapters III and IV is the necessity of utilizing cross-linking film architectures to control the swelling and mechanical properties of the selective layer. Untreated LbL films, even those with strongly charged functional groups, are not robust enough to be useful under RO conditions. This is confirmed not only by the author's experience with the work presented in chapter III, but additionally by the literature discussed in section 1.8.3.

On the alternative materials presented in chapters V and VI, the only material system the author would exclude from future consideration would be the GO platelet architectures. The relatively lower charge density of the GO platelets, concentrated along the outside edge of the platelet, make them difficult to incorporate into LbL architectures that would be appropriate for RO selective layers. MMT clay, along with other higher aspect ratio, charged nanomaterials, are a good area of potential development (discussed in 7.4 below).

Taken as a whole, these findings represent an opportunity for further development of LbL-assembled clay composite formulations that can be adapted to water filtration applications.

Furthermore, high-flux clay composite membranes provide a high throughput alternative for wastewater and brackish water treatment and potentially for forward osmosis applications.

7.4 – Recommendations for Future Investigation

Should investigators continue working on clay composite selective layers, there are interesting areas where this work may be built upon. In this section are potential improvements, projects, and areas of interest for future work on selective layers for RO membranes, particularly those assembled via spray-LbL and with incorporated nanostructures such as clay platelets.

7.4.1 – Clay Composite Selective Layers

Further optimization with the LAP clay could be conducted. The author believes reducing overall film thickness and incorporating chemical cross-linking film architectures with LAP clay will generate a more efficient salt-selective layer. With the actual material systems employed in this report, investigating whether the fouling properties are significantly affected is another question that should be pursued, given how important this question is for the industrial application of RO. There is a significant body of literature that indicates clay composites are more resistant to biofouling for medical applications, but very little to indicate whether the same can be expected with algae, cyanobacteria, and other common foulants in RO applications. The possibility of even using an ordinary TFC membrane with a clay capping layer to reduce fouling is another potential area of investigation.

Although at face value the application of MMT clay to generate even more tortuous diffusive pathways appears a promising area, the actual impact may be significantly lower than expected. If the newly introduced salt rejection method is size exclusion, it matters relatively little how tortuous the diffusive pathway is so long as the nano-channels can be consistently manufactured to the targeted specification. Instead, this may have a detrimental impact on the overall water permeability and thus be less attractive than the LAP-containing film architectures explored in this report on the basis of water production rate. This could perhaps be counterbalanced by utilizing thinner films, but there is no reason to not explore the same with the LAP-clay containing architectures explored above.

More fully characterizing the mechanical properties of the films, especially under RO conditions including high salinity, higher applied pressures, and cross-flow RO testing, would likely yield insights into whether such a system could be scaled up industrially.

7.4.2 – Catechol-Modified Polyelectrolyte Selective Layers

Fundamentally, the idea behind replacing the time- and temperature-intensive cross-linking process with a chemical-driven cross-linking process is sound. However, there are a few concerns and design challenges that would have to be overcome. First, the uniformity of the catechol-modified polyelectrolytes was a consistent source of concern in this report, and switching to an alternative cross-linking scheme involving more uniform materials may be a better route of

investigation for a materials science/chemical engineering-focused project. There are a number of possible alternatives, such as combining the clay composite film architectures explored in this report with the glutaraldehyde cross-linked material systems discussed in the recent work published by Kentish et al. This would allow the assembly of thin clay composites with an effective cross-linker and take full advantage of the LbL assembly process that lets us incorporate nanomaterials into the thin film in a way that cannot be done via interfacial polymerization. The route explored in this paper is particularly promising, as they were able to introduce chlorine resistance to a relatively thin film (10-20 bilayer depositions) and maintain very effective barrier properties. A film architecture consisting of 10 or so clay composite base bilayers with a few capping layers of the polymer bilayer containing SPS, all thoroughly cross-linked, would likely generate a mechanically strong and salt selective thin film that would obsolete the core work done in chapters III and IV of this report.

7.4.3 – Thoughts on Future Research in Selective Layers for RO Membranes

The author believes it would be most interesting to develop a lower-waste highly efficient technique to deposit high clay content composite films without spray-LbL. One of the key challenges to scaling up this technology to the industrial scale, as mentioned in 7.3, is the vast amount of waste generated via the spray-LbL deposition process. There is interesting work being done in startups and research at the bench scale to address the waste issue with spray-LbL, but an investigation of other film deposition techniques may be equally viable.

Particularly, a method to build a film through a sequential interfacial polymerization with clay platelets would be interesting, where the sequence involves alternating the deposition of clay layers between the interfacial polymerization steps. This would have the effect of generating a nanostructured film similar to what can be accomplished via spray-LbL and possibly with the same fractional weight of clay, but also yield significant advantages in terms of material used and overall mechanical strength.

Appendix 1: Mathematical Method for Permeability Calculation

A1.1 – Water Permeability

As discussed in section 1.6, the Spiegler-Kedem model used for the water permeability data analysis in this report takes the form of:

$$J_w = P_w(\Delta p - \sigma \Delta \pi)$$

...where J_w is the observed water flux, P_w is the generalized water permeability coefficient for the membrane, Δp is the applied pressure gradient across the membrane, $\Delta \pi$ is the osmotic pressure gradient, and σ is the reflection coefficient, a fitted parameter that ensures the flux is zero when the applied pressure is equal to the osmotic pressure of the feed solution. Mathematically, this is calculated by the following equation:

$$\sigma = \left. \left(\frac{\Delta p}{\Delta \pi} \right) \right|_{J_w = 0}$$

Additionally, the pressure gradients can be approximated by neglecting horizontal diffusion and using axial coordinates:

$$\Delta p \approx \frac{dP}{dz}, \qquad \Delta \pi \approx \frac{d\pi}{dz}$$

...where the z-coordinate corresponds to the thickness of the selective layer.

This model can be used to evaluate a water permeability constant across a membrane given experimental data on the water flux (measured via collecting samples from a Sterlitech HP4750 dead-end permeation cell) and the thickness of the membrane (measured via the profilometry on the LbL-assembled selective layers given in Chapters III, IV, and V). Flux data was collected from at least 4 different operating pressures in 50 psig increments, from 50 psig to 200 psig, and preferably additional measurements up to 300 psig to obtain more data for the linear regression. Average water fluxes for applied pressures, $J_w(P_{app})$, were calculated via the formula:

$$J_w(P_{app}) = \frac{1}{n} \sum_n \frac{m_n(P_{app})}{At_n}$$

...where $m_n(P_{app})$ was the mass of permeate collected at the applied pressure P_{app}, t_n was the time over which the permeate was collected, and A was the membrane area of the permeation cell ($9.08 \cdot 10^{-4}$ m² based on the 3.4 cm diameter of the active area). This flux was plotted against the derivative of pressure with respect to membrane thickness. This was approximated by taking the pressure drop from the feed to permeate side of the membrane and dividing by the thickness of the selective layer obtained via profilometry:

$$\frac{dP}{dz} \approx \frac{P_{app} - P_{atm}}{\Delta z}$$

...where P_{app} is the applied pressure, P_{atm} is the atmospheric pressure, and Δz is the thickness of the selective layer.

For the water permeability measurement on deionized water, the osmotic pressure term is effectively zero and can be dropped from the equation. At this point, a linear regression is conducted on the flux data plotted against the derivative to generate an estimate for the water permeability, P_w:

$$J_w = P_w \frac{dP}{dz}.$$

A1.2 – Salt Rejection

Salt rejection was calculated from the ratio of the measured permeate concentration to the feed concentration of chloride ions. This corresponds to the observed salt rejection metric[144], as it does not account for the CP boundary layer on the feed side of the membrane:

$$R = 1 - \frac{C_p}{C_f}$$

...where R is the salt rejection (reported as percentage), C_p is the salt concentration of the permeate, and C_f is the feed concentration, often 10,000 ppm NaCl for the experiments in this report.

Appendix 2: Permeation Cells

A2.1 – Dead-End Permeation Cell

An HP4750 dead-end permeation cell was purchased from Sterlitech and used to generate the majority of the permeation data presented in this report. The permeation cell was connected to a N_2 tank via a regulator with a release valve to both terminate the experiments as well as serve as an emergency release system (Figure A2-1, A2-2). The cell was operated on a stir plate with a stir bar setup to insure the feed solution stayed well-mixed during operation. Flux data in the form of mass of permeate collected divided by the operation time was collected along with the conductivity data, measured via a conductivity meter and/or a chloride ion probe.
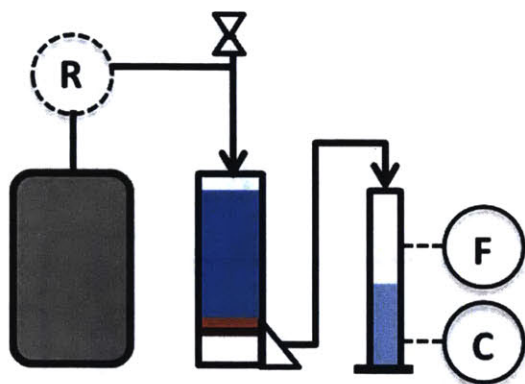
Figure A2-1: Schematic of dead-end permeation cell.
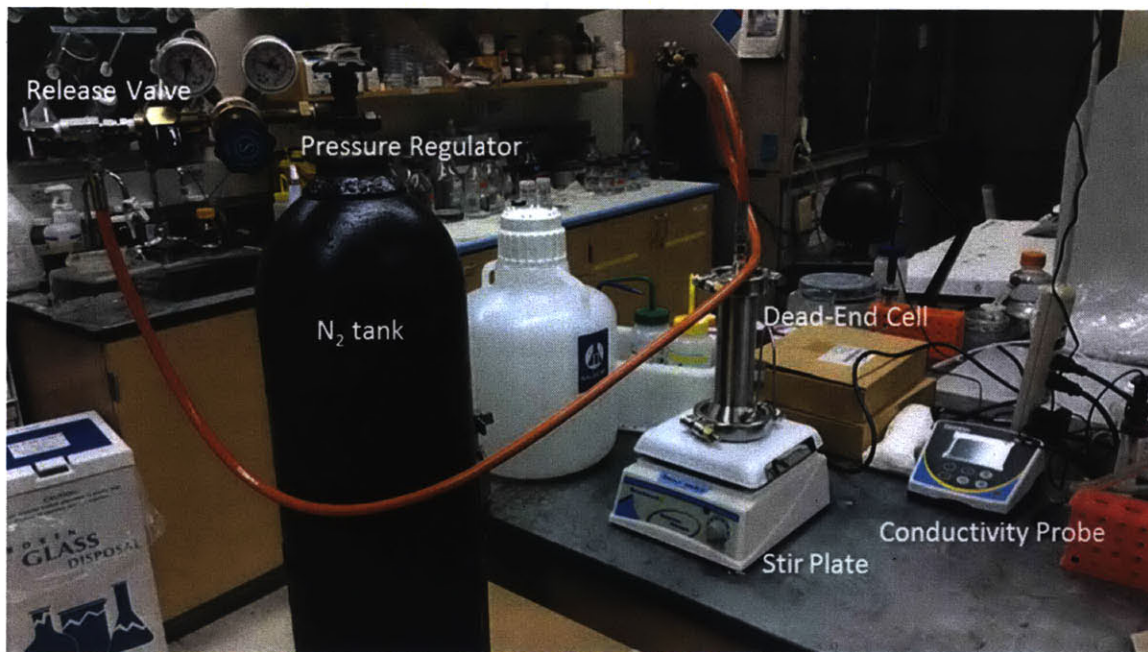
Figure A2-2: Image of completed dead-end permeation cell.

The maximum operable pressure for the system was 1,000 psig for the regulator and tubing assembly and 1,200 psig for the permeation cell, although no trials above 700 psig were conducted. The active membrane area is a 3.4 cm-diameter circle, yielding an area of $9.08 \cdot 10^{-4}$ m², and the total volume of the chamber is approximately 350 mL. For salt permeation trials, a maximum of 20 mL was drawn off, resulting in a maximum feed concentration change of approximately 5%. Best practices involved drawing off 5 mL of permeate and diluting to obtain a sample large enough for the conductivity probe, and then algebraically determining the permeate concentration.

A2.2 – Cross-Flow Permeation Cell

In conjunction with collaborators on the CCWCE project, a cross-flow RO permeation cell was designed and constructed. This device was designed to monitor water and salt permeation over a long term period (over the course of 1-4 days) with electronic measurement and record of key experimental values such as applied pressure, temperature, flow, and solution conductivity. A schematic of this equipment is shown in Figure A2-1 and a picture of the cart in Figure A2-2.
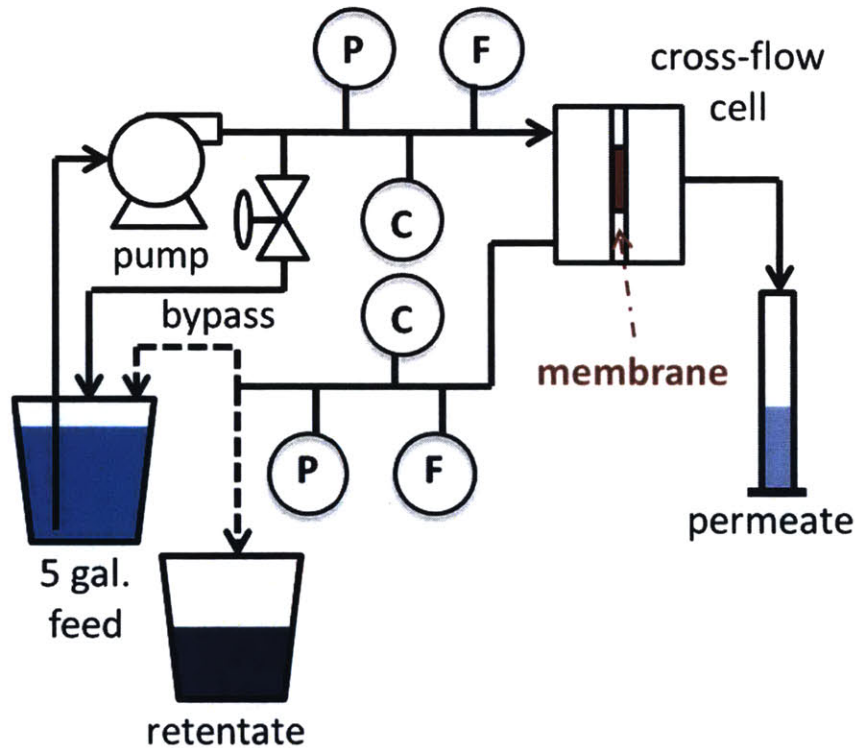
Figure A2-3: Schematic of cross-flow permeation cell.
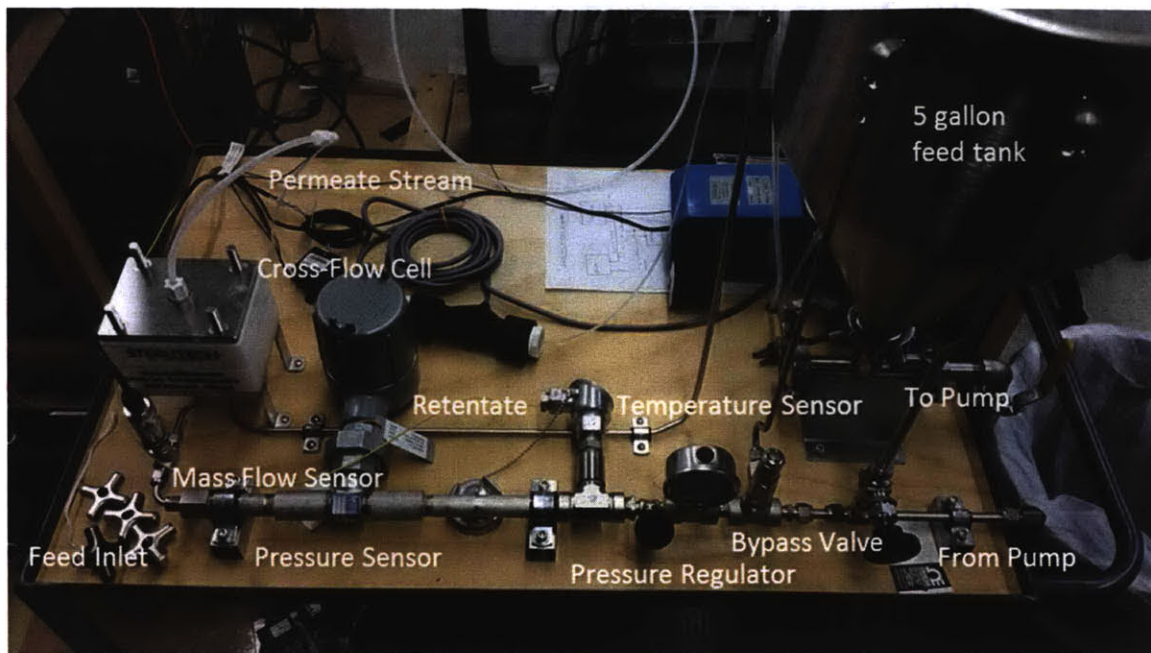
Figure A2-4: Image of completed cross-flow permeation cell.

The pump increased the temperature of the brine as it was cycled through the system, which has a significant impact on the rate of diffusion. Thus, the feed was run through a heat exchanger with a room temperature water bath to maintain the temperature at 25°C. A temperature sensor is also installed so that the temperature of the feed stream can be monitored along with the flux and conductivity data. The feed tank has a volume of approximately 5 gallons, although a fraction of that volume is taken up by the heat exchanger (a coiled pipe around the exterior) that interacts with the water bath. Preliminary testing has shown this cell can run continuously for 96 hours (4 days), although monitoring is required during the startup phase to ensure the pressure stays close to the set point.

The software employed for the real-time monitoring was DAQView, with the sensors assigned to the following channels:

0. Feed Line – Pressure Gauge
1. Feed Line – Thermocouple
2. Permeate – Flow Meter
4. Permeate – Conductivity Meter
5. Feed Line – Flow Meter

Referenced Works

1. *Meeting the Mdg Drinking Water and Sanitation Target : A Mid-Term Assessment of Progress*, ed. Unicef and O. World Health. 2004, Geneva, Switzerland : New York: World Health Organization ; United Nations Children's Fund.
2. Service, R.F., *Desalination Freshens Up.* Science, 2006. **313**(5790): p. 1088-1090.
3. Montgomery, M.A. and M. Elimelech, *Water and Sanitation in Developing Countries: Including Health in the Equation.* Environmental Science & Technology, 2007. **41**(1): p. 17-24.
4. Arnell, N.W., *Climate Change and Global Water Resources.* Global Environmental Change, 1999. **9, Supplement 1**(0): p. S31-S49.
5. Vorosmarty, C.J., P. Green, J. Salisbury, and R.B. Lammers, *Global Water Resources: Vulnerability from Climate Change and Population Growth.* Science, 2000. **289**(5477): p. 284-288.
6. Bates, B., Z.W. Kundzewicz, S. Wu, and J. Palutikof, *Climate Change and Water.* 2008: Intergovernmental Panel on Climate Change (IPCC).
7. Doney, S.C., V.J. Fabry, R.A. Feely, and J.A. Kleypas, *Ocean Acidification: The Other Co2 Problem.* Annual Review of Marine Science, 2009. **1**: p. 169-192.
8. Vorosmarty, C.J., P.B. McIntyre, M.O. Gessner, D. Dudgeon, A. Prusevich, P. Green, S. Glidden, S.E. Bunn, C.A. Sullivan, C.R. Liermann, and P.M. Davies, *Global Threats to Human Water Security and River Biodiversity.* Nature, 2010. **467**(7315): p. 555-561.
9. Turral, H., J.J. Burke, and J.-M. Faurès, *Climate Change, Water and Food Security.* 2011: Food and Agriculture Organization of the United Nations Rome.
10. Allouche, J., *The Sustainability and Resilience of Global Water and Food Systems: Political Analysis of the Interplay between Security, Resource Scarcity, Political Systems and Global Trade.* Food Policy, 2011. **36, Supplement 1**(0): p. S3-S8.
11. Loo, S.L., A.G. Fane, W.B. Krantz, and T.T. Lim, *Emergency Water Supply: A Review of Potential Technologies and Selection Criteria.* Water Research, 2012. **46**(10): p. 3125-3151.
12. Toole, M.J. and R.J. Waldman, *The Public Health Aspects of Complex Emergencies and Refugee Situations.* Annual Review of Public Health, 1997. **18**: p. 283-312.
13. Mosley, L.M., *Drought Impacts on the Water Quality of Freshwater Systems; Review and Integration.* Earth-Science Reviews, 2015. **140**(0): p. 203-214.
14. Hinkebein, T.E. and M.K. Price, *Progress with the Desalination and Water Purification Technologies Us Roadmap.* Desalination, 2005. **182**(1-3): p. 19-28.
15. Sayre, I.M., *International Standards for Drinking-Water.* Journal American Water Works Association, 1988. **80**(1): p. 53-60.
16. *Title 40 Protection of the Environment*, U.S.E.P. Agency, Editor. 2008, National Archives and Records Administration.
17. Greenlee, L.F., D.F. Lawler, B.D. Freeman, B. Marrot, and P. Moulin, *Reverse Osmosis Desalination: Water Sources, Technology, and Today's Challenges.* Water Research, 2009. **43**(9): p. 2317-2348.
18. *Safe Drinking Water Act*, in *42 U.S.C.* 1974: United States of America.
19. Gleick, P.H., *The World's Water: The Biennial Report on Freshwater Resources.* Vol. 8. 2014, Washington, DC: Island Press.
20. Roy Chester, T.J., *Marine Geochemistry, 3rd Edition.* 3rd Edition ed. 2012: Wiley.
21. Millero, F.J., R. Feistel, D.G. Wright, and T.J. McDougall, *The Composition of Standard Seawater and the Definition of the Reference-Composition Salinity Scale.* Deep-Sea Research Part I-Oceanographic Research Papers, 2008. **55**(1): p. 50-72.
22. Pereira, L.S., T. Oweis, and A. Zairi, *Irrigation Management under Water Scarcity.* Agricultural Water Management, 2002. **57**(3): p. 175-206.

23. Qadir, M. and J.D. Oster, *Crop and Irrigation Management Strategies for Saline-Sodic Soils and Waters Aimed at Environmentally Sustainable Agriculture.* Science of the Total Environment, 2004. **323**(1-3): p. 1-19.

24. Shannon, M.A., P.W. Bohn, M. Elimelech, J.G. Georgiadis, B.J. Marinas, and A.M. Mayes, *Science and Technology for Water Purification in the Coming Decades.* Nature, 2008. **452**(7185): p. 301-310.

25. Dudka, S. and D.C. Adriano, *Environmental Impacts of Metal Ore Mining and Processing: A Review.* Journal of Environmental Quality, 1997. **26**(3): p. 590-602.

26. Akcil, A. and S. Koldas, *Acid Mine Drainage (Amd): Causes, Treatment and Case Studies.* Journal of Cleaner Production, 2006. **14**(12-13): p. 1139-1145.

27. Nagajyoti, P.C., K.D. Lee, and T.V.M. Sreekanth, *Heavy Metals, Occurrence and Toxicity for Plants: A Review.* Environmental Chemistry Letters, 2010. **8**(3): p. 199-216.

28. Lee, J., S. Mahendra, and P.J.J. Alvarez, *Nanomaterials in the Construction Industry: A Review of Their Applications and Environmental Health and Safety Considerations.* Acs Nano, 2010. **4**(7): p. 3580-3590.

29. Sipma, J., M.B. Osuna, M.A.E. Emanuelsson, and P.M.L. Castro, *Biotreatment of Industrial Wastewaters under Transient-State Conditions: Process Stability with Fluctuations of Organic Load, Substrates, Toxicants, and Environmental Parameters.* Critical Reviews in Environmental Science and Technology, 2010. **40**(2): p. 147-197.

30. Lin, S.H. and W.J. Lan, *Waste Oil/Water Emulsion Treatment by Membrane Processes.* Journal of Hazardous Materials, 1998. **59**(2-3): p. 189-199.

31. Torcellini, P., N. Long, and R. Judkoff, *Consumptive Water Use for U.S. Power Production,* N.R.E. Lab, Editor. 2003, U.S. Department of Energy: Golden, CO. p. 18.

32. Foley, J.A., R. DeFries, G.P. Asner, C. Barford, G. Bonan, S.R. Carpenter, F.S. Chapin, M.T. Coe, G.C. Daily, H.K. Gibbs, J.H. Helkowski, T. Holloway, E.A. Howard, C.J. Kucharik, C. Monfreda, J.A. Patz, I.C. Prentice, N. Ramankutty, and P.K. Snyder, *Global Consequences of Land Use.* Science, 2005. **309**(5734): p. 570-574.

33. Van der Bruggen, B. and C. Vandecasteele, *Distillation Vs. Membrane Filtration: Overview of Process Evolutions in Seawater Desalination.* Desalination, 2002. **143**(3): p. 207-218.

34. Charcosset, C., *A Review of Membrane Processes and Renewable Energies for Desalination.* Desalination, 2009. **245**(1-3): p. 214-231.

35. Helal, A.M. and M. Odeh, *The Once-through Msf Design. Feasibility for Future Large Capacity Desalination Plants.* Desalination, 2004. **166**(1-3): p. 25-39.

36. Xu, T.W., *Ion Exchange Membranes: State of Their Development and Perspective.* Journal of Membrane Science, 2005. **263**(1-2): p. 1-29.

37. El-Bourawi, M.S., Z. Ding, R. Ma, and M. Khayet, *A Framework for Better Understanding Membrane Distillation Separation Process.* Journal of Membrane Science, 2006. **285**(1-2): p. 4-29.

38. Lawson, K.W. and D.R. Lloyd, *Membrane Distillation.* Journal of Membrane Science, 1997. **124**(1): p. 1-25.

39. Círillo, M., G. Capasso, V.A.D. Leo, and N.G.D. Santo, *A History of Salt.* American Journal of Nephrology, 1994. **14**(4-6): p. 426-431.

40. Bridbury, A.R., *England and the Salt Trade in the Later Middle Ages.* 1955: Clarendon Press.

41. Alexander, J., *The Prehistoric Salt Trade in Europe.* Nature, 1982. **300**: p. 577-578.

42. Raymond, R.S.L.I.W. and O.R. Constable, *Medieval Trade in the Mediterranean World: Illustrative Documents.* 2013: Columbia University Press.

43. Robb, J.E. and R.H. Farr, *Substances in Motion: Neolithic Mediterranean 'Trade'.* The archaeology of mediterranean prehistory, 2005. **1**: p. 24-46.

44.   Good, C.M., *Salt, Trade, and Disease: Aspects of Development in Africa's Northern Great Lakes Region.* The International Journal of African Historical Studies, 1972. **5**(4): p. 543-586.

45.   Andrews, A.P. and S.B. Mock, *Chapter Eleven New Perspectives on the Prehispanic Maya Salt Trade.* Ancient Maya Political Economies, 2002: p. 307.

46.   Good, C., *Salt Production and Commerce in Guerrero, Mexico. An Ethnographic Contribution to Historical Reconstruction.* Ancient Mesoamerica, 1995. **6**: p. 1-13.

47.   Chiang, T.-C., *The Salt Trade in Ch'ing China.* Modern Asian Studies, 1983. **17**(02): p. 197-219.

48.   Chandra, M., *Trade and Trade Routes in Ancient India.* 1977: Abhinav Publications.

49.   Kim, D.H., *A Review of Desalting Process Techniques and Economic Analysis of the Recovery of Salts from Retentates.* Desalination, 2011. **270**(1-3): p. 1-8.

50.   Bolen, W., *2013 Minerals Yearbook: Salt,* U.S.D.o.t. Interior, Editor. 2015, U.S. Geological Survey. p. 26.

51.   Ingram, M. and A. Kitchell, *Salt as a Preservative for Foods.* International Journal of Food Science & Technology, 1967. **2**(1): p. 1-15.

52.   Durack, E., M. Alonso-Gomez, and M.G. Wilkinson, *Salt: A Review of Its Role in Food Science and Public Health.* Current Nutrition & Food Science, 2008. **4**(4): p. 290-297.

53.   Man, C., D. Kilcast, and F. Angus, *Technological Functions of Salt in Food Products.* Reducing salt in foods: Practical strategies, 2007: p. 157-173.

54.   Stoner, W.D., J.K. Millhauser, E. Rodriguez-Alegria, L. Overholtzer, and M.D. Glascock, *Taken with a Grain of Salt: Experimentation and the Chemistry of Archaeological Ceramics from Xaltocan, Mexico.* Journal of Archaeological Method and Theory, 2014. **21**(4): p. 862-898.

55.   Abbott, D.R., *Extensive and Long-Term Specialization: Hohokam Ceramic Production in the Phoenix Basin, Arizona.* American Antiquity, 2009. **74**(3): p. 531-557.

56.   Tite, M.S., *Pottery Production, Distribution, and Consumption—the Contribution of the Physical Sciences.* Journal of Archaeological Method and Theory, 1999. **6**(3): p. 181-233.

57.   Morris, E.L., *Production and Distribution of Pottery and Salt in Iron Age Britain: A Review.* Proceedings of the Prehistoric Society, 1994. **60**: p. 371-393.

58.   Zaslavsky, C., *Africa Counts: Number and Pattern in African Cultures.* 1999: Chicago Review Press, Incorporated.

59.   Guyer, J.I., *Wealth in People and Self-Realization in Equatorial Africa.* Man, 1993. **28**(2): p. 243-265.

60.   Godelier, M., *"Salt Currency" and the Circulation of Commodities among the Baruya of New Guinea.* Studies in Economic Anthropology, ed. G. Dalton. 1971, Washington, DC: American Anthropological Association.

61.   Abdel-Maksoud, G. and A.R. El-Amin, *A Review on the Materials Used During the Mummification Processes in Ancient Egypt.* Mediterranean Archaeology & Archaeometry, 2011. **11**(2): p. 129-150.

62.   *Desalination: A National Perspective,* N.A.o. Sciences, Editor. 2008, The National Academies Press: Washington, DC. p. 312.

63.   Armistead, J.P., *Navy Programs in Water Desalination.* Abstracts of Papers of the American Chemical Society, 2010. **239**.

64.   Sourirajan, S., *Mechanism of Demineralization of Aqueous Sodium Chloride Solutions by Flow, under Pressure, through Porous Membranes.* Industrial & Engineering Chemistry Fundamentals, 1963. **2**(1): p. 51-&.

65.   Riley, R.L., R.L. Fox, C.R. Lyons, C.E. Milstead, M.W. Seroy, and M. Tagami, *Spiral-Wound Poly(Ether-Amide) Thin-Film Composite Membrane Systems.* Desalination, 1976. **19**(1-3): p. 113-126.

66.   Thamaraiselvan, C. and M. Noel, *Membrane Processes for Dye Wastewater Treatment: Recent Progress in Fouling Control.* Critical Reviews in Environmental Science and Technology, 2015. **45**(10): p. 1007-1040.

67.   Cincinelli, A., T. Martellini, E. Coppini, D. Fibbi, and A. Katsoyiannis, *Nanotechnologies for Removal of Pharmaceuticals and Personal Care Products from Water and Wastewater. A Review.* Journal of Nanoscience and Nanotechnology, 2015. **15**(5): p. 3333-3347.

68.   Zhu, Y.Z., D. Wang, L. Jiang, and J. Jin, *Recent Progress in Developing Advanced Membranes for Emulsified Oil/Water Separation.* Npg Asia Materials, 2014. **6**.

69.   Wolska, J. and M. Bryjak, *Methods for Boron Removal from Aqueous Solutions - a Review.* Desalination, 2013. **310**: p. 18-24.

70.   Pal, P., M. Sen, A. Manna, J. Pal, P. Pal, S. Roy, and P. Roy, *Contamination of Groundwater by Arsenic: A Review of Occurrence, Causes, Impacts, Remedies and Membrane-Based Purification.* Journal of Integrative Environmental Sciences, 2009. **6**(4): p. 295-316.

71.   Bellona, C., J.E. Drewes, P. Xu, and G. Amy, *Factors Affecting the Rejection of Organic Solutes During Nf/Ro Treatment - a Literature Review.* Water Research, 2004. **38**(12): p. 2795-2809.

72.   Plakas, K.V. and A.J. Karabelas, *Removal of Pesticides from Water by Nf and Ru Membranes - a Review.* Desalination, 2012. **287**: p. 255-265.

73.   Schafer, A.I., G. Hughes, and B.S. Richards, *Renewable Energy Powered Membrane Technology: A Leapfrog Approach to Rural Water Treatment in Developing Countries?* Renewable & Sustainable Energy Reviews, 2014. **40**: p. 542-556.

74.   Arjunan, T.V., H.S. Aybar, and N. Nedunchezhian, *Status of Solar Desalination in India.* Renewable & Sustainable Energy Reviews, 2009. **13**(9): p. 2408-2418.

75.   Klaysom, C., T.Y. Cath, T. Depuydt, and I.F.J. Vankelecom, *Forward and Pressure Retarded Osmosis: Potential Solutions for Global Challenges in Energy and Water Supply.* Chemical Society Reviews, 2013. **42**(16): p. 6959-6989.

76.   Al-Karaghouli, A., D. Renne, and L.L. Kazmerski, *Technical and Economic Assessment of Photovoltaic-Driven Desalination Systems.* Renewable Energy, 2010. **35**(2): p. 323-328.

77.   Eltawil, M.A., Z. Zhengming, and L.Q. Yuan, *A Review of Renewable Energy Technologies Integrated with Desalination Systems.* Renewable & Sustainable Energy Reviews, 2009. **13**(9): p. 2245-2262.

78.   Callow, J.A. and M.E. Callow, *Trends in the Development of Environmentally Friendly Fouling-Resistant Marine Coatings.* Nature Communications, 2011. **2**.

79.   Kang, G.D. and Y.M. Cao, *Development of Antifouling Reverse Osmosis Membranes for Water Treatment: A Review.* Water Research, 2012. **46**(3): p. 584-600.

80.   Tang, C.Y.Y., T.H. Chong, and A.G. Fane, *Colloidal Interactions and Fouling of Nf and Ro Membranes: A Review.* Advances in Colloid and Interface Science, 2011. **164**(1-2): p. 126-143.

81.   Kim, E.S., Y. Liu, and M.G. El-Din, *Evaluation of Membrane Fouling for in-Line Filtration of Oil Sands Process-Affected Water: The Effects of Pretreatment Conditions.* Environmental Science & Technology, 2012. **46**(5): p. 2877-2884.

82.   Liyanaarachchi, S., L. Shu, S. Muthukumaran, V. Jegatheesan, and K. Baskaran, *Problems in Seawater Industrial Desalination Processes and Potential Sustainable Solutions: A Review.* Reviews in Environmental Science and Bio-Technology, 2014. **13**(2): p. 203-214.

83.   Sheikholeslami, R., *Strategies for Future Research and Development in Desalination - Challenges Ahead.* Desalination, 2009. **248**(1-3): p. 218-224.

84.   Ahmad, N. and R.E. Baddour, *A Review of Sources, Effects, Disposal Methods, and Regulations of Brine into Marine Environments.* Ocean & Coastal Management, 2014. **87**: p. 1-7.

85. Chelme-Ayala, P., D.W. Smith, and M.G. El-Din, *Membrane Concentrate Management Options: A Comprehensive Critical Review.* Canadian Journal of Civil Engineering, 2009. **36**(6): p. 1107-1119.

86. Tularam, G.A. and M. Ilahee, *Environmental Concerns of Desalinating Seawater Using Reverse Osmosis.* Journal of Environmental Monitoring, 2007. **9**(8): p. 805-813.

87. Roberts, D.A., E.L. Johnston, and N.A. Knott, *Impacts of Desalination Plant Discharges on the Marine Environment: A Critical Review of Published Studies.* Water Research, 2010. **44**(18): p. 5117-5128.

88. El-Ghonemy, A.M.K., *Future Sustainable Water Desalination Technologies for the Saudi Arabia: A Review.* Renewable & Sustainable Energy Reviews, 2012. **16**(9): p. 6566-6597.

89. Schiermeier, Q., *Purification with a Pinch of Salt.* Nature, 2008. **452**(7185): p. 260-261.

90. Mickley, M., *Desalination and Water Purification Research and Development Program Report No. 123*, U.S.D.o.t. Interior, Editor. 2006, US. DoI Bureau of Reclamation: Denver, CO. p. 298.

91. Semiat, R., *Energy Issues in Desalination Processes.* Environmental Science & Technology, 2008. **42**(22): p. 8193-8201.

92. Elimelech, M. and W.A. Phillip, *The Future of Seawater Desalination: Energy, Technology, and the Environment.* Science, 2011. **333**(6043): p. 712-717.

93. Fritzmann, C., J. Lowenberg, T. Wintgens, and T. Melin, *State-of-the-Art of Reverse Osmosis Desalination.* Desalination, 2007. **216**(1-3): p. 1-76.

94. Al-Ahmad, M., F.A.A. Aleem, A. Mutiri, and A. Ubaisy, *Biofuoling in Ro Membrane Systems Part 1: Fundamentals and Control.* Desalination, 2000. **132**(1-3): p. 173-179.

95. Gao, W., H. Liang, J. Ma, M. Han, Z.L. Chen, Z.S. Han, and G.B. Li, *Membrane Fouling Control in Ultrafiltration Technology for Drinking Water Production: A Review.* Desalination, 2011. **272**(1-3): p. 1-8.

96. Vrouwenvelder, J.S., D.A.G. von der Schulenburg, J.C. Kruithof, M.L. Johns, and M.C.M. van Loosdrecht, *Biofouling of Spiral-Wound Nanofiltration and Reverse Osmosis Membranes: A Feed Spacer Problem.* Water Research, 2009. **43**(3): p. 583-594.

97. Bacchin, P., P. Aimar, and R.W. Field, *Critical and Sustainable Fluxes: Theory, Experiments and Applications.* Journal of Membrane Science, 2006. **281**(1-2): p. 42-69.

98. Cohen-Tanugi, D., R.K. McGovern, S.H. Dave, J.H. Lienhard, and J.C. Grossman, *Quantifying the Potential of Ultra-Permeable Membranes for Water Desalination.* Energy & Environmental Science, 2014. **7**(3): p. 1134-1141.

99. Bhattacharya, A. and P. Ghosh, *Nanofiltration and Reverse Osmosis Membranes: Theory and Application in Separation of Electrolytes.* Reviews in Chemical Engineering, 2004. **20**(1-2): p. 111-173.

100. Pages, N., A. Yaroshchuk, O. Gibert, and J.L. Cortina, *Rejection of Trace Ionic Solutes in Nanofiltration: Influence of Aqueous Phase Composition.* Chemical Engineering Science, 2013. **104**: p. 1107-1115.

101. Kabay, N., O. Arar, F. Acar, A. Ghazal, U. Yuksel, and M. Yuksel, *Removal of Boron from Water by Electrodialysis: Effect of Feed Characteristics and Interfering Ions.* Desalination, 2008. **223**(1-3): p. 63-72.

102. Kimura, S. and Souriraj.S, *Analysis of Data in Reverse Osmosis with Porous Cellulose Acetate Membranes Used.* Aiche Journal, 1967. **13**(3): p. 497-&.

103. Petersen, R.J., *Composite Reverse Osmosis and Nanofiltration Membranes.* Journal of Membrane Science, 1993. **83**(1): p. 81-150.

104. Geise, G.M., D.R. Paul, and B.D. Freeman, *Fundamental Water and Salt Transport Properties of Polymeric Materials.* Progress in Polymer Science, 2014. **39**(1): p. 1-42.

105. Escobar, I.C. *Membranes for Water Treatment.* in *23rd Annual Meeting of the North American Membrane Society.* 2013. Boise, ID: North American Membrane Society.

106. Morgan, P.W. and S.L. Kwolek, *Interfacial Polycondensation .2. Fundamentals of Polymer Formation at Liquid Interfaces.* Journal of Polymer Science, 1959. **40**(137): p. 299-327.

107. Tang, C.Y.Y., Y.N. Kwon, and J.O. Leckie, *Probing the Nano- and Micro-Scales of Reverse Osmosis Membranes - a Comprehensive Characterization of Physiochemical Properties of Uncoated and Coated Membranes by Xps, Tem, Atr-Ftir, and Streaming Potential Measurements.* Journal of Membrane Science, 2007. **287**(1): p. 146-156.

108. Pacheco, F.A., I. Pinnau, M. Reinhard, and J.O. Leckie, *Characterization of Isolated Polyamide Thin Films of Ro and Nf Membranes Using Novel Tem Techniques.* Journal of Membrane Science, 2010. **358**(1-2): p. 51-59.

109. Ghosh, A.K., B.H. Jeong, X.F. Huang, and E.M.V. Hoek, *Impacts of Reaction and Curing Conditions on Polyamide Composite Reverse Osmosis Membrane Properties.* Journal of Membrane Science, 2008. **311**(1-2): p. 34-45.

110. Zhang, M.Q. and M.Z. Rong, *Self-Healing Polymers and Polymer Composites.* 2011: Wiley.

111. Lau, W.J., A.F. Ismail, N. Misdan, and M.A. Kassim, *A Recent Progress in Thin Film Composite Membrane: A Review.* Desalination, 2012. **287**: p. 190-199.

112. Lee, K.P., T.C. Arnot, and D. Mattia, *A Review of Reverse Osmosis Membrane Materials for Desalination-Development to Date and Future Potential.* Journal of Membrane Science, 2011. **370**(1-2): p. 1-22.

113. Tung, K.L., Y.C. Jean, D. Nanda, K.R. Lee, W.S. Hung, C.H. Lo, and J.Y. Lai, *Characterization of Multilayer Nanofiltration Membranes Using Positron Annihilation Spectroscopy.* Journal of Membrane Science, 2009. **343**(1-2): p. 147-156.

114. Tiraferri, A., N.Y. Yip, W.A. Phillip, J.D. Schiffman, and M. Elimelech, *Relating Performance of Thin-Film Composite Forward Osmosis Membranes to Support Layer Formation and Structure.* Journal of Membrane Science, 2011. **367**(1-2): p. 340-352.

115. Mulder, J., *Basic Principles of Membrane Technology.* 1996: Springer Netherlands.

116. Guillen, G.R., Y.J. Pan, M.H. Li, and E.M.V. Hoek, *Preparation and Characterization of Membranes Formed by Nonsolvent Induced Phase Separation: A Review.* Industrial & Engineering Chemistry Research, 2011. **50**(7): p. 3798-3817.

117. vandeWitte, P., P.J. Dijkstra, J.W.A. vandenBerg, and J. Feijen, *Phase Separation Processes in Polymer Solutions in Relation to Membrane Formation.* Journal of Membrane Science, 1996. **117**(1-2): p. 1-31.

118. Wienk, I.M., R.M. Boom, M.A.M. Beerlage, A.M.W. Bulte, C.A. Smolders, and H. Strathmann, *Recent Advances in the Formation of Phase Inversion Membranes Made from Amorphous or Semi-Crystalline Polymers.* Journal of Membrane Science, 1996. **113**(2): p. 361-371.

119. Camacho, L.M., L. Dumee, J.H. Zhang, J.D. Li, M. Duke, J. Gomez, and S. Gray, *Advances in Membrane Distillation for Water Desalination and Purification Applications.* Water, 2013. **5**(1): p. 94-196.

120. Goebel, P., D. Olson, D.M. Polizzotti, and A.R. Khwaja, *Spiral Wound Membrane Element and Treatment of Sagd Produced Water or Other High Temperature Alkaline Fluids.* 2012, Google Patents.

121. LaTerra, T., *Liquid Purification Using Reverse Osmosis Hollow Fibers.* 1983, Google Patents.

122. Ulrich, M., *Reverse Osmosis Membrane Module.* 1968, Google Patents.

123. Marriott, J. and E. Sorensen, *A General Approach to Modelling Membrane Modules.* Chemical Engineering Science, 2003. **58**(22): p. 4975-4990.

124. Zhu, A.Z., P.D. Christofides, and Y. Cohen, *Effect of Thermodynamic Restriction on Energy Cost Optimization of Ro Membrane Water Desalination.* Industrial & Engineering Chemistry Research, 2009. **48**(13): p. 6010-6021.

125. Mansoor, M.A.M. and B.J. Sandmann, *Applied Physical Pharmacy.* 1 ed. Vol. 1. 2002: McGraw-Hill Professional. 462.

126.	Song, L.F., J.Y. Hu, S.L. Ong, W.J. Ng, M. Elimelech, and M. Wilf, *Emergence of Thermodynamic Restriction and Its Implications for Full-Scale Reverse Osmosis Processes.* Desalination, 2003. **155**(3): p. 213-228.

127.	Spiegler, K.S. and Y.M. El-Sayed, *The Energetics of Desalination Processes.* Desalination, 2001. **134**(1-3): p. 109-128.

128.	Lu, Y.B., M. Qin, H.Y. Yuan, I.M. Abu-Reesh, and Z. He, *When Bioelectrochemical Systems Meet Forward Osmosis: Accomplishing Wastewater Treatment and Reuse through Synergy.* Water, 2015. **7**(1): p. 38-50.

129.	Linares, R.V., Z. Li, S. Sarp, S.S. Bucs, G. Amy, and J.S. Vrouwenvelder, *Forward Osmosis Niches in Seawater Desalination and Wastewater Reuse.* Water Research, 2014. **66**: p. 122-139.

130.	Lutchmiah, K., A.R.D. Verliefde, K. Roest, L.C. Rietveld, and E.R. Cornelissen, *Forward Osmosis for Application in Wastewater Treatment: A Review.* Water Research, 2014. **58**: p. 179-197.

131.	Cath, T.Y., A.E. Childress, and M. Elimelech, *Forward Osmosis: Principles, Applications, and Recent Developments.* Journal of Membrane Science, 2006. **281**(1-2): p. 70-87.

132.	Zhang, J.F., V.W.C. Chang, A. Giannis, and J.Y. Wang, *Removal of Cytostatic Drugs from Aquatic Environment: A Review.* Science of the Total Environment, 2013. **445**: p. 281-298.

133.	Coday, B.D., B.G.M. Yaffe, P. Xu, and T.Y. Cath, *Rejection of Trace Organic Compounds by Forward Osmosis Membranes: A Literature Review.* Environmental Science & Technology, 2014. **48**(7): p. 3612-3624.

134.	Yap, W.J., J.S. Zhang, W.C.L. Lay, B. Cao, A.G. Fane, and Y. Liu, *State of the Art of Osmotic Membrane Bioreactors for Water Reclamation.* Bioresource Technology, 2012. **122**: p. 217-222.

135.	Luo, W.H., F.I. Hai, W.E. Price, W.S. Guo, H.H. Ngo, K. Yamamoto, and L.D. Nghiem, *High Retention Membrane Bioreactors: Challenges and Opportunities.* Bioresource Technology, 2014. **167**: p. 539-546.

136.	Yip, N.Y., A. Tiraferri, W.A. Phillip, J.D. Schiffman, and M. Elimelech, *High Performance Thin-Film Composite Forward Osmosis Membrane.* Environmental Science & Technology, 2010. **44**(10): p. 3812-3818.

137.	Pardeshi, P. and A.A. Mungray, *Synthesis, Characterization and Application of Novel High Flux Fo Membrane by Layer-by-Layer Self-Assembled Polyelectrolyte.* Journal of Membrane Science, 2014. **453**: p. 202-211.

138.	Alsvik, I.L. and M.B. Hagg, *Pressure Retarded Osmosis and Forward Osmosis Membranes: Materials and Methods.* Polymers, 2013. **5**(1): p. 303-327.

139.	Zhao, S.F., L. Zou, C.Y.Y. Tang, and D. Mulcahy, *Recent Developments in Forward Osmosis: Opportunities and Challenges.* Journal of Membrane Science, 2012. **396**: p. 1-21.

140.	Chekli, L., S. Phuntsho, H.K. Shon, S. Vigneswaran, J. Kandasamy, and A. Chanan, *A Review of Draw Solutes in Forward Osmosis Process and Their Use in Modern Applications.* Desalination and Water Treatment, 2012. **43**(1-3): p. 167-184.

141.	Ge, Q.C. and T.S. Chung, *Hydroacid Complexes: A New Class of Draw Solutes to Promote Forward Osmosis (Fo) Processes.* Chemical Communications, 2013. **49**(76): p. 8471-8473.

142.	McGovern, R.K. and J.H. Lienhard, *On the Potential of Forward Osmosis to Energetically Outperform Reverse Osmosis Desalination.* Journal of Membrane Science, 2014. **469**: p. 245-250.

143.	Okada, T. and T. Matsuura, *A New Transport Model for Pervaporation.* Journal of membrane science, 1991. **59**(2): p. 133-149.

144.	Wang, J., D.S. Dlamini, A.K. Mishra, M.T.M. Pendergast, M.C.Y. Wong, B.B. Mamba, V. Freger, A.R.D. Verliefde, and E.M.V. Hoek, *A Critical Review of Transport through Osmotic Membranes.* Journal of Membrane Science, 2014. **454**: p. 516-537.

145.   Van der Bruggen, B., J. Schaep, D. Wilms, and C. Vandecasteele, *Influence of Molecular Size, Polarity and Charge on the Retention of Organic Molecules by Nanofiltration.* Journal of Membrane Science, 1999. **156**(1): p. 29-41.

146.   Steinle-Darling, E. and M. Reinhard, *Nanofiltration for Trace Organic Contaminant Removal: Structure, Solution, and Membrane Fouling Effects on the Rejection of Perfluorochemicals.* Environmental Science & Technology, 2008. **42**(14): p. 5292-5297.

147.   Drewes, J.E., M. Reinhard, and P. Fox, *Comparing Microfiltration-Reverse Osmosis and Soil-Aquifer Treatment for Indirect Potable Reuse of Water.* Water Research, 2003. **37**(15): p. 3612-3621.

148.   Le-Minh, N., S.J. Khan, J.E. Drewes, and R.M. Stuetz, *Fate of Antibiotics During Municipal Water Recycling Treatment Processes.* Water Research, 2010. **44**(15): p. 4295-4323.

149.   Hung, W.S., M. De Guzman, S.H. Huang, K.R. Lee, Y.C. Jean, and J.Y. Lai, *Characterizing Free Volumes and Layer Structures in Asymmetric Thin-Film Polymeric Membranes in the Wet Condition Using the Variable Monoenergy Slow Positron Beam.* Macromolecules, 2010. **43**(14): p. 6127-6134.

150.   Stawikowska, J. and A.G. Livingston, *Nanoprobe Imaging Molecular Scale Pores in Polymeric Membranes.* Journal of Membrane Science, 2012. **413-414**: p. 1-16.

151.   Boussu, K., J. De Baerdemaeker, C. Dauwe, M. Weber, K.G. Lynn, D. Depla, S. Aldea, I.F.J. Vankelecom, C. Vandecasteele, and B. Van Der Bruggen, *Physico-Chemical Characterization of Nanofiltration Membranes.* ChemPhysChem, 2007. **8**(3): p. 370-379.

152.   Hilal, N., H. Al-Zoubi, N.A. Darwish, and A.W. Mohammad, *Characterisation of Nanofiltration Membranes Using Atomic Force Microscopy.* Desalination, 2005. **177**(1-3): p. 187-199.

153.   Bowen, W.R., A.W. Mohammad, and N. Hilal, *Characterisation of Nanofiltration Membranes for Predictive Purposes - Use of Salts, Uncharged Solutes and Atomic Force Microscopy.* Journal of Membrane Science, 1997. **126**(1): p. 91-105.

154.   Kärger, J. and R. Valiullin, *Diffusion in Porous Media,* in *Emagres.* 2007, John Wiley & Sons, Ltd.

155.   Grathwohl, P., *Diffusion in Natural Porous Media.* 2002: Kluwer.

156.   Welty, J., C.E. Wicks, G.L. Rorrer, and R.E. Wilson, *Fundamentals of Momentum, Heat and Mass Transfer.* 2007: Wiley.

157.   Koneshan, S., R.M. Lynden-Bell, and J.C. Rasaiah, *Friction Coefficients of Ions in Aqueous Solution at 25 Degrees C.* Journal of the American Chemical Society, 1998. **120**(46): p. 12041-12050.

158.   Ohshima, H. and T. Kondo, *Electrostatic Repulsion of Ion Penetrable Charged Membranes: Role of Donnan Potential.* Journal of Theoretical Biology, 1987. **128**(2): p. 187-194.

159.   Wolynes, P.G., *Molecular Theory of Solvated Ion Dynamics.* The Journal of Chemical Physics, 1978. **68**(2): p. 473-483.

160.   Chen, J.H. and S.A. Adelman, *Macroscopic Model for Solvated Ion Dynamics.* The Journal of Chemical Physics, 1980. **72**(4): p. 2819-2831.

161.   Eliad, L., G. Salitra, A. Soffer, and D. Aurbach, *Ion Sieving Effects in the Electrical Double Layer of Porous Carbon Electrodes: Estimating Effective Ion Size in Electrolytic Solutions.* The Journal of Physical Chemistry B, 2001. **105**(29): p. 6880-6887.

162.   Marcus, Y., *Ionic Radii in Aqueous Solutions.* Chemical Reviews, 1988. **88**(8): p. 1475-1498.

163.   Rips, I., J. Klafter, and J. Jortner, *Dynamics of Ionic Solvation.* The Journal of chemical physics, 1988. **88**(5): p. 3246-3252.

164.   Schaep, J., B. Van der Bruggen, C. Vandecasteele, and D. Wilms, *Influence of Ion Size and Charge in Nanofiltration.* Separation and Purification Technology, 1998. **14**(1–3): p. 155-162.

165.   Latour, L.L., R.L. Kleinberg, P.P. Mitra, and C.H. Sotak, *Pore-Size Distributions and Tortuosity in Heterogeneous Porous-Media.* Journal of Magnetic Resonance Series A, 1995. **112**(1): p. 83-91.

166.   Zalc, J.M., S.C. Reyes, and E. Iglesia, *Monte-Carlo Simulations of Surface and Gas Phase Diffusion in Complex Porous Structures.* Chemical Engineering Science, 2003. **58**(20): p. 4605-4617.

167.   Gouze, P., Y. Melean, T. Le Borgne, M. Dentz, and J. Carrera, *Non-Fickian Dispersion in Porous Media Explained by Heterogeneous Microscale Matrix Diffusion.* Water Resources Research, 2008. **44**(11).

168.   Haus, J.W. and K.W. Kehr, *Diffusion in Regular and Disordered Lattices.* Physics Reports-Review Section of Physics Letters, 1987. **150**(5-6): p. 263-406.

169.   Nielsen, L.E., *Models for the Permeability of Filled Polymer Systems.* Journal of Macromolecular Science—Chemistry, 1967. **1**(5): p. 929-942.

170.   Cussler, E.L., S.E. Hughes, W.J. Ward Iii, and R. Aris, *Barrier Membranes.* Journal of Membrane Science, 1988. **38**(2): p. 161-174.

171.   Jang, W.S., I. Rawson, and J.C. Grunlan, *Layer-by-Layer Assembly of Thin Film Oxygen Barrier.* Thin Solid Films, 2008. **516**(15): p. 4819-4825.

172.   DeRocher, J.P., B.T. Gettelfinger, J. Wang, E.E. Nuxoll, and E.L. Cussler, *Barrier Membranes with Different Sizes of Aligned Flakes.* Journal of Membrane Science, 2005. **254**(1-2): p. 21-30.

173.   Bharadwaj, R.K., A.R. Mehrabi, C. Hamilton, C. Trujillo, M. Murga, R. Fan, A. Chavira, and A.K. Thompson, *Structure-Property Relationships in Cross-Linked Polyester-Clay Nanocomposites.* Polymer, 2002. **43**(13): p. 3699-3705.

174.   Osman, M.A., V. Mittal, M. Morbidelli, and U.W. Suter, *Epoxy-Layered Silicate Nanocomposites and Their Gas Permeation Properties.* Macromolecules, 2004. **37**(19): p. 7250-7257.

175.   Osman, M.A., J.E.P. Rupp, and U.W. Suter, *Gas Permeation Properties of Polyethylene-Layered Silicate Nanocomposites.* Journal of Materials Chemistry, 2005. **15**(12): p. 1298-1304.

176.   Sánchez-Valdes, S., M.L. López-Quintanilla, E. Ramírez-Vargas, F.J. Medellín-Rodríguez, and J.M. Gutierrez-Rodriguez, *Effect of Ionomeric Compatibilizer on Clay Dispersion in Polyethylene/Clay Nanocomposites.* Macromolecular Materials and Engineering, 2006. **291**(2): p. 128-136.

177.   Banerjee, P. and S. De, *Coupled Concentration Polarization and Pore Flow Modeling of Nanofiltration of an Industrial Textile Effluent.* Separation and Purification Technology, 2010. **73**(3): p. 355-362.

178.   Matsuura, T. and S. Sourirajan, *Reverse Osmosis Transport through Capillary Pores under the Influence of Surface Forces.* Industrial & Engineering Chemistry, Process Design and Development, 1981. **20**(2): p. 273-282.

179.   Jain, S. and S.K. Gupta, *Analysis of Modified Surface Force Pore Flow Model with Concentration Polarization and Comparison with Spiegler-Kedem Model in Reverse Osmosis Systems.* Journal of Membrane Science, 2004. **232**(1-2): p. 45-61.

180.   Mehdizadeh, H. and J.M. Dickson, *Theoretical Modification of the Surface Force-Pore Flow Model for Reverse Osmosis Transport.* Journal of Membrane Science, 1989. **42**(1-2): p. 119-145.

181.   Freger, V., *Nanoscale Heterogeneity of Polyamide Membranes Formed by Interfacial Polymerization.* Langmuir, 2003. **19**(11): p. 4791-4797.

182.   Mehdizadeh, H. and J.M. Dickson, *Evaluation of Surface Force-Pore Flow and Modified Surface Force-Pore Flow Models for Reverse Osmosis Transport.* Chemical Engineering Communications, 1991. **103**(1): p. 65-82.

183. Connell, P.J. and J.M. Dickson, *Modeling Reverse Osmosis Separations with Strong Solute-Membrane Affinity at Different Temperatures Using the Finely Porous Model.* Journal of Applied Polymer Science, 1988. **35**(5): p. 1129-1148.

184. Mehdizadeh, H. and J.M. Dickson, *Theoretical Modification of the Finely Porous Model for Reverse Osmosis Transport.* Journal of Applied Polymer Science, 1991. **42**(4): p. 1143-1154.

185. Lonsdale, H.K., U. Merten, and R.L. Riley, *Transport Properties of Cellulose Acetate Osmotic Membranes.* Journal of Applied Polymer Science, 1965. **9**(4): p. 1341-1362.

186. Soltanieh, M. and W.N. Gill, *Review of Reverse Osmosis Membranes and Transport Models.* Chemical Engineering Communications, 1981. **12**(4-6): p. 279-363.

187. Fierro, D., A. Boschetti-de-Fierro, and V. Abetz, *The Solution-Diffusion with Imperfections Model as a Method to Understand Organic Solvent Nanofiltration of Multicomponent Systems.* Journal of Membrane Science, 2012. **413-414**: p. 91-101.

188. Yaroshchuk, A.E., *Solution-Diffusion-Imperfection Model Revised.* Journal of Membrane Science, 1995. **101**(1-2): p. 83-87.

189. Yaroshchuk, A.E., *The Role of Imperfections in the Solute Transfer in Nanofiltration.* Journal of Membrane Science, 2004. **239**(1): p. 9-15.

190. Geens, J., K. Boussu, C. Vandecasteele, and B. Van der Bruggen, *Modelling of Solute Transport in Non-Aqueous Nanofiltration.* Journal of Membrane Science, 2006. **281**(1-2): p. 139-148.

191. Peng, F., X. Huang, A. Jawor, and E.M.V. Hoek, *Transport, Structural, and Interfacial Properties of Poly(Vinyl Alcohol)-Polysulfone Composite Nanofiltration Membranes.* Journal of Membrane Science, 2010. **353**(1-2): p. 169-176.

192. Spiegler, K.S. and O. Kedem, *Thermodynamics of Hyperfiltration (Reverse-Osmosis) - Criteria for Efficient Membranes.* Current Contents/Engineering Technology & Applied Sciences, 1983(5): p. 16-16.

193. Kedem, O. and A. Katchalsky, *Permeability of Composite Membranes. Part 1.-Electric Current, Volume Flow and Flow of Solute through Membranes.* Transactions of the Faraday Society, 1963. **59**(0): p. 1918-1930.

194. Wijmans, J.G. and R.W. Baker, *The Solution-Diffusion Model: A Review.* Journal of Membrane Science, 1995. **107**(1-2): p. 1-21.

195. Kleinfeld, E.R. and G.S. Ferguson, *Stepwise Formation of Multilayered Nanostructural Films from Macromolecular Precursors.* Science, 1994. **265**(5170): p. 370-373.

196. Alexandre, M. and P. Dubois, *Polymer-Layered Silicate Nanocomposites: Preparation, Properties and Uses of a New Class of Materials.* Materials Science and Engineering: R: Reports, 2000. **28**(1–2): p. 1-63.

197. Sinha Ray, S. and M. Okamoto, *Polymer/Layered Silicate Nanocomposites: A Review from Preparation to Processing.* Progress in Polymer Science, 2003. **28**(11): p. 1539-1641.

198. Pavlidou, S. and C.D. Papaspyrides, *A Review on Polymer-Layered Silicate Nanocomposites.* Progress in Polymer Science, 2008. **33**(12): p. 1119-1198.

199. Choudalakis, G. and A.D. Gotsis, *Permeability of Polymer/Clay Nanocomposites: A Review.* European Polymer Journal, 2009. **45**(4): p. 967-984.

200. Alateyah, A.I., H.N. Dhakal, and Z.Y. Zhang, *Processing, Properties, and Applications of Polymer Nanocomposites Based on Layer Silicates: A Review.* Advances in Polymer Technology, 2013. **32**(4).

201. Rawat, K., S. Agarwal, A. Tyagi, A.K. Verma, and H.B. Bohidar, *Aspect Ratio Dependent Cytotoxicity and Antimicrobial Properties of Nanoclay.* Applied Biochemistry and Biotechnology, 2014. **174**(3): p. 936-944.

202. Ul-Islam, M., T. Khan, and J.K. Park, *Nanoreinforced Bacterial Cellulose–Montmorillonite Composites for Biomedical Applications.* Carbohydrate Polymers, 2012. **89**(4): p. 1189-1197.

203. Priolo, M.A., D. Gamboa, and J.C. Grunlan, *Transparent Clay-Polymer Nano Brick Wall Assemblies with Tailorable Oxygen Barrier.* Acs Applied Materials & Interfaces, 2010. **2**(1): p. 312-320.

204. Laufer, G., C. Kirkland, A.A. Cain, and J.C. Grunlan, *Clay-Chitosan Nanobrick Walls: Completely Renewable Gas Barrier and Flame-Retardant Nanocoatings.* Acs Applied Materials & Interfaces, 2012. **4**(3): p. 1643-1649.

205. Priolo, M.A., K.M. Holder, S.M. Greenlee, B.E. Stevens, and J.C. Grunlan, *Precisely Tuning the Clay Spacing in Nanobrick Wall Gas Barrier Thin Films.* Chemistry of Materials, 2013. **25**(9): p. 1649-1655.

206. Priolo, M.A., D. Gamboa, K.M. Holder, and J.C. Grunlan, *Super Gas Barrier of Transparent Polymer-Clay Multi Layer Ultrathin Films.* Nano Letters, 2010. **10**(12): p. 4970-4974.

207. Gaskell, E.E. and A.R. Hamilton, *Antimicrobial Clay-Based Materials for Wound Care.* Future Medicinal Chemistry, 2014. **6**(6): p. 641-655.

208. Hsu, S.-h., M.-C. Wang, and J.-J. Lin, *Biocompatibility and Antimicrobial Evaluation of Montmorillonite/Chitosan Nanocomposites.* Applied Clay Science, 2012. **56**(0): p. 53-62.

209. Katti, K.S., A.H. Ambre, N. Peterka, and D.R. Katti, *Use of Unnatural Amino Acids for Design of Novel Organomodified Clays as Components of Nanocomposite Biomaterials.* Philosophical Transactions of the Royal Society a-Mathematical Physical and Engineering Sciences, 2010. **368**(1917): p. 1963-1980.

210. Kokabi, M., M. Sirousazar, and Z.M. Hassan, *Pva–Clay Nanocomposite Hydrogels for Wound Dressing.* European Polymer Journal, 2007. **43**(3): p. 773-781.

211. Lvov, Y. and E. Abdullayev, *Functional Polymer-Clay Nanotube Composites with Sustained Release of Chemical Agents.* Progress in Polymer Science, 2013. **38**(10-11): p. 1690-1719.

212. Boo, W.J., L. Sun, G.L. Warren, E. Moghbelli, H. Pham, A. Clearfield, and H.J. Sue, *Effect of Nanoplatelet Aspect Ratio on Mechanical Properties of Epoxy Nanocomposites.* Polymer, 2007. **48**(4): p. 1075-1082.

213. Wang, T. and J.L. Keddie, *Design and Fabrication of Colloidal Polymer Nanocomposites.* Advances in Colloid and Interface Science, 2009. **147-48**: p. 319-332.

214. Podsiadlo, P., A.K. Kaushik, E.M. Arruda, A.M. Waas, B.S. Shim, J.D. Xu, H. Nandivada, B.G. Pumplin, J. Lahann, A. Ramamoorthy, and N.A. Kotov, *Ultrastrong and Stiff Layered Polymer Nanocomposites.* Science, 2007. **318**(5847): p. 80-83.

215. Kim, W.G. and S. Nair, *Membranes from Nanoporous 1d and 2d Materials: A Review of Opportunities, Developments, and Challenges.* Chemical Engineering Science, 2013. **104**: p. 908-924.

216. Sanyal, O. and I. Lee, *Recent Progress in the Applications of Layer-by-Layer Assembly to the Preparation of Nanostructured Ion-Rejecting Water Purification Membranes.* Journal of Nanoscience and Nanotechnology, 2014. **14**(3): p. 2178-2189.

217. Humplik, T., J. Lee, S.C. O'Hern, B.A. Fellman, M.A. Baig, S.F. Hassan, M.A. Atieh, F. Rahman, T. Laoui, R. Karnik, and E.N. Wang, *Nanostructured Materials for Water Desalination.* Nanotechnology, 2011. **22**(29).

218. Bakajin, O., A. Noy, F. Fornasiero, C.P. Grigoropoulos, J.K. Holt, J.B. In, S. Kim, and H.G. Park, *Nanofluidic Carbon Nanotube Membranes: Applications for Water Purification and Desalination.* Nanotechnology Applications for Clean Water, 2009: p. 77-93.

219. Fornasiero, F., H.G. Park, J.K. Holt, M. Stadermann, C.P. Grigoropoulos, A. Noy, and O. Bakajin, *Ion Exclusion by Sub-2-Nm Carbon Nanotube Pores.* Proceedings of the National Academy of Sciences of the United States of America, 2008. **105**(45): p. 17250-17255.

220. Chan, W.F., H.Y. Chen, A. Surapathi, M.G. Taylor, X.H. Hao, E. Marand, and J.K. Johnson, *Zwitterion Functionalized Carbon Nanotube/Polyamide Nanocomposite Membranes for Water Desalination.* Acs Nano, 2013. **7**(6): p. 5308-5319.

221. Wu, H.Q., B.B. Tang, and P.Y. Wu, *Mwnts/Polyester Thin Film Nanocomposite Membrane: An Approach to Overcome the Trade-Off Effect between Permeability and Selectivity.* Journal of Physical Chemistry C, 2010. **114**(39): p. 16395-16400.

222. Zhao, H.Y., S. Qiu, L.G. Wu, L. Zhang, H.L. Chen, and C.J. Gao, *Improving the Performance of Polyamide Reverse Osmosis Membrane by Incorporation of Modified Multi-Walled Carbon Nanotubes.* Journal of Membrane Science, 2014. **450**: p. 249-256.

223. Holt, J.K., H.G. Park, Y. Wang, M. Stadermann, A.B. Artyukhin, C.P. Grigoropoulos, A. Noy, and O. Bakajin, *Fast Mass Transport through Sub-2-Nanometer Carbon Nanotubes.* Science, 2006. **312**(5776): p. 1034-1037.

224. Kim, E.S., G. Hwang, M.G. El-Din, and Y. Liu, *Development of Nanosilver and Multi-Walled Carbon Nanotubes Thin-Film Nanocomposite Membrane for Enhanced Water Treatment.* Journal of Membrane Science, 2012. **394**: p. 37-48.

225. Cohen-Tanugi, D. and J.C. Grossman, *Water Desalination across Nanoporous Graphene.* Nano Letters, 2012. **12**(7): p. 3602-3608.

226. Choi, W., J. Choi, J. Bang, and J.H. Lee, *Layer-by-Layer Assembly of Graphene Oxide Nanosheets on Polyamide Membranes for Durable Reverse-Osmosis Applications.* Acs Applied Materials & Interfaces, 2013. **5**(23): p. 12510-12519.

227. Balta, S., A. Sotto, P. Luis, L. Benea, B. Van der Bruggen, and J. Kim, *A New Outlook on Membrane Enhancement with Nanoparticles: The Alternative of Zno.* Journal of Membrane Science, 2012. **389**: p. 155-161.

228. Lee, H.S., S.J. Im, J.H. Kim, H.J. Kim, J.P. Kim, and B.R. Min, *Polyamide Thin-Film Nanofiltration Membranes Containing Tio2 Nanoparticles.* Desalination, 2008. **219**(1-3): p. 48-56.

229. Tiraferri, A., Y. Kang, E.P. Giannelis, and M. Elimelech, *Highly Hydrophilic Thin-Film Composite Forward Osmosis Membranes Functionalized with Surface-Tailored Nanoparticles.* Acs Applied Materials & Interfaces, 2012. **4**(9): p. 5044-5053.

230. Emadzadeh, D., W.J. Lau, T. Matsuura, M. Rahbari-Sisakht, and A.F. Ismail, *A Novel Thin Film Composite Forward Osmosis Membrane Prepared from Psf-Tio2 Nanocomposite Substrate for Water Desalination.* Chemical Engineering Journal, 2014. **237**: p. 70-80.

231. Yin, J., E.S. Kim, J. Yang, and B.L. Deng, *Fabrication of a Novel Thin-Film Nanocomposite (Tfn) Membrane Containing Mcm-41 Silica Nanoparticles (Nps) for Water Purification.* Journal of Membrane Science, 2012. **423**: p. 238-246.

232. Jeong, B.H., E.M.V. Hoek, Y.S. Yan, A. Subramani, X.F. Huang, G. Hurwitz, A.K. Ghosh, and A. Jawor, *Interfacial Polymerization of Thin Film Nanocomposites: A New Concept for Reverse Osmosis Membranes.* Journal of Membrane Science, 2007. **294**(1-2): p. 1-7.

233. Lind, M.L., A.K. Ghosh, A. Jawor, X.F. Huang, W. Hou, Y. Yang, and E.M.V. Hoek, *Influence of Zeolite Crystal Size on Zeolite-Polyamide Thin Film Nanocomposite Membranes.* Langmuir, 2009. **25**(17): p. 10139-10145.

234. Fathizadeh, M., A. Aroujalian, and A. Raisi, *Effect of Added Nax Nano-Zeolite into Polyamide as a Top Thin Layer of Membrane on Water Flux and Salt Rejection in a Reverse Osmosis Process.* Journal of Membrane Science, 2011. **375**(1-2): p. 88-95.

235. Huang, H., X.Y. Qu, H. Dong, L. Zhang, and H.L. Chen, *Role of Naa Zeolites in the Interfacial Polymerization Process Towards a Polyamide Nanocomposite Reverse Osmosis Membrane.* Rsc Advances, 2013. **3**(22): p. 8203-8207.

236. Liu, N., L.X. Li, B. McPherson, and R. Lee, *Removal of Organics from Produced Water by Reverse Osmosis Using Mfi-Type Zeolite Membranes.* Journal of Membrane Science, 2008. **325**(1): p. 357-361.

237. Li, L.X. and R. Lee, *Purification of Produced Water by Ceramic Membranes: Material Screening, Process Design and Economics.* Separation Science and Technology, 2009. **44**(15): p. 3455-3484.

238. Das, R., M.E. Ali, S.B. Abd Hamid, S. Ramakrishna, and Z.Z. Chowdhury, *Carbon Nanotube Membranes for Water Purification: A Bright Future in Water Desalination.* Desalination, 2014. **336**: p. 97-109.

239. Das, R., S.B.A. Hamid, M.E. Ali, A.F. Ismail, M.S.M. Annuar, and S. Ramakrishna, *Multifunctional Carbon Nanotubes in Water Treatment: The Present, Past and Future.* Desalination, 2014. **354**: p. 160-179.

240. Ahn, C.H., Y. Baek, C. Lee, S.O. Kim, S. Kim, S. Lee, S.H. Kim, S.S. Bae, J. Park, and J. Yoon, *Carbon Nanotube-Based Membranes: Fabrication and Application to Desalination.* Journal of Industrial and Engineering Chemistry, 2012. **18**(5): p. 1551-1559.

241. Ma, H.Y., C. Burger, B.S. Hsiao, and B. Chu, *Highly Permeable Polymer Membranes Containing Directed Channels for Water Purification.* Acs Macro Letters, 2012. **1**(6): p. 723-726.

242. Adhikari, M. and S.K. Ghosh, *Microporous Clay Membrane Materials for Reverse-Osmosis Applications .1. Performance-Characteristics from Osmotic Studies.* Journal of Applied Polymer Science, 1989. **37**(4): p. 1125-1136.

243. Tarasevich, Y.I., *Application of Natural Adsorbents and Adsorption-Active Materials Based Thereon in the Processes of Water Purification,* in *Adsorption and Its Applications in Industry and Environmental Protection, Vol Ii: Applications in Environmental Protection,* A. Dabrowski, Editor. 1999, Elsevier Science Bv: Amsterdam. p. 659-722.

244. Abbasi, M., A. Salahi, M. Mirfendereski, T. Mohammadi, F. Rekabdar, and M. Hemmati, *Oily Wastewater Treatment Using Mullite Ceramic Membrane.* Desalination and Water Treatment, 2012. **37**(1-3): p. 21-30.

245. Lutkenhaus, J.L., E.A. Olivetti, E.A. Verploegen, B.M. Cord, D.R. Sadoway, and P.T. Hammond, *Anisotropic Structure and Transport in Self-Assembled Layered Polymer-Clay Nanocomposites.* Langmuir, 2007. **23**(16): p. 8515-8521.

246. Decher, G., *Fuzzy Nanoassemblies: Toward Layered Polymeric Multicomposites.* Science, 1997. **277**(5330): p. 1232-1237.

247. Kharlampieva, E. and S.A. Sukhishvili, *Hydrogen-Bonded Layer-by-Layer Polymer Films.* Polymer Reviews, 2006. **46**(4): p. 377-395.

248. Hoogeveen, N.G., M.A.C. Stuart, G.J. Fleer, and M.R. Bohmer, *Formation and Stability of Multilayers of Polyelectrolytes.* Langmuir, 1996. **12**(15): p. 3675-3681.

249. Clark, S.L. and P.T. Hammond, *Engineering the Microfabrication of Layer-by-Layer Thin Films.* Advanced Materials, 1998. **10**(18): p. 1515-+.

250. Park, S.Y., M.F. Rubner, and A.M. Mayes, *Free Energy Model for Layer-by-Layer Processing of Polyelectrolyte Multilayer Films.* Langmuir, 2002. **18**(24): p. 9600-9604.

251. Shiratori, S.S. and M.F. Rubner, *Ph-Dependent Thickness Behavior of Sequentially Adsorbed Layers of Weak Polyelectrolytes.* Macromolecules, 2000. **33**(11): p. 4213-4219.

252. Bertrand, P., A. Jonas, A. Laschewsky, and R. Legras, *Ultrathin Polymer Coatings by Complexation of Polyelectrolytes at Interfaces: Suitable Materials, Structure and Properties.* Macromolecular Rapid Communications, 2000. **21**(7): p. 319-348.

253. Picart, C., P. Lavalle, P. Hubert, F.J.G. Cuisinier, G. Decher, P. Schaaf, and J.C. Voegel, *Buildup Mechanism for Poly(L-Lysine)/Hyaluronic Acid Films onto a Solid Surface.* Langmuir, 2001. **17**(23): p. 7414-7424.

254. Choi, J. and M.F. Rubner, *Influence of the Degree of Ionization on Weak Polyelectrolyte Multilayer Assembly.* Macromolecules, 2005. **38**(1): p. 116-124.

255. Porcel, C., P. Lavalle, G. Decher, B. Senger, J.C. Voegel, and P. Schaaf, *Influence of the Polyelectrolyte Molecular Weight on Exponentially Growing Multilayer Films in the Linear Regime.* Langmuir, 2007. **23**(4): p. 1898-1904.

256. Lavalle, P., C. Picart, J. Mutterer, C. Gergely, H. Reiss, J.C. Voegel, B. Senger, and P. Schaaf, *Modeling the Buildup of Polyelectrolyte Multilayer Films Having Exponential Growth.* Journal of Physical Chemistry B, 2004. **108**(2): p. 635-648.

257. Elzbieciak-Wodka, M., M. Kolasinska-Sojka, P. Nowak, and P. Warszynski, *Comparison of Permeability of Poly(Allylamine Hydrochloride)/and Poly(Diallyldimethylammonium Chloride)/Poly(4-Styrenesulfonate) Multilayer Films: Linear Vs. Exponential Growth.* Journal of Electroanalytical Chemistry, 2015. **738**: p. 195-202.

258. Mamedov, A.A., N.A. Kotov, M. Prato, D.M. Guldi, J.P. Wicksted, and A. Hirsch, *Molecular Design of Strong Single-Wall Carbon Nanotube/Polyelectrolyte Multilayer Composites.* Nature Materials, 2002. **1**(3): p. 190-194.

259. Hong, T.K., D.W. Lee, H.J. Choi, H.S. Shin, and B.S. Kim, *Transparent, Flexible Conducting Hybrid Multi Layer Thin Films of Multiwalled Carbon Nanotubes with Graphene Nanosheets.* Acs Nano, 2010. **4**(7): p. 3861-3868.

260. Srivastava, S. and N.A. Kotov, *Composite Layer-by-Layer (Lbl) Assembly with Inorganic Nanoparticles and Nanowires.* Accounts of Chemical Research, 2008. **41**(12): p. 1831-1841.

261. Kotov, N.A., I. Dekany, and J.H. Fendler, *Layer-by-Layer Self-Assembly of Polyelectrolyte-Semiconductor Nanoparticle Composite Films.* Journal of Physical Chemistry, 1995. **99**(35): p. 13065-13069.

262. Lee, D., M.F. Rubner, and R.E. Cohen, *All-Nanoparticle Thin-Film Coatings.* Nano Letters, 2006. **6**(10): p. 2305-2312.

263. Batys, P. and P. Weronski, *Porosity and Tortuosity of Layer-by-Layer Assemblies of Spherical Particles.* Modelling and Simulation in Materials Science and Engineering, 2014. **22**(6).

264. Keller, S.W., H.N. Kim, and T.E. Mallouk, *Layer-by-Layer Assembly of Intercalation Compounds and Heterostructures on Surfaces - toward Molecular Beaker Epitaxy.* Journal of the American Chemical Society, 1994. **116**(19): p. 8817-8818.

265. Fendler, J.H., *Self-Assembled Nanostructured Materials.* Chemistry of Materials, 1996. **8**(8): p. 1616-1624.

266. Findenig, G., R. Kargl, K. Stana-Keinschek, and V. Ribitsch, *Interaction and Structure in Polyelectrolyte/Clay Multilayers: A Qcm-D Study.* Langmuir, 2013. **29**(27): p. 8544-8553.

267. Szabo, T.S., M. Szekeres, I. Dekany, C. Jackers, S. De Feyter, C.T. Johnston, and R.A. Schoonheydt, *Layer-by-Layer Construction of Ultrathin Hybrid Films with Proteins and Clay Minerals.* Journal of Physical Chemistry C, 2007. **111**(34): p. 12730-12740.

268. Chen, C.M., Q.H. Yang, Y.G. Yang, W. Lv, Y.F. Wen, P.X. Hou, M.Z. Wang, and H.M. Cheng, *Self-Assembled Free-Standing Graphite Oxide Membrane.* Advanced Materials, 2009. **21**(29): p. 3007-+.

269. Kuila, T., S. Bose, A.K. Mishra, P. Khanra, N.H. Kim, and J.H. Lee, *Chemical Functionalization of Graphene and Its Applications.* Progress in Materials Science, 2012. **57**(7): p. 1061-1105.

270. Yang, M., Y. Hou, and N.A. Kotov, *Graphene-Based Multilayers: Critical Evaluation of Materials Assembly Techniques.* Nano Today, 2012. **7**(5): p. 430-447.

271. Ariga, K., Y. Lvov, and T. Kunitake, *Assembling Alternate Dye-Polyion Molecular Films by Electrostatic Layer-by-Layer Adsorption.* Journal of the American Chemical Society, 1997. **119**(9): p. 2224-2231.

272. Becker, A.L., A.P.R. Johnston, and F. Caruso, *Layer-by-Layer-Assembled Capsules and Films for Therapeutic Delivery.* Small, 2010. **6**(17): p. 1836-1852.

273. Johnston, A.P.R., C. Cortez, A.S. Angelatos, and F. Caruso, *Layer-by-Layer Engineered Capsules and Their Applications.* Current Opinion in Colloid & Interface Science, 2006. **11**(4): p. 203-209.

274. Shukla, A., S.N. Avadhany, J.C. Fang, and P.T. Hammond, *Tunable Vancomycin Releasing Surfaces for Biomedical Applications.* Small, 2010. **6**(21): p. 2392-2404.

275. Shmueli, R.B., D.G. Anderson, and J.J. Green, *Electrostatic Surface Modifications to Improve Gene Delivery.* Expert Opinion on Drug Delivery, 2010. **7**(4): p. 535-550.

276. Johnston, A.P.R., G.K. Such, S.L. Ng, and F. Caruso, *Challenges Facing Colloidal Delivery Systems: From Synthesis to the Clinic.* Current Opinion in Colloid & Interface Science, 2011. **16**(3): p. 171-181.

277. Elbakry, A., A. Zaky, R. Liebkl, R. Rachel, A. Goepferich, and M. Breunig, *Layer-by-Layer Assembled Gold Nanoparticles for Sirna Delivery.* Nano Letters, 2009. **9**(5): p. 2059-2064.

278. Castleberry, S., M. Wang, and P.T. Hammond, *Nanolayered Sirna Dressing for Sustained Localized Knockdown.* Acs Nano, 2013. **7**(6): p. 5251-5261.

279. Boudou, T., T. Crouzier, K.F. Ren, G. Blin, and C. Picart, *Multiple Functionalities of Polyelectrolyte Multilayer Films: New Biomedical Applications.* Advanced Materials, 2010. **22**(4): p. 441-467.

280. Picart, C., *Polyelectrolyte Multilayer Films: From Physico-Chemical Properties to the Control of Cellular Processes.* Current Medicinal Chemistry, 2008. **15**(7): p. 685-697.

281. Ariga, K., J.P. Hill, and Q.M. Ji, *Biomaterials and Biofunctionality in Layered Macromolecular Assemblies.* Macromolecular Bioscience, 2008. **8**(11): p. 981-990.

282. Hammond, P.T., *Polyelectrolyte Multilayered Nanoparticles: Using Nanolayers for Controlled and Targeted Systemic Release.* Nanomedicine, 2012. **7**(5): p. 619-622.

283. Zhou, Y.L., N.F. Hu, Y.H. Zeng, and J.F. Rusling, *Heme Protein-Clay Films: Direct Electrochemistry and Electrochemical Catalysis.* Langmuir, 2002. **18**(1): p. 211-219.

284. Ariga, K., J.P. Hill, M.V. Lee, A. Vinu, R. Charvet, and S. Acharya, *Challenges and Breakthroughs in Recent Research on Self-Assembly.* Science and Technology of Advanced Materials, 2008. **9**(1).

285. Wang, Y., A.S. Angelatos, and F. Caruso, *Template Synthesis of Nanostructured Materials Via Layer-by-Layer Assembly.* Chemistry of Materials, 2008. **20**(3): p. 848-858.

286. Shimomura, M. and T. Sawadaishi, *Bottom-up Strategy of Materials Fabrication: A New Trend in Nanotechnology of Soft Materials.* Current Opinion in Colloid & Interface Science, 2001. **6**(1): p. 11-16.

287. Lu, C.H., I. Donch, M. Nolte, and A. Fery, *Au Nanoparticle-Based Multilayer Ultrathin Films with Covalently Linked Nanostructures: Spraying Layer-by-Layer Assembly and Mechanical Property Characterization.* Chemistry of Materials, 2006. **18**(26): p. 6204-6210.

288. Hammond, P.T., *Form and Function in Multilayer Assembly: New Applications at the Nanoscale.* Advanced Materials, 2004. **16**(15): p. 1271-1293.

289. Clark, S.L. and P.T. Hammond, *The Role of Secondary Interactions in Selective Electrostatic Multilayer Deposition.* Langmuir, 2000. **16**(26): p. 10206-10214.

290. Lutkenhaus, J.L., K. McEnnis, and P.T. Hammond, *Nano- and Microporous Layer-by-Layer Assemblies Containing Linear Poly(Ethylenimine) and Poly(Acrylic Acid).* Macromolecules, 2008. **41**(16): p. 6047-6054.

291. Jaber, J.A. and J.B. Schlenoff, *Recent Developments in the Properties and Applications of Polyelectrolyte Multilayers.* Current Opinion in Colloid & Interface Science, 2006. **11**(6): p. 324-329.

292. Hammond, P.T., *Recent Explorations in Electrostatic Multilayer Thin Film Assembly.* Current Opinion in Colloid & Interface Science, 1999. **4**(6): p. 430-442.

293. Hammond, P.T., *Building Biomedical Materials Layer-by-Layer.* Materials Today, 2012. **15**(5): p. 196-206.

294. Sukhishvili, S.A., *Responsive Polymer Films and Capsules Via Layer-by-Layer Assembly.* Current Opinion in Colloid & Interface Science, 2005. **10**(1-2): p. 37-44.

295. Ariga, K., Y. Yamauchi, G. Rydzek, Q.M. Ji, Y. Yonamine, K.C.W. Wu, and J.P. Hill, *Layer-by-Layer Nanoarchitectonics: Invention, Innovation, and Evolution.* Chemistry Letters, 2014. **43**(1): p. 36-68.

296. Joseph, N., P. Ahmadiannamini, R. Hoogenboom, and I.F.J. Vankelecom, *Layer-by-Layer Preparation of Polyelectrolyte Multilayer Membranes for Separation.* Polymer Chemistry, 2014. **5**(6): p. 1817-1831.

297. Ai, H., S.A. Jones, and Y.M. Lvov, *Biomedical Applications of Electrostatic Layer-by-Layer Nano-Assembly of Polymers, Enzymes, and Nanoparticles.* Cell Biochemistry and Biophysics, 2003. **39**(1): p. 23-43.

298. Siqueira, J.R., L. Caseli, F.N. Crespilho, V. Zucolotto, and O.N. Oliveira, *Immobilization of Biomolecules on Nanostructured Films for Biosensing.* Biosensors & Bioelectronics, 2010. **25**(6): p. 1254-1263.

299. Iost, R.M. and F.N. Crespilho, *Layer-by-Layer Self-Assembly and Electrochemistry: Applications in Biosensing and Bioelectronics.* Biosensors & Bioelectronics, 2012. **31**(1): p. 1-10.

300. Lutkenhaus, J.L. and P.T. Hammond, *Electrochemically Enabled Polyelectrolyte Multilayer Devices: From Fuel Cells to Sensors.* Soft Matter, 2007. **3**(7): p. 804-816.

301. Xiang, Y., S.F. Lu, and S.P. Jiang, *Layer-by-Layer Self-Assembly in the Development of Electrochemical Energy Conversion and Storage Devices from Fuel Cells to Supercapacitors.* Chemical Society Reviews, 2012. **41**(21): p. 7291-7321.

302. Eckle, M. and G. Decher, *Tuning the Performance of Layer-by-Layer Assembled Organic Light Emitting Diodes by Controlling the Position of Isolating Clay Barrier Sheets.* Nano Letters, 2001. **1**(1): p. 45-49.

303. Bhattacharya, P., S. Ghosh, and A.D. Stiff-Roberts, *Quantum Dot Opto-Electronic Devices.* Annual Review of Materials Research, 2004. **34**: p. 1-40.

304. DeLongchamp, D. and P.T. Hammond, *Layer-by-Layer Assembly of Pedot/Polyaniline Electrochromic Devices.* Advanced Materials, 2001. **13**(19): p. 1455-+.

305. Qi, M.H., E. Lidorikis, P.T. Rakich, S.G. Johnson, J.D. Joannopoulos, E.P. Ippen, and H.I. Smith, *A Three-Dimensional Optical Photonic Crystal with Designed Point Defects.* Nature, 2004. **429**(6991): p. 538-542.

306. Farhat, T.R. and J.B. Schlenoff, *Ion Transport and Equilibria in Polyelectrolyte Multilayers.* Langmuir, 2001. **17**(4): p. 1184-1192.

307. Zhuk, A., R. Mirza, and S. Sukhishvili, *Multiresponsive Clay-Containing Layer-by-Layer Films.* Acs Nano, 2011. **5**(11): p. 8790-8799.

308. Priolo, M.A., K.M. Holder, T. Guin, and J.C. Grunlan, *Recent Advances in Gas Barrier Thin Films Via Layer-by-Layer Assembly of Polymers and Platelets.* Macromolecular Rapid Communications, 2015: p. n/a-n/a.

309. Zhao, L.L., H.X. Sun, N. Kim, J. Lee, Y. Kong, and P. Li, *Hydrogen Gas Barrier Property of Polyelectrolyte/Go Layer-by-Layer Films.* Journal of Applied Polymer Science, 2015. **132**(20).

310. von Klitzing, R. and B. Tieke, *Polyelectrolyte Membranes.* Polyelectrolytes with Defined Molecular Architecture I, 2004. **165**: p. 177-210.

311. El-Hashani, A., A. Toutianoush, and B. Tieke, *Use of Layer-by-Layer Assembled Ultrathin Membranes of Dicopper- 18 Azacrown-N-6 Complex and Polyvinylsulfate for Water Desalination under Nanofiltration Conditions.* Journal of Membrane Science, 2008. **318**(1-2): p. 65-70.

312. Ritcharoen, W., P. Supaphol, and P. Pavasant, *Development of Polyelectrolyte Multilayer-Coated Electrospun Cellulose Acetate Fiber Mat as Composite Membranes.* European Polymer Journal, 2008. **44**(12): p. 3963-3968.

313. Qiu, C.Q., S.R. Qi, and C.Y.Y. Tang, *Synthesis of High Flux Forward Osmosis Membranes by Chemically Crosslinked Layer-by-Layer Polyelectrolytes.* Journal of Membrane Science, 2011. **381**(1-2): p. 74-80.

314. Jin, W.Q., A. Toutianoush, and B. Tieke, *Use of Polyelectrolyte Layer-by-Layer Assemblies as Nanofiltration and Reverse Osmosis Membranes.* Langmuir, 2003. **19**(7): p. 2550-2553.

315. Fadhillah, F., S.M.J. Zaidi, Z. Khan, M.M. Khaled, F. Rahman, and P.T. Hammond, *Development of Polyelectrolyte Multilayer Thin Film Composite Membrane for Water Desalination Application.* Desalination, 2013. **318**: p. 19-24.

316. Gu, J.E., S. Lee, C.M. Stafford, J.S. Lee, W. Choi, B.Y. Kim, K.Y. Baek, E.P. Chan, J.Y. Chung, J. Bang, and J.H. Lee, *Molecular Layer-by-Layer Assembled Thin-Film Composite Membranes for Water Desalination.* Advanced Materials, 2013. **25**(34): p. 4778-4782.

317. Krogman, K.C., N.S. Zacharia, S. Schroeder, and P.T. Hammond, *Automated Process for Improved Uniformity and Versatility of Layer-by-Layer Deposition.* Langmuir, 2007. **23**(6): p. 3137-3141.

318. Izquierdo, A., S.S. Ono, J.C. Voegel, P. Schaaf, and G. Decher, *Dipping Versus Spraying: Exploring the Deposition Conditions for Speeding up Layer-by-Layer Assembly.* Langmuir, 2005. **21**(16): p. 7558-7567.

319. Porcel, C.H., A. Izquierdo, V. Ball, G. Decher, J.C. Voegel, and P. Schaaf, *Ultrathin Coatings and (Poly(Glutamic Acid)/Polyallylamine) Films Deposited by Continuous and Simultaneous Spraying.* Langmuir, 2005. **21**(2): p. 800-802.

320. Krogman, K.C., J.L. Lowery, N.S. Zacharia, G.C. Rutledge, and P.T. Hammond, *Spraying Asymmetry into Functional Membranes Layer-by-Layer.* Nature Materials, 2009. **8**(6): p. 512-518.

321. Kolasinska, M., R. Krastev, T. Gutberlet, and P. Warszynski, *Layer-by-Layer Deposition of Polyelectrolytes. Dipping Versus Spraying.* Langmuir, 2009. **25**(2): p. 1224-1232.

322. Schaaf, P., J.C. Voegel, L. Jierry, and F. Boulmedais, *Spray-Assisted Polyelectrolyte Multilayer Buildup: From Step-by-Step to Single-Step Polyelectrolyte Film Constructions.* Advanced Materials, 2012. **24**(8): p. 1001-1016.

323. Nogueira, G.M., D. Banerjee, R.E. Cohen, and M.F. Rubner, *Spray-Layer-by-Layer Assembly Can More Rapidly Produce Optical-Quality Multistack Heterostructures.* Langmuir, 2011. **27**(12): p. 7860-7867.

324. Yang, Y.H., F.A. Malek, and J.C. Grunlan, *Influence of Deposition Time on Layer-by-Layer Growth of Clay-Based Thin Films.* Industrial & Engineering Chemistry Research, 2010. **49**(18): p. 8501-8509.

325. Kim, D.W., J. Kumar, and A. Blumstein, *Ordered Assembly of Conjugated Ionic Polyacetylenes within Clay Nanoplatelets: Layer-by-Layer Assembly and Intercalative Polymerization.* Applied Clay Science, 2005. **30**(2): p. 134-140.

326. Podsiadlo, P., M. Michel, J. Lee, E. Verploegen, N.W.S. Kam, V. Ball, J. Lee, Y. Qi, A.J. Hart, P.T. Hammond, and N.A. Kotov, *Exponential Growth of Lbl Films with Incorporated Inorganic Sheets.* Nano Letters, 2008. **8**(6): p. 1762-1770.

327. Malaisamy, R. and M.L. Bruening, *High-Flux Nanofiltration Membranes Prepared by Adsorption of Multilayer Polyelectrolyte Membranes on Polymeric Supports.* Langmuir, 2005. **21**(23): p. 10587-10592.

328. Park, J., J. Park, S.H. Kim, J. Cho, and J. Bang, *Desalination Membranes from Ph-Controlled and Thermally-Crosslinked Layer-by-Layer Assembled Multilayers.* Journal of Materials Chemistry, 2010. **20**(11): p. 2085-2091.

329. Hoffmann, K., T. Friedrich, and B. Tieke, *Layer-by-Layer Assembled Polyelectrolyte Blend Membranes and Their Use for Ion Separation and Rejection.* Polymer Engineering and Science, 2011. **51**(8): p. 1497-1506.

330. Lajimi, R.H., A.B. Abdallah, E. Ferjani, M.S. Roudesli, and A. Deratani, *Change of the Performance Properties of Nanofiltration Cellulose Acetate Membranes by Surface Adsorption of Polyelectrolyte Multilayers.* Desalination, 2004. **163**(1–3): p. 193-202.

331. Liu, X.Y. and M.L. Bruening, *Size-Selective Transport of Uncharged Solutes through Multilayer Polyelectrolyte Membranes.* Chemistry of Materials, 2004. **16**(2): p. 351-357.
332. Harris, J.J., J.L. Stair, and M.L. Bruening, *Layered Polyelectrolyte Films as Selective, Ultrathin Barriers for Anion Transport.* Chemistry of Materials, 2000. **12**(7): p. 1941-1946.
333. Cho, K.L., A.J. Hill, F. Caruso, and S.E. Kentish, *Chlorine Resistant Glutaraldehyde Crosslinked Polyelectrolyte Multilayer Membranes for Desalination.* Advanced Materials, 2015: p. n/a-n/a.
334. Persson, K.M., V. Gekas, and G. Tragardh, *Study of Membrane Compaction and Its Influence on Ultrafiltration Water Permeability.* Journal of Membrane Science, 1995. **100**(2): p. 155-162.
335. Choong, L.T., M.M. Mannarino, S. Basu, and G.C. Rutledge, *Compressibility of Electrospun Fiber Mats.* Journal of Materials Science, 2013. **48**(22): p. 7827-7836.
336. Lowery, J.L., N. Datta, and G.C. Rutledge, *Effect of Fiber Diameter, Pore Size and Seeding Method on Growth of Human Dermal Fibroblasts in Electrospun Poly(Epsilon-Caprolactone) Fibrous Mats.* Biomaterials, 2010. **31**(3): p. 491-504.
337. Wang, R., Y. Liu, B. Li, B.S. Hsiao, and B. Chu, *Electrospun Nanofibrous Membranes for High Flux Microfiltration.* Journal of Membrane Science, 2012. **392**: p. 167-174.
338. Kalia, S., B.S. Kaith, and I. Kaur, *Pretreatments of Natural Fibers and Their Application as Reinforcing Material in Polymer Composites-a Review.* Polymer Engineering and Science, 2009. **49**(7): p. 1253-1272.
339. Liston, E.M., L. Martinu, and M.R. Wertheimer, *Plasma Surface Modification of Polymers for Improved Adhesion - a Critical-Review.* Journal of Adhesion Science and Technology, 1993. **7**(10): p. 1091-1127.
340. Wang, Y.J., L. Lu, Y.D. Zheng, and X.F. Chen, *Improvement in Hydrophilicity of Phbv Films by Plasma Treatment.* Journal of Biomedical Materials Research Part A, 2006. **76A**(3): p. 589-595.
341. Saitoh, K., M. Kondo, M. Fukawa, T. Nishimiya, A. Matsuda, W. Futako, and I. Shimizu, *Role of the Hydrogen Plasma Treatment in Layer-by-Layer Deposition of Microcrystalline Silicon.* Applied Physics Letters, 1997. **71**(23): p. 3403-3405.
342. Lee, C.K., A.S.T. Chiang, and C.S. Tsay, *The Characterization of Porous Solids from Gas Adsorption Measurements.* Porous Ceramic Materials, 1996. **115**: p. 21-43.
343. Barrett, E.P., L.G. Joyner, and P.P. Halenda, *The Determination of Pore Volume and Area Distributions in Porous Substances. I. Computations from Nitrogen Isotherms.* Journal of the American Chemical society, 1951. **73**(1): p. 373-380.
344. Liu, D.S., J.N. Ashcraft, M.M. Mannarino, M.N. Silberstein, A.A. Argun, G.C. Rutledge, M.C. Boyce, and P.T. Hammond, *Spray Layer-by-Layer Electrospun Composite Proton Exchange Membranes.* Advanced Functional Materials, 2013. **23**(24): p. 3087-3095.
345. Mannarino, M.M., D.S. Liu, P.T. Hammond, and G.C. Rutledge, *Mechanical and Transport Properties of Layer-by-Layer Electrospun Composite Proton Exchange Membranes for Fuel Cell Applications.* Acs Applied Materials & Interfaces, 2013. **5**(16): p. 8155-8164.
346. Glinel, K., A. Laschewsky, and A.M. Jonas, *Ordered Polyelectrolyte "Multilayers". 3. Complexing Clay Platelets with Polycations of Varying Structure.* Macromolecules, 2001. **34**(15): p. 5267-5274.
347. Puhr, J.T., B.E. Swerdlow, D.K. Reid, and J.L. Lutkenhaus, *The Effect of Nanoparticle Location and Shape on Thermal Transitions Observed in Hydrated Layer-by-Layer Assemblies.* Soft Matter, 2014. **10**(40): p. 8107-8115.
348. Min, J., R.D. Braatz, and P.T. Hammond, *Tunable Staged Release of Therapeutics from Layer-by-Layer Coatings with Clay Interlayer Barrier.* Biomaterials, 2014. **35**(8): p. 2507-2517.
349. Rodionova, G.P., A.A. Perminov, and N.S. Smirnov, *Comparative-Study of Natural Clays and the Synthetic Clay Laponite.* Glass and Ceramics, 1978. **35**(11-1): p. 743-745.

350. Thompson, D.W. and J.T. Butterworth, *The Nature of Laponite and Its Aqueous Dispersions.* Journal of Colloid and Interface Science, 1992. **151**(1): p. 236-243.

351. Shalkevich, A., A. Stradner, S.K. Bhat, F. Muller, and P. Schurtenberger, *Cluster, Glass, and Gel Formation and Viscoelastic Phase Separation in Aqueous Clay Suspensions.* Langmuir, 2007. **23**(7): p. 3570-3580.

352. Nicolai, T. and S. Cocard, *Light Scattering Study of the Dispersion of Laponite.* Langmuir, 2000. **16**(21): p. 8189-8193.

353. Mongondry, P., J.F. Tassin, and T. Nicolai, *Revised State Diagram of Laponite Dispersions.* Journal of Colloid and Interface Science, 2005. **283**(2): p. 397-405.

354. Mourchid, A. and P. Levitz, *Long-Term Gelation of Laponite Aqueous Dispersions.* Physical Review E, 1998. **57**(5): p. R4887-R4890.

355. Huang, A.Y. and J.C. Berg, *High-Salt Stabilization of Laponite Clay Particles.* Journal of Colloid and Interface Science, 2006. **296**(1): p. 159-164.

356. Leach, E.S.H., A. Hopkinson, K. Franklin, and J.S. van Duijneveldt, *Nonaqueous Suspensions of Laponite and Montmorillonite.* Langmuir, 2005. **21**(9): p. 3821-3830.

357. Ray, S.S. and M. Okamoto, *Polymer/Layered Silicate Nanocomposites: A Review from Preparation to Processing.* Progress in Polymer Science, 2003. **28**(11): p. 1539-1641.

358. Podsiadlo, P., S. Paternel, J.M. Rouillard, Z.F. Zhang, J. Lee, J.W. Lee, L. Gulari, and N.A. Kotov, *Layer-by-Layer Assembly of Nacre-Like Nanostructured Composites with Antimicrobial Properties.* Langmuir, 2005. **21**(25): p. 11915-11921.

359. Zhou, Y.L., Z. Li, N.F. Hu, Y.H. Zeng, and J.F. Rusling, *Layer-by-Layer Assembly of Ultrathin Films of Hemoglobin and Clay Nanoparticles with Electrochemical and Catalytic Activity.* Langmuir, 2002. **18**(22): p. 8573-8579.

360. Nicolai, T. and S. Cocard, *Structure of Gels and Aggregates of Disk-Like Colloids.* European Physical Journal E, 2001. **5**(2): p. 221-227.

361. Krogman, K.C., *Functionalized Multilayer Thin Films for Protection against Acutely Toxic Agents*, in *Department of Chemical Engineering*. 2009, Massachusetts Institute of Technology: Massachusetts Institute of Technology.

362. Gifford, J.H., *Optimization of the Automated Spray Layer-by-Layer Technique for Thin Film Deposition*, in *Department of Chemical Engineering*. 2010, Massachusetts Institute of Technology: Massachusetts Institute of Technology.

363. Wavhal, D.S. and E.R. Fisher, *Hydrophilic Modification of Polyethersulfone Membranes by Low Temperature Plasma-Induced Graft Polymerization.* Journal of Membrane Science, 2002. **209**(1): p. 255-269.

364. Lavalle, P., J.C. Voegel, D. Vautier, B. Senger, P. Schaaf, and V. Ball, *Dynamic Aspects of Films Prepared by a Sequential Deposition of Species: Perspectives for Smart and Responsive Materials.* Advanced Materials, 2011. **23**(10): p. 1191-1221.

365. Porcel, C., P. Lavalle, V. Ball, G. Decher, B. Senger, J.C. Voegel, and P. Schaaf, *From Exponential to Linear Growth in Polyelectrolyte Multilayers.* Langmuir, 2006. **22**(9): p. 4376-4383.

366. Rmaile, H.H. and J.B. Schlenoff, *"Internal Pk(a)'S" in Polyelectrolyte Multilayers: Coupling Protons And.* Langmuir, 2002. **18**(22): p. 8263-8265.

367. Glinel, K., A. Moussa, A.M. Jonas, and A. Laschewsky, *Influence of Polyelectrolyte Charge Density on the Formation of Multilayers of Strong Polyelectrolytes at Low Ionic Strength.* Langmuir, 2002. **18**(4): p. 1408-1412.

368. Schonhoff, M., *Layered Polyelectrolyte Complexes: Physics of Formation and Molecular Properties.* Journal of Physics-Condensed Matter, 2003. **15**(49): p. R1781-R1808.

369. Francis, S., L. Varshney, and S. Sabharwal, *Thermal Degradation Behavior of Radiation Synthesized Polydiallyldimethylammonium Chloride.* European Polymer Journal, 2007. **43**(6): p. 2525-2531.

370. Saetia, K., *Layer-by-Layer Carbon Nanotube Electrodes for Flexible Chemical Sensor and Energy Storage Applications*, in *Department of Chemical Engineering*. 2013, Massachusetts Institute of Technology: Massachusetts Institute of Technology.

371. Laugel, N., J. Hemmerlé, C. Porcel, J.-C. Voegel, P. Schaaf, and V. Ball, *Nanocomposite Silica/Polyamine Films Prepared by a Reactive Layer-by-Layer Deposition.* Langmuir, 2007. **23**(7): p. 3706-3711.

372. Yoo, D., S.S. Shiratori, and M.F. Rubner, *Controlling Bilayer Composition and Surface Wettability of Sequentially Adsorbed Multilayers of Weak Polyelectrolytes.* Macromolecules, 1998. **31**(13): p. 4309-4318.

373. Cranford, S.W., C. Ortiz, and M.J. Buehler, *Mechanomutable Properties of a Paa/Pah Polyelectrolyte Complex: Rate Dependence and Ionization Effects on Tunable Adhesion Strength.* Soft Matter, 2010. **6**(17): p. 4175-4188.

374. Tong, W. and C. Gao, *Stable Microcapsules Assembled Stepwise from Weak Polyelectrolytes Followed by Thermal Crosslinking.* Polymers for Advanced Technologies, 2005. **16**(11-12): p. 827-833.

375. Harris, J.J., P.M. DeRose, and M.L. Bruening, *Synthesis of Passivating, Nylon-Like Coatings through Cross-Linking of Ultrathin Polyelectrolyte Films.* Journal of the American Chemical Society, 1999. **121**(9): p. 1978-1979.

376. Wood, K.C., H.F. Chuang, R.D. Batten, D.M. Lynn, and P.T. Hammond, *Controlling Interlayer Diffusion to Achieve Sustained, Multiagent Delivery from Layer-by-Layer Thin Films.* Proceedings of the National Academy of Sciences, 2006. **103**(27): p. 10207-10212.

377. Hiller, J.A., J.D. Mendelsohn, and M.F. Rubner, *Reversibly Erasable Nanoporous Anti-Reflection Coatings from Polyelectrolyte Multilayers.* Nature materials, 2002. **1**(1): p. 59-63.

378. Burke, S.E. and C.J. Barrett, *Acid-Base Equilibria of Weak Polyelectrolytes in Multilayer Thin Films.* Langmuir, 2003. **19**(8): p. 3297-3303.

379. Mendelsohn, J.D., C.J. Barrett, V.V. Chan, A.J. Pal, A.M. Mayes, and M.F. Rubner, *Fabrication of Microporous Thin Films from Polyelectrolyte Multilayers.* Langmuir, 2000. **16**(11): p. 5017-5023.

380. Fery, A., B. Scholer, T. Cassagneau, and F. Caruso, *Nanoporous Thin Films Formed by Salt-Induced Structural Changes in Multilayers of Poly(Acrylic Acid) and Poly(Allylamine).* Langmuir, 2001. **17**(13): p. 3779-3783.

381. Harris, J.J. and M.L. Bruening, *Electrochemical and in Situ Ellipsometric Investigation of the Permeability and Stability of Layered Polyelectrolyte Films.* Langmuir, 2000. **16**(4): p. 2006-2013.

382. Alonso, R.H., L. Estevez, H.Q. Lian, A. Kelarakis, and E.P. Giannelis, *Nafion-Clay Nanocomposite Membranes: Morphology and Properties.* Polymer, 2009. **50**(11): p. 2402-2410.

383. Cho, J., J.F. Quinn, and F. Caruso, *Fabrication of Polyelectrolyte Multilayer Films Comprising Nanoblended Layers.* Journal of the American Chemical Society, 2004. **126**(8): p. 2270-2271.

384. Waite, J.H., *Adhesion À La Moule.* Integrative and Comparative Biology, 2002. **42**(6): p. 1172-1180.

385. Wu, J.J., L. Zhang, Y.X. Wang, Y.H. Long, H. Gao, X.L. Zhang, N. Zhao, Y.L. Cai, and J. Xu, *Mussel-Inspired Chemistry for Robust and Surface-Modifiable Multilayer Films.* Langmuir, 2011. **27**(22): p. 13684-13691.

386. Rzepecki, L.M., K.M. Hansen, and J.H. Waite, *Characterization of a Cystine-Rich Polyphenolic Protein Family from the Blue Mussel Mytilus-Edulis-L.* Biological Bulletin, 1992. **183**(1): p. 123-137.

387. Lee, H., S.M. Dellatore, W.M. Miller, and P.B. Messersmith, *Mussel-Inspired Surface Chemistry for Multifunctional Coatings.* Science, 2007. **318**(5849): p. 426-430.

388. Min, Y.J. and P.T. Hammond, *Catechol-Modified Polyions in Layer-by-Layer Assembly to Enhance Stability and Sustain Release of Biomolecules: A Bioinspired Approach.* Chemistry of Materials, 2011. **23**(24): p. 5349-5357.

389. Choi, D. and J. Hong, *Layer-by-Layer Assembly of Multilayer Films for Controlled Drug Release.* Archives of Pharmacal Research, 2014. **37**(1): p. 79-87.

390. Xu, J.K., G.M. Soliman, J. Barralet, and M. Cerruti, *Mollusk Glue Inspired Mucoadhesives for Biomedical Applications.* Langmuir, 2012. **28**(39): p. 14010-14017.

391. Zucolotto, V., A.P.A. Pinto, T. Tumolo, M.L. Moraes, M.S. Baptista, A. Riul, A.P.U. Araujo, and O.N. Oliveira, *Catechol Biosensing Using a Nanostructured Layer-by-Layer Film Containing Cl-Catechol 1,2-Dioxygenase.* Biosensors & Bioelectronics, 2006. **21**(7): p. 1320-1326.

392. Faure, E., C. Falentin-Daudre, C. Jerome, J. Lyskawa, D. Fournier, P. Woisel, and C. Detrembleur, *Catechols as Versatile Platforms in Polymer Chemistry.* Progress in Polymer Science, 2013. **38**(1): p. 236-270.

393. Ma, W., H. Xu, and A. Takahara, *Substrate-Independent Underwater Superoleophobic Surfaces Inspired by Fish-Skin and Mussel-Adhesives.* Advanced Materials Interfaces, 2014. **1**(3).

394. Lee, H., Y. Lee, A.R. Statz, J. Rho, T.G. Park, and P.B. Messersmith, *Substrate-Independent Layer-by-Layer Assembly by Using Mussel-Adhesive-Inspired Polymers.* Advanced Materials, 2008. **20**(9): p. 1619-1623.

395. An, J.H., N.T. Huynh, Y.S. Jeon, and J.H. Kim, *Surface Modification Using Bio-Inspired Adhesive Polymers Based on Polyaspartamide Derivatives.* Polymer International, 2011. **60**(11): p. 1581-1586.

396. Kang, S.M., J. Rho, I.S. Choi, P.B. Messersmith, and H. Lee, *Norepinephrine: Material-Independent, Multifunctional Surface Modification Reagent.* Journal of the American Chemical Society, 2009. **131**(37): p. 13224-13225.

397. Chaubaroux, C., E. Vrana, C. Debry, P. Schaaf, B. Senger, J.C. Voegel, Y. Haikel, C. Ringwald, J. Hemmerle, P. Lavalle, and F. Boulmedais, *Collagen-Based Fibrillar Multilayer Films Cross-Linked by a Natural Agent.* Biomacromolecules, 2012. **13**(7): p. 2128-2135.

398. Podsiadlo, P., Z.Q. Liu, D. Paterson, P.B. Messersmith, and N.A. Kotov, *Fusion of Seashell Nacre and Marine Bioadhesive Analogs: High-Strength Nanocompoisite by Layer-by-Layer Assembly of Clay and L-3,4-Dihydroxyphenylaianine Polymer.* Advanced Materials, 2007. **19**(7): p. 949-.